Doctoral theses at NTNU, 2020:77

Vibeke Devold Valderhaug

Structure-function relationships in biological neural networks and the influence of neurodegenerative processes on such dynamics

Doctoral thesis

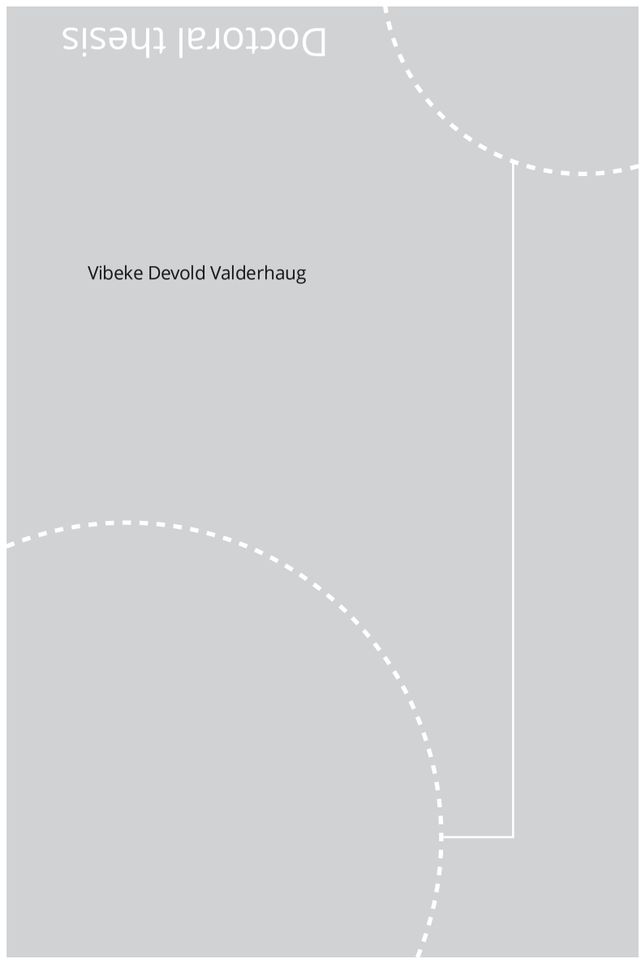

ISBN 978-82-326-4506-0 (printed ver.)
ISBN 978-82-326-4507-7 (electronic ver.)
ISSN 1503-8181

NTNU
Norwegian University of
Science and Technology

NTNU
Norwegian University of Science and Technology
Thesis for the Degree of
Philosophiae Doctor
Faculty of Medicine and Health Sciences
Department of Neuromedicine and Movement
Science

Doctoral theses at NTNU, 2020:77

NTNU
Norwegian University of
Science and Technology

Vibeke Devold Valderhaug

Structure-function relationships in biological neural networks and the influence of neurodegenerative processes on such dynamics

Thesis for the Degree of Philosophiae Doctor

Trondheim, March 2020

Norwegian University of Science and Technology
Faculty of Medicine and Health Sciences
Department of Neuromedicine and Movement Science

NTNU
Norwegian University of
Science and Technology

NTNU
Norwegian University of Science and Technology

Thesis for the Degree of Philosophiae Doctor

Faculty of Medicine and Health Sciences
Department of Neuromedicine and Movement Science

ISBN 978-82-326-4506-0 (printed ver.)
ISBN 978-82-326-4507-7 (electronic ver.)
ISSN 1503-8181

Doctoral theses at NTNU, 2020:77

Printed by NTNU Grafisk senter

Forholdene mellom struktur og funksjon i biologiske nevrale nettverk og hvordan disse påvirkes av nevrodegenerative prosesser

Fokuset for dette vitenskapelige arbeidet ligger på de gjensidige og dynamiske forholdene mellom struktur og funksjon i nevrale nettverk. Det har videre blitt lagt særskilt vekt på hvordan disse forholdene påvirkes av nevrodegenerative prosesser, spesielt tilknyttet Parkinsons sykdom. Gjennom en kombinasjon av strategier har relevante, biologiske nevrale nettverk blitt etablert *in vitro* og benyttet som modellsystem i undersøkelsen av struktur-funksjonsforhold. Av de mest sentrale forhold undersøkt finner man elektrofysiologisk nettverksaktivitet, konnektivitet, «small-worldness», og selvorganisert kritikalitet. Videre har disse forholdene blitt knyttet til uttrykk for Parkinsons-relatert patologi, som nevronal levedyktighet, proteinaggregering, -degradering, samt mitokondriell dysfunksjon.

I den første vitenskapelige artikkelen presentert i denne avhandlingen ble induserte pluripotente stamceller (iPSC) differensiert til nevroner og brukt til å etablere nevrale nettverk på multi-elektrode arrayer (MEA). Den tiltredende elektrofysiologiske aktiviteten ble målt før, og i en periode på tre uker etter, pre-formerte fibriller av alpha-synuclein ble introdusert i media for å indusere Parkinsons-relatert patologi. Disse målingene ble brukt til analyse av nettverksaktiviteten, hvorpå utvikling av patologien viste seg å gi uttrykk i nettverkets kritikalitet, men ikke i standard mål for nettverksfunksjon (som gjennomsnittlig fyringsrate og kryss-korrelasjon).

I den andre vitenskapelige artikkelen benyttes iPSC-deriverte nevroner med og uten den Parkinsons-relaterte genetiske mutasjonen G2019S. Mikrofluidiske plattformer ble brukt til å strukturere parallelle nettverk med og uten integrerte MEAs for måling av nettverksaktivitet. Struktur og funksjon i nettverkene med og uten mutasjon, samt deres respons til en kortvarig overstimulering av diskrete nettverksnoder, ble undersøkt på flere nivå. Resultatene viste at de muterte nettverkene hadde avvik både i struktur og funksjon sammenlignet med nettverkene uten mutasjon, samt at de responderte ulikt på perturberingen.

I den siste vitenskapelige artikkelen benyttes nevrale stamceller fra rotter sammen med biokompatible polymer-partikler for å etablere nevrale nettverk med 3D topologi. Struktur og funksjon av de resulterende nettverkene ble undersøkt og diskutert opp mot det sentrale nettverksbegrepet «small-worldness».

Som bakgrunn for dette forskningsarbeidet ligger hypotesen om at friske og perturberte nevrale nettverk vil utvise ulike egenskaper når det kommer til funksjon og konnektivitet, og at de vil respondere ulikt på patologiske prosesser. I forbindelse med denne hypotesen har materiell for *in vitro* etablering av ulike biologiske nevrale nettverk stått sentralt, samt verktøy for elektrofysiologiske målinger på nettverksnivå, hvilket ble muliggjort av et oppsett for MEA. Videre har flere metoder for lys-, konfokal og superresolusjonsmikroskopi blitt benyttet for å identifisere og avbilde cellulære elementer markert ved hjelp av immunocytokjemi, eller aktive cellulære prosesser i levende cellekulturer.

Navn kandidat: Vibeke Devold Valderhaug
Institutt: Nevromedisin og Bevegelsesvitenskap (INB)
Veileder(e): Ioanna Sandvig, Axel Sandvig og Geir Bråthen
Finansieringskilde: INB og Samarbeidsorganet HMN-NTNU

Ovennevnte avhandling er funnet verdig til å forsvares offentlig for graden PhD i Medisin.
Disputas finner sted i auditorium ØHA11 på Øya Helsehus, 06.03.2020 , kl.10.15.

Acknowledgements

This work was funded by The Department of Neuromedicine and Movement Science, Faculty of Medicine and Health Sciences, as well as The Liaison Committee for Education, Research and Innovation in Central Norway (Samarbeidsorganet HMN), NTNU.

First, I would like to thank Ioanna and Axel Sandvig, for believing in me, and giving me the opportunity to pursuit a PhD in Neuroscience in your research group. Your genuine dedication and enthusiasm towards research, towards me and my fellow students, to our development as independent thinkers, scientific writers, and researchers, is a true inspiration. I would also like to especially thank my main supervisor, Ioanna, for her continued and thorough follow up, feedback, and support. I really appreciate all the space and time you have provided for genuine conversation, concerns, problem solving, and celebration of sometimes small, but important, victories. I have learned a lot from you and look forward to the continuation of our relationship, hopefully both within and outside academia.

To Ola and Roos, thank you for being such wonderful colleagues, for turning lab cries into laughs, and for becoming my lifelong friends. It has been a true pleasure working with and getting to know you, and your team spirit, openness, and willingness to share with and help others has been an inspiration. I would also like to thank Ingrid for bringing me into the lab, for sharing her knowledge, and for being a great friend.

To all the other wonderful people whom I´ve had the pleasure of working with, especially Ulrich, Lars, Vegard, Janelle, Kristine, and Irene, thank you for becoming my friends, for helping me out when I have needed it, for our weird lunchtime conversation, great discussions, dinner parties, lab socials, and willingness to share your knowledge.

To my family, thank you for supporting me and my choices, for always cheering me on, for sharing my frustrations, and for being my safe harbour. To my grandma, Liv, thank you for your expert contribution to the Norwegian summary in this thesis, and for thinking what I do is cool.

To my husband Eirik, thank you for your endless support, for scooping also my share of dog poop, for seeing the solutions when I am blinded by frustration, and for being my reason for going home.

Table of Contents

1. Introduction

1.1 The Central Nervous System (CNS)

1.1.1 Self-organization, Emergence, and Plasticity

The intricate architecture of the human brain emerges through self-organization principles, which collectively orchestrate the shaping of about 100 billion neurons (and about the same number of glial cells), with up to 100,000 synapses each, and 100,000 km of interconnections, into complex, hierarchical neural networks (Hofman, 2014, von Bartheld et al., 2016). The highly specific anatomy and function of the human brain develops under tight molecular control, where inherent, sequential mapping rules dictate the migration routes, differentiation of subtype specific neurons, and targets of axonal projections (Goodman and Shatz, 1993). The largest and most intricately connected part of the mammalian brain is the cerebral cortex, the outermost structure consisting of hierarchically organized, sheet-like arrays of nerve cells in six distinct layers. Two main neuronal subtypes populate it, namely projection neurons and interneurons, which send their axons to distal brain target and locally within circuits, respectively. During early stages of cortical development (corticogenesis), undifferentiated (progenitor) neuroepithelial cells begin to proliferate and differentiate into radial glia, establishing the ventricular zone (VZ) (Haubensak et al., 2004). These cells in turn differentiate, establishing the subventricular zone (SVZ) (Noctor et al., 2004, Noctor et al., 2007) and additional progenitor classes, each of which have distinct morphological properties, patterns of cell division, and further differentiation (Molyneaux et al., 2007). Newly born neurons migrate away from the ventricular zones, establishing the cortex in an inside-out fashion, with early born neurons populating the innermost cortical layers, and later-born neurons migrating past them to progressively populate more superficial layers (Tau and Peterson, 2010, Greig et al., 2013).

Axonal growth and guidance are fundamental parts of the initial establishment of connections between neurons in the brain (Tessier-Lavigne and Goodman, 1996), where spouting neurites extend and engage in a dynamical search for connecting partners. This process relies on the growth cone, a highly specialized structure crucial for cell motility and successful network wiring, situated at the tip of neurites. The growth cone consists of dynamic cytoskeletal elements and a membrane embedded with receptors expertly tuned for navigation and pathfinding based on electrical, chemical- and structural guidance cues present in the environment surrounding the neuron (Song and Poo, 2001, Dickson et al., 2002, Dent and Gertler, 2003, Dent et al., 2011, Bellon and Mann, 2018). Once the target is reached, the growth cone matures into a synapse. Synapses are intercellular junctions specialized for fast, point-to-point information transfer (Sudhof, 2018). The development of astrocytes is spatially and temporally coincident with this process of synaptogenesis in developing neurons, and astrocyte-neuron interactions have been shown to help guide neuronal axons to their destination, as well as to be necessary for synaptic formation, postsynaptic function, stability and maintenance (Ullian et al., 2004, Barker and Ullian, 2008, Pfrieger, 2010, Minocha et al., 2015, Allen and Lyons, 2018). The initial establishment of connectivity is further typified by a transient

overshoot phase, i.e. an overproduction of axons, neuritic branches and synaptic connections (Innocenti et al., 1977, Innocenti and Price, 2005, Bressoud and Innocenti, 1999, Webster et al., 1991, Rakic et al., 1986). During subsequent maturation, a process of selection occurs, in which synaptic pruning and elimination of transient projections ensures the removal of superfluous contacts while functional synaptic connections are retained and further strengthened or modified through activity-dependent mechanisms (O'Leary, 1992, Katz and Shatz, 1996). Microglia serve as "synaptic gardeners" during this process, where they participate in both the formation and scavenging of synapses (Paolicelli et al., 2011, Miyamoto et al., 2016, Ikegami et al., 2019).

The self-organizing process during the initial phase of network establishment is largely activity-independent, while with the emergence of internally generated spontaneous activity, the process becomes activity-dependent/modulated (Katz and Shatz, 1996). Due to the selectively permeable membrane and basic electrochemical properties of single neurons and their interconnections, spontaneous electrophysiological activity emerges and gives rise to a variety of electrical signals that transmit information. With maturation, the developing brain relies progressively less on internally generated spontaneous activity, and increasingly on external experience/ stimuli as the sensory organs mature (Katz et al., 1989, Katz and Shatz, 1996, Hubel and Wiesel, 1970, Hubel et al., 1977, Wiesel and Hubel, 1963). In turn, experience-dependent neural activity in turn further shapes the basic structural and functional components of the brain, i.e. the neural circuits. It guides the formation, elimination and rearrangement of synapses to establish functionally connected and organized ensembles of neurons that process specific kinds of information. Furthermore, different regions of the brain are further sub-organized into discrete structural and functional areas that are specialized for hierarchical and parallel processing, as well as integration, of different sensory and motor modalities.

Both the anatomical and functional architecture of brain neural circuits are plastic. Neuroplasticity, i.e. the brain´s innate capacity for adaptation, is key in self-organization and influences the process of neural network wiring and rewiring at several levels during development. Moreover, in this capacity for change also lies our ability to acquire and incorporate new skills, information and experiences into an already existing meshwork of circuitry, as entire neural circuits can be remodeled, functional areas can be remapped, and the connections between neurons can be modulated, removed, or created through activity dependent, Hebbian-like or homeostatic processes throughout life (Hubel and Wiesel, 1970, LeVay et al., 1980, Lo, 1995, Bear and Malenka, 1994, Turrigiano et al., 1998, Abbott and Nelson, 2000, Albert and Barabasi, 2000, Turrigiano and Nelson, 2004, Turrigiano, 2008, Turrigiano, 2012, Majewska and Sur, 2006, Blackman et al., 2012). Hebbian and homeostatic plasticity work in tandem to refine neural circuit function, where the strengthening and weakening of synapses determined by coincidence of firing in classical Hebbian mechanisms are counterbalanced by local and global homeostatic plasticity mechanisms serving to balance and maintain circuit activity and function (Turrigiano, 2012). Furthermore, glial cells play major roles in such plasticity processes not only during development, but also in the mature brain, where microglia continuously regulate the number of functional synapses (Ji et al., 2013),

oligodendrocytes dynamically regulate myelination and thus conduction velocity in specific circuits in response to neuronal signals (Almeida and Lyons, 2017, Allen and Lyons, 2018), and astrocytes stabilize, eliminate, and modify synaptic connections (Pfrieger, 2010, Adamsky et al., 2018, Allen and Lyons, 2018).

The self-organization and plasticity of the central nervous system (CNS) is of great importance as the structural connectivity of the brain, i.e. the pattern of anatomical axons interconnecting local and distal neuronal ensembles, inherently shapes the functional capacity of the neural networks (Laughlin and Sejnowski, 2003, Avena-Koenigsberger et al., 2017). The length of the axonal fibers for instance, i.e. the distance a signal has to travel between interconnected distal nodes in the network, puts physical constrains on the maximum processing speed of the system. The sharing of information between anatomically and functionally segregated neural circuits or areas in the brain has been shown to be mediated through a few reciprocal, long-range connections or pathways, which allow for dynamic interaction between neuronal clusters over large distances (Gilbert and Wiesel, 1989, Kaiser and Hilgetag, 2006, Sporns et al., 2004). Structural connectivity thus shapes the functional connectivity, i.e. the large-scale patterns of temporal correlations and co-activation that can be generated through these dynamical interactions across the brain. This topic is further discussed in the next section.

1.1.2 Structure-Function relationships and Self-Organized Criticality

Simultaneous capacity for information segregation and integration are the two main neural network phenomena in the brain that are recognized as the basis of behavior (Zeki and Shipp, 1988, Tononi et al., 1998, Sporns et al., 2000a, Sporns et al., 2000b, Sporns et al., 2004, Tognoli and Kelso, 2014). These collective network phenomena naturally develop from the spontaneous electrophysiological activity of neural networks, termed "emergent network behavior". Computational functions which are segregated, both spatially and temporally, into functional modules in the brain are dynamically engaged and disengaged through transient phase or frequency locking, and thus integrated into transitory coordinated global functions (Tognoli and Kelso, 2014, Sporns et al., 2000a). Furthermore, the dynamic and plastic self-organizing processes underlying this function are hypothesized to drive the activity of the brain towards a "critical state" (Freeman and Holmes, 2005, Rubinov et al., 2011, Shew and Plenz, 2013, Hesse and Gross, 2014, Valverde et al., 2015, Massobrio et al., 2015, Langton, 1990). This is a universal feature of any spatially extended dynamic system stemming from the physics of phase transitions (Bak et al., 1988). Self-organized criticality (SoC) represents the state of optimal function and computational capability, the critical point between resilience against perturbation and adaptational flexibility, which appears without the need for fine-tuning of parameters (Tetzlaff et al., 2010, Hesse and Gross, 2014, Rybarsch and Bornholdt, 2014, Massobrio et al., 2015, Valverde et al., 2015, Yada et al., 2017, Pasquale et al., 2008, Muñoz, 2018, Hoffmann and Payton, 2018). This dynamic state is characterized by cascades of spontaneous activity with power-law size distributions, which is electrophysiologically measurable in neural networks and termed "neuronal avalanches" (Bak et al., 1988, Beggs and Plenz, 2003, Beggs and Plenz, 2004, Tetzlaff et al., 2010, Friedman and Landsberg, 2013, Moretti and Munoz, 2013). Although a "true" point of criticality does not exist in any finite system, the brain shows evidence of a critical-like region (Moretti and Munoz, 2013, Muñoz, 2018), within which

certain qualities diverge and a rapid transition between different states can be maintained, such as in brain synchronization transition (Tognoli and Kelso, 2014). Several lines of evidence exist for criticality in the brain (Ribeiro et al., 2010, Tagliazucchi et al., 2012, Gautam et al., 2015, Stoop and Gomez, 2016, Clawson et al., 2017, Daffertshofer et al., 2018), where functional advantages in signal detection and processing are gained within such a critical-like activity region (Shew and Plenz, 2013, Muñoz, 2018).

As already highlighted, the functional dynamics of complex systems like the brain are highly influenced by the systems underlying structural architecture. Several studies have shown that the neural networks in the brain exhibit a "small-world" organization, a network configuration characterized through high local clustering and short path lengths between any distant pair of nodes (clusters of neurons), the latter arising from relatively few, long-range connections (Watts and Strogatz, 1998, Zeki and Shipp, 1988, Sporns et al., 2000a, Bassett and Bullmore, 2006, Bassett and Bullmore, 2017). This organization has major implications for the behavior of the network, allowing for the simultaneous specialization/segregation and distribution/integration characteristic of information processing in the brain. The majority of connections are short, reflecting local processing of information as well as spatial and energetic constraints, while long-range connections enable integration of information between spatially segregated neuronal ensembles, providing both complexity and redundancies that promote robustness (Latora and Marchiori, 2001, Betzel and Bassett, 2018). By application of graph-theory, i.e. treating functional and/or structural clusters in the brain as nodes and their connections as links in a graph, this topological organization is visible both in structural and functional measures of the human brain, at several scales (Sporns et al., 2000a, Sporns et al., 2000b, Bassett and Bullmore, 2006, Bassett and Bullmore, 2017, Bullmore and Sporns, 2009).

1.1.3 CNS DAMAGE AND NEURODEGENERATION

In the healthy mature brain, structural and neurochemical alterations which naturally occur are compensated for through for instance reorganization and redistribution of functional circuits, as well as recruitment of additional cortical and subcortical areas, in order to maintain performance levels (Johansson, 2004, Ward and Frackowiak, 2003, Talelli et al., 2008, Mattay et al., 2006, Mattay et al., 2002). This natural development is as such dependent on the ability to adapt, repair and remodel neural circuits, as well as on the capacity for behavioral compensation (Lo, 2010). However, in the face of damage or disease which disrupts the structure and function of neural circuits, the regenerative capacity of the adult human brain is severely restricted. This limited regenerative capacity is partly related to the neurogenic capability of the mature human brain, i.e. the capacity for producing new neurons to repopulate affected neural circuits. This capacity is minimal, confined to a few specialized regions, and decreasing with age (Gage, 2000, Ming and Song, 2011, Zhao et al., 2008). Another limiting factor to CNS regeneration relates to the intrinsic mechanisms of axonal regrowth, which contrary to the peripheral nervous system (PNS), where they can lead to spontaneous and robust regeneration and functional recovery, these intrinsic capabilities are limited while they are also hampered by and inhibitory factors in the tissue environment and the poor neurogenic capacity of the adult CNS (Chen et al., 2007, Liu et al., 2011, Schwab and Strittmatter, 2014, Mahar and Cavalli, 2018). In contrast to adult neurons in the PNS, adult neurons of the CNS fail to

reactivate intrinsic growth programs after injury (Chen et al., 2007, Tedeschi and Bradke, 2017). These regenerative processes are also affected by the complexity and size of the neural circuit, where newly generated neurons have to migrate from confined neurogenic niches, i.e. from the SVZ and sub granular zone (SGZ), to local and distal sites of damage in the brain, while sprouting axons and nerve fibers need to regrow over long distances. Furthermore, regenerating neurons often have to traverse non-permissive signaling environments expressing growth inhibitory factors such as Nogo, which collapse the growth cone and stop neurite elongation (Schwab and Strittmatter, 2014). Other prominent extrinsic barriers also exist, such as neuroinflammation (Glass et al., 2010) and the glial scar (Silver et al., 2014). Moreover, regenerating neurons have to form functional synapses with regional specificity and fidelity of connections, as well as remyelinate, and integrate into already established, complex neural network circuitry in an adaptive way (Fornito et al., 2015, Lo, 2010, Tedeschi and Bradke, 2017).

Glial cells are also heavily involved in the regenerative capacity of the CNS. The structural plasticity in white matter (myelinated regions of the brain) for instance, is known to be much lower than in gray matter (unmyelinated regions), and oligodendrocyte myelin has been found to be enriched with potent growth inhibitory factors such as Nogo, myelin-associated protein (MAG) and oligodendrocyte-myelin glycoprotein (OMgp) (Sandvig et al., 2004, Zatorre et al., 2012, Silver et al., 2014). Furthermore, CNS disruption causes immune cell infiltration and inflammatory reactions by rapidly responding astrocytes and microglia, which release pro- or anti-inflammatory factors depending on the evolution of pathology over time (Hirsch and Hunot, 2009, Lucin and Wyss-Coray, 2009, Glass et al., 2010). Although immunological and inflammatory responses are part of a tissue repair process, sustained or uncontrolled inflammation is harmful, where for instance the release of proinflammatory cytokines by microglia has been linked to precipitation of cell death in several neurodegenerative diseases such as Parkinson's disease (PD) Alzheimer's disease (AD), and Amyotrophic lateral sclerosis (ALS) (Mount et al., 2007, Boillee et al., 2006, Lucin and Wyss-Coray, 2009).

In the case of neurodegenerative disease, in which neurons and their interconnections are progressively affected and lost, several homeostatic and regenerative mechanisms may be initially engaged in maintaining the normal function of the perturbed circuits. However, as progressively more neurons degenerate, with limited endogenous means of regenerating the affected circuits, restoring function becomes increasingly difficult. At some point, disease pathology overcomes these endogenous efforts of compensation and stabilization. As a result, diagnosis after advanced neurodegeneration is already prominent is a common issue in neurodegenerative disease, where mainly the homeostatic plasticity mechanisms are believed to mask the initial development, hindering symptoms of dysfunction from becoming prominent until later in disease progression (Lo, 2010). In PD for instance, the clinical symptoms have been shown to lag behind the pathological changes in the brain (Kordower et al., 2013), resulting in PD patients being diagnosed after a significant proportion (30%) of the dopaminergic neurons in the substantia nigra pars compacta (SNpc), and an even larger amount (50-70%) of their striatal terminal (Cheng et al., 2010), have already been lost to degeneration, posing irreparable damage to both the structure and function of the affected circuitry.

The effect of structural damage on function, and *vice versa*, in neural networks has also been investigated within the field of connectomics, which aims to produce a comprehensive map of all neural elements and connections of the brain, where the level of interconnectivity in the brain has been shown to inherently shape how it responds to perturbation (Tononi et al., 1998, Young et al., 2000, Breakspear and Stam, 2005, Bullmore and Sporns, 2009, Fornito and Bullmore, 2015, Fornito et al., 2015). By using neuroanatomical data for modelling, functional impairment has been found to be highly correlated with the number of direct projections between the lesion site and the affected node, and the number of connections in a given neuronal structure to determine both its impact on other structures as a lesion site, as well as its vulnerability to lesions originating elsewhere in the network. Importantly, functional impairments have also been found to spread well beyond the direct projections in a network, affecting distal nodes indirectly linked to the lesion site (Young et al., 2000), a mechanism which was termed diaschisis by von Monakow already in 1914 (Wiesendanger, 2006). This means that the interconnectivity of the particular brain regions affected by damage or disease, such as the dopaminergic neurons in the SNpc of PD patients, critically affects how the pathology develops and functionally affects the individual (Honey and Sporns, 2008, Alstott et al., 2009, Kitsak et al., 2010, Raj et al., 2012, Zhou et al., 2012, Fornito et al., 2015). Furthermore, these findings highlight the importance of understanding network disturbances, such as those posed by neurodegenerative diseases, as disruptions of complex interconnected systems, not as discrete pathology localized only to a specific sub-region of the brain (Fornito and Bullmore, 2015).

Further corroborating the importance of the structure-function relationships in the context of disease development, the small-world architecture of the brain has been shown to propagate pathology more easily than other network architectures (Moore and Newman, 2000). Intriguingly, this likely relates to the manifestation and progression of several neurodegenerative diseases, such as PD, AD, and ALS. Although the mechanistic triggers and aetiologies of these diseases may be different and largely unknown, a shared feature in all of the above is the characteristic development of abnormal aggregates of specific proteins, i.e. proteinopathies, and the progressive patterned spread of pathology through seemingly selectively vulnerable neuronal populations to other interconnected neural networks (Braak and Braak, 1991, Braak et al., 2002, Braak et al., 2003a, Braak and Del Tredici, 2009, Kipps et al., 2005, Arai et al., 2006, Andersen, 2006, Andersen et al., 1996, Ash et al., 2013, Bidhendi et al., 2016). Proteinopathy refers to the phenomenon in which a native protein misfolds and undergoes a conformational change, a structural switch from which toxic protein species result (Verma et al., 2015). In PD, intracellular Lewy bodies and Lewy neurites are characteristic of the disease, and mainly consist of aggregated forms of alpha-synuclein, while the plaques and neurofibrillary tangles constituting neuropathological hallmarks of AD mainly consist of amyloid beta (Aβ) and hyperphosphorylated tau proteins. In ALS, several different proteins have been found to accumulate depending on the nature of the mutation (such as tar-DNA-binding protein 43 (TDP-43), fused-in-sarcoma (FUS) and superoxide dismutase 1 (SOD1) and C90rf72). Each of these distinct protein aggregates have been hypothesized to act as “seeds of pathology” that propagate through interconnected areas, causing the progressive spread of disease between CNS regions in a prion-like fashion (Verma et al., 2015, Goedert et al., 2017).

These neuropathological protein aggregates have been found to localize, early in disease progression, to neuronal structures and neuronal subtypes believed to be selectively vulnerable, such as the SNpc in PD, the entorhinal cortex in AD, and to the upper- and/or lower motor neurons in ALS. From these selectively vulnerable sites the "seeds of pathology" are hypothesized to subsequently spread to highly interconnected brain regions in a topographical progression (Braak and Braak, 1991, Braak et al., 2003a, Braak et al., 2003b). Although several possible routes exist, axonal and synaptic contacts in particular have been hypothesized to act as the sites of propagation for such disease processes. In line with this notion, characteristic staging of CNS pathology has been found in AD, PD, and ALS (Braak and Braak, 1991, Braak et al., 2003b, Golde et al., 2013, Turner and Swash, 2015, Bidhendi et al., 2016, Ekhtiari Bidhendi et al., 2018, De Vos and Hafezparast, 2017, Kwiatkowski et al., 2009).

1.2 Neural network modelling

In vitro neural networks represent a highly valuable modelling approach when it comes to elucidating principles governing both the structure and function of brain neural networks in healthy and diseased states. The following sections focus on the aspects of CNS development and structure-function relationships that are recapitulated by *in vitro* neural networks, and the different sources for establishing human neural networks *in vitro*.

1.2.1 Recapitulation of Self-Organization and Emergent network activity

In vitro neural networks recapitulate two fundamental principles of neural network behavior in the developing brain, namely self-organization and emergent network activity. When neural lineage cells are seeded onto the surface of a cell culture vessel, they undergo a spatiotemporal organization, where their motile and sprouting neurites are extended within hours and, guided by the growth cone, dynamically engage in the search of a connecting partner. This innate neural outgrowth and pathfinding behavior is encoded into neurons, and is part of the initial phase of both CNS wiring and *in vitro* network formation. As in CNS development, the initial phase of establishing connections is followed by a network overshoot phase (Innocenti and Price, 2005), characterized by strong neuronal outgrowth and synaptogenesis, creating an over-expression of branches and synaptic boutons that results in a transient phase of overconnectivity in the network. During subsequent maturation, synaptic pruning and homeostatic scaling occur, in which superfluous synaptic contacts are removed while functional synaptic connections are strengthened or modified through activity-dependent mechanisms (Giugliano et al., 2006). As in the developing brain, this self-organizing process during the initial phase of network establishment is largely activity-independent, while with the emergence of spontaneous activity, the process becomes activity-dependent /modulated. Correlated with the phases of structural self-organization, *in vitro* neural networks exhibit several forms of spontaneous electrical activity measurable through electrophysiology techniques, such as multielectrode arrays (MEAs). The initial phase of network formation and wiring is largely characterized through no or uncorrelated firing. This activity further develops into sporadic or clustered action potentials from single cells, and is followed by a period of synchronous regular bursting

activity. After this, a more complicated, non-periodic network pattern emerges, a form of activity which represents the "mature" state of the network.

Further expanding on the structure-function relationships recapitulated by *in vitro* neural networks, there is accumulating evidence of the characteristic small-world organization of the brain also emerging in maturing neural networks *in vitro* (Bettencourt et al., 2007, Srinivas et al., 2007, Massobrio et al., 2015, Poli et al., 2015, Pasquale et al., 2008). As previously mentioned, this network configuration has major functional implications, and is particularly relevant in the context of studying neurodegeneration and related spread of pathology, as this network architecture has been shown to propagate pathology and disease more easily than other network configurations (Moore and Newman, 2000). Furthermore, certain features of network activity, such as neuronal avalanches, which are measurable through the use of MEAs, can be used to determine whether the network is in a critical state (Beggs and Plenz, 2003, Beggs and Plenz, 2004, Massobrio et al., 2015, Michiels van Kessenich et al., 2016). As in any other spatially extended dynamic system, *in vitro* neural networks approach a state of SoC with maturation (Bak et al., 1988, Tetzlaff et al., 2010, Hesse and Gross, 2014, Massobrio et al., 2015, Valverde et al., 2015, Yada et al., 2017, Muñoz, 2018).

1.2.2 Sources for generating neural networks in vitro

In 2006, the retroviral introduction of 4 factors (Oct3/4, Sox2, c-Myc and Klf4) was shown to successfully reprogram adult mouse fibroblasts into induced pluripotent stem cells (iPSC)(Takahashi and Yamanaka, 2006). Not long after, adult human fibroblasts were successfully reprogrammed into iPSCs (Takahashi et al., 2007, Yu et al., 2007), a finding which has had a significant impact on neuroscience. iPSCs are similar to embryonic stem cells as the important capabilities of unlimited self-renewal and potential for production of cells originating from all three germ layers (pluripotency) are retained. Importantly, this successful fate reversion from terminally differentiated, adult, somatic cells back to a stem cell state has opened up new possibilities for studying complex human conditions *in vitro*, as patient-specific iPSCs can be derived from minimally-invasive skin cell biopsies or blood cells. This morphogenetic neuroengineering approach has led to the establishment of several methods for induction and differentiation of iPSCs or embryonic stem cells into neurons (Pereira et al., 2014, Chambers et al., 2009), and further into subtype-specifications such as dopaminergic-, spinal motor- and cortical neurons (Doi et al., 2014, Kriks et al., 2011, Kirkeby et al., 2012a, Kirkeby et al., 2012b, Sanchez-Danes et al., 2012a, Arenas et al., 2015, Sances et al., 2016, Amoroso et al., 2013, Maroof et al., 2013). Moreover, as neurodegenerative diseases like PD, AD, and ALS are human-specific conditions that have no naturally existing equivalent in any other species, basing disease modelling systems on human tissue sources could hold great potential for knowledge advancement.

By incorporating strategies for targeted genetic alterations such as CRISPR-Cas9 (Horvath and Barrangou, 2010, Jinek et al., 2012, Pennisi, 2013), identified genetic disease-related mutations can be corrected or inserted for *in vitro* modelling purposes (Kime et al., 2016). Furthermore, such an approach could hold promise for allogenic transplantation (Raikwar et al., 2019), where the patient's own genetically corrected cells can be differentiated into subtype-specific cells

and transplanted back where they are needed. However, concerns are rightfully raised about the safety of transplanting iPSC-derived cells, as their defining trait of unlimited self-renewal and potential for becoming every cell type in the body effectively means that they can produce teratomas, i.e. cancer. Furthermore, reprogramming through the iPSC stage has been shown to remove the epigenetic and age-related imprint, which rejuvenates the resulting cells by telomerase lengthening, effectively preventing chromosome aging and allowing for indefinite expansion in culture (Lapasset et al., 2011, Patterson et al., 2012). The continuous proliferation makes them very suitable for experiments, however, the characteristics and morphology of the cells change after several passages, and the cells may eventually express genetic patterns not found *in vi*vo. Some of these unfavorable characteristics have led to the establishment of several methods for "direct conversion", where the intermediate iPSC stage can be circumvented, and mature somatic cells can be reprogrammed directly into (more fate-restricted) neurons or sub-type specific neurons (Vierbuchen et al., 2010, Caiazzo et al., 2011, Yoo et al., 2011, Pfisterer et al., 2011, Karow et al., 2012, Dai et al., 2015). Direct conversion retains the epigenetic imprint of the source material (Mertens et al., 2015, Huh et al., 2016, Lu and Yoo, 2018), which enables the *in vitro* recapitulation and investigation of other key aspect of neurodegeneration, namely epigenetic mechanisms as well as age-dependency.

1.2.3. Measuring electrophysiological neural network activity using Multielectrode Arrays (MEAs)

The most widely used MEAs for measurement of neural network activity *in vitro*, are planar MEAs, the first of which was described as early as 1972 (Thomas et al., 1972). MEAs usually consist of a substrate coated cell culture chamber embedded with an array of electrodes, on top of which neural networks can be seeded and their spontaneous, extracellular electrophysiological activity can be simultaneously recorded with minimal interference *in vitro.* These platforms allow for long-term, population-based activity measurements with submillisecond resolution, acquiring electrophysiological signals within the frequency domain of both local field potentials (1-300Hz) and extracellular action potentials (300-3000Hz), i.e. spikes, with a sampling rate of up to 50kHZ per second. The spatial resolution of the acquired signal is determined by the number, spacing, and receptive field of the electrodes. The most commonly used MEAs have 60 electrodes with 100-200µm interelectrode spacing, where each electrode can detect spikes up to 50µm away from the cell body, as well as deliver local electrical stimulation. Several factors can influence the quality of the recordings and the neural network activity, however, such as impedance of the electrodes and noise, as well as physiological factors like temperature and metabolic state of the culture, which need to be considered when planning MEA based experiments.

1.3. Studying neural network structure-function relationships in the context of PD-related neurodegenerative processes

Through a combination of *in vitro* neural network-based strategies, several aspects of structure-function relationships, such as network topology, plasticity, criticality, and small-worldness, have been investigated and applied within the context of neurodegenerative disease processes for this thesis. PD represents the second most common neurodegenerative disease after AD and other dementias (Feigin et al., 2017, Dorsey et al., 2018), and its related pathologies in particular

have been selected to study neurodegenerative processes and their effect on neural network structure-function relationships. As highlighted in other sections of the introduction, PD shares many features with other neurodegenerative diseases such as AD and ALS, including proteinopathy and topographically patterned development of disease related pathology, which progressively spreads from seemingly selective vulnerable neuronal populations to other interconnected neural networks. Furthermore, PD is age-related, idiopathic and primarily sporadic, three complicating facts shared with most other neurodegenerative diseases.

PD is a heterogenous disease, characterized by a range of neurological symptoms such as difficulty with initiating and sustaining movement, resting tremors, rigidity, muscle stiffness and postural changes. Other symptoms include impaired olfactory function, constipation, sleep disturbances, dementia, depression, apathy and anxiety, as well as impairments in executive functions such as problem solving and planning (Rodriguez-Oroz et al., 2009, Kouli et al., 2018). These symptoms arise as a consequence of a neurodegenerative process, wherein the dopaminergic neurons in the SNpc are particularly affected and progressively depleted. Although some prodromal mild impairments can be detected up to 10-14 years prior to diagnosis (Postuma et al., 2012, Darweesh et al., 2017), the motor symptoms of PD only manifest clearly after about 30% of the SNpc dopaminergic neurons and 50-70% of their striatal terminals are lost, which complicates and limits treatment options for PD patients as they are generally diagnosed late in the disease progression (Cheng et al., 2010). This onset of cardinal motor symptoms further correlates with the point where the dopamine concentration in the motor region of the striatum falls below 60-70% (Rodriguez-Oroz et al., 2009).

Although the movement related impairments of PD are largely ascribed to the characteristic loss of dopaminergic neurons in the SNpc, and the degeneration of the nigrostriatal (dorsal striatal) pathway, the disease is much more systemic, affecting both the mesolimbic dopaminergic pathway (ventral striatal) pathway, the mesocortical pathway, as well as several other neuronal populations throughout the brain as it progresses (Verstreken, 2017). Furthermore, the non-motoric symptoms of PD are linked to widespread alpha-synuclein inclusions in both central, peripheral and autonomic parts of the nervous system, as well as in multiple organs, illustrating the multisystem involvement of the disease (Goedert et al., 2013, Jellinger, 2014).

To reiterate a key point, protein aggregates, such as the fibrillary or misfolded forms of alpha-synuclein proteins in PD, are hypothesized to act as the pathogenic seeds propagating neurodegenerative processes through highly interconnected areas, spreading self-propagating pathology from particularly vulnerable network sites and neuronal subtypes (Spillantini et al., 1997, Verma et al., 2015, Del Tredici and Braak, 2016, Goedert et al., 2017, Surmeier et al., 2017a, Surmeier et al., 2017b, Alegre-Abarrategui et al., 2019, Mehra et al., 2019). Perhaps the most compelling proof of this spread between interconnected brain regions, are the reports from transplantations of human foetal midbrain tissue into the striatum of Parkinson's disease patients, which provide strong evidence for host-to-graft disease propagation. Autopsies obtained 10 years post-transplantation revealed that 2%-5% of the grafted cells contained alpha-synuclein inclusions, while as much as 11%-12% of the grafted cells exhibited alpha-synuclein inclusions after 24 years (Kordower et al., 2008, Li et al., 2008, Li et al., 2016).

The initial hypothesis of propagating pathology was put forward by Heiko Braak and colleagues in relation to sporadic PD (Braak et al., 2002, Braak et al., 2003a). " Braak's hypothesis" was based on numerous brain autopsies showing that the characteristic alpha-synuclein inclusions, i.e. Lewy body (LB) and Lewy neurites (LN), begin developing at early time-points in the brains of PD patients, before any noticeable somatomotor dysfunction, and that they seemingly spread to anatomically highly interconnected brain structures in an "evolving topographical progression". Subsequently, as the first signs of alpha synuclein inclusions were found in the nasal cavity and the gut, where the olfactory receptor neurons and gut branches of the vagal nerve are exposed to exogenous molecules from the outside world, an unidentified pathogen originating outside the CNS was hypothesized to initiate sporadic PD (Braak et al., 2003b). Such a pathogen could be taken up in the extraneuronal space and either be carried directly, or initiate a proteinopathic conformational change in endogenous alpha-synuclein which again could be carried, via axonal transport and transmitted transneuronally through selectively vulnerable neuronal subtypes (Braak et al., 2003b, Braak et al., 2006, Hawkes et al., 2007, Hawkes et al., 2009, Del Tredici and Braak, 2016).

In the first research paper included in this thesis, alpha-synuclein pathology has been induced in human iPSCs-derived neurons through the addition of alpha-synuclein pre-formed fibril (PFF) seeds to study the impact of this neurodegenerative process on network function and network criticality state. Functional network measurements are enabled through the use of MEAs, which allow for the electrophysiological measurement of network activity. In animal models of PD, it has been shown that a single synthetic PFF seed is enough to spread pathological alpha-synuclein through cell-to-cell transmission from the intrastriatal inoculation site to interconnected frontal-, thalamic- and neocortical areas (Luk et al., 2012a, Luk et al., 2012b). *In vitro* studies using primary neuronal cultures from rodents have also shown that alpha-synuclein PFFs can spread intercellularly between connected neural networks (Volpicelli-Daley et al., 2014). This neuron-to-neuron transfer or release of alpha-synuclein can be mediated through different pathways, comprising intracellular axonal transport (Freundt et al., 2012), intercellular cargo transportation through lysosomes in tunneling nanotubes (TNTs) (Abounit et al., 2016), and exosome release or direct exocytosis (Bieri et al., 2017).

Moreover, the development of PD is believed to be caused by a combination of both genetic susceptibility and environmental factors as the vast majority (95%) of cases are sporadic, while only about 5% of PD cases can be definitely linked to a genetic cause. Age represents the greatest risk factor with a prevalence of 1% in the population over the age of 60, and 4% in the population over the age of 85(Lees et al., 2009, Deng et al., 2018). Large cross-cultural variations also exist, with individuals from Europe, North- and South America having a higher prevalence of PD than other populations (Kalia and Lang, 2015). Some environmental factors have also been implicated in PD, where exposure to pesticide and herbicides are correlated with an increase in the risk of developing PD, while cigarette smoking and coffee drinking is correlated with a reduced risk (Kouli et al., 2018, Ball et al., 2019). Genetic predisposition also plays a significant role, where mutations in 23 so called PARK genes have been linked to PD to date (Deng et al., 2018).

Although several genes have been linked to PD, the pathogenic variants of one gene in particular, the leucine-rich repeat kinase 2 (LRRK2), have been termed a potential “Rosetta stone” of the disease, as it exhibits (i) all the major pathologies related to parkinsonism, as well as (ii) end-stage variability in pathology even within families carrying the same pathogenic variant (Zimprich et al., 2004, Joanne Trinh et al., 2006, Wider et al., 2010, Cookson, 2015, Lewis, 2019). In the second research paper presented in this thesis, the particular G2019S mutation in the ROC-COR domain of the LRRK2 protein, which has been linked to both familial and sporadic forms of PD, and which is common in certain populations (Ozelius et al., 2006, Djaldetti et al., 2008, Lewis, 2019), was chosen as a basis for investigating structure-function relationships in human neural networks carrying a PD-related genetic modification. Equivalent neural networks with and without this mutation were structured using microfluidic chips interfaced with MEAs, a set-up which allowed for the simultaneous observation of both structural and functional network aspects. Furthermore, in line with the notion that PD might develop though a combination of genetic and environmental factors, confined parts of these structured neural networks were transiently subjected to chemical overexcitation, and micro- and mesoscale responses were monitored.

The third research paper presented in this thesis relates more directly to network topology. As disease has been shown to spread more effectively within networks with a small-world architecture (Moore and Newman, 2000), we investigate the topological effect of structuring neural networks using surface-grafted polymer particles.

2. AIMS AND OBJECTIVES

The overarching aim of this thesis was to investigate dynamic structure-function relationships in biological neural networks at the micro- and mesoscale with special focus on the influence of neurodegenerative processes on such relationships in the context of Parkinson´s disease.

The work is based on the underlying hypothesis that healthy and perturbed neural networks demonstrate different emergent behavior in terms of function and connectivity and also respond differently to pathology in terms of critical states.

Thus, the main objectives of this work were (i) the application of advanced disease modelling for the recapitulation and study of relevant pathological processes *in vitro,* and (ii) the identification and extraction of key morphology-activity relationships at the micro- and mesoscale. Identification and extraction of such relationships in the face of ongoing pathological neurodegenerative processes in biologically relevant neural networks is highly relevant for understanding early disease onset and mechanisms and, as such, can significantly improve our ability to develop novel, clinically relevant interventions.

3. Synopsis of Results

Paper 1: Criticality as a measure of developing proteinopathy in biological human neural networks

Authors: Vibeke D. Valderhaug, Kristine Heiney, Ola Huse Ramstad, Geir Bråthen, Wei-Li Kuan, Stefano Nichele, Axel Sandvig, and Ioanna Sandvig

Submitted to Frontiers in Neural Circuits (19.11.2019)

Background
The presence of proteinopathy and the patterned spread of pathology through selectively vulnerable neuronal populations represent commonalities in neurodegenerative diseases such as PD, AD and ALS. The aim of this study was to investigate whether the developing alpha-synuclein proteinopathy characteristic of PD was reflected in functional measures of network activity, and whether they could be related to the network state of self-organized criticality.

Methods
Human iPSCs were reprogrammed *in vitro* into neurons (Kirkeby et al., 2012b, Kirkeby et al., 2016, Doi et al., 2014), and seeded onto multielectrode arrays (MEAs) (n = 8). Seeds of pre-formed alpha-synuclein fibrils (PFFs) were introduced to the media of mature networks to induce alpha-synuclein pathology, while control neural networks received either PBS or alpha-synuclein monomers (Volpicelli-Daley et al., 2011, Volpicelli-Daley et al., 2014, Polinski et al., 2018, Tanik et al., 2013). The developing activity of all neural networks was monitored prior to, and for three weeks following this point of perturbation.

Results
Induced pathology was verified ultrastructurally by transmission electron microscopy through the identification of intracellular fibrils and inclusion bodies, as well as necrotic and apoptotic extracellular elements. Analysis of developing electrophysiological network activity revealed no clear difference between PFF treated and control cultures in standard functional measurements such as mean firing rate, cross-correlation, inter-spike intervals, or population inter-spike intervals. Assessment of criticality however, revealed a trend in alteration of network criticality states between the PFF and PBS controls, where the PFF networks largely ended up in a critical state, while the PBS controls ended up in a largely non-critical state.

Conclusions
This study shows that although the developing pathology is not clearly manifest in standard measurements of network function, it is expressed in network criticality states. Furthermore, the results suggest that induction of PD-related proteinopathy alters the developmental trajectory of the neural networks in relation to SoC.

PAPER 2: STRUCTURAL AND FUNCTIONAL ALTERATIONS RELATED TO THE LRRK2 G2019S MUTATION REVEALED IN STRUCTURED HUMAN NEURAL NETWORKS

Authors: Vibeke Devold Valderhaug, Rosanne van de Wijdeven, Ola Huse Ramstad, Kristine Heiney, Stefano Nichele, Axel Sandvig, and Ioanna Sandvig

Manuscript under revision by The European Journal of Neuroscience (EJN) (submitted 18.07.2019)

Background
The pathogenic variants of the leucine-rich repeat kinase 2 (LRRK2) gene has been termed a potential "Rosetta stone" of PD. Although rare, the particular G2019S variant has been shown to contribute uniquely to both familial and sporadic forms of the disease. The aim of this work was to study the effect of the G2019S mutation on the structure-function relationships of developing neural networks *in vitro*, and to investigate whether possible mutation-related features would emerge following a stressful challenge.

Methods
Human iPSC-derived neural stem cells with and without the LRRK2 G2019S mutation were structured using three-nodal microfluidic chips, some of which were also interfaced with MEAs. Following baseline neuronal activity measurements, a single, transient, confined overexcitation event was elicited in the networks using kainic acid (KA) (or PBS for controls), and the resulting structural and functional network responses were monitored immediately after, and at 24 hours following the stressful challenge.

Results
Baseline electrophysiology measures revealed a consistent difference in activity between the two groups, with LRRK2 neural networks exhibiting a 2-fold mean firing rate (MFR) compared to the control neural networks (average 4.5 vs 2 spikes/sec), while simultaneously displaying a lower total network correlation ($r = 0.085$ vs $r = 0.12$). Furthermore, light microscopy, immunocytochemistry, as well as live imaging of active mitochondria (using tetramethylrhodamine) revealed a much greater density of neurites and number of active mitochondria within the axonal compartments of the LRRK2 networks compared to the controls. Following the sublethal KA stimulation, the control neural networks displayed a more prominent reduction in active mitochondria and MFR, as well as increased neuritic remodeling and synaptic alterations 24 hours later, compared to the LRRK2 neural networks.

Conclusions
We provide the first evidence of increased neuritic density related to the G2019S mutation, where the aberrant neuritic profile interconnecting these neuronal networks likely affects neurotransmission efficacy, perhaps explaining the elevated MFR and simultaneous low correlation observed compared to controls. Together with the difference observed between the mutated and control neural networks following the KA stimulation, these results suggest impaired axonal growth, guidance, and synaptic plasticity, related to the G2019S mutation.

PAPER 3: FORMATION OF NEURAL NETWORKS WITH STRUCTURAL AND FUNCTIONAL FEATURES CONSISTENT WITH SMALL-WORLD NETWORK TOPOLOGY ON SURFACE-GRAFTED POLYMER PARTICLES

Authors: Vibeke D. Valderhaug, Wilhelm Robert Glomm, Eugenia Mariana Sandru, Masahiro Yasuda, Axel Sandvig and Ioanna Sandvig

Published in the journal Royal Society Open Science (23.10.2019); Vol.6, issue 10; https://doi.org/10.1098/rsos.191086

Background

Although standard *in vitro* neural network modelling systems capture many qualities of neural networks *in vivo*, the basic three-dimensionality of the brain represents a largely disregarded feature. In this study, we combine *in vitro* neural cell culture with a biologically compatible scaffolding substrate, surface-grafted polymer particles (PPs), to develop neural networks with 3D topology, and investigate the resulting structure and function of the neural networks within context of small-worldness.

Methods

Rat neural stem cells were seeded onto PPs, differentiated and subsequently matured over a period of 4 weeks. The developing neural network activity was monitored using MEAs with 3D electrodes. Scanning electron microscopy (SEM), lipophilic tracers, and standard immunocytochemistry were used to assess the structural profile of the PP structured neural networks.

Results

Long-term culture of neural networks structured on PPs was demonstrated through attachment, differentiation, maturation, and survival of the neural networks for over four weeks. 3D MEA measurements of the developing PP structured neural networks demonstrated the spontaneous emergence of network activity consistent with computational capability, i.e. activity patterns suggestive of information segregation (desynchronized spikes and local bursts) and information integration (network spikes). Furthermore, SEM investigations of the structural connections revealed suspended axonal bundles interconnecting nodes of neurons on otherwise distant and independent surface areas, providing topological "shortcuts" between remote neuronal clusters, consistent with a small-world topology.

Conclusions

The application of neural interfaces such as the presented PPs has the potential of recapitulating an important aspect of self-organization and connectivity, namely the 3D character of biological neural networks. PP structuring increases the possible connectedness between remote, local neuronal clusters through suspended axon bundles, i.e. 'structural shortcuts', thus capturing a topological feature consistent with the small-world architecture of the brain.

4. Discussion

The overarching aim of this thesis was to investigate dynamic structure-function relationships in biological neural networks at the micro- and mesoscale, with special focus on the influence of neurodegenerative processes on such relationships in the context of Parkinson´s disease. Through a combination of *in vitro* neural network-based strategies, several mesoscale aspects of structure-function relationships, such as network activity, connectivity, small-worldness, and criticality have been investigated. These mesoscale network features have in turn been considered in relation to microscale expression of dysfunction and pathology in the context of PD-related perturbations. The following discussion will focus and expand on some key observations from the presented experimental studies, as well as on their relationship to neurodegenerative disease and PD pathology.

4.1 How does SoC in in vitro neural networks relate to evolving network pathology?

SoC has been proposed by other investigators to be a mechanism that guides the spontaneous activity of developing neural networks into transient and homeostatically regulated patterns of activity, or into "meta-stable dynamics" (Haldeman and Beggs, 2005, Pu et al., 2013) and brain state transitions (Freeman and Holmes, 2005). These dynamics are in turn part of the regular developmental trajectory of *in vitro* neural networks, and have been found to occur only in neural networks with activity propagating within the critical mode (Pu et al., 2013). Furthermore, some reports of *in vitro* neural network criticality (using dissociated rat cortical neurons) have found most, but not necessarily all, of the neural networks investigated to mainly stay within the critical regime after a certain point in their development (Pu et al., 2013, Pasquale et al., 2008, Tetzlaff et al., 2010). Some mature neural networks fall into the super- or subcritical regime. Nevertheless, the difference in the trend of network criticality state alteration found (in Paper 1), with the PFF neural networks largely displaying activity consistent with SoC, and the control neural networks largely ending up in a non-critical state, suggests a perturbation of the developmental trajectory as a result of the induced alpha-synucleinopathy.

A partial explanation for the direction of network criticality state alterations found after pathology induction, and the baseline measurements showing fluctuating criticality states in all neural networks, could lie in the slower development and maturation of iPSC-derived neural networks suggested by some recent studies, compared to the more commonly used primary neural networks (Marom and Shahaf, 2002, Kirwan et al., 2015, Cotterill et al., 2016). The main body of research used to characterize the stages of spontaneous electrophysiological activity development in neural networks *in vitro* (as described in the introduction), is based on cultures of primary cortical neurons (mainly from mice and rats) (Giugliano et al., 2006), and has been reviewed in detail in (Marom and Shahaf, 2002). However, following the advancements of morphogenetic neuroengineering, this picture has become more multifaceted, and the dynamics of emergent network activity may vary substantially in their time of onset and persistence based on the distribution of cell types and sup-type specificity of the neurons comprising the *in vitro* neural network (Kirwan et al., 2015, Cotterill et al., 2016). The heterogeneous cell composition of the resulting iPSC-derived neural networks likely also produces variable time courses of maturation for sub-type specific cells. As the neural networks in our experiment were found to fluctuate between critical and non-critical states within the baseline measurements (prior to any

pathology induction), this points towards the neural networks not having reached the "certain point in development" where activity mainly stays within the critical regime (Pasquale et al., 2008, Stewart and Plenz, 2008, Yada et al., 2017, Tetzlaff et al., 2010, Pu et al., 2013), or that the developmental trajectory in itself was different in our iPSC-derived neural networks compared to the more commonly used primary neural networks.

Some authors argue that biological neural networks produce "dirty criticality", as neural network activity hovers around a critical region, rather than a true point of criticality, a situation which can never be fully compatible with standard SoC (Kinouchi et al., 2018, Muñoz, 2018). As a result, two variants of SoC have been proposed as better suited models for biological neural networks, models which could fit with our observations of fluctuating network states of criticality. The first variant, *self-organized quasi-criticality (SoqC),* describes a mechanism which drags the system back and forth around a stretched region of criticality (Bonachela et al., 2009, Bonachela and Munoz, 2009, Moretti and Munoz, 2013, Kinouchi et al., 2018). The second variant, *adaptational criticality,* is similar to SoqC, but also takes into consideration the changing structural dynamics in biological neural networks, *via* simple local rewiring rules, creating a co-adaptive process between network architecture and dynamics, resulting in nonrandom network configurations (Bornholdt and Rohl, 2003, Bornholdt and Rohlf, 2000, Rybarsch and Bornholdt, 2014, Nykter et al., 2008). Based on this variant, an explanation for moving from a non-critical to a critical regime following perturbation could lie in the neuronal loss that results from the induced proteinopathy. Loss of connections could lead to this direction of alteration if the network was in a supercritical, overconnected state prior to perturbation, as a loss of connections in this situation has been found to pull the network towards criticality (Rybarsch and Bornholdt, 2014). Furthermore, in a recent related study involving our lab, it was demonstrated that developing neural networks that have settled into a supercritical state can be brought into a state of criticality through chemical manipulation of the inhibitory-excitatory balance (Heiney et al., 2019).

In *in vitro* neural networks, the state of criticality represents the borderline between two qualitatively different types of network behavior, where the behavior of a subcritical network is characterized through highly ordered, oscillating activity fluctuating between few network states, while supercritical behavior is best described as disordered, displaying chaotic and largely random activity (Muñoz, 2018). Avalanche activity, which is used as a basis for determining criticality, is defined as any number of consecutive time bins where a sequence of continuous activity is recorded, and which is preceded and superseded by a quiescent time bin (Beggs and Plenz, 2003). This measure speaks to the propagation of activity within a network, where the size of an avalanche is determined by the number of electrodes activated during the continuous activity sequence. This definition captures a large variety of spatiotemporal activity patterns, where its scale-free nature makes it less sensitive to the choice of time bin and threshold for spike detection compared to other measures of network activity (Beggs and Plenz, 2003, Tagliazucchi et al., 2012, Massobrio et al., 2015, Muñoz, 2018). Other commonly used measures of network activity, such as temporal correlation of single spikes across nodes and synchronized bursts, are more discrete and can be related to established biological rules for information coding. A physical connection, a transfer of information, as well as potential for synaptic plasticity between nodes in a network is inferred from the coincident timing of spikes

across different nodes. Furthermore, the number and duration of synchronized bursts have been associated with the degree of network connectivity, synapse formation, facilitation and depression, as well as LTP and LTD, among other things (Maeda et al., 1995, Lisman, 1997, Thomas et al., 1998, Krahe and Gabbiani, 2004, Froemke et al., 2006). The biological rules underlying avalanche-like propagation of activity however, are less clear. The temporal organization of neural avalanches might be caused by the alternation of high and low activity states, as well as the balancing of the excitation and inhibition in a critical network (Lombardi et al., 2012). Furthermore, during cortical maturation, the repetitive formation of neural avalanches has been suggested to provide an intrinsic template for selectively linking external inputs to spatially diverse, but synchronized neuronal groups in developing superficial cortical layers (Gireesh and Plenz, 2008). Nevertheless, the biological relevance of avalanche-like propagation of activity within the context of neural network criticality has been demonstrated multiple times, as this network activity has proven optimal for maximal dynamic range, information storage/capacity, transmission capability, processing, and variability of phase synchronization (Beggs and Plenz, 2004, Shew and Plenz, 2013, Yang et al., 2012).

The trend of altered network criticality states found following the induced proteinopathy (in Paper 1) is important as it points towards the assessment of criticality being useful in the identification of early stage pathology development. As was highlighted in the introduction, homeostatic plasticity mechanisms are likely to mask the underlying pathology developing in PD patients, such that clear behavioral symptoms surfacing only after significant neurodegeneration has already occurred. As other neurodegenerative diseases such as AD and ALS are also commonly diagnosed after substantial neurodegeneration has already occurred, and they share the neuropathological traits of proteinopathy early in disease development, as well as the patterned spread of diseases processes through interconnected neural networks, it is reasonable to suggest that the assessment of criticality could be used to identify early pathology development in these diseases as well. Although further corroborating studies are needed to conclude on the usefulness of this approach, these results give us reason to be optimistic about possible new avenues for early identification of neurodegenerative processes, as the state of criticality could potentially be assessed in the brains of humans through non-invasive measurements such as functional magnetic resonance imaging (fMRI), magnetoencephalography (MEG), electroencephalography (EEG), and electro-corticography (ECoG) (Poil et al., 2008, Tagliazucchi et al., 2012, Alonso et al., 2014). Furthermore, the criticality assessment should unbiasedly reflect disease development irrespective of what the source(s) of neurodegeneration turn out to be.

4.2 Microscale signs of dysfunction: The Protein degradation and Mitochondrial link to PD

Modelling neural networks *in vitro* enable the simultaneous investigation of ongoing micro- and mesoscale processes across several different time scales. These process "snapshots" represent observation windows which would not be obtainable *in vivo*, and open up the possibility for investigating the interplay between several different coincident small- and large-scale processes. Microscale investigation of active mitochondria, ROS production and synaptic modification, as well as nanoscale investigation (TEM) of intracellular fibrillization and

vacuolization conducted in paper 1 and 2 for instance, could all be related to mesoscale measures of functional network activity, suggesting potential causal relationships between these observations and alterations in functional network activity. Some of our observations support the growing body of evidence suggesting that dysfunctional mitochondrial homeostasis (Hsieh et al., 2016, Verma et al., 2017, Verma et al., 2018) and impairments in the protein degradation machinery, may play pivotal roles in neurodegeneration (Kopito, 2000, Todde et al., 2009, Friedman et al., 2012a, Abeliovich and Gitler, 2016, Bieri et al., 2017). Whether these processes represent primary causes of disease or downstream consequences of other underlying disease-causing processes however, remains to be clarified. The next sections will focus on the observations relating to protein degradation and mitochondrial dysfunction in our studies, and how they relate to PD.

The super-resolution investigation of intracellular elements conducted as part of the criticality article (Paper 1) revealed both fibrillization and high activation of the protein degradation pathway in the condition with induced alpha-synuclein pathology (PFF condition). Although alpha-synuclein aggregates are considered the main constituent, and the prime suspect in the formation of the hallmark Lewy pathology of PD, proteasome analysis has revealed the contribution of over 300 proteins in LBs. This profile implicates several different processes, where 90 of the identified proteins are associated with alpha-synuclein, the protein degradation system, and mitochondria (Goedert et al., 2013, Wakabayashi et al., 2013). Moreover, in a recent publication, Shahmoradian and colleagues used correlative light and electron microscopy to study and compare the Lewy pathology in brain tissue from several PD brain donors (Shahmoradian et al., 2019). They demonstrated that LBs and LNs are heterogenous structures with various morphology, and, importantly, that they contain an abundance of membranous material (primarily alpha-synuclein, filaments, lipids, lysosomal and autophagosomal structures, as well as mitochondria) crowded together. Reasonable explanations for the co-occurrence of all these materials exist, where lipids for instance have been reported to be caused by alpha-synuclein aggregation, as well as to have various effects on alpha-synuclein aggregation once present, ranging from inhibition of aggregation to triggering of fibrillation and apoptotic signaling (Zhu and Fink, 2003, Zhao et al., 2004, Ruiperez et al., 2010, Galvagnion et al., 2015, Flagmeier et al., 2017). Our superresolution electron microscopy observations are well in line with these reports, as an abundance of fibrils and filaments, lysosomes, autophagosomes, vesicles, and lipid bodies were observed crowding the intracellular space of intact neurons, as well as within the necrotic and apoptotic elements with high filament condensation, in the induced alpha-synuclein pathology condition (Paper 1, Fig. S4-S7).

There are strong links tying the protein degradation system and intracellular organelle trafficking to alpha-synuclein and processes of neurodegeneration. Firstly, alpha-synuclein has been shown to interact with specific ubiquitin and Rab proteins, as well as with the lysosomal pathway through interaction with the SNARE protein family (Gitler et al., 2008, Benskey et al., 2016, Hunn et al., 2015, Calo et al., 2016, Sacino et al., 2017). Secondly, studies suggest that alpha-synuclein plays a regulatory role in autophagosome synthesis, as depletion leads to autophagy enhancement (Winslow et al., 2010), and targeted disruption of autophagy results in accumulation of abnormal alpha-synuclein at the presynaptic compartment, dystrophic axons

and dendrites, and the formation of somatic and dendritic ubiquitinated inclusions (Friedman et al., 2012a). Interestingly, the mentioned effects of targeted autophagic disruption correspond with the initial signs of alpha-synuclein pathology, where dystrophic terminals, axonal and synaptic swelling, as well as small presynaptic aggregates have been observed prior to the formation of LBs and LNs (Kramer and Schulz-Schaeffer, 2007, Calo et al., 2016). Activation of the autophagic and lysosomal machinery regulates cellular homeostasis, and their function of degrading and recycling cell constituents becomes particularly important in the face of aggregate-prone protein forms, such as the PFF seeds used to induce alpha-synuclein pathology in the neural networks of the criticality article (Paper 1). Furthermore, lysosomes have been shown to mediate intercellular transfer of fibrillar alpha-synuclein though tunneling nanotubes, providing a possible route of pathology propagation (Abounit et al., 2016, Bieri et al., 2017). Abnormal protein aggregation is believed to eventually saturate the protein degradation machinery, where the resulting failure in autophagic and lysosomal function precipitates pathological inclusion formation, ultimately leading to neuronal death (Meredith et al., 2002, Tanik et al., 2013, Ragagnin et al., 2013). The ultrastructural investigation of neural networks from the PFF condition, and from the monomer alpha-synuclein control condition, fits well with this outlined route of neurodegeneration. As alpha-synuclein in itself affects autophagic activation, it comes as no surprise that the mean number of autophagosomal/lysosomal elements observed in both the PFF and monomer condition was high (15-16 per neuron, Fig.S5). However, as there was a significant difference observed in apoptotic and necrotic elements, with a clear reduction in health and survival of the neurons in the PFF condition compared to the monomer condition, this points towards the most affected neurons in the PFF condition already having succumbed to neurodegeneration and died at the time of ultrastructural assessment.

Intriguingly, although alterations at the synapse and neurites in the neural networks from the PFF condition were observed in super-resolution, together with poor health and survival of the neurons, the induced alpha-synuclein pathology did not result in identifiable functional impairment in any of the most commonly used network activity measures (mean firing rate, cross-correlation, inter-spike intervals, or population inter-spike intervals). In line with our observations, some *in vivo* studies have reported a lack of behavioral deficits despite moderate to robust propagation of inclusion pathology after PFF infusion (Sacino et al., 2014, Nouraei et al., 2018, Luk et al., 2012a). This raises the question of whether development of proteinopathy actually has a causal, or just a correlative, relationship with the development of cognitive deficits in PD. However, some functional measures might just be more efficient in identifying disturbances elicited by this type of pathology, where Volpicelley-Daley and colleagues (2011) for instance found impaired neuronal activity after PFF addition in alpha-synuclein overexpressing neurons using calcium imaging (Volpicelli-Daley et al., 2011), which has already been discussed in some previous sections, we found differences in the mesoscale measure of network criticality states.

Mitochondrial instability or dysfunction is also heavily linked to alpha-synuclein and PD. As already noted, many of the proteins found within LBs are related to mitochondria, and mitochondria are found contained within and surrounding LB in brain tissue from PD patients (Wakabayashi et al., 2013, Shahmoradian et al., 2019). Alpha-synuclein has also been found to

influence mitochondrial homeostasis through interaction with the mitochondria membranes well as with the mitochondria-associated endoplasmic reticulum membranes (Viennet et al., 2018, Wong and Krainc, 2017). Furthermore, mitochondria can usually be found at the presynaptic terminal, where alpha-synuclein is heavily involved in mediation of membrane interactions and remodeling, in binding lipids, in modulation of synaptic vesicle release and recycling, as well as in maintenance of the synaptic vesicle pool (Gitler et al., 2008, Bellani et al., 2010, Boassa et al., 2013, Burre, 2015, Calo et al., 2016). Importantly, the interaction of alpha-synuclein with vesicles and mitochondrial membranes has been shown to be able to catalyze the formation of alpha-synuclein filaments, and its membrane association to modulate aggregation propensity (Zhu et al., 2003, Fusco et al., 2016). This might give a pointer as to why synapses often represent the initial site of observable alpha-synuclein pathology, with dystrophic terminals and small aggregates forming at the presynaptic compartment prior to LBs and LNs (Kramer and Schulz-Schaeffer, 2007, Calo et al., 2016).

This leads us to the microscale investigation of active mitochondria in equivalent networks from healthy and LRRK2 mutated neural populations (Paper 2), which was conducted both before and after a transient KA stimulation. Signs of mitochondrial dysfunction are prominently displayed in tissue samples from PD patients, and faulty mitochondrial motility and function have been widely linked to PD related mutations, including the particular G2019S mutation investigated in this study (Singh et al., 2019, Mortiboys et al., 2010, Li et al., 2014, Esteves et al., 2014, MacLeod et al., 2006, Lin and Beal, 2006, Yue et al., 2015), as well as to neurodegenerative disease at large (Valko et al., 2007). Thus, as we found a statistically significant reduction in active mitochondria contained within the neurites of the healthy (control) neural networks after KA stimulation, but not within the neurites of the LRRK2 neural networks, this could reasonably be interpreted as a sign of mitochondrial dysfunction in the latter population (Paper 2, Fig.3I). As cell metabolism required for maintenance of neuronal activity and presynaptic integrity relies on the ATP production of mitochondria, such a mitochondrial dysfunction could underlie the two-fold mean firing rate and simultaneously low cross-correlation measured in the LRRK2 neural networks compared to the healthy neural networks.

As a final note relating to mitochondrial dysfunction, some of the most interesting microscale data obtained during these experiments were not presented in the LRRK2 article due to ongoing practical challenges with data analysis, namely the live movement of active mitochondria contained within the neurites of the structured neural networks. The mitochondrial motility in neurites of LRRK2 and control neural networks was captured through live fluorescence imaging every second for the duration of 1 minute, where qualitative inspection of the time-lapse videos created from the image series suggested impaired mitochondrial motility in LRRK2 compared to the control neural networks, especially following the overexcitation event. This could explain some of the morphological and electrophysiological differences observed both at baseline and 24 hours post overexcitation, as healthy mitochondrial function and transport are essential for cell metabolism, maintaining neuronal activity and structural integrity through production of required ATP molecules (Saxton and Hollenbeck, 2012). Dysfunctional mitochondrial motility could as such also underlie the impaired synaptic plasticity indicated through the immunocytochemistry investigations of the LRRK2 networks. However, these data

will be the subject of a future paper as a method for reliable mitochondrial movement tracking is still under development.

4.3. How can structuring in vitro neural networks help us understand neurodegenerative disease processes?

As has been extensively highlighted in the introduction, the physical structure of the neural networks in the brain shapes their function, and *vice versa*. The strategy of physically structuring the *in vitro* neural networks in the presented studies, either through tailor made microfluidic chips or PPs, made it possible to study several aspects of neural network formation and related functional consequences. In the LRRK2 study (Paper 2), the intranodal correlation of the structured neural networks was found to be consistently greater that the between-nodal correlation. Furthermore, greater MFR were consistently found in the outermost nodes compared to the middle node, illustrating the reproducible functional connectivity pattern created by the physical structuring. This is in line with other studies using microfluidic chips, which have found the microfluidic structure to influence the developmental process of the patterned networks. For instance, structuring has been found to result in more robust electrical activity and greater synaptic density when compared to random networks during the first three weeks of network development (Chang et al., 2001, Chang and Wheeler, 2006). This means that through structuring neural networks, a more complex, reproducible, and realistic model can be approached, where both the structural and functional connectomes of target brain micro-circuits can be better recapitulated.

The experimental setup in the LRRK2 study combining physical structuring with electrophysiological measurements was mainly used to assess the structural and functional consequences of the G2019S mutation, as well as the short-term outcome of a stimulation confined to a single node in the network. However, it opens up the possibility of assessing more long-term functional consequences of developing pathology selectively initiated at a single node in the network, for instance to induced alpha-synucleinopathy, to model the patterned spread of proteinopathy characteristic of many neurodegenerative diseases. Initially, a major part of the criticality study (Paper 1) was directly related to this, as microfluidic chips were used to structure the iPSC-derived neural networks. Confined nodes in the networks were also used to selectively induce alpha-synucleinopathy through the addition of PFFs, and the anterograde-retrograde pattern of propagation, as well as the order of interconnected neurons the pathology spread through, would be investigated using immunocytochemistry. However, as the microfluidic chips were not interfaced with the MEAs at this point, and the immunostaining efforts for showing pathological alpha-synuclein were inconclusive due to consistent background and unspecific labelling in the control conditions, this part of the study was not pursued further. Nevertheless, the cumulative findings from these two studies show that this would indeed be a feasible approach for studying the more long-term functional consequences of such a pathological process. Moreover, the principle of diaschisis, i.e. the functional consequences of disease to indirectly linked nodes in a network, could be studied by separating the electrophysiological measures originating from each of the nodes in the microfluidic chip structured networks.

Furthermore, the defining trait of the small-world architecture characteristic of brain neural networks, namely high local clustering and short path-lengths between any distant pair of nodes in the network (Watts and Strogatz, 1998), seems to be structurally recapitulated by the three-nodal microfluidic chip set-up, as well as functionally based on the correlation maps and MFR distribution of the neural networks in the LRRK2 study. As highlighted in Paper 3, recapitulating this feature might be of great importance when it comes to understanding neurodegenerative disease processes, as such a network configuration propagates pathology more easily than other network configurations (Moore and Newman, 2000). In further support of this, one study found the degree of small-worldness to determine the transition from subcritical to critical activity in *in vitro* networks (Massobrio et al., 2015), which intuitively makes sense as the promotion of both information segregation and integration through this network architecture should favor the generation of neuronal avalanches of all sizes, and thus criticality (Friedman et al., 2012b). Thus, forcing key structural features of small-worldness through physical patterning of neural networks reproduces functional aspects of small-worldness, which in turn might push the network activity towards criticality. Moreover, this fits with the aforementioned finding that neural network structuring influences the developmental process, resulting in a more mature profile with greater synaptic density and more robust electrical activity at an earlier timepoint compared to unstructured networks (Chang et al., 2001, Chang and Wheeler, 2006). This has clear practical implications for *in vitro* disease modelling, as for instance the slower maturation of iPSC-derived neurons could perhaps be compensated for by physical structuring of the developing neural networks, reducing the necessary maturation time and thus also the chance of contamination.

Another interesting aspect which emerged with neural network structuring relates to the striking difference in neuronal morphology between the G2019S mutated and control neural networks in Paper 2. Based on the findings of previous studies of this mutation, which contrary to our results, have either found reduced arborization or no difference in neuritic profile (West et al., 2005, Smith et al., 2006, MacLeod et al., 2006, Plowey et al., 2008, Nguyen et al., 2011, Chan et al., 2011, Winner et al., 2011, Sanchez-Danes et al., 2012b, Cherra et al., 2013, Reinhardt et al., 2013, Qing et al., 2017, Dagda et al., 2014, Greggio et al., 2006), physical structuring, combined with the particular surface coating substrates used, has likely influenced the phenotypic expression of the G2019S mutation when it comes to neurite morphology (Sepulveda et al., 2013). In line with axonal guidance mechanisms underlying initial connectivity establishment of brain neural networks during development, structural cues have been found to influence the orientation and morphology of neurons and their arborizations *in vitro,* and might also enhance or reduce morphological traits in the context of mutations (Dowell-Mesfin et al., 2004, Micholt et al., 2013, Bugnicourt et al., 2014, Tomba et al., 2014). The aberrant neuritic outgrowth profile observed in the G2019S population compared to controls, with bundles of neurites crossing perpendicular to the axon tunnels in the synaptic chambers, as well as massive ramification of neurites in the inlet and outlet chambers (Paper 2, Fig.S1,S2,S6), suggests a connection between impaired axonal guidance and the specific PD-related mutation. Some morphological and functional characteristics of developing neural networks are thus facilitated through structural cues, and might never become apparent using solely standard, unstructured *in vitro* neural networks. This part of the work thus adds to the

body of research investigating normal and abnormal structure and function in *in vitro* neural networks. Importantly, it highlights how the choice of culture vessel can influence multiple aspects of neural network formation and maturation, and thus the neurodegenerative processes under investigation.

4.4 The problem of representation

From a philosophical perspective, a model is a functional representation of a feature in the real-world system it tries to model. It depicts what something is, in terms of some of its measurable aspects, to gain insight into how it works (Teller, 2001, Frigg and Hartmann, 2018, Bassett et al., 2018). It is thus important to consider the implications of a model-based approach to neuroscience in terms of realism, reductionisms, and the possible accuracy and translational value of the results. In the introduction, a substantial portion of text was allocated to highlighting the degree of similarity or "likeness of nature" between *in vitro* neural networks and neural networks in the brain. Self-organization, emergence of electrophysiological network activity, SoC and small-worldness represent important measurable features of *in vitro* neural networks that can be justified in terms of actual brain neural network data, providing construct and explanatory validity of the *in vitro* neural network model (Bassett et al., 2018, Calabrese, 2018).

However, in the reductionist *in vitro* approach, one is looking at a limited set of properties in an isolated population, where one might also be stripping away properties of real brain neural networks which might be relevant to the problem at hand. One such property, which is regularly disregarded in *in vitro* neuroscientific models, is the three-dimensional character of brain neural networks, a feature which was highlighted and addressed in paper 3 through PP structuring of the networks. Considering all of the findings presented in this thesis, there can be no doubt that there is a reciprocal relationship between physical structure and function of a network. However, the particular simplification provided by reducing the network dimension from 3D to 2D might be a necessary step in order to be able to extrapolate basic information on how neural networks develop and work in healthy and disease states, a problem which is too complicated to address and observe in developing brain neural networks. Nevertheless, it is important to keep this dimension limitation in mind when investigating features of neural networks which are likely affected by it.

Another important feature which needs consideration is the lack of classical "behavior" as a system output in *in vitro* neural networks. With this lack of behavior as an observable, it is difficult to determine, for instance, whether a plasticity response is adaptive or maladaptive. Assumptions can be made based on the electrophysiological and morphological characteristics of the networks, as more abstracted measures of network structure and function can be used to determine a network "normal" at baseline, and a network "abnormal" following for instance a perturbation. Based on these assumptions, and accumulated knowledge on neural networks in general, an evaluation of functional or structural "recovery" or compensation after perturbation can be made. However, one should be careful with translating such an evaluation to, or equated it with, the behavioral observation of *in vivo* models, or as such, the behavioral symptoms of patients.

4.5 Methodological considerations

In the criticality article (Paper 1), the electrophysiological recordings should ideally have been longer. Due to low avalanche activity, several of the recording time points did not contain enough avalanche samples for criticality assessment, and the data points were thus not represented in the final graph or considered in the main discussion. The picture would perhaps be more complete if we had performed longer and more frequent recordings. However, our final dataset consisted of over 100 recordings with a duration of about 7 minutes for each individual recording, collected with a standard 10kHz sampling rate, which amounts to over 200GB of raw-data. The massive accumulation of data was part of the reason for the relatively short recording durations, as the increasing complexity of file storage, moving, sharing, and processing cannot be overstated. Furthermore, the neural networks were intentionally not recorded for 48 hours after a media change, as major fluctuations in over-all network activity were consistently observed as a result.

Moreover, it is important to note that in the TEM investigations of intracellular elements and induced pathology for the criticality article (Paper 1), it was impossible to distinguish alpha-synuclein filaments from abundant cytoskeletal filaments as they are morphological similar and exist within the same size range (5-15nm vs 10nm, respectively) (Arima et al., 1998, Spillantini et al., 1998). Furthermore, this ultrastructural indistinguishability between cytoskeletal filaments and alpha-synuclein filaments is a common cautionary element in studies of Lewy pathology as was, for instance, most recently reported a publication by Shahmoradian and colleagues (Shahmoradian et al., 2019). However, as other well documented hallmarks of neuropathology co-occurred with the abundant and condensed filaments observed in the PFF condition only, such as lipids and multilamellar bodies, it is reasonable to assume that this was a result of pathology induction through PFF addition (Hariri et al., 2000, Zhu and Fink, 2003, Zhao et al., 2004, Galvagnion et al., 2015).

Although some structural and functional aspects of small-worldness were recapitulated in the PP structured neural networks (Paper 3), there were several methodological complications which limit the potential usefulness of PPs in combination with neuronal cells, especially with regard to their potential for longer-term studies of neural networks. These limiting factors include variability in cell attachment, variable mechanical stress due to movement of the PPs, poor cell viability, visibility, and general reproducibility due to difficulties with handling the PPs. The influence of such factors on neural network establishment and maintenance can therefore not be excluded.

5. Conclusion

The main objectives of this work were (i) the application of advanced disease modelling for the recapitulation and study of relevant pathological processes *in vitro,* and (ii) the identification and extraction of key morphology-activity relationships at the micro- and mesoscale. In accordance with these objectives, the experimental studies presented in papers 1 and 2 incorporate different advanced disease modelling approaches, which enabled the study of PD-related pathological processes, and the extraction of key morphology-activity relationships, in biologically relevant neural networks. Based on the developing principles of *in vitro* chemotemporal neural differentiation and morphogenetic neuroengineering, iPSC-derived neural networks were established and applied in the investigation of developing alpha-synuclein pathology induced through addition of PFF seeds in paper 1. This approach allowed for the extraction of several morphology-activity relationships key to PD, such as standard measures of network function and, importantly, in network criticality states, as well as ultrastructural investigation of alpha-synuclein pathology. In paper 2, iPSC-derived neural stem cells with and without the PD-related CRISPR-Cas9 inserted G2019S mutation were used to establish structured neural networks in microfluidic chips. This approach enabled the investigation of micro- and mesoscale effects of a PD-specific mutation, where microscale aspects relating to mitochondrial dysfunction and impaired synaptic plasticity was revealed. Perhaps most interestingly, this approach enabled the linking of aberrant neuritic outgrowth to "abnormal" network function, observed as elevated MFR and reduced cross-correlation, compared to controls. The third and final paper presented in this thesis was more directly relevant to the second objective, by investigating the neural network topology within the context of small-worldness.

Based on the finding from these experimental studies, we can conclude that:

1) Network criticality states can be extracted from electrophysiological recordings and applied to identify developing alpha-synuclein pathology in *in vitro* neural networks;
2) The aberrant neuritic outgrowth observed in microfluidic chip structured neural networks with the G2019S mutation likely underlies the consistent deviations in both morphology and function of these neural networks compared to healthy controls;
3) Important features of self-organization and connectivity, such as small-worldness and 3-dimensionality, can be recapitulated *in vitro* by application of interfaces such as the presented PPs, however, the applicability and potential usefulness of this particular approach in combination with neural cells is currently limited by methodological issues.

Combined, these approaches have enabled the identification of key morphology-activity relationships in biologically relevant neural networks, as well as the extraction of such dynamics in the face of PD-related neurodegenerative processes. The resulting findings add to the body of investigations aimed at understanding micro- and mesoscale dynamics underlying early disease onset and mechanisms in neurodegeneration. Furthermore, these findings highlight the relevance of robustness of advanced *in vitro* modelling approaches as a tool for investigation in preclinical research. The relevant insights can thus be utilized to further improve our ability to develop novel, clinically relevant interventions.

6. References

ABBOTT, L. F. & NELSON, S. B. 2000. Synaptic plasticity: taming the beast. *Nat Neurosci,* 3 Suppl**,** 1178-83.

ABELIOVICH, A. & GITLER, A. D. 2016. Defects in trafficking bridge Parkinson's disease pathology and genetics. *Nature,* 539**,** 207-216.

ABOUNIT, S., BOUSSET, L., LORIA, F., ZHU, S., DE CHAUMONT, F., PIERI, L., OLIVO-MARIN, J. C., MELKI, R. & ZURZOLO, C. 2016. Tunneling nanotubes spread fibrillar alpha-synuclein by intercellular trafficking of lysosomes. *Embo j,* 35**,** 2120-2138.

ADAMSKY, A., KOL, A., KREISEL, T., DORON, A., OZERI-ENGELHARD, N., MELCER, T., REFAELI, R., HORN, H., REGEV, L., GROYSMAN, M., LONDON, M. & GOSHEN, I. 2018. Astrocytic Activation Generates De Novo Neuronal Potentiation and Memory Enhancement. *Cell,* 174**,** 59-71.e14.

ALBERT, R. & BARABASI, A. L. 2000. Topology of evolving networks: local events and universality. *Phys Rev Lett,* 85**,** 5234-7.

ALEGRE-ABARRATEGUI, J., BRIMBLECOMBE, K. R., ROBERTS, R. F., VELENTZA-ALMPANI, E., TILLEY, B. S., BENGOA-VERGNIORY, N. & PROUKAKIS, C. 2019. Selective vulnerability in alpha-synucleinopathies. *Acta Neuropathol*.

ALLEN, N. J. & LYONS, D. A. 2018. Glia as architects of central nervous system formation and function. *Science,* 362**,** 181-185.

ALMEIDA, R. G. & LYONS, D. A. 2017. On Myelinated Axon Plasticity and Neuronal Circuit Formation and Function. *J Neurosci,* 37**,** 10023-10034.

ALONSO, L. M., PROEKT, A., SCHWARTZ, T. H., PRYOR, K. O., CECCHI, G. A. & MAGNASCO, M. O. 2014. Dynamical criticality during induction of anesthesia in human ECoG recordings. *Front Neural Circuits,* 8**,** 20.

ALSTOTT, J., BREAKSPEAR, M., HAGMANN, P., CAMMOUN, L. & SPORNS, O. 2009. Modeling the impact of lesions in the human brain. *PLoS Comput Biol,* 5**,** e1000408.

AMOROSO, M. W., CROFT, G. F., WILLIAMS, D. J., O'KEEFFE, S., CARRASCO, M. A., DAVIS, A. R., ROYBON, L., OAKLEY, D. H., MANIATIS, T., HENDERSON, C. E. & WICHTERLE, H. 2013. Accelerated high-yield generation of limb-innervating motor neurons from human stem cells. *J Neurosci,* 33**,** 574-86.

ANDERSEN, P. M. 2006. Amyotrophic lateral sclerosis associated with mutations in the CuZn superoxide dismutase gene. *Curr Neurol Neurosci Rep,* 6**,** 37-46.

ANDERSEN, P. M., FORSGREN, L., BINZER, M., NILSSON, P., ALA-HURULA, V., KERANEN, M. L., BERGMARK, L., SAARINEN, A., HALTIA, T., TARVAINEN, I., KINNUNEN, E., UDD, B. & MARKLUND, S. L. 1996. Autosomal recessive adult-onset amyotrophic lateral sclerosis associated with homozygosity for Asp90Ala CuZn-superoxide dismutase mutation. A clinical and genealogical study of 36 patients. *Brain,* 119 (Pt 4)**,** 1153-72.

ARAI, T., HASEGAWA, M., AKIYAMA, H., IKEDA, K., NONAKA, T., MORI, H., MANN, D., TSUCHIYA, K., YOSHIDA, M., HASHIZUME, Y. & ODA, T. 2006. TDP-43 is a component of ubiquitin-positive tau-negative inclusions in frontotemporal lobar degeneration and amyotrophic lateral sclerosis. *Biochem Biophys Res Commun,* 351**,** 602-11.

ARENAS, E., DENHAM, M. & VILLAESCUSA, J. C. 2015. How to make a midbrain dopaminergic neuron. *Development,* 142**,** 1918-36.

ARIMA, K., UEDA, K., SUNOHARA, N., HIRAI, S., IZUMIYAMA, Y., TONOZUKA-UEHARA, H. & KAWAI, M. 1998. Immunoelectron-microscopic demonstration of NACP/alpha-synuclein-epitopes on the filamentous component of Lewy bodies in Parkinson's disease and in dementia with Lewy bodies. *Brain Res,* 808**,** 93-100.

ASH, P. E., BIENIEK, K. F., GENDRON, T. F., CAULFIELD, T., LIN, W. L., DEJESUS-HERNANDEZ, M., VAN BLITTERSWIJK, M. M., JANSEN-WEST, K., PAUL, J. W., 3RD, RADEMAKERS, R., BOYLAN, K. B., DICKSON, D. W. & PETRUCELLI, L. 2013. Unconventional translation of C9ORF72 GGGGCC expansion generates insoluble polypeptides specific to c9FTD/ALS. *Neuron,* 77**,** 639-46.

AVENA-KOENIGSBERGER, A., MISIC, B. & SPORNS, O. 2017. Communication dynamics in complex brain networks. *Nat Rev Neurosci,* 19**,** 17-33.
BAK, P., TANG, C. & WIESENFELD, K. 1988. Self-organized criticality. *Phys Rev A Gen Phys,* 38**,** 364-374.
BALL, N., TEO, W. P., CHANDRA, S. & CHAPMAN, J. 2019. Parkinson's Disease and the Environment. *Front Neurol,* 10**,** 218.
BARKER, A. J. & ULLIAN, E. M. 2008. New roles for astrocytes in developing synaptic circuits. *Commun Integr Biol,* 1**,** 207-11.
BASSETT, D. S. & BULLMORE, E. 2006. Small-world brain networks. *Neuroscientist,* 12**,** 512-23.
BASSETT, D. S. & BULLMORE, E. T. 2017. Small-World Brain Networks Revisited. *Neuroscientist,* 23**,** 499-516.
BASSETT, D. S., ZURN, P. & GOLD, J. I. 2018. On the nature and use of models in network neuroscience. *Nat Rev Neurosci,* 19**,** 566-578.
BEAR, M. F. & MALENKA, R. C. 1994. Synaptic plasticity: LTP and LTD. *Curr Opin Neurobiol,* 4**,** 389-99.
BEGGS, J. M. & PLENZ, D. 2003. Neuronal avalanches in neocortical circuits. *J Neurosci,* 23**,** 11167-77.
BEGGS, J. M. & PLENZ, D. 2004. Neuronal avalanches are diverse and precise activity patterns that are stable for many hours in cortical slice cultures. *J Neurosci,* 24**,** 5216-29.
BELLANI, S., SOUSA, V. L., RONZITTI, G., VALTORTA, F., MELDOLESI, J. & CHIEREGATTI, E. 2010. The regulation of synaptic function by alpha-synuclein. *Commun Integr Biol,* 3**,** 106-9.
BELLON, A. & MANN, F. 2018. Keeping up with advances in axon guidance. *Curr Opin Neurobiol,* 53**,** 183-191.
BENSKEY, M. J., PEREZ, R. G. & MANFREDSSON, F. P. 2016. The contribution of alpha synuclein to neuronal survival and function - Implications for Parkinson's disease. *J Neurochem,* 137**,** 331-59.
BETTENCOURT, L. M., STEPHENS, G. J., HAM, M. I. & GROSS, G. W. 2007. Functional structure of cortical neuronal networks grown in vitro. *Phys Rev E Stat Nonlin Soft Matter Phys,* 75**,** 021915.
BETZEL, R. F. & BASSETT, D. S. 2018. Specificity and robustness of long-distance connections in weighted, interareal connectomes. *Proc Natl Acad Sci U S A,* 115**,** E4880-e4889.
BIDHENDI, E. E., BERGH, J., ZETTERSTROM, P., ANDERSEN, P. M., MARKLUND, S. L. & BRANNSTROM, T. 2016. Two superoxide dismutase prion strains transmit amyotrophic lateral sclerosis-like disease. *J Clin Invest,* 126**,** 2249-53.
BIERI, G., GITLER, A. D. & BRAHIC, M. 2017. Internalization, axonal transport and release of fibrillar forms of alpha-synuclein. *Neurobiol Dis*.
BLACKMAN, M. P., DJUKIC, B., NELSON, S. B. & TURRIGIANO, G. G. 2012. A critical and cell-autonomous role for MeCP2 in synaptic scaling up. *J Neurosci,* 32**,** 13529-36.
BOASSA, D., BERLANGA, M. L., YANG, M. A., TERADA, M., HU, J., BUSHONG, E. A., HWANG, M., MASLIAH, E., GEORGE, J. M. & ELLISMAN, M. H. 2013. Mapping the subcellular distribution of alpha-synuclein in neurons using genetically encoded probes for correlated light and electron microscopy: implications for Parkinson's disease pathogenesis. *J Neurosci,* 33**,** 2605-15.
BOILLEE, S., YAMANAKA, K., LOBSIGER, C. S., COPELAND, N. G., JENKINS, N. A., KASSIOTIS, G., KOLLIAS, G. & CLEVELAND, D. W. 2006. Onset and progression in inherited ALS determined by motor neurons and microglia. *Science,* 312**,** 1389-92.
BONACHELA, J. A., ALAVA, M. & MUNOZ, M. A. 2009. Cusps, self-organization, and absorbing states. *Phys Rev E Stat Nonlin Soft Matter Phys,* 79**,** 050106.
BONACHELA, J. A. & MUNOZ, M. A. 2009. Self-organization without conservation: true or just apparent scale-invariance? *Journal of Statistical Mechanics,* 2009**,** P09009.
BORNHOLDT, S. & ROHL, T. 2003. Self-organized critical neural networks. *Phys Rev E Stat Nonlin Soft Matter Phys,* 67**,** 066118.
BORNHOLDT, S. & ROHLF, T. 2000. Topological evolution of dynamical networks: global criticality from local dynamics. *Phys Rev Lett,* 84**,** 6114-7.
BREAKSPEAR, M. & STAM, C. J. 2005. Dynamics of a neural system with a multiscale architecture. *Philos Trans R Soc Lond B Biol Sci,* 360**,** 1051-74.

BRESSOUD, R. & INNOCENTI, G. M. 1999. Typology, early differentiation, and exuberant growth of a set of cortical axons. *J Comp Neurol,* 406**,** 87-108.
BRAAK, H. & BRAAK, E. 1991. Neuropathological stageing of Alzheimer-related changes. *Acta Neuropathol,* 82**,** 239-59.
BRAAK, H., DE VOS, R. A., BOHL, J. & DEL TREDICI, K. 2006. Gastric alpha-synuclein immunoreactive inclusions in Meissner's and Auerbach's plexuses in cases staged for Parkinson's disease-related brain pathology. *Neurosci Lett,* 396**,** 67-72.
BRAAK, H. & DEL TREDICI, K. 2009. Neuroanatomy and pathology of sporadic Parkinson's disease. *Adv Anat Embryol Cell Biol,* 201**,** 1-119.
BRAAK, H., DEL TREDICI, K., BRATZKE, H., HAMM-CLEMENT, J., SANDMANN-KEIL, D. & RUB, U. 2002. Staging of the intracerebral inclusion body pathology associated with idiopathic Parkinson's disease (preclinical and clinical stages). *J Neurol,* 249 Suppl 3**,** Iii/1-5.
BRAAK, H., DEL TREDICI, K., RUB, U., DE VOS, R. A., JANSEN STEUR, E. N. & BRAAK, E. 2003a. Staging of brain pathology related to sporadic Parkinson's disease. *Neurobiol Aging,* 24**,** 197-211.
BRAAK, H., RUB, U., GAI, W. P. & DEL TREDICI, K. 2003b. Idiopathic Parkinson's disease: possible routes by which vulnerable neuronal types may be subject to neuroinvasion by an unknown pathogen. *J Neural Transm (Vienna),* 110**,** 517-36.
BUGNICOURT, G., BROCARD, J., NICOLAS, A. & VILLARD, C. 2014. Nanoscale surface topography reshapes neuronal growth in culture. *Langmuir,* 30**,** 4441-9.
BULLMORE, E. & SPORNS, O. 2009. Complex brain networks: graph theoretical analysis of structural and functional systems. *Nat Rev Neurosci,* 10**,** 186-98.
BURRE, J. 2015. The Synaptic Function of alpha-Synuclein. *J Parkinsons Dis,* 5**,** 699-713.
CAIAZZO, M., DELL'ANNO, M. T., DVORETSKOVA, E., LAZAREVIC, D., TAVERNA, S., LEO, D., SOTNIKOVA, T. D., MENEGON, A., RONCAGLIA, P., COLCIAGO, G., RUSSO, G., CARNINCI, P., PEZZOLI, G., GAINETDINOV, R. R., GUSTINCICH, S., DITYATEV, A. & BROCCOLI, V. 2011. Direct generation of functional dopaminergic neurons from mouse and human fibroblasts. *Nature,* 476**,** 224-7.
CALABRESE, R. L. 2018. Inconvenient Truth to Principle of Neuroscience. *Trends Neurosci,* 41**,** 488-491.
CALO, L., WEGRZYNOWICZ, M., SANTIVANEZ-PEREZ, J. & GRAZIA SPILLANTINI, M. 2016. Synaptic failure and alpha-synuclein. *Mov Disord,* 31**,** 169-77.
CHAMBERS, S. M., FASANO, C. A., PAPAPETROU, E. P., TOMISHIMA, M., SADELAIN, M. & STUDER, L. 2009. Highly efficient neural conversion of human ES and iPS cells by dual inhibition of SMAD signaling. *Nat Biotechnol,* 27**,** 275-80.
CHAN, D., CITRO, A., CORDY, J. M., SHEN, G. C. & WOLOZIN, B. 2011. Rac1 protein rescues neurite retraction caused by G2019S leucine-rich repeat kinase 2 (LRRK2). *J Biol Chem,* 286**,** 16140-9.
CHANG, C. C. & WHEELER, B. C. 2006. Pattern Technologies for Structuring Neuronal Networks on MEAs. *In:* TAKETANI, M. & BAUDRY, M. (eds.) *Advances in Network Electrophysiology*. Springer Science.
CHANG, J. C., BREWER, G. J. & WHEELER, B. C. 2001. Modulation of neural network activity by patterning. *Biosens Bioelectron,* 16**,** 527-33.
CHEN, Z. L., YU, W. M. & STRICKLAND, S. 2007. Peripheral regeneration. *Annu Rev Neurosci,* 30**,** 209-33.
CHENG, H. C., ULANE, C. M. & BURKE, R. E. 2010. Clinical progression in Parkinson disease and the neurobiology of axons. *Ann Neurol,* 67**,** 715-25.
CHERRA, S. J., 3RD, STEER, E., GUSDON, A. M., KISELYOV, K. & CHU, C. T. 2013. Mutant LRRK2 elicits calcium imbalance and depletion of dendritic mitochondria in neurons. *Am J Pathol,* 182**,** 474-84.
CLAWSON, W. P., WRIGHT, N. C., WESSEL, R. & SHEW, W. L. 2017. Adaptation towards scale-free dynamics improves cortical stimulus discrimination at the cost of reduced detection. *PLoS Comput Biol,* 13**,** e1005574.
COOKSON, M. R. 2015. LRRK2 Pathways Leading to Neurodegeneration. *Curr Neurol Neurosci Rep,* 15**,** 42.

COTTERILL, E., CHARLESWORTH, P., THOMAS, C. W., PAULSEN, O. & EGLEN, S. J. 2016. A comparison of computational methods for detecting bursts in neuronal spike trains and their application to human stem cell-derived neuronal networks. *J Neurophysiol,* 116**,** 306-21.

DAFFERTSHOFER, A., TON, R., KRINGELBACH, M. L., WOOLRICH, M. & DECO, G. 2018. Distinct criticality of phase and amplitude dynamics in the resting brain. *Neuroimage,* 180**,** 442-447.

DAGDA, R. K., PIEN, I., WANG, R., ZHU, J., WANG, K. Z., CALLIO, J., BANERJEE, T. D., DAGDA, R. Y. & CHU, C. T. 2014. Beyond the mitochondrion: cytosolic PINK1 remodels dendrites through protein kinase A. *J Neurochem,* 128**,** 864-77.

DAI, P., HARADA, Y. & TAKAMATSU, T. 2015. Highly efficient direct conversion of human fibroblasts to neuronal cells by chemical compounds. *J Clin Biochem Nutr,* 56**,** 166-70.

DARWEESH, S. K., VERLINDEN, V. J., STRICKER, B. H., HOFMAN, A., KOUDSTAAL, P. J. & IKRAM, M. A. 2017. Trajectories of prediagnostic functioning in Parkinson's disease. *Brain,* 140**,** 429-441.

DE VOS, K. J. & HAFEZPARAST, M. 2017. Neurobiology of axonal transport defects in motor neuron diseases: Opportunities for translational research? *Neurobiol Dis,* 105**,** 283-299.

DEL TREDICI, K. & BRAAK, H. 2016. Review: Sporadic Parkinson's disease: development and distribution of alpha-synuclein pathology. *Neuropathol Appl Neurobiol,* 42**,** 33-50.

DENG, H., WANG, P. & JANKOVIC, J. 2018. The genetics of Parkinson disease. *Ageing Res Rev,* 42**,** 72-85.

DENT, E. W. & GERTLER, F. B. 2003. Cytoskeletal dynamics and transport in growth cone motility and axon guidance. *Neuron,* 40**,** 209-27.

DENT, E. W., GUPTON, S. L. & GERTLER, F. B. 2011. The growth cone cytoskeleton in axon outgrowth and guidance. *Cold Spring Harb Perspect Biol,* 3.

DICKSON, T. C., MINTZ, C. D., BENSON, D. L. & SALTON, S. R. 2002. Functional binding interaction identified between the axonal CAM L1 and members of the ERM family. *J Cell Biol,* 157**,** 1105-12.

DJALDETTI, R., HASSIN-BAER, S., FARRER, M. J., VILARINO-GUELL, C., ROSS, O. A., KOLIANOV, V., YUST-KATZ, S., TREVES, T. A., BARHUM, Y., HULIHAN, M. & MELAMED, E. 2008. Clinical characteristics of Parkinson's disease among Jewish Ethnic groups in Israel. *J Neural Transm (Vienna),* 115**,** 1279-84.

DOI, D., SAMATA, B., KATSUKAWA, M., KIKUCHI, T., MORIZANE, A., ONO, Y., SEKIGUCHI, K., NAKAGAWA, M., PARMAR, M. & TAKAHASHI, J. 2014. Isolation of human induced pluripotent stem cell-derived dopaminergic progenitors by cell sorting for successful transplantation. *Stem Cell Reports,* 2**,** 337-50.

DORSEY, E. R., ELBAZ, A., NICHOLS, E., ABD-ALLAH, F., ABDELALIM, A., ADSUAR, J. C., ANSHA, M. G., BRAYNE, C., CHOI, J. Y. J., COLLADO-MATEO, D. & DAHODWALA, N. 2018. Global, regional, and national burden of Parkinson's disease, 1990-2016: a systematic analysis for the Global Burden of Disease Study 2016. *Lancet Neurol,* 17**,** 939-953.

DOWELL-MESFIN, N. M., ABDUL-KARIM, M. A., TURNER, A. M., SCHANZ, S., CRAIGHEAD, H. G., ROYSAM, B., TURNER, J. N. & SHAIN, W. 2004. Topographically modified surfaces affect orientation and growth of hippocampal neurons. *J Neural Eng,* 1**,** 78-90.

EKHTIARI BIDHENDI, E., BERGH, J., ZETTERSTROM, P., FORSBERG, K., PAKKENBERG, B., ANDERSEN, P. M., MARKLUND, S. L. & BRANNSTROM, T. 2018. Mutant superoxide dismutase aggregates from human spinal cord transmit amyotrophic lateral sclerosis. *Acta Neuropathol,* 136**,** 939-953.

ESTEVES, A. R., SWERDLOW, R. H. & CARDOSO, S. M. 2014. LRRK2, a puzzling protein: insights into Parkinson's disease pathogenesis. *Exp Neurol,* 261**,** 206-16.

FEIGIN, V. L., ABAJOBIR, A. A., ABATE, K. H., ABD-ALLAH, F., ABDULLE, A. M., ABERA, S. F., ABYU, G. Y., AHMED, M. B., AICHOUR, A. N., AICHOUR, I. & AICHOUR, M. T. E. 2017. Global, regional, and national burden of neurological disorders during 1990–2015: a systematic analysis for the Global Burden of Disease Study 2015. *Lancet Neurology,* 16**,** 877-897.

FLAGMEIER, P., DE, S., WIRTHENSOHN, D. C., LEE, S. F., VINCKE, C., MUYLDERMANS, S., KNOWLES, T. P. J., GANDHI, S., DOBSON, C. M. & KLENERMAN, D. 2017. Ultrasensitive Measurement of Ca(2+)

Influx into Lipid Vesicles Induced by Protein Aggregates. *Angew Chem Int Ed Engl,* 56**,** 7750-7754.
FORNITO, A. & BULLMORE, E. T. 2015. Connectomics: a new paradigm for understanding brain disease. *Eur Neuropsychopharmacol,* 25**,** 733-48.
FORNITO, A., ZALESKY, A. & BREAKSPEAR, M. 2015. The connectomics of brain disorders. *Nat Rev Neurosci,* 16**,** 159-72.
FREEMAN, W. J. & HOLMES, M. D. 2005. Metastability, instability, and state transition in neocortex. *Neural Netw,* 18**,** 497-504.
FREUNDT, E. C., MAYNARD, N., CLANCY, E. K., ROY, S., BOUSSET, L., SOURIGUES, Y., COVERT, M., MELKI, R., KIRKEGAARD, K. & BRAHIC, M. 2012. Neuron-to-neuron transmission of alpha-synuclein fibrils through axonal transport. *Ann Neurol,* 72**,** 517-24.
FRIEDMAN, E. J. & LANDSBERG, A. S. 2013. Hierarchical networks, power laws, and neuronal avalanches. *Chaos,* 23**,** 013135.
FRIEDMAN, L. G., LACHENMAYER, M. L., WANG, J., HE, L., POULOSE, S. M., KOMATSU, M., HOLSTEIN, G. R. & YUE, Z. 2012a. Disrupted autophagy leads to dopaminergic axon and dendrite degeneration and promotes presynaptic accumulation of alpha-synuclein and LRRK2 in the brain. *J Neurosci,* 32**,** 7585-93.
FRIEDMAN, N., ITO, S., BRINKMAN, B. A., SHIMONO, M., DEVILLE, R. E., DAHMEN, K. A., BEGGS, J. M. & BUTLER, T. C. 2012b. Universal critical dynamics in high resolution neuronal avalanche data. *Phys Rev Lett,* 108**,** 208102.
FRIGG, R. & HARTMANN, S. 2018. Models in Science. *In:* ZALTA, E. N. (ed.) *The Stanford Encyclopedia of Philosophy.* Summer 2018 ed.: Metaphysics Research Lab, Stanford University.
FROEMKE, R. C., TSAY, I. A., RAAD, M., LONG, J. D. & DAN, Y. 2006. Contribution of individual spikes in burst-induced long-term synaptic modification. *J Neurophysiol,* 95**,** 1620-9.
FUSCO, G., PAPE, T., STEPHENS, A. D., MAHOU, P., COSTA, A. R., KAMINSKI, C. F., KAMINSKI SCHIERLE, G. S., VENDRUSCOLO, M., VEGLIA, G., DOBSON, C. M. & DE SIMONE, A. 2016. Structural basis of synaptic vesicle assembly promoted by alpha-synuclein. *Nat Commun,* 7**,** 12563.
GAGE, F. H. 2000. Mammalian neural stem cells. *Science,* 287**,** 1433-8.
GALVAGNION, C., BUELL, A. K., MEISL, G., MICHAELS, T. C., VENDRUSCOLO, M., KNOWLES, T. P. & DOBSON, C. M. 2015. Lipid vesicles trigger alpha-synuclein aggregation by stimulating primary nucleation. *Nat Chem Biol,* 11**,** 229-34.
GAUTAM, S. H., HOANG, T. T., MCCLANAHAN, K., GRADY, S. K. & SHEW, W. L. 2015. Maximizing Sensory Dynamic Range by Tuning the Cortical State to Criticality. *PLoS Comput Biol,* 11**,** e1004576.
GILBERT, C. D. & WIESEL, T. N. 1989. Columnar specificity of intrinsic horizontal and corticocortical connections in cat visual cortex. *J Neurosci,* 9**,** 2432-42.
GIREESH, E. D. & PLENZ, D. 2008. Neuronal avalanches organize as nested theta- and beta/gamma-oscillations during development of cortical layer 2/3. *Proc Natl Acad Sci U S A,* 105**,** 7576-81.
GITLER, A. D., BEVIS, B. J., SHORTER, J., STRATHEARN, K. E., HAMAMICHI, S., SU, L. J., CALDWELL, K. A., CALDWELL, G. A., ROCHET, J. C., MCCAFFERY, J. M., BARLOWE, C. & LINDQUIST, S. 2008. The Parkinson's disease protein alpha-synuclein disrupts cellular Rab homeostasis. *Proc Natl Acad Sci U S A,* 105**,** 145-50.
GIUGLIANO, M., ARSIERO, M., DARBON, P., STREIT, J. & LÜSCHER, H. 2006. Emerging Network Activity in Dissociated Cultures of Neocortex: Novel Electrophysiological Protocols and Mathematical Modeling. *In:* TAKETANI, M. & BAUDRY, M. (eds.) *Advances in Network Electrophysiology.* Boston: Springer.
GLASS, C. K., SAIJO, K., WINNER, B., MARCHETTO, M. C. & GAGE, F. H. 2010. Mechanisms underlying inflammation in neurodegeneration. *Cell,* 140**,** 918-34.
GOEDERT, M., MASUDA-SUZUKAKE, M. & FALCON, B. 2017. Like prions: the propagation of aggregated tau and alpha-synuclein in neurodegeneration. *Brain,* 140**,** 266-278.
GOEDERT, M., SPILLANTINI, M. G., DEL TREDICI, K. & BRAAK, H. 2013. 100 years of Lewy pathology. *Nat Rev Neurol,* 9**,** 13-24.

GOLDE, T. E., BORCHELT, D. R., GIASSON, B. I. & LEWIS, J. 2013. Thinking laterally about neurodegenerative proteinopathies. *J Clin Invest,* 123**,** 1847-55.
GOODMAN, C. S. & SHATZ, C. J. 1993. Developmental mechanisms that generate precise patterns of neuronal connectivity. *Cell,* 72 Suppl**,** 77-98.
GREGGIO, E., JAIN, S., KINGSBURY, A., BANDOPADHYAY, R., LEWIS, P., KAGANOVICH, A., VAN DER BRUG, M. P., BEILINA, A., BLACKINTON, J., THOMAS, K. J., AHMAD, R., MILLER, D. W., KESAVAPANY, S., SINGLETON, A., LEES, A., HARVEY, R. J., HARVEY, K. & COOKSON, M. R. 2006. Kinase activity is required for the toxic effects of mutant LRRK2/dardarin. *Neurobiol Dis,* 23**,** 329-41.
GREIG, C., WOODWORTH, M., GALAZO, M., PADMANABHAN, H. & MACKLIS, J. 2013. Molecular logic of neocortical projection neuron spesification, development and diversity. *Nature Reviews: Neuroscience,* 14.
HALDEMAN, C. & BEGGS, J. M. 2005. Critical branching captures activity in living neural networks and maximizes the number of metastable States. *Phys Rev Lett,* 94**,** 058101.
HARIRI, M., MILLANE, G., GUIMOND, M. P., GUAY, G., DENNIS, J. W. & NABI, I. R. 2000. Biogenesis of multilamellar bodies via autophagy. *Mol Biol Cell,* 11**,** 255-68.
HAUBENSAK, W., ATTARDO, A., DENK, W. & HUTTNER, W. B. 2004. Neurons arise in the basal neuroepithelium of the early mammalian telencephalon: a major site of neurogenesis. *Proc Natl Acad Sci U S A,* 101**,** 3196-201.
HAWKES, C. H., DEL TREDICI, K. & BRAAK, H. 2007. Parkinson's disease: a dual-hit hypothesis. *Neuropathol Appl Neurobiol,* 33**,** 599-614.
HAWKES, C. H., DEL TREDICI, K. & BRAAK, H. 2009. Parkinson's disease: the dual hit theory revisited. *Ann N Y Acad Sci,* 1170**,** 615-22.
HEINEY, K., VALDERHAUG, V. D., SANDVIG, I., SANDVIG, A., TUFTE, G., HAMMER, H. L. & NICHELE, S. 2019. Evaluation of the criticality of in vitro neuronal networks: Towards an assessment of computational capacity. *arXiv*.
HESSE, J. & GROSS, T. 2014. Self-organized criticality as a fundamental property of neural systems. *Front Syst Neurosci,* 8**,** 166.
HIRSCH, E. C. & HUNOT, S. 2009. Neuroinflammation in Parkinson's disease: a target for neuroprotection? *Lancet Neurol,* 8**,** 382-97.
HOFFMANN, H. & PAYTON, D. W. 2018. Optimization by Self-Organized Criticality. *Sci Rep,* 8**,** 2358.
HOFMAN, M. A. 2014. Evolution of the human brain: when bigger is better. *Front Neuroanat,* 8**,** 15.
HONEY, C. J. & SPORNS, O. 2008. Dynamical consequences of lesions in cortical networks. *Hum Brain Mapp,* 29**,** 802-9.
HORVATH, P. & BARRANGOU, R. 2010. CRISPR/Cas, the immune system of bacteria and archaea. *Science,* 327**,** 167-70.
HSIEH, C. H., SHALTOUKI, A., GONZALEZ, A. E., BETTENCOURT DA CRUZ, A., BURBULLA, L. F., ST LAWRENCE, E., SCHULE, B., KRAINC, D., PALMER, T. D. & WANG, X. 2016. Functional Impairment in Miro Degradation and Mitophagy Is a Shared Feature in Familial and Sporadic Parkinson's Disease. *Cell Stem Cell,* 19**,** 709-724.
HUBEL, D. H. & WIESEL, T. N. 1970. The period of susceptibility to the physiological effects of unilateral eye closure in kittens. *J Physiol,* 206**,** 419-36.
HUBEL, D. H., WIESEL, T. N. & LEVAY, S. 1977. Plasticity of ocular dominance columns in monkey striate cortex. *Philos Trans R Soc Lond B Biol Sci,* 278**,** 377-409.
HUH, C. J., ZHANG, B., VICTOR, M. B., DAHIYA, S., BATISTA, L. F., HORVATH, S. & YOO, A. S. 2016. Maintenance of age in human neurons generated by microRNA-based neuronal conversion of fibroblasts. *Elife,* 5.
HUNN, B. H., CRAGG, S. J., BOLAM, J. P., SPILLANTINI, M. G. & WADE-MARTINS, R. 2015. Impaired intracellular trafficking defines early Parkinson's disease. *Trends Neurosci,* 38**,** 178-88.
IKEGAMI, A., HARUWAKA, K. & WAKE, H. 2019. Microglia: Lifelong modulator of neural circuits. *Neuropathology,* 39**,** 173-180.

INNOCENTI, G. M., FIORE, L. & CAMINITI, R. 1977. Exuberant projection into the corpus callosum from the visual cortex of newborn cats. *Neurosci Lett,* 4**,** 237-42.
INNOCENTI, G. M. & PRICE, D. J. 2005. Exuberance in the development of cortical networks. *Nat Rev Neurosci,* 6**,** 955-65.
JELLINGER, K. A. 2014. The pathomechanisms underlying Parkinson's disease. *Expert Rev Neurother,* 14**,** 199-215.
JI, K., AKGUL, G., WOLLMUTH, L. P. & TSIRKA, S. E. 2013. Microglia actively regulate the number of functional synapses. *PLoS One,* 8**,** e56293.
JINEK, M., CHYLINSKI, K., FONFARA, I., HAUER, M., DOUDNA, J. A. & CHARPENTIER, E. 2012. A programmable dual-RNA-guided DNA endonuclease in adaptive bacterial immunity. *Science,* 337**,** 816-21.
JOANNE TRINH, MATTHEW FARRER, OWEN A ROSS & GUELLA, I. 2006. LRRK2-Related Parkinsons Disease. *In:* ADAM MP, ARDINGER HH & RA, P. (eds.). Seattle (WA): University of Washington, Seattle: GeneReviews® [Internet].
JOHANSSON, B. B. 2004. Brain plasticity in health and disease. *Keio J Med,* 53**,** 231-46.
KAISER, M. & HILGETAG, C. C. 2006. Nonoptimal component placement, but short processing paths, due to long-distance projections in neural systems. *PLoS Comput Biol,* 2**,** e95.
KALIA, L. V. & LANG, A. E. 2015. Parkinson's disease. *Lancet,* 386**,** 896-912.
KAROW, M., SANCHEZ, R., SCHICHOR, C., MASSERDOTTI, G., ORTEGA, F., HEINRICH, C., GASCON, S., KHAN, M. A., LIE, D. C., DELLAVALLE, A., COSSU, G., GOLDBRUNNER, R., GOTZ, M. & BERNINGER, B. 2012. Reprogramming of pericyte-derived cells of the adult human brain into induced neuronal cells. *Cell Stem Cell,* 11**,** 471-6.
KATZ, L. C., GILBERT, C. D. & WIESEL, T. N. 1989. Local circuits and ocular dominance columns in monkey striate cortex. *J Neurosci,* 9**,** 1389-99.
KATZ, L. C. & SHATZ, C. J. 1996. Synaptic activity and the construction of cortical circuits. *Science,* 274**,** 1133-8.
KIME, C., MANDEGAR, M. A., SRIVASTAVA, D., YAMANAKA, S., CONKLIN, B. R. & RAND, T. A. 2016. Efficient CRISPR/Cas9-Based Genome Engineering in Human Pluripotent Stem Cells. *Curr Protoc Hum Genet,* 88**,** Unit 21.4.
KINOUCHI, O., BROCHINI, L., COSTA, A., CAMPOS, J. & COPELLI, M. J. A. P. A. 2018. Stochastic oscillations produce dragon king avalanches in self-organized quasi-critical systems.
KIPPS, C. M., DUGGINS, A. J., MAHANT, N., GOMES, L., ASHBURNER, J. & MCCUSKER, E. A. 2005. Progression of structural neuropathology in preclinical Huntington's disease: a tensor based morphometry study. *J Neurol Neurosurg Psychiatry,* 76**,** 650-5.
KIRKEBY, A., GREALISH, S., WOLF, D. A., NELANDER, J., WOOD, J., LUNDBLAD, M., LINDVALL, O. & PARMAR, M. 2012a. Generation of regionally specified neural progenitors and functional neurons from human embryonic stem cells under defined conditions. *Cell Rep,* 1**,** 703-14.
KIRKEBY, A., NELANDER, J. & PARMAR, M. 2012b. Generating regionalized neuronal cells from pluripotency, a step-by-step protocol. *Front Cell Neurosci,* 6**,** 64.
KIRKEBY, A., NOLBRANT, S., TIKLOVA, T., HEUER, A., KEE, N., CARDOSO, T., OTTOSSON, D. R., LELOS, M. J., RIFES, P., DUNNETT, S., GREALISH, S., PERLMANN, T. & PARMAR, M. 2016. Predictive Markers Guide Differentiation to Improve Graft Outcome in Clinical Translation of hESC-Based Therapy for Parkinson's Disease. *Cell Stem Cell,* 20**,** 1-14.
KIRWAN, P., TURNER-BRIDGER, B., PETER, M., MOMOH, A., ARAMBEPOLA, D., ROBINSON, H. P. & LIVESEY, F. J. 2015. Development and function of human cerebral cortex neural networks from pluripotent stem cells in vitro. *Development,* 142**,** 3178-87.
KITSAK, M., GALLOS, L. K., HAVLIN, S., LILJEROS, F., MUCHNIK, L., STANLEY, H. E. & MAKSE, H. A. 2010. Identification of influential spreaders in complex networks. *Nature Physics,* 6**,** 888.
KOPITO, R. R. 2000. Aggresomes, inclusion bodies and protein aggregation. *Trends Cell Biol,* 10**,** 524-30.

KORDOWER, J. H., CHU, Y., HAUSER, R. A., FREEMAN, T. B. & OLANOW, C. W. 2008. Lewy body-like pathology in long-term embryonic nigral transplants in Parkinson's disease. *Nat Med,* 14**,** 504-6.
KORDOWER, J. H., OLANOW, C. W., DODIYA, H. B., CHU, Y., BEACH, T. G., ADLER, C. H., HALLIDAY, G. M. & BARTUS, R. T. 2013. Disease duration and the integrity of the nigrostriatal system in Parkinson's disease. *Brain,* 136**,** 2419-31.
KOULI, A., TORSNEY, K. M. & KUAN, W. L. 2018. Parkinson's Disease: Etiology, Neuropathology, and Pathogenesis. *In:* STOKER, T. B. & GREENLAND, J. C. (eds.) *Parkinson's Disease: Pathogenesis and Clinical Aspects.* Brisbane (AU): Codon Publications

KRAHE, R. & GABBIANI, F. 2004. Burst firing in sensory systems. *Nat Rev Neurosci,* 5**,** 13-23.
KRAMER, M. L. & SCHULZ-SCHAEFFER, W. J. 2007. Presynaptic alpha-synuclein aggregates, not Lewy bodies, cause neurodegeneration in dementia with Lewy bodies. *J Neurosci,* 27**,** 1405-10.
KRIKS, S., SHIM, J. W., PIAO, J., GANAT, Y. M., WAKEMAN, D. R., XIE, Z., CARRILLO-REID, L., AUYEUNG, G., ANTONACCI, C., BUCH, A., YANG, L., BEAL, M. F., SURMEIER, D. J., KORDOWER, J. H., TABAR, V. & STUDER, L. 2011. Dopamine neurons derived from human ES cells efficiently engraft in animal models of Parkinson's disease. *Nature,* 480**,** 547-551.
KWIATKOWSKI, T. J., JR., BOSCO, D. A., LECLERC, A. L., TAMRAZIAN, E., VANDERBURG, C. R., RUSS, C., DAVIS, A., GILCHRIST, J., KASARSKIS, E. J., MUNSAT, T., VALDMANIS, P., ROULEAU, G. A., HOSLER, B. A., CORTELLI, P., DE JONG, P. J., YOSHINAGA, Y., HAINES, J. L., PERICAK-VANCE, M. A., YAN, J., TICOZZI, N., SIDDIQUE, T., MCKENNA-YASEK, D., SAPP, P. C., HORVITZ, H. R., LANDERS, J. E. & BROWN, R. H., JR. 2009. Mutations in the FUS/TLS gene on chromosome 16 cause familial amyotrophic lateral sclerosis. *Science,* 323**,** 1205-8.
LANGTON, C. G. 1990. Computation at the edge of chaos: phase transitions and emergent computation. *Physica D: Nonlinear Phenomena,* 42**,** 12-37.
LAPASSET, L., MILHAVET, O., PRIEUR, A., BESNARD, E., BABLED, A., AIT-HAMOU, N., LESCHIK, J., PELLESTOR, F., RAMIREZ, J. M., DE VOS, J., LEHMANN, S. & LEMAITRE, J. M. 2011. Rejuvenating senescent and centenarian human cells by reprogramming through the pluripotent state. *Genes Dev,* 25**,** 2248-53.
LATORA, V. & MARCHIORI, M. 2001. Efficient behavior of small-world networks. *Phys Rev Lett,* 87**,** 198701.
LAUGHLIN, S. B. & SEJNOWSKI, T. J. 2003. Communication in neuronal networks. *Science,* 301**,** 1870-4.
LEES, A. J., HARDY, J. & REVESZ, T. 2009. Parkinson's disease. *Lancet,* 373**,** 2055-66.
LEVAY, S., WIESEL, T. N. & HUBEL, D. H. 1980. The development of ocular dominance columns in normal and visually deprived monkeys. *J Comp Neurol,* 191**,** 1-51.
LEWIS, P. A. 2019. Leucine rich repeat kinase 2: a paradigm for pleiotropy. *J Physiol,* 597**,** 3511-3521.
LI, J. Q., TAN, L. & YU, J. T. 2014. The role of the LRRK2 gene in Parkinsonism. *Mol Neurodegener,* 9**,** 47.
LI, J. Y., ENGLUND, E., HOLTON, J. L., SOULET, D., HAGELL, P., LEES, A. J., LASHLEY, T., QUINN, N. P., REHNCRONA, S., BJORKLUND, A., WIDNER, H., REVESZ, T., LINDVALL, O. & BRUNDIN, P. 2008. Lewy bodies in grafted neurons in subjects with Parkinson's disease suggest host-to-graft disease propagation. *Nat Med,* 14**,** 501-3.
LI, W., ENGLUND, E., WIDNER, H., MATTSSON, B., VAN WESTEN, D., LATT, J., REHNCRONA, S., BRUNDIN, P., BJORKLUND, A., LINDVALL, O. & LI, J. Y. 2016. Extensive graft-derived dopaminergic innervation is maintained 24 years after transplantation in the degenerating parkinsonian brain. *Proc Natl Acad Sci U S A,* 113**,** 6544-9.
LIN, M. T. & BEAL, M. F. 2006. Mitochondrial dysfunction and oxidative stress in neurodegenerative diseases. *Nature,* 443**,** 787-95.
LISMAN, J. E. 1997. Bursts as a unit of neural information: making unreliable synapses reliable. *Trends Neurosci,* 20**,** 38-43.
LIU, K., TEDESCHI, A., PARK, K. K. & HE, Z. 2011. Neuronal intrinsic mechanisms of axon regeneration. *Annu Rev Neurosci,* 34**,** 131-52.

LO, D. C. 1995. Neurotrophic factors and synaptic plasticity. *Neuron,* 15**,** 979-81.
LO, E. H. 2010. Degeneration and repair in central nervous system disease. *Nat Med,* 16**,** 1205-9.
LOMBARDI, F., HERRMANN, H. J., PERRONE-CAPANO, C., PLENZ, D. & DE ARCANGELIS, L. 2012. Balance between excitation and inhibition controls the temporal organization of neuronal avalanches. *Phys Rev Lett,* 108**,** 228703.
LU, Y. L. & YOO, A. S. 2018. Mechanistic Insights Into MicroRNA-Induced Neuronal Reprogramming of Human Adult Fibroblasts. *Front Neurosci,* 12**,** 522.
LUCIN, K. M. & WYSS-CORAY, T. 2009. Immune activation in brain aging and neurodegeneration: too much or too little? *Neuron,* 64**,** 110-22.
LUK, K. C., KEHM, V., CARROLL, J., ZHANG, B., O'BRIEN, P., TROJANOWSKI, J. Q. & LEE, V. M. 2012a. Pathological alpha-synuclein transmission initiates Parkinson-like neurodegeneration in nontransgenic mice. *Science,* 338**,** 949-53.
LUK, K. C., KEHM, V. M., ZHANG, B., O'BRIEN, P., TROJANOWSKI, J. Q. & LEE, V. M. 2012b. Intracerebral inoculation of pathological alpha-synuclein initiates a rapidly progressive neurodegenerative alpha-synucleinopathy in mice. *J Exp Med,* 209**,** 975-86.
MACLEOD, D., DOWMAN, J., HAMMOND, R., LEETE, T., INOUE, K. & ABELIOVICH, A. 2006. The familial Parkinsonism gene LRRK2 regulates neurite process morphology. *Neuron,* 52**,** 587-93.
MAEDA, E., ROBINSON, H. P. & KAWANA, A. 1995. The mechanisms of generation and propagation of synchronized bursting in developing networks of cortical neurons. *J Neurosci,* 15**,** 6834-45.
MAHAR, M. & CAVALLI, V. 2018. Intrinsic mechanisms of neuronal axon regeneration. *Nat Rev Neurosci,* 19**,** 323-337.
MAJEWSKA, A. K. & SUR, M. 2006. Plasticity and specificity of cortical processing networks. *Trends Neurosci,* 29**,** 323-9.
MAROM, S. & SHAHAF, G. 2002. Development, learning and memory in large random networks of cortical neurons: lessons beyond anatomy. *Q Rev Biophys,* 35**,** 63-87.
MAROOF, A. M., KEROS, S., TYSON, J. A., YING, S. W., GANAT, Y. M., MERKLE, F. T., LIU, B., GOULBURN, A., STANLEY, E. G., ELEFANTY, A. G., WIDMER, H. R., EGGAN, K., GOLDSTEIN, P. A., ANDERSON, S. A. & STUDER, L. 2013. Directed differentiation and functional maturation of cortical interneurons from human embryonic stem cells. *Cell Stem Cell,* 12**,** 559-72.
MASSOBRIO, P., PASQUALE, V. & MARTINOIA, S. 2015. Self-organized criticality in cortical assemblies occurs in concurrent scale-free and small-world networks. *Sci Rep,* 5**,** 10578.
MATTAY, V. S., FERA, F., TESSITORE, A., HARIRI, A. R., BERMAN, K. F., DAS, S., MEYER-LINDENBERG, A., GOLDBERG, T. E., CALLICOTT, J. H. & WEINBERGER, D. R. 2006. Neurophysiological correlates of age-related changes in working memory capacity. *Neurosci Lett,* 392**,** 32-7.
MATTAY, V. S., FERA, F., TESSITORE, A., HARIRI, A. R., DAS, S., CALLICOTT, J. H. & WEINBERGER, D. R. 2002. Neurophysiological correlates of age-related changes in human motor function. *Neurology,* 58**,** 630-5.
MEHRA, S., SAHAY, S. & MAJI, S. K. 2019. alpha-Synuclein misfolding and aggregation: Implications in Parkinson's disease pathogenesis. *Biochim Biophys Acta Proteins Proteom,* 1867**,** 890-908.
MEREDITH, G. E., TOTTERDELL, S., PETROSKE, E., SANTA CRUZ, K., CALLISON, R. C., JR. & LAU, Y. S. 2002. Lysosomal malfunction accompanies alpha-synuclein aggregation in a progressive mouse model of Parkinson's disease. *Brain Res,* 956**,** 156-65.
MERTENS, J., PAQUOLA, A. C. M., KU, M., HATCH, E., BOHNKE, L., LADJEVARDI, S., MCGRATH, S., CAMPBELL, B., LEE, H., HERDY, J. R., GONCALVES, J. T., TODA, T., KIM, Y., WINKLER, J., YAO, J., HETZER, M. W. & GAGE, F. H. 2015. Directly Reprogrammed Human Neurons Retain Aging-Associated Transcriptomic Signatures and Reveal Age-Related Nucleocytoplasmic Defects. *Cell Stem Cell,* 17**,** 705-718.
MICHIELS VAN KESSENICH, L., DE ARCANGELIS, L. & HERRMANN, H. J. 2016. Synaptic plasticity and neuronal refractory time cause scaling behaviour of neuronal avalanches. *Sci Rep,* 6**,** 32071.
MICHOLT, L., GARTNER, A., PRODANOV, D., BRAEKEN, D., DOTTI, C. G. & BARTIC, C. 2013. Substrate topography determines neuronal polarization and growth in vitro. *PLoS One,* 8**,** e66170.

MING, G. L. & SONG, H. 2011. Adult neurogenesis in the mammalian brain: significant answers and significant questions. *Neuron,* 70**,** 687-702.
MINOCHA, S., VALLOTON, D., YPSILANTI, A. R., FIUMELLI, H., ALLEN, E. A., YANAGAWA, Y., MARIN, O., CHEDOTAL, A., HORNUNG, J. P. & LEBRAND, C. 2015. Nkx2.1-derived astrocytes and neurons together with Slit2 are indispensable for anterior commissure formation. *Nat Commun,* 6**,** 6887.
MIYAMOTO, A., WAKE, H., ISHIKAWA, A. W., ETO, K., SHIBATA, K., MURAKOSHI, H., KOIZUMI, S., MOORHOUSE, A. J., YOSHIMURA, Y. & NABEKURA, J. 2016. Microglia contact induces synapse formation in developing somatosensory cortex. *Nat Commun,* 7**,** 12540.
MOLYNEAUX, B. J., ARLOTTA, P., MENEZES, J. R. & MACKLIS, J. D. 2007. Neuronal subtype specification in the cerebral cortex. *Nat Rev Neurosci,* 8**,** 427-37.
MOORE, C. & NEWMAN, M. E. 2000. Epidemics and percolation in small-world networks. *Phys Rev E Stat Phys Plasmas Fluids Relat Interdiscip Topics,* 61**,** 5678-82.
MORETTI, P. & MUNOZ, M. A. 2013. Griffiths phases and the stretching of criticality in brain networks. *Nat Commun,* 4**,** 2521.
MORTIBOYS, H., JOHANSEN, K. K., AASLY, J. O. & BANDMANN, O. 2010. Mitochondrial impairment in patients with Parkinson disease with the G2019S mutation in LRRK2. *Neurology,* 75**,** 2017-20.
MOUNT, M. P., LIRA, A., GRIMES, D., SMITH, P. D., FAUCHER, S., SLACK, R., ANISMAN, H., HAYLEY, S. & PARK, D. S. 2007. Involvement of interferon-gamma in microglial-mediated loss of dopaminergic neurons. *J Neurosci,* 27**,** 3328-37.
MUÑOZ, M. A. 2018. Colloquium: Criticality and dynamical scaling in living systems. *Reviews of Modern Physics,* 90.
NGUYEN, H. N., BYERS, B., CORD, B., SHCHEGLOVITOV, A., BYRNE, J., GUJAR, P., KEE, K., SCHULE, B., DOLMETSCH, R. E., LANGSTON, W., PALMER, T. D. & PERA, R. R. 2011. LRRK2 mutant iPSC-derived DA neurons demonstrate increased susceptibility to oxidative stress. *Cell Stem Cell,* 8**,** 267-80.
NOCTOR, S. C., MARTINEZ-CERDENO, V., IVIC, L. & KRIEGSTEIN, A. R. 2004. Cortical neurons arise in symmetric and asymmetric division zones and migrate through specific phases. *Nat Neurosci,* 7**,** 136-44.
NOCTOR, S. C., MARTINEZ-CERDENO, V. & KRIEGSTEIN, A. R. 2007. Contribution of intermediate progenitor cells to cortical histogenesis. *Arch Neurol,* 64**,** 639-42.
NOURAEI, N., MASON, D. M., MINER, K. M., CARCELLA, M. A., BHATIA, T. N., DUMM, B. K., SONI, D., JOHNSON, D. A., LUK, K. C. & LEAK, R. K. 2018. Critical appraisal of pathology transmission in the alpha-synuclein fibril model of Lewy body disorders. *Exp Neurol,* 299**,** 172-196.
NYKTER, M., PRICE, N. D., LARJO, A., AHO, T., KAUFFMAN, S. A., YLI-HARJA, O. & SHMULEVICH, I. J. P. R. L. 2008. Critical networks exhibit maximal information diversity in structure-dynamics relationships. 100**,** 058702.
O'LEARY, D. D. 1992. Development of connectional diversity and specificity in the mammalian brain by the pruning of collateral projections. *Curr Opin Neurobiol,* 2**,** 70-7.
OZELIUS, L. J., SENTHIL, G., SAUNDERS-PULLMAN, R., OHMANN, E., DELIGTISCH, A., TAGLIATI, M., HUNT, A. L., KLEIN, C., HENICK, B., HAILPERN, S. M., LIPTON, R. B., SOTO-VALENCIA, J., RISCH, N. & BRESSMAN, S. B. 2006. LRRK2 G2019S as a cause of Parkinson's disease in Ashkenazi Jews. *N Engl J Med,* 354**,** 424-5.
PAOLICELLI, R. C., BOLASCO, G., PAGANI, F., MAGGI, L., SCIANNI, M., PANZANELLI, P., GIUSTETTO, M., FERREIRA, T. A., GUIDUCCI, E., DUMAS, L., RAGOZZINO, D. & GROSS, C. T. 2011. Synaptic pruning by microglia is necessary for normal brain development. *Science,* 333**,** 1456-8.
PASQUALE, V., MASSOBRIO, P., BOLOGNA, L. L., CHIAPPALONE, M. & MARTINOIA, S. 2008. Self-organization and neuronal avalanches in networks of dissociated cortical neurons. *Neuroscience,* 153**,** 1354-69.
PATTERSON, M., CHAN, D. N., HA, I., CASE, D., CUI, Y., VAN HANDEL, B., MIKKOLA, H. K. & LOWRY, W. E. 2012. Defining the nature of human pluripotent stem cell progeny. *Cell Res,* 22**,** 178-93.
PENNISI, E. 2013. The CRISPR craze. *Science,* 341**,** 833-6.

PEREIRA, M., PFISTERER, U., RYLANDER, D., TORPER, O., LAU, S., LUNDBLAD, M., GREALISH, S. & PARMAR, M. 2014. Highly efficient generation of induced neurons from human fibroblasts that survive transplantation into the adult rat brain. *Sci Rep,* 4**,** 6330.

PFISTERER, U., KIRKEBY, A., TORPER, O., WOOD, J., NELANDER, J., DUFOUR, A., BJORKLUND, A., LINDVALL, O., JAKOBSSON, J. & PARMAR, M. 2011. Direct conversion of human fibroblasts to dopaminergic neurons. *Proc Natl Acad Sci U S A,* 108**,** 10343-8.

PFRIEGER, F. W. 2010. Role of glial cells in the formation and maintenance of synapses. *Brain Res Rev,* 63**,** 39-46.

PLOWEY, E. D., CHERRA, S. J., 3RD, LIU, Y. J. & CHU, C. T. 2008. Role of autophagy in G2019S-LRRK2-associated neurite shortening in differentiated SH-SY5Y cells. *J Neurochem,* 105**,** 1048-56.

POIL, S. S., VAN OOYEN, A. & LINKENKAER-HANSEN, K. 2008. Avalanche dynamics of human brain oscillations: relation to critical branching processes and temporal correlations. *Hum Brain Mapp,* 29**,** 770-7.

POLI, D., PASTORE, V. P. & MASSOBRIO, P. 2015. Functional connectivity in in vitro neuronal assemblies. *Front Neural Circuits,* 9**,** 57.

POLINSKI, N. K., VOLPICELLI-DALEY, L. A., SORTWELL, C. E., LUK, K. C., CREMADES, N., GOTTLER, L. M., FROULA, J., DUFFY, M. F., LEE, V. M. Y., MARTINEZ, T. N. & DAVE, K. D. 2018. Best Practices for Generating and Using Alpha-Synuclein Pre-Formed Fibrils to Model Parkinson's Disease in Rodents. *J Parkinsons Dis,* 8**,** 303-322.

POSTUMA, R. B., AARSLAND, D., BARONE, P., BURN, D. J., HAWKES, C. H., OERTEL, W. & ZIEMSSEN, T. 2012. Identifying prodromal Parkinson's disease: pre-motor disorders in Parkinson's disease. *Mov Disord,* 27**,** 617-26.

PU, J., GONG, H., LI, X. & LUO, Q. 2013. Developing neuronal networks: Self-organized criticality predicts the future. *Scientific Reports,* 3**,** 1081.

QING, X., WALTER, J., JARAZO, J., ARIAS-FUENZALIDA, J., HILLJE, A. L. & SCHWAMBORN, J. C. 2017. CRISPR/Cas9 and piggyBac-mediated footprint-free LRRK2-G2019S knock-in reveals neuronal complexity phenotypes and alpha-Synuclein modulation in dopaminergic neurons. *Stem Cell Res,* 24**,** 44-50.

RAGAGNIN, A., GUILLEMAIN, A., GRANT, N. J. & BAILLY, Y. J. R. 2013. Neuronal Autophagy and Prion Proteins. *In:* BAILLY, Y. J. R. (ed.) *Autophagy - A Double-Edged Sword.*

RAIKWAR, S. P., KIKKERI, N. S., SAKURU, R., SAEED, D., ZAHOOR, H., PREMKUMAR, K., MENTOR, S., THANGAVEL, R., DUBOVA, I., AHMED, M. E., SELVAKUMAR, G. P., KEMPURAJ, D., ZAHEER, S., IYER, S. S. & ZAHEER, A. 2019. Next Generation Precision Medicine: CRISPR-mediated Genome Editing for the Treatment of Neurodegenerative Disorders. *J Neuroimmune Pharmacol*.

RAJ, A., KUCEYESKI, A. & WEINER, M. 2012. A network diffusion model of disease progression in dementia. *Neuron,* 73**,** 1204-15.

RAKIC, P., BOURGEOIS, J. P., ECKENHOFF, M. F., ZECEVIC, N. & GOLDMAN-RAKIC, P. S. 1986. Concurrent overproduction of synapses in diverse regions of the primate cerebral cortex. *Science,* 232**,** 232-5.

REINHARDT, P., SCHMID, B., BURBULLA, L. F., SCHONDORF, D. C., WAGNER, L., GLATZA, M., HOING, S., HARGUS, G., HECK, S. A., DHINGRA, A., WU, G., MULLER, S., BROCKMANN, K., KLUBA, T., MAISEL, M., KRUGER, R., BERG, D., TSYTSYURA, Y., THIEL, C. S., PSATHAKI, O. E., KLINGAUF, J., KUHLMANN, T., KLEWIN, M., MULLER, H., GASSER, T., SCHOLER, H. R. & STERNECKERT, J. 2013. Genetic correction of a LRRK2 mutation in human iPSCs links parkinsonian neurodegeneration to ERK-dependent changes in gene expression. *Cell Stem Cell,* 12**,** 354-67.

RIBEIRO, T. L., COPELLI, M., CAIXETA, F., BELCHIOR, H., CHIALVO, D. R., NICOLELIS, M. A. & RIBEIRO, S. 2010. Spike avalanches exhibit universal dynamics across the sleep-wake cycle. *PLoS One,* 5**,** e14129.

RODRIGUEZ-OROZ, M. C., JAHANSHAHI, M., KRACK, P., LITVAN, I., MACIAS, R., BEZARD, E. & OBESO, J. A. 2009. Initial clinical manifestations of Parkinson's disease: features and pathophysiological mechanisms. *Lancet Neurol,* 8**,** 1128-39.

RUBINOV, M., SPORNS, O., THIVIERGE, J. P. & BREAKSPEAR, M. 2011. Neurobiologically realistic determinants of self-organized criticality in networks of spiking neurons. *PLoS Comput Biol,* 7**,** e1002038.

RUIPEREZ, V., DARIOS, F. & DAVLETOV, B. 2010. Alpha-synuclein, lipids and Parkinson's disease. *Prog Lipid Res,* 49**,** 420-8.

RYBARSCH, M. & BORNHOLDT, S. 2014. Avalanches in self-organized critical neural networks: a minimal model for the neural SOC universality class. *PLoS One,* 9**,** e93090.

SACINO, A. N., BROOKS, M., THOMAS, M. A., MCKINNEY, A. B., MCGARVEY, N. H., RUTHERFORD, N. J., CEBALLOS-DIAZ, C., ROBERTSON, J., GOLDE, T. E. & GIASSON, B. I. 2014. Amyloidogenic alpha-synuclein seeds do not invariably induce rapid, widespread pathology in mice. *Acta Neuropathol,* 127**,** 645-65.

SACINO, A. N., BROOKS, M. M., CHAKRABARTY, P., SAHA, K., KHOSHBOUEI, H., GOLDE, T. E. & GIASSON, B. I. 2017. Proteolysis of alpha-synuclein fibrils in the lysosomal pathway limits induction of inclusion pathology. *J Neurochem,* 140**,** 662-678.

SANCES, S., BRUIJN, L. I., CHANDRAN, S., EGGAN, K., HO, R., KLIM, J. R., LIVESEY, M. R., LOWRY, E., MACKLIS, J. D., RUSHTON, D., SADEGH, C., SAREEN, D., WICHTERLE, H., ZHANG, S. C. & SVENDSEN, C. N. 2016. Modeling ALS with motor neurons derived from human induced pluripotent stem cells. *Nat Neurosci,* 16**,** 542-53.

SANCHEZ-DANES, A., CONSIGLIO, A., RICHAUD, Y., RODRIGUEZ-PIZA, I., DEHAY, B., EDEL, M., BOVE, J., MEMO, M., VILA, M., RAYA, A. & IZPISUA BELMONTE, J. C. 2012a. Efficient generation of A9 midbrain dopaminergic neurons by lentiviral delivery of LMX1A in human embryonic stem cells and induced pluripotent stem cells. *Hum Gene Ther,* 23**,** 56-69.

SANCHEZ-DANES, A., RICHAUD-PATIN, Y., CARBALLO-CARBAJAL, I., JIMENEZ-DELGADO, S., CAIG, C., MORA, S., DI GUGLIELMO, C., EZQUERRA, M., PATEL, B., GIRALT, A., CANALS, J. M., MEMO, M., ALBERCH, J., LOPEZ-BARNEO, J., VILA, M., CUERVO, A. M., TOLOSA, E., CONSIGLIO, A. & RAYA, A. 2012b. Disease-specific phenotypes in dopamine neurons from human iPS-based models of genetic and sporadic Parkinson's disease. *EMBO Mol Med,* 4**,** 380-95.

SANDVIG, A., BERRY, M., BARRETT, L. B., BUTT, A. & LOGAN, A. 2004. Myelin-, reactive glia-, and scar-derived CNS axon growth inhibitors: expression, receptor signaling, and correlation with axon regeneration. *Glia,* 46**,** 225-51.

SAXTON, W. M. & HOLLENBECK, P. J. 2012. The axonal transport of mitochondria. *J Cell Sci,* 125**,** 2095-104.

SCHWAB, M. E. & STRITTMATTER, S. M. 2014. Nogo limits neural plasticity and recovery from injury. *Curr Opin Neurobiol,* 27**,** 53-60.

SEPULVEDA, B., MESIAS, R., LI, X., YUE, Z. & BENSON, D. L. 2013. Short- and long-term effects of LRRK2 on axon and dendrite growth. *PLoS One,* 8**,** e61986.

SHAHMORADIAN, S. H., LEWIS, A. J., GENOUD, C., HENCH, J., MOORS, T. E., NAVARRO, P. P., CASTANO-DIEZ, D., SCHWEIGHAUSER, G., GRAFF-MEYER, A., GOLDIE, K. N., SUTTERLIN, R., HUISMAN, E., INGRASSIA, A., GIER, Y., ROZEMULLER, A. J. M., WANG, J., PAEPE, A., ERNY, J., STAEMPFLI, A., HOERNSCHEMEYER, J., GROSSERUSCHKAMP, F., NIEDIEKER, D., EL-MASHTOLY, S. F., QUADRI, M., VAN, I. W. F. J., BONIFATI, V., GERWERT, K., BOHRMANN, B., FRANK, S., BRITSCHGI, M., STAHLBERG, H., VAN DE BERG, W. D. J. & LAUER, M. E. 2019. Lewy pathology in Parkinson's disease consists of crowded organelles and lipid membranes. *Nat Neurosci,* 22**,** 1099-1109.

SHEW, W. L. & PLENZ, D. 2013. The functional benefits of criticality in the cortex. *Neuroscientist,* 19**,** 88-100.

SILVER, J., SCHWAB, M. E. & POPOVICH, P. G. 2014. Central nervous system regenerative failure: role of oligodendrocytes, astrocytes, and microglia. *Cold Spring Harb Perspect Biol,* 7**,** a020602.

SINGH, A., ZHI, L. & ZHANG, H. 2019. LRRK2 and mitochondria: Recent advances and current views. *Brain Res,* 1702**,** 96-104.

SMITH, W. W., PEI, Z., JIANG, H., DAWSON, V. L., DAWSON, T. M. & ROSS, C. A. 2006. Kinase activity of mutant LRRK2 mediates neuronal toxicity. *Nat Neurosci,* 9**,** 1231-3.

SONG, H. & POO, M. 2001. The cell biology of neuronal navigation. *Nat Cell Biol,* 3**,** E81-8.

SPILLANTINI, M. G., CROWTHER, R. A., JAKES, R., HASEGAWA, M. & GOEDERT, M. 1998. alpha-Synuclein in filamentous inclusions of Lewy bodies from Parkinson's disease and dementia with lewy bodies. *Proc Natl Acad Sci U S A,* 95**,** 6469-73.
SPILLANTINI, M. G., SCHMIDT, M. L., LEE, V. M., TROJANOWSKI, J. Q., JAKES, R. & GOEDERT, M. 1997. Alpha-synuclein in Lewy bodies. *Nature,* 388**,** 839-40.
SPORNS, O., CHIALVO, D. R., KAISER, M. & HILGETAG, C. C. 2004. Organization, development and function of complex brain networks. *Trends Cogn Sci,* 8**,** 418-25.
SPORNS, O., TONONI, G. & EDELMAN, G. M. 2000a. Connectivity and complexity: the relationship between neuroanatomy and brain dynamics. *Neural Netw,* 13**,** 909-22.
SPORNS, O., TONONI, G. & EDELMAN, G. M. 2000b. Theoretical neuroanatomy: relating anatomical and functional connectivity in graphs and cortical connection matrices. *Cereb Cortex,* 10**,** 127-41.
SRINIVAS, K. V., JAIN, R., SAURAV, S. & SIKDAR, S. K. 2007. Small-world network topology of hippocampal neuronal network is lost, in an in vitro glutamate injury model of epilepsy. *Eur J Neurosci,* 25**,** 3276-86.
STEWART, C. V. & PLENZ, D. 2008. Homeostasis of neuronal avalanches during postnatal cortex development in vitro. *J Neurosci Methods,* 169**,** 405-16.
STOOP, R. & GOMEZ, F. 2016. Auditory Power-Law Activation Avalanches Exhibit a Fundamental Computational Ground State. *Phys Rev Lett,* 117**,** 038102.
SUDHOF, T. C. 2018. Towards an Understanding of Synapse Formation. *Neuron,* 100**,** 276-293.
SURMEIER, D. J., OBESO, J. A. & HALLIDAY, G. M. 2017a. Parkinson's Disease Is Not Simply a Prion Disorder. *J Neurosci,* 37**,** 9799-9807.
SURMEIER, D. J., OBESO, J. A. & HALLIDAY, G. M. 2017b. Selective neuronal vulnerability in Parkinson disease. *Nat Rev Neurosci,* 18**,** 101-113.
TAGLIAZUCCHI, E., BALENZUELA, P., FRAIMAN, D. & CHIALVO, D. R. 2012. Criticality in large-scale brain fMRI dynamics unveiled by a novel point process analysis. *Frontiers in Physiology,* 3**,** 15.
TAKAHASHI, K., TANABE, K., OHNUKI, M., NARITA, M., ICHISAKA, T., TOMODA, K. & YAMANAKA, S. 2007. Induction of pluripotent stem cells from adult human fibroblasts by defined factors. *Cell,* 131**,** 861-72.
TAKAHASHI, K. & YAMANAKA, S. 2006. Induction of pluripotent stem cells from mouse embryonic and adult fibroblast cultures by defined factors. *Cell,* 126**,** 663-76.
TALELLI, P., EWAS, A., WADDINGHAM, W., ROTHWELL, J. C. & WARD, N. S. 2008. Neural correlates of age-related changes in cortical neurophysiology. *Neuroimage,* 40**,** 1772-81.
TANIK, S. A., SCHULTHEISS, C. E., VOLPICELLI-DALEY, L. A., BRUNDEN, K. R. & LEE, V. M. 2013. Lewy body-like alpha-synuclein aggregates resist degradation and impair macroautophagy. *J Biol Chem,* 288**,** 15194-210.
TAU, G. Z. & PETERSON, B. S. 2010. Normal development of brain circuits. *Neuropsychopharmacology,* 35**,** 147-68.
TEDESCHI, A. & BRADKE, F. 2017. Spatial and temporal arrangement of neuronal intrinsic and extrinsic mechanisms controlling axon regeneration. *Curr Opin Neurobiol,* 42**,** 118-127.
TELLER, P. 2001. Twilight of the perfect model model. *Erkenntnis,* 55**,** 393-415.
TESSIER-LAVIGNE, M. & GOODMAN, C. S. 1996. The molecular biology of axon guidance. *Science,* 274**,** 1123-33.
TETZLAFF, C., OKUJENI, S., EGERT, U., WORGOTTER, F. & BUTZ, M. 2010. Self-organized criticality in developing neuronal networks. *PLoS Comput Biol,* 6**,** e1001013.
THOMAS, C. A., JR., SPRINGER, P. A., LOEB, G. E., BERWALD-NETTER, Y. & OKUN, L. M. 1972. A miniature microelectrode array to monitor the bioelectric activity of cultured cells. *Exp Cell Res,* 74**,** 61-6.
THOMAS, M. J., WATABE, A. M., MOODY, T. D., MAKHINSON, M. & O'DELL, T. J. 1998. Postsynaptic complex spike bursting enables the induction of LTP by theta frequency synaptic stimulation. *J Neurosci,* 18**,** 7118-26.

TODDE, V., VEENHUIS, M. & VAN DER KLEI, I. J. 2009. Autophagy: principles and significance in health and disease. *Biochim Biophys Acta,* 1792**,** 3-13.
TOGNOLI, E. & KELSO, J. A. 2014. The metastable brain. *Neuron,* 81**,** 35-48.
TOMBA, C., BRAINI, C., WU, B., GOV, N. S. & VILLARD, C. 2014. Tuning the adhesive geometry of neurons: length and polarity control. *Soft Matter,* 10**,** 2381-7.
TONONI, G., EDELMAN, G. M. & SPORNS, O. 1998. Complexity and coherency: integrating information in the brain. *Trends Cogn Sci,* 2**,** 474-84.
TURNER, M. R. & SWASH, M. 2015. The expanding syndrome of amyotrophic lateral sclerosis: a clinical and molecular odyssey. *J Neurol Neurosurg Psychiatry,* 86**,** 667-73.
TURRIGIANO, G. 2012. Homeostatic synaptic plasticity: local and global mechanisms for stabilizing neuronal function. *Cold Spring Harb Perspect Biol,* 4**,** a005736.
TURRIGIANO, G. G. 2008. The self-tuning neuron: synaptic scaling of excitatory synapses. *Cell,* 135**,** 422-35.
TURRIGIANO, G. G., LESLIE, K. R., DESAI, N. S., RUTHERFORD, L. C. & NELSON, S. B. 1998. Activity-dependent scaling of quantal amplitude in neocortical neurons. *Nature,* 391**,** 892-6.
TURRIGIANO, G. G. & NELSON, S. B. 2004. Homeostatic plasticity in the developing nervous system. *Nat Rev Neurosci,* 5**,** 97-107.
ULLIAN, E. M., CHRISTOPHERSON, K. S. & BARRES, B. A. 2004. Role for glia in synaptogenesis. *Glia,* 47**,** 209-16.
VALKO, M., LEIBFRITZ, D., MONCOL, J., CRONIN, M. T., MAZUR, M. & TELSER, J. 2007. Free radicals and antioxidants in normal physiological functions and human disease. *Int J Biochem Cell Biol,* 39**,** 44-84.
VALVERDE, S., OHSE, S., TURALSKA, M., WEST, B. J. & GARCIA-OJALVO, J. 2015. Structural determinants of criticality in biological networks. *Front Physiol,* 6**,** 127.
VERMA, M., CALLIO, J., OTERO, P. A., SEKLER, I., WILLS, Z. P. & CHU, C. T. 2017. Mitochondrial Calcium Dysregulation Contributes to Dendrite Degeneration Mediated by PD/LBD-Associated LRRK2 Mutants. *J Neurosci,* 37**,** 11151-11165.
VERMA, M., VATS, A. & TANEJA, V. 2015. Toxic species in amyloid disorders: Oligomers or mature fibrils. *Ann Indian Acad Neurol,* 18**,** 138-45.
VERMA, M., WILLS, Z. & CHU, C. T. 2018. Excitatory Dendritic Mitochondrial Calcium Toxicity: Implications for Parkinson's and Other Neurodegenerative Diseases. *Front Neurosci,* 12**,** 523.
VERSTREKEN, P. (ed.) 2017. *Parkinson's Disease: Molecular Mechanisms Underlying Pathology* Academic Press.
VIENNET, T., WORDEHOFF, M. M., ULUCA, B., POOJARI, C., SHAYKHALISHAHI, H., WILLBOLD, D., STRODEL, B., HEISE, H., BUELL, A. K., HOYER, W. & ETZKORN, M. 2018. Structural insights from lipid-bilayer nanodiscs link alpha-Synuclein membrane-binding modes to amyloid fibril formation. *Commun Biol,* 1**,** 44.
VIERBUCHEN, T., OSTERMEIER, A., PANG, Z. P., KOKUBU, Y., SUDHOF, T. C. & WERNIG, M. 2010. Direct conversion of fibroblasts to functional neurons by defined factors. *Nature,* 463**,** 1035-41.
VOLPICELLI-DALEY, L. A., LUK, K. C. & LEE, V. M. 2014. Addition of exogenous alpha-synuclein preformed fibrils to primary neuronal cultures to seed recruitment of endogenous alpha-synuclein to Lewy body and Lewy neurite-like aggregates. *Nat Protoc,* 9**,** 2135-46.
VOLPICELLI-DALEY, L. A., LUK, K. C., PATEL, T. P., TANIK, S. A., RIDDLE, D. M., STIEBER, A., MEANEY, D. F., TROJANOWSKI, J. Q. & LEE, V. M. 2011. Exogenous alpha-synuclein fibrils induce Lewy body pathology leading to synaptic dysfunction and neuron death. *Neuron,* 72**,** 57-71.
VON BARTHELD, C. S., BAHNEY, J. & HERCULANO-HOUZEL, S. 2016. The search for true numbers of neurons and glial cells in the human brain: A review of 150 years of cell counting. *J Comp Neurol,* 524**,** 3865-3895.
WAKABAYASHI, K., TANJI, K., ODAGIRI, S., MIKI, Y., MORI, F. & TAKAHASHI, H. 2013. The Lewy body in Parkinson's disease and related neurodegenerative disorders. *Mol Neurobiol,* 47**,** 495-508.
WARD, N. S. & FRACKOWIAK, R. S. 2003. Age-related changes in the neural correlates of motor performance. *Brain,* 126**,** 873-88.

WATTS, D. J. & STROGATZ, S. H. 1998. Collective dynamics of 'small-world' networks. *Nature,* 393**,** 440-2.
WEBSTER, M. J., UNGERLEIDER, L. G. & BACHEVALIER, J. 1991. Connections of inferior temporal areas TE and TEO with medial temporal-lobe structures in infant and adult monkeys. *J Neurosci,* 11**,** 1095-116.
WEST, A. B., MOORE, D. J., BISKUP, S., BUGAYENKO, A., SMITH, W. W., ROSS, C. A., DAWSON, V. L. & DAWSON, T. M. 2005. Parkinson's disease-associated mutations in leucine-rich repeat kinase 2 augment kinase activity. *Proc Natl Acad Sci U S A,* 102**,** 16842-7.
WIDER, C., DICKSON, D. W. & WSZOLEK, Z. K. 2010. Leucine-rich repeat kinase 2 gene-associated disease: redefining genotype-phenotype correlation. *Neurodegener Dis,* 7**,** 175-9.
WIESEL, T. N. & HUBEL, D. H. 1963. EFFECTS OF VISUAL DEPRIVATION ON MORPHOLOGY AND PHYSIOLOGY OF CELLS IN THE CATS LATERAL GENICULATE BODY. *J Neurophysiol,* 26**,** 978-93.
WIESENDANGER, M. 2006. Constantin von Monakow (1853-1930): a pioneer in interdisciplinary brain research and a humanist. *C R Biol,* 329**,** 406-18.
WINNER, B., MELROSE, H. L., ZHAO, C., HINKLE, K. M., YUE, M., KENT, C., BRAITHWAITE, A. T., OGHOLIKHAN, S., AIGNER, R., WINKLER, J., FARRER, M. J. & GAGE, F. H. 2011. Adult neurogenesis and neurite outgrowth are impaired in LRRK2 G2019S mice. *Neurobiol Dis,* 41**,** 706-16.
WINSLOW, A. R., CHEN, C. W., CORROCHANO, S., ACEVEDO-AROZENA, A., GORDON, D. E., PEDEN, A. A., LICHTENBERG, M., MENZIES, F. M., RAVIKUMAR, B., IMARISIO, S., BROWN, S., O'KANE, C. J. & RUBINSZTEIN, D. C. 2010. alpha-Synuclein impairs macroautophagy: implications for Parkinson's disease. *J Cell Biol,* 190**,** 1023-37.
WONG, Y. C. & KRAINC, D. 2017. alpha-synuclein toxicity in neurodegeneration: mechanism and therapeutic strategies. *Nat Med,* 23**,** 1-13.
YADA, Y., MITA, T., SANADA, A., YANO, R., KANZAKI, R., BAKKUM, D. J., HIERLEMANN, A. & TAKAHASHI, H. 2017. Development of neural population activity toward self-organized criticality. *Neuroscience,* 343**,** 55-65.
YANG, H., SHEW, W. L., ROY, R. & PLENZ, D. J. J. O. N. 2012. Maximal variability of phase synchrony in cortical networks with neuronal avalanches. 32**,** 1061-1072.
YOO, A. S., SUN, A. X., LI, L., SHCHEGLOVITOV, A., PORTMANN, T., LI, Y., LEE-MESSER, C., DOLMETSCH, R. E., TSIEN, R. W. & CRABTREE, G. R. 2011. MicroRNA-mediated conversion of human fibroblasts to neurons. *Nature,* 476**,** 228-31.
YOUNG, M. P., HILGETAG, C. C. & SCANNELL, J. W. 2000. On imputing function to structure from the behavioural effects of brain lesions. *Philos Trans R Soc Lond B Biol Sci,* 355**,** 147-61.
YU, J., VODYANIK, M. A., SMUGA-OTTO, K., ANTOSIEWICZ-BOURGET, J., FRANE, J. L., TIAN, S., NIE, J., JONSDOTTIR, G. A., RUOTTI, V., STEWART, R., SLUKVIN, II & THOMSON, J. A. 2007. Induced pluripotent stem cell lines derived from human somatic cells. *Science,* 318**,** 1917-20.
YUE, M., HINKLE, K. M., DAVIES, P., TRUSHINA, E., FIESEL, F. C., CHRISTENSON, T. A., SCHROEDER, A. S., ZHANG, L., BOWLES, E., BEHROUZ, B., LINCOLN, S. J., BEEVERS, J. E., MILNERWOOD, A. J., KURTI, A., MCLEAN, P. J., FRYER, J. D., SPRINGER, W., DICKSON, D. W., FARRER, M. J. & MELROSE, H. L. 2015. Progressive dopaminergic alterations and mitochondrial abnormalities in LRRK2 G2019S knock-in mice. *Neurobiol Dis,* 78**,** 172-95.
ZATORRE, R. J., FIELDS, R. D. & JOHANSEN-BERG, H. 2012. Plasticity in gray and white: neuroimaging changes in brain structure during learning. *Nat Neurosci,* 15**,** 528-36.
ZEKI, S. & SHIPP, S. 1988. The functional logic of cortical connections. *Nature,* 335**,** 311-7.
ZHAO, C., DENG, W. & GAGE, F. H. 2008. Mechanisms and functional implications of adult neurogenesis. *Cell,* 132**,** 645-60.
ZHAO, H., TUOMINEN, E. K. & KINNUNEN, P. K. 2004. Formation of amyloid fibers triggered by phosphatidylserine-containing membranes. *Biochemistry,* 43**,** 10302-7.
ZHOU, J., GENNATAS, E. D., KRAMER, J. H., MILLER, B. L. & SEELEY, W. W. 2012. Predicting regional neurodegeneration from the healthy brain functional connectome. *Neuron,* 73**,** 1216-27.

ZHU, M. & FINK, A. L. 2003. Lipid binding inhibits alpha-synuclein fibril formation. *J Biol Chem,* 278**,** 16873-7.

ZHU, M., LI, J. & FINK, A. L. 2003. The association of alpha-synuclein with membranes affects bilayer structure, stability, and fibril formation. *J Biol Chem,* 278**,** 40186-97.

ZIMPRICH, A., BISKUP, S., LEITNER, P., LICHTNER, P., FARRER, M., LINCOLN, S., KACHERGUS, J., HULIHAN, M., UITTI, R. J., CALNE, D. B., STOESSL, A. J., PFEIFFER, R. F., PATENGE, N., CARBAJAL, I. C., VIEREGGE, P., ASMUS, F., MULLER-MYHSOK, B., DICKSON, D. W., MEITINGER, T., STROM, T. M., WSZOLEK, Z. K. & GASSER, T. 2004. Mutations in LRRK2 cause autosomal-dominant parkinsonism with pleomorphic pathology. *Neuron,* 44**,** 601-7.

8. Contributions (Papers)

PAPER 1

Criticality as a measure of developing proteinopathy in biological human neural networks

Authors: Vibeke D. Valderhaug[1], Kristine Heiney[2], Ola Huse Ramstad[1], Geir Bråthen[1], Wei-Li Kuan[3], Stefano Nichele[2], Axel Sandvig[1,4,5], and Ioanna Sandvig[1*]

[1]Department of Neuromedicine and Movement Science, Faculty of Medicine, Norwegian University of Science and Technology (NTNU), Trondheim, Norway
[2]Department of Computer Science, Faculty of Technology, Art and Design; Oslo Metropolitan University (OsloMet), Oslo, Norway
[3]John van Geest Centre for Brain Repair, Department of Clinical Neurosciences, University of Cambridge, UK
[4]Department of Neurology and Clinical Neurophysiology, St Olav´s Hospital, Trondheim, Norway
[5]Department of Pharmacology and Clinical Neuroscience, Division of Neuro, Head and Neck, Umeå University Hospital, Umeå, Sweden

***Corresponding author**
Ioanna Sandvig PhD
Department of Neuromedicine and Movement Science, NTNU
3rd Floor, Nevro East
Edvard Grieg´s gate 8
7030 Trondheim, Norway
Email: ioanna.sandvig@ntnu.no
Tel: +47 72575620

Keywords: SoC, function, electrophysiology, plasticity, alpha-synuclein, pre-formed fibrils, PFF

Word count: 5788
Figures: 7 in main text, 7 in the supplementary file

Submitted to Frontiers in Neural Circuits (19.11.2019)

Abstract

A patterned spread of proteinopathy represents a common characteristic of many neurodegenerative diseases. In Parkinson's disease (PD), misfolded forms of alpha-synuclein proteins aggregate and accumulate in hallmark pathological inclusions termed Lewy bodies and Lewy neurites, which seems to affect selectively vulnerable neuronal populations and propagate within interconnected neuronal networks. Research findings suggest that these proteinopathic inclusions are present at very early timepoints in disease development, even before strong behavioural symptoms of dysfunction arise, but that these underlying pathologies might be masked by homeostatic processes working to maintain the function of the degenerating neural circuits. This study investigates whether inducing the PD-related alpha-synuclein pathology in biological human neural networks can be associated with changes in network function, and particularly with alterations in network criticality states. Self-organised criticality represents the critical point between resilience against perturbation and adaptational flexibility, which appears as a functional trait in self-organising neural networks, both in vitro and in vivo. By monitoring the developing neural network activity through the use of multielectrode arrays (MEAs) for a period of three weeks following proteinopathy induction, we show that this developing pathology is not clearly manifest in standard measurements of network function, but rather expressed in network criticality states.

Introduction

Neurodegenerative diseases, such as Parkinson's disease (PD), Alzheimer's disease (AD) and amyotrophic lateral sclerosis (ALS), represent a common cause of morbidity and cognitive impairments in older adults. Although characterised through complex pathologies and unknown aetiologies, some prominent commonalities, such as the presence of proteinopathy and the patterned spread of pathology through selectively vulnerable neuronal populations, cannot be ignored (1-9). Focusing on the second most common neurodegenerative disease, PD, the implicated proteinopathy mainly consists of misfolded and aggregated forms of alpha-synuclein. These intracellular alpha-synuclein inclusions are termed Lewy bodies or Lewy neurites, and can be found propagating throughout central, peripheral and autonomic parts of the nervous system, as well as in multiple organs, as the disease progresses (6, 7, 10-14). Furthermore, the neurodegenerative process characteristic of PD particularly affects and progressively depletes the dopaminergic neurons in the substantia nigra pars compacta (SNpc), a process which is thought to underlie most of the movement-related symptoms.

The neurodegenerative process underlying PD inevitably affects both the structural and functional connectivity of local and distal circuitry in the brain. As already noted, the movement-related impairments in PD are largely ascribed to the characteristic loss of dopaminergic neurons in the SNpc, and the degeneration of the nigrostriatal (dorsal striatal) pathway. However, the disease is much more systemic, affecting both the mesolimbic dopaminergic (ventral striatal) pathway and the mesocortical pathway, as well as several other neuronal populations throughout the brain as it progresses (15). As clusters of neurons and their interconnections degenerate, homeostatic plasticity mechanisms likely compensate to maintain stable function through regulation and rearrangement of synapses and synaptic elements in local and distal neural networks (16-19). The network disturbances likely imposed by the degeneration of neurons and their interconnections are thus counterbalanced, keeping clear symptoms of dysfunction from arising at early stages of disease development and thus patients from being diagnosed before advanced neurodegeneration is already present (20).

Interestingly, the high interconnectivity of the brain has been shown to inherently shape how it responds to perturbation, and the particular sites affected, as well as their level of connectedness to other brain regions, to determine how pathology can spread (21-24). This relates directly to the hallmark pathology of PD, namely the widespread alpha-synuclein inclusions, which have been suggested to propagate between anatomically highly interconnected areas in an "evolving topographical progression" (6, 7, 25). Based on this, neuroscientific research has narrowed in on two likely pathological mechanisms that could underlie the propagating pattern of neurodegeneration seen in PD (as well as in AD and ALS), namely selective neuronal vulnerability and pathological proteinopathic seeds (2, 3, 6, 23, 26-28). At this point, research efforts have uncovered several mechanisms of neuron-to-neuron transfer of pathological seeds of alpha-synuclein pre-formed fibrils (PFFs) (29-33), both in vitro and in vivo (11, 13), highlighting its contribution as a source of pathological propagation, however, the functional consequences of this interneuronal spread remain to be elucidated.

How can the functional consequences of such pathological mechanisms be studied? As mentioned, fundamental homeostatic plasticity mechanisms, which serve to maintain stable function in neural circuits in the face of perturbation, likely help mask the ongoing pathological processes underlying the progressive neurodegenerative pattern of PD (16, 17). However, although early network disturbances caused by the presence of pathological aggregates and the degeneration of neurons and their interconnections might be concealed in terms of behavioural

symptoms, they may be detectable as fluctuations or deviations in some measures of the network function and activity state. As such, the universal attribute of neural network development towards the state of self-organized criticality (SoC) seems a logical point of focus and of particular interest. SoC represents the critical point between resilience against perturbation and adaptational flexibility, which appears without the need for fine-tuning of parameters through basic self-organizing processes in neural networks, both in vivo and in vitro. This dynamic state is characterized by cascades of spontaneous activity with power-law size distributions, activity which is electrophysiologically measurable and termed "neuronal avalanches" (34-46). As damage spreads within a neural network, it is highly conceivable that the system approaches a "damage threshold", where restoring network function becomes increasingly difficult, and which represents a deviation from the criticality state (43, 47). Since SoC also appears in neural networks in vitro (48), functional network alterations resulting from induced pathology such as proteinopathy can be studied within this paradigm.

To investigate whether a developing PD-related proteinopathy can be associated with alterations in network criticality states, we have induced proteinopathy in engineered human neural networks in vitro and applied computational analysis to identify criticality in electrophysiological microelectrode array (MEA) recordings of the resulting network activity. Specifically, we measured the developing network activity prior to and for three weeks following exogenous addition of alpha-synuclein PFF seeds, and aimed to investigate how this induced PD-related pathology is reflected in several measures of network function and in the network criticality states compared to control neural networks. Our results suggest that induction of proteinopathy alters the developmental trajectory of the neural networks in relation to SoC. To the best of our knowledge, this is the first study to investigate SoC in biological, human induced pluripotent stem cell (iPSC)-derived neural networks.

Materials and methods

Reprogramming of human iPSCs to neural progenitor cells

Human induced pluripotent stem cells (iPSCs) (ChiPSC18, Takara Bioscience) were reprogrammed using a protocol for midbrain dopaminergic neurons adapted from Kirkeby et. al 2012 (49) and 2016 (50) and Doi et al. 2014 (51) (**Fig.1, Supplem.1**). Briefly, the human iPSC were seeded on human recombinant laminin 111 (LN111, BioLamina) at a density of 10.000 cells/cm^2, where they were exposed to dual-SMAD inhibition (LDN1931892 and SB43152), followed by Wnt signalling activation through the GSKβ inhibitor CHIR99021, and sonic hedgehog introduction (Shh C25ll) (day 0-9). On day 11 the cells were dissociated using accutase and reseeded on LN111 at a density of 50.000cells/cm^2. FGF8b was added from day 9-16, at which point the reprogramming was concluded and the human iPSC-derived neurons were left for maturation.

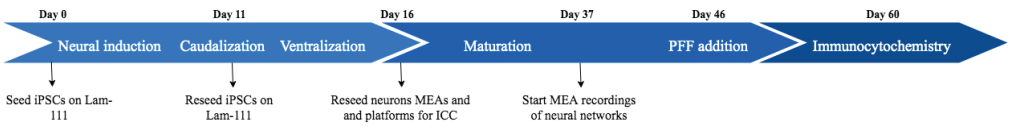

Fig.1 Experiment layout. The timeline shows the chemotemporal reprograming protocol for the human iPSC-derived neurons, followed by the establishment and maturation of the neural networks on multielectrode arrays (MEAs). Following 30 days of maturation, sonicated pre-formed alpha-synuclein fibrils were added to the engineered neural networks.

Formation of alpha-synuclein pre-formed fibrils (PFFs)
Alpha-synuclein PFFs were formed following a modification of the procedure described in the Volpicelli-Daley et al. protocol (31). Briefly, 1mg alpha-synuclein monomers (S-1001-1, rPeptide) was resuspended in 1mL MilliQ water, giving 1mg/mL in 20mM Tris-HCL, pH7.4, 100mM NaCl. The suspension was then centrifuged at 3600xg for 60 minutes in an Amicon Ultra 3K membrane device, which was then inverted and spun down in a tube for 1000xg for 2 minutes to transfer the concentrated sample. The concentrated solute was then resuspended to a final volume of 500ul (5mg/mL) in 10mM Tris-HCL (1.576g/L), pH 7.6, 50mM NaCl (2.922g/L), and shaken for 7 days at 1000r.p.m. in a 37°C theromixer. The PFFs were subsequently aliquoted into 5ul tubes and stored in -80°C until used for in vitro assays.

UV-visible spectroscopy of alpha-synuclein PFFs
Absorbance of alpha-synuclein PFFs in phosphate buffered saline (PBS) was measured on a NanoDrop One/One^{C} UV-visible absorbance spectrophotometer in the range 200-300nm. A dilution of 0.1μg/μL was prepared from a PFF stock solution of 5μg/μL, and added as a droplet (2μL) to the pedestal after different timepoints of ultrasonication (Branson CPXH Series Ultrasonic bath, 2.8L) (37, 40, 21˚C). Data was collected with OneViewer Software.

Atomic Force Microscopy (AFM)
AFM was performed with ScanAsyst Air tapping mode using an AFM Veeco, Multimode V. Samples were applied on mica and spread out to dry. Results were analysed with NanoScope Analysis 1.5 software.

Microelectrode array (MEA) based electrophysiology
The spontaneous electrophysiological activity of the neural networks was recorded using an MEA2100 *in vitro* system together with the MEA suite software (Multi Channel System). The engineered neural networks were maintained on 60-electrode planar microelectrode arrays (MEAs) (60MEA200/30iR-Ti; Multi Channel Systems) with ring covers. Prior to seeding, the MEAs were briefly washed with 65% ethanol, incubated in sterile water and UV-treated. Subsequently, they were treated with foetal bovine serum for 30-60 minutes to make the surface hydrophilic, before being coated with 0.01% poly-L-ornithine (PLO) solution and L15/laminin. Each MEA (n=8) was seeded with 100,000 iPSC-derived neurons and kept in a standard humidified air incubator (5% CO^2, 20%O^2, 37°C). 50% of the media was changed every 3-4 days. Following 34 days of maturation, the PFFs were added to the neural networks. A 5μg/μL aliquot was thawed in room temperature and diluted in 245ul sterile PBS (0.1μg/μL). A water bath ultrasonicator (Branson CPXH Series Ultrasonic bath, 2.8L) was used to sonicate the PFFs for 1 hour (37, 40, 21˚C), before 10uL of the PFF seeds (0.1ug/uL), or equivalent amounts of alpha-synuclein monomers or PBS, were added directly to the culture media. The MEA cultures were randomly assigned to the different test conditions: PFF group (n=4), PBS (n=2) and alpha-synuclein monomers (n=2). Network activity was sampled throughout the experimental period (7-minute recordings), where 5 baseline recordings, and 13 recordings after intervention was performed per MEA. To avoid inadvertent fluctuations in electrophysiological activity directly related to media changes, no recordings were performed in the first 48 hours following a media change.

MEA data analysis
All data analysis, including the criticality analysis described in the following section, was carried out in MATLAB R2018b (The MathWorks, Inc.). The raw data from the MEA system was first bandpass filtered with a second-order Butterworth filter with a passband of 300 Hz to 3 kHz, and spike detection was performed on the filtered data using a threshold of 5 standard

deviations below the median of the signal. After visual inspection of the filtered waveform-signal from each electrode, clear artefactual signals (outlier electrodes) were identified and removed from further analysis. A total of 11 such instances were identified, 9 of which were caused by the same electrode across multiple MEAs.

Four basic parameters were evaluated in an attempt to identify different functional behaviours in the different types of networks: the mean firing rate (MFR), inter-spike interval (ISI), population inter-spike interval (PISI), and cross-correlation (XC). All of the parameters were obtained from spike trains generated for each recording channel, where a spike train is given as a series of impulses with each impulse occurring at the time at which the peak voltage was recorded for each detected spike. The MFR for each recording channel was calculated as the total number of spikes detected on that channel divided by the total recording time. The MFR for a given network at a given time point was then taken as the average over all recording channels. The ISI for each recording channel was calculated as the average time interval between consecutive spikes detected on the same channel, and this was then also averaged over all channels for a given network at a given time point, excluding any intervals greater than 100 ms. The PISI was calculated by obtaining a population vector of the unique spike timings on all recording channels and averaging the intervals between them, excluding any intervals greater than 100 ms. The XC was obtained by computing the autocorrelation-normalized magnitude of the cross-correlation of pairs of spike histograms for each pair of recording channels and averaging over all possible pairs. Spike histograms were obtained by temporally binning the spike trains with a bin size of 10 ms. The maximum lag considered in the XC calculation was 50 ms.

Computational analysis of criticality

A flowchart showing the main steps of the criticality analysis can be found in **Fig. 2**. Preliminary analysis using the same method has been previously reported for one of the control networks from this dataset (52). Filtering and spike detection were first performed as described in the previous section (step 1, **Fig. 2**).

Avalanche detection was then performed using the following procedure, based on the method originally described by Beggs and Plenz (35) (step 2, **Fig. 2**). The spike data were binned with a bin width of 1 ms, and avalanches were detected as any number of consecutive active time bins (bins containing one or more spikes) bounded before and after by empty time bins (bins containing no spikes). Typically, the average PISI is used to define the bin size; however, this fixed smaller bin size yields a larger number of avalanches, which provides a better basis for the fitting. Additionally, as the current analysis is not concerned with the actual value of the slope but instead only with whether a network can be classified as critical, the selection of the bin width may be set arbitrarily (35, 48). The avalanche size was computed as the number of active recording channels in the avalanche. (See the schematic in step 2 of Fig. 2 for an example.) The size probability distribution was then obtained by creating a histogram of the number of avalanches of each possible size (1 to 60 electrodes) and normalizing it with respect to the total number of avalanches.

As described by Beggs and Plenz (35), a hallmark of criticality is the avalanche size distribution following a power law. Thus, to determine whether or not the networks were in the critical state at a given time point, power law fitting was performed on the avalanche size distributions using the method described by (53). The fitted power law takes the form

$$P(x) \propto x^{-\alpha},$$

where x is the avalanche size, $P(x)$ is the probability of an avalanche having size x, and α is the exponent of the power law. The fitting was performed for avalanche sizes ranging from 2 to 59 electrodes, following previous studies (e.g., (48)). Beggs and Plenz (35) originally reported α as taking a value of 1.5 in slice cultures, and this has been supported by other studies on dissociated cultures (e.g., (48)). When the fitted power law is plotted in log–log space, it appears as a line with a slope of $-\alpha$. The goodness of fit was determined by generating N = 1,000 synthetic datasets from the fitted power law and computing the Kolmogorov–Smirnov (KS) distances for the empirical distribution and each of the synthetic distributions, where a greater KS distance indicates a poorer fit. The fraction p of synthetic distributions that had a KS distance greater than that of the empirical distribution (i.e., the fraction of cases where the empirical data were better described by the power law fit than were the synthetic data) was then calculated, and the fitting was rejected if $p < 0.1$. Thus, in the case where the fitting satisfied $p \geq 0.1$, the network was presumed to be in a critical state.

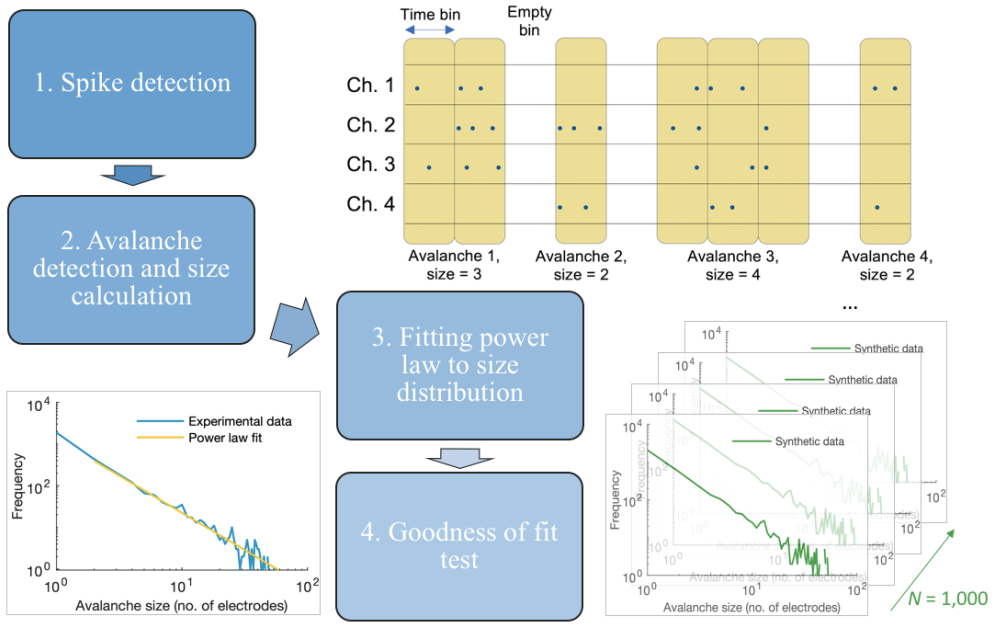

Fig.2 Step-by-step Criticality assessment

Immunocytochemistry

The engineered neural networks were fixed at room temperature with either 4% paraformaldehyde for 15 minutes, or 4% paraformaldehyde/4% sucrose/1% TritonX-100 (Sigma-Aldrich), as described in (31, 54) for protein extraction, at ranges between 10-20 minutes, followed by 3x15min washings with DPBS. TritonX-100 extraction should leave only insoluble inclusions, not showing any of the remaining presynaptic alpha-synuclein that has not converted to aggregates (15,20). Blocking was performed with a solution of 5% normal goat serum and 0.6% TritonX-100 in DPBS for 1 hour on a rotator at room temperature. Primary antibodies were subsequently applied overnight at 4°C, on a rotator, in a solution containing 2.5% normal goat serum and 0.3% TritonX-100. The following primary antibodies were used: rabbit polyclonal anti-alpha synuclein antibody 1:200 (ab131508, Abcam), mouse monoclonal anti-tyrosine hydroxylase antibody 1:300 (MA1-24654, Invitrogen), rabbit monoclonal anti-alpha synuclein (phospho S129) antibody 1:750 (ab51253, Abcam), chicken polyclonal anti-neurofilament heavy polypeptide 1:150 (ab46800, Abcam), and mouse monoclonal anti-beta-3

tubulin antibody 1:800 (ab119100, Abscam). The samples were then washed 3x15 min in DPBS at room temperature before being incubated in secondary solution containing 2.5% normal goat serum, 0.3% TritonX-100 and fluorophore-conjugated secondary antibodies 1:1000 (AlexaFluor 488, 568, 647, Life Technologies) for 3 hours. During the final 5 minutes of incubation, Hoechst was added at a final concentration of 1:10000. The samples were then washed 3x15 min in DPBS on a rotator. Some samples were also incubated with Phalloidin-iFluor 647 reagent – cytopainter 1:100 (ab176759, Abcam) for 20 minutes, before being washed 3x15min in DPBS again. Subsequently the samples were briefly washed in MilliQ-water, and mounted on Menzel glass-slides (Thermo Scientific) using FluorSave reagent (EMD Millipore USA).

Transmission Electron Microscopy (TEM)

The neuronal cultures from two MEAs (one from the PFF group, one from the monomer control group) were detached from the surface of the MEAs by light suction using a 1000ul pipette and washed in DPBS, and immersed directly in 2.5% glutataldehyde without dissociation. The samples were subsequently stored at 4°C until further processing. In preparation for TEM, samples were gelatine embedded, dehydrated, infiltrated and blocked. A detailed description of the process can be found in the supplementary section.

Following processing for TEM, the embedded samples were sectioned (Ultramicrotome, Leica EM UC7) into 45-55nm thin sections, placed on grids, viewed with a Transmission Electron Microscope FEI Tecnai 12, and imaged with a Morada digital camera. Image processing was done using iTEM and Fiji.

Results

Formation and characterization of engineered neural networks on MEAs

After concluding the reprogramming protocol for human iPSC-derived neurons, the cells were seeded on MEAs and ibidi chips, where they spontaneously formed interconnections and extensive neural networks throughout the maturation period (**Fig.3**). Immunocytochemistry revealed neurons positive for beta-III tubulin, neurofilament heavy, and tyrosine hydroxylase in the engineered neural networks after 30 days of maturation. Importantly, the neural networks also expressed endogenous alpha-synuclein, which is a prerequisite for the induction of alpha-synuclein aggregation and pathology (**Supplementary Fig.S1**) (31).

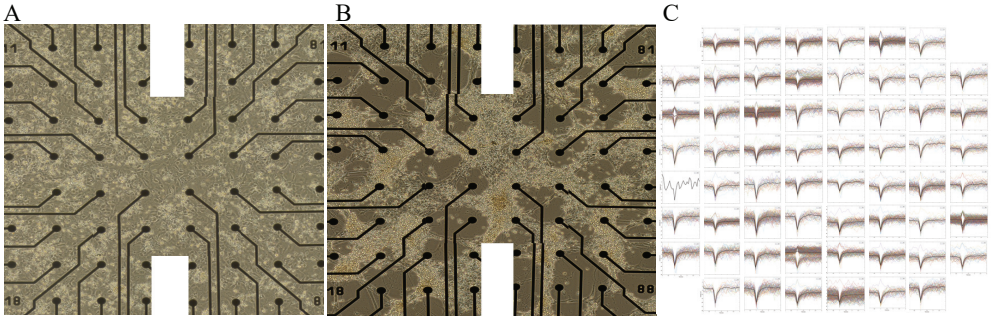

Fig.3 Formation and maturation of human neural networks on MEAs. **A**) shows a tiled microscopy image overviewing the electrode area of a newly seeded MEA (day 2 post seeding). **B**) shows how an extensive interconnected neural network has developed on the MEA surface 20 days post seeding. **C**) shows the spike shape cut-outs (relative axis) recorded from each of the electrodes during a single recording session, demonstrating the electrophysiological activity obtained from a neural network as shown in **B**).

Inducing alpha-synuclein pathology in neural networks

UV-visible absorbance spectra and AFM verified the breaking up of alpha-synuclein PFFs into smaller seeds by water bath ultrasonication, as a clear difference in both absorbance and structure of the PFFs was visible before and after sonication (**Supplementary Fig.S2**). Two weeks after the addition of sonicated PFF seeds, neural networks on ibidi chips were fixed and stained with the antibody for alpha-synuclein phosphorylated at S129 (ab51253) to visualize intracellular alpha-synuclein aggregates by immunofluorescence (**Supplementary Fig.S3**). Although consistent positive intracellular labelling by the S129 antibody was observed in the PFF treated neural networks, both perinuclearly and at distal neuronal sites, background staining and unspecific labelling was also consistently observed in the control conditions, even following TritonX-100 protein extraction, rendering the immunocytochemistry inconclusive.

Verification of induced pathology in super resolution

Ultrastructural analysis of the neural networks collected from the MEAs showed evidence of perinuclear fibrillization in the samples from the PFF condition **(Fig.4)**, but not in the samples from the monomer control condition. Signs of neuritic atrophy, as well as several fibrillous structures were observed in the cytosol and within neurites of samples taken from the PFF condition. Furthermore, an abundance of membrane-enveloped “inclusion bodies” in line with recent publications (55), were observed in the PFF condition, but not in samples from the monomer control condition **(Supplementary S4).**

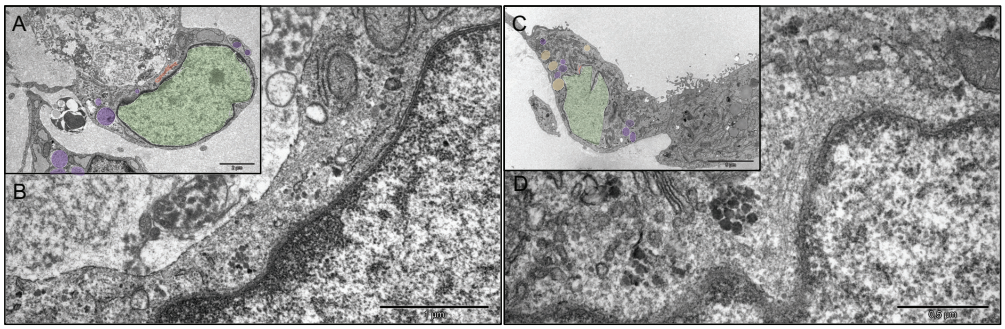

Fig. 4 Perinuclear fibrillization. Ultrastructural image of perinuclear fibrillization in neural network samples from the PFF condition (not observed in monomer control condition). (**A, C**) overview of single cell together with highlighted intracellular features of interest, (**B, D**) ultrastructure of perinuclear fibril. Nucleus (green), perinuclear fibrils (red), autophagosomal/lysosomal activation (purple), lipid body (yellow).

Furthermore, the ultrastructural analysis revealed a significant difference in observed necrotic and apoptotic elements in the extracellular environment surrounding neurons in the samples taken from the PFF treated condition and in the samples taken from the monomer control condition (t_{14}=2,481, p<.05). In addition, the intracellular environment of single neurons revealed prominent autophagosomal and lysosomal vacuolization in samples from both the PFF treated condition and from the monomer control condition (with no significant differences between the conditions ($t_{15.549}$=-.111, p>.05). (**Supplementary Fig.S5**). Representative overview images of samples used for ultrastructural analysis of extracellular necrotic/apoptotic elements, as well as intracellular autophagosomal and lysosomal vacuolization, can be found in the supplementary **(Fig.S6,S7).**

MEA recordings and analysis

After 3 weeks of maturation on the MEAs, the baseline activity of the engineered neural networks (n=8) was recorded for 5 sessions until the point of PFF/monomer/PBS addition. After this point, 13 recordings (spanning across a total of 3 weeks) were made from the neural networks on each MEA (**Fig.5**).

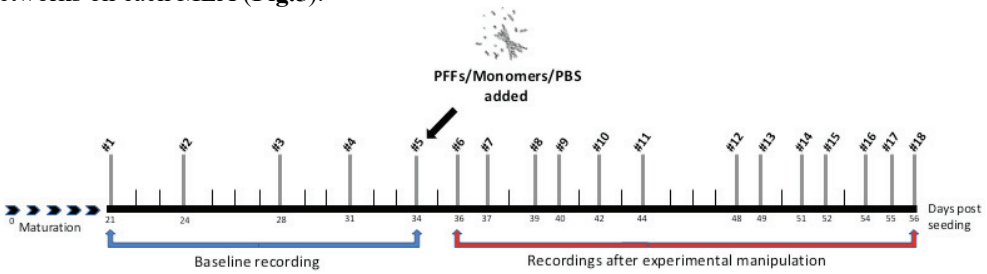

Fig.5 Timeline depicting the recordings from the engineered neural networks on the microelectrode arrays. # numbers indicate each recording time point, with the axis displaying the corresponding culture age (days post seeding). The arrow indicates the point of experimental intervention, where either PFFs, monomers or PBS were added to the neural networks after the 5th baseline recording.

Four basic parameters were evaluated to observe how the networks matured: the MFR, ISI, PISI, and XC. The MFR describes the overall amount of activity in the network, and the ISI gives an indication of burstiness or the degree to which spikes from the same neuron occur in close temporal proximity. The PISI reflects network-wide spiking intervals and thus is expected

to give an indication of connectivity or synchrony. Similarly, the XC describes the similarity between the spike trains from two recording channels and thus also gives an indication of connectivity or synchrony within the network.

Fig. 6A shows the mean baseline values of these parameters obtained for each group, and **Fig. 6B-E** shows plots of the time evolution of the parameters as percentages of the baseline values. The error bars represent the standard deviations among each group. One outlier recording from a neural network in the PFF group (MEA 16, time point 15) was eliminated because it had a high level of noise and appeared to yield many false positives in the spike detection, producing a spurious peak in the MFR and XC values. As shown in the results in **Fig. 6**, no significant difference was observed among the evolution of these parameters, and thus no strong conclusions could be drawn about the difference in behaviour among the three groups.

A

Baseline values	**PBS**		**PFF**		**Monomers**	
	Average	std	Average	std	Average	std
MFR [spike/s]	0.29	0.10	0.36	0.16	0.60	0.26
ISI [ms]	51.25	4.51	50.49	6.84	54.52	7.55
PISI [ms]	36.34	2.51	32.72	2.60	28.98	3.58
XC	0.17	0.03	0.17	0.02	0.17	0.02

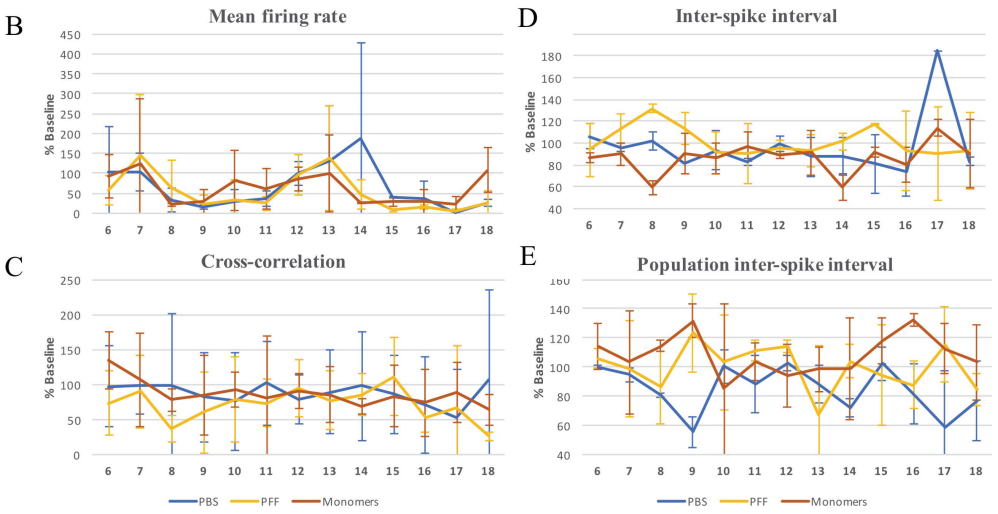

Fig.6 Descriptive electrophysiological values obtained throughout the recording period for all neural networks A) table showing the average measures of the mean firing rate (MFR), inter-spike interval (ISI), population inter-spike interval (PISI), and cross-correlation (XC) measured across the 5 baseline time points for each group (PBS, PFF, and Monomer conditions), with standard deviations (std). **B-E**) shows a graphical representation of the MFR, XC, ISI, and PISI development, respectively, of all groups after the baseline period, with error bars representing the standard deviation across the networks in each group. Each value is given as a percentage of the baseline measures listed in table **A**).

Assessment of Criticality

Criticality assessment of the 8 neural networks (2 monomer controls, 2 PBS controls, 4 PFF condition) revealed two clear outliers which were subsequently excluded, both of which were from the monomer control condition. One of these networks consistently displayed non-critical activity (during all 18 recording time points, both at baseline and following monomer addition), while the other network either displayed too few neuronal avalanches for criticality assessment or non-critical activity.

Recording time points where more than half of the neural networks did not exhibit enough neuronal avalanche activity for computational analysis of criticality have been omitted from the graphical representation in **Fig.7** (recording numbers 3, 8-11, 16- 18). The absence of robust neuronal avalanche activity at recording number 8-11 is perhaps particularly noteworthy, as this equals day 5-10 after perturbation. Nevertheless, the criticality assessment at 4 baseline time points, as well as 6 time points following PFF addition are presented for 2 MEAs in the PBS condition (control), and 4 in the PFF condition (**Fig.7**). Analysis of criticality revealed fluctuating neural network states in both the PFF and PBS conditions. As can be seen from **Fig.7**, all neural networks (with the exception of network number 2 and 3 in the PFF condition) show probability size distributions of neuronal avalanche activity consistent with both critical and non-critical states during baseline measures, that is, before any perturbation. Furthermore, although some data points are missing (due to too few avalanches during the recording), most measurements during the baseline period are consistent with non-critical states (10/17 data points). After addition of alpha-synuclein PFF seeds to the neural networks in the PFF condition (represented by a black separation line in **Fig.7**), the majority of these perturbed neural networks (with the exception of PFF 4) mainly display critical activity states (11/17 data points). Contrary to this, the two neural networks in the PBS condition collectively display mostly non-critical activity during these time points (6/9 data points).

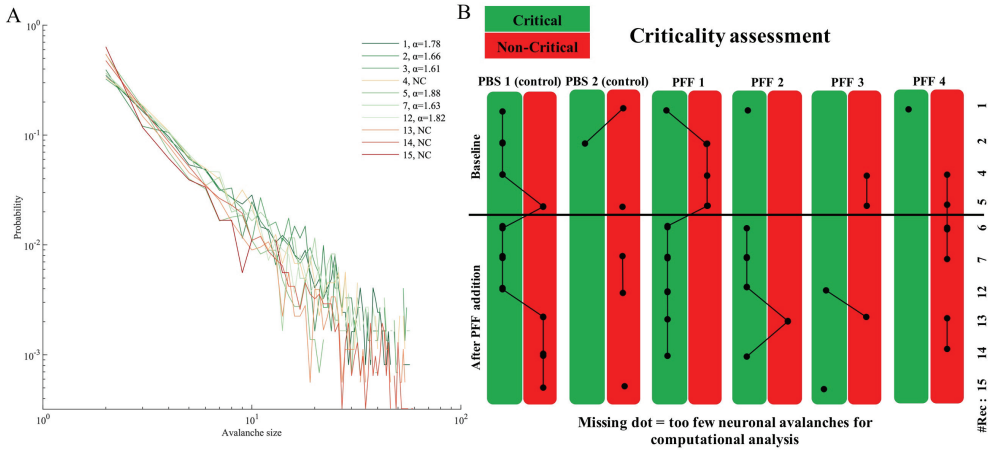

Fig.7 Criticality analysis. A) Shows the probablility distribution of the avalanche size for the 10 recording timepoints included (4 baseline, 6 after PBS addition) from the PBS 1 (control) neural network, with the power law exponent α values indicated for each time point where the power law fitting results indicated criticality. **B)** shows the cumulative criticality assessment for each of the 6 neural networks (2 from the PBS condition, 4 from the PFF condition) during the 10 recording time points included in the assessment. The point of perturbation (addition of PFF seeds, or PBS in the control condition) is indicated by the horizontal separation line. The green columns indicate neural network activity with avalanche size distributions following a power law distribution, consistent with a critical state ($p \geq 0.1$), while red columns indicate a poor power law fit consistent with non-critical activity ($p < 0.1$). During the baseline time points, all neural networks (with the exception of PFF 2 and 3) fluctuated between citical and non-critical activity. Furthermore, collectively, most of the data points at baseline are consistent with non-critical states (10/17 data points). After the point of perturbation, the control neural networks (PBS 1 and 2) collectively display mainly non-critical activity states (6/9 data points), while the PFF neural networks mainly display critical activity states (with the exception of PFF 4) (11/17 data points).

Discussion

Self-organized criticality

To investigate whether development of PD-related proteinopathy can be associated with alterations in network states of criticality, we induced alpha-synuclein proteinopathy in engineered human neural networks in vitro, and applied computational analysis to identify SoC in electrophysiological MEA recordings from the resulting network activity. As hypothesized, a difference between the PFF condition and the PBS control condition was observed in criticality states following perturbation (**Fig.7**). However, contrary to what was expected, the analysis showed that the PFF perturbed neural networks largely ended up within the critical regime (10/17 data points), consistent with SoC, while the PBS controls ended up in a largely non-critical regime (6/9 data points). SoC has been proposed as a mechanism that guides the spontaneous activity of developing neural networks into transient and homeostatically regulated patterns, or "meta-stable dynamics" (56, 57). These meta-stable dynamics are in turn part of the regular developmental trajectory of neural networks in vitro, and have been found to occur only in neural networks where the activity propagates within the critical mode (57). The surprising result is thus the direction of the alteration in criticality, where the networks with PFF induced pathology displayed neuronal avalanche activity largely consistent with SoC, while the control neural networks largely displayed non-critical activity. Nevertheless, this trend in alteration points towards a difference in developmental trajectory between the neural networks with PFF-induced pathology and the PBS control neural networks, highlight the potential relevance of SoC in unveiling functional alterations resulting from such an evolving pathology within the networks.

Evaluation of SoC through neuronal avalanche size distributions has been shown to provide a good representation of "damage spread" in perturbation experiments where identical replicas of the same system have different conditions and are investigated over time, even if the actual underlying dynamics are much more complicated (43). As can be seen from **Fig.5** summarizing the results of the standard electrophysiological analysis for the neural networks (MFR, XC, ISI and PISI) after perturbation, there is no clear trend separating the neural networks in the PFF condition from the networks in the control conditions, although the ultrastructural analysis revealed clear signs of induced pathology in the former (**Fig.3, S4-7**). This lack of a pathology expression in the functional activity of the perturbed neural networks is well in line with the aforementioned compensatory network mechanisms, such as homeostatic plasticity and circuit reconfiguration, which will work to maintain the functional capacity and present state of the network for as long as possible, effectively masking the developing PD-related pathology. However, as already noted, our results indicate a trend in alteration of the network criticality state, where the assessment of criticality should reflect the actual pathological development, whether it produces a linear, abrupt, or fluctuating change in the system dynamics, if enough time points and samples are incorporated (43).

Furthermore, the criticality analysis of neuronal avalanche activity revealed that the neural networks fluctuated between critical and non-critical states, both at baseline and after perturbation, for networks in both the PFF condition and the PBS control condition. Some other reports of in vitro neural network criticality (using dissociated rat cortical neurons) have found that most, but not all, of the neural networks investigated tend to stay within the critical regime after a certain point in their development (48, 57). The baseline activity of our human iPSC-derived neural networks mostly display activity consistent with a non-critical regime, suggesting a different developmental trajectory from networks derived from rodent primary neurons. This is indeed conceivable as the epigenetic and age-related imprint is removed

through cell reprogramming through the iPSC stage (58, 59), resulting in a population of rejuvenated cells, from which our human neural networks were derived. Some studies indicate a slower development and maturation of neural networks derived from iPSCs compared to primary neurons (60-62), which could point towards a partial explanation of the largely non-critical activity observed at baseline in our neural networks. On the other hand, the non-homogenous population of cells represented within the iPSC-derived neural networks produces a more complex environment for development than pure neuronal cultures, which likely speeds up the developmental trajectory. For instance, the presence of astrocytes facilitates the formation and maturation of synaptic connections (63). However, as no other published study has investigated criticality in iPSC-derived neural networks, this remains to be elucidated, while other currently unknown influencing factors cannot be excluded at this point.

Inducing pathology through alpha-synuclein PFFs

In a recent publication, Van den Berge et al., (13) showed that alpha-synuclein PFF seeds injected into the duodenum wall of a transgenic rat model induce an alpha-synuclein pathology which propagates transynaptically and bidirectionally through the parasympathetic and sympathetic nervous system to the brain stem in a pattern which fully recapitulates Braak's hypothesis (6) of the development of a patterned pathological propagation in PD. This finding, together with the seminal demonstration of PFF induced pathology propagating from the gastrointestinal tract to the brains in rats (11), strengthens the growing suspicion of idiopathic PD originating from a yet unidentified pathogen capable of passing the mucosal barrier (64). Thus, our investigation of alpha-synuclein PFF induced pathology in human iPSC-derived neural networks is highly relevant and in line with the current direction of PD research.

As has been reported by several other studies investigating alpha-synuclein PFF induced pathology (65-70), we experienced issues with unequivocal identification of pathological alpha-synuclein aggregates using immunocytochemistry (**Fig.S3**), even after TritonX-1000 protein extraction, which should leave only insoluble inclusions (31, 32, 70). Although neural networks from the PFF condition consistently displayed positive immunolabeling of alpha-synuclein phosphorylated at S129, unspecific labelling and background staining were also consistently observed in control conditions, rendering the immunoassays inconclusive. We therefore aimed to identify alpha-synuclein inclusions based on ultrastructural morphology and localization using TEM. In samples from the PFF condition, but not in samples from the monomer control condition, we observed several intracellular structures whose shape, size, and localization are consistent with alpha-synuclein aggregates found in previous studies (31, 65, 71)(**Fig.3, S4**). Furthermore, our neural network samples were analysed with respect to additional structural/morphological characteristics associated with reduced cell health and viability, and which are heavily linked to pathological intracellular aggregates (55). These include extracellular residual elements of apoptosis, necrosis and necroptosis (**Fig. S5, S6),** as well as intracellular elements of autophagic and lysosomal activation **(Fig. S5, S7).** The latter is of particular interest as they are key regulators of cellular homeostasis, degrading and recycling proteins and cell constituents. As neurons are faced with disease related and aggregate-prone protein forms such as alpha-synuclein PFFs, this regulatory function becomes even more critical, as failure precipitates inclusion formation (72, 73). As pathological protein aggregation eventually saturates the autophagic machinery, the resulting imbalance in autophagic flux is believed to lead to neurodegeneration and cell death (74). This corresponds well with our results, as significantly more apoptotic and necrotic residues were found in the samples from PFF condition compared to the monomer control condition (**Fig.S5**). Furthermore, many of these apoptotic and necrotic elements showed signs of pathological fibril condensation (**Fig. S4**). As no significant difference in autophagic and lysosomal activation

was found between the two conditions, these results suggest that most of the neurons affected by the PFF induced pathology had already succumbed to neurodegeneration and cell death at the point of ultrastructural analysis (38 days post perturbation).

Limitations

Although our dataset was relatively large (>>100 different recordings), some of the recording points contained too few neuronal avalanches for computational analysis. This relative lack of avalanche activity is likely a result of low baseline activity in the neural networks combined with "short" (7 minute) recording sessions. Furthermore, it should be noted that the monomer condition might be a poor control, particularly for the feature of lysosomal and autophagic activation, as it has been recently shown to produce some level of toxicity by itself (70, 75, 76), and samples from both the PFF and monomer condition displayed relatively high numbers of autophagic/lysosomal elements.

Conclusion

Our study shows that developing PD-related proteinopathy can be associated with alterations in network criticality states. Furthermore, the results suggest that induction of proteinopathy changes the developmental trajectory of the neural networks in relation to SoC. Although the evolving pathology was not visible through common functional activity measures such as MFR, XC, ISI and PISI, a clear trend in criticality separates the PFF neural networks from the control neural networks, where the former largely displayed neuronal avalanche activity consistent with criticality, while the latter mainly displayed non-critical activity, after the point of perturbation. Although the direction of this criticality alteration was contrary to our expectations, the slower development and maturation of iPSC-derived neural networks compared to more commonly used primary neural networks suggested by some recent studies likely underlies this finding. Nevertheless, this first report associating network criticality state alterations with induced proteinopathy in human iPSC-derived neural networks opens up exciting new avenues for identifying and understanding developing pathologies underlying neurodegenerative diseases.

Abbreviations

PD - Parkinson's disease
AD - Alzheimer's disease
ALS - Amyotrophic lateral sclerosis
SNpc - Substantia Nigra pars compacta
MEA - multielectrode array
SoC - Self-organized criticality
PFF - alpha-synucelin pre-formed fibrils
iPSC - induced pluripotent stem cells
PBS - Phosphate buffered saline
AFM - Atomic force microscopy
TEM - Transmission electron microscopy
MFR - Mean firing rate
ISI - Inter-spike intervals
PISI - Population inter-spike interval
XC - Cross-correlation

Acknowledgements

This work was supported by The Department of Neuromedicine and Movement Science, Faculty of Medicine and Health Sciences, NTNU; The Liaison Committee for Education, Research and Innovation in Central Norway (Samarbeidsorganet HMN, NTNU); and the

SOCRATES project (NFR project agreement 270961). The TEM preparation was performed at the Cellular and Molecular Imaging Core Facility (CMIC, NTNU); The AFM and UV-vis spectroscopy were performed by Birgitte Hjelmeland McDonagh at the Norwegian Micro- and Nano-Fabrication Facility (NorFab), Norwegian University of Science and Technology (NTNU).

Author contributions

VV designed the study, conducted the experiments, collected and analyzed the data, and wrote the paper; KH performed all electrophysiological data analysis, wrote parts of the paper, and contributed with critical discussion and interpretation of the findings; OR contributed with operationalizing the electrophysiological recordings and data analysis; WK created the PFFs, contributed with valuable feedback during the experimental process, and critically reviewed the paper; GB critically reviewed the paper; SN provided supervision and valuable discussion in relation to the electrophysiological data analysis and techniques; AS conceived and supervised the study, contributed to the study design, and critically reviewed the paper; IS conceived and supervised the study, contributed to the study design and interpretation of results, edited, and critically reviewed the paper.

Competing interests

The authors declare no competing interests.

Data availability

The datasets generated for this study are available on request to the corresponding author.

References

1. Goedert M, Jakes R, Spillantini MG. The Synucleinopathies: Twenty Years On. J Parkinsons Dis. 2017;7(s1):S53-s71.
2. Goedert M, Masuda-Suzukake M, Falcon B. Like prions: the propagation of aggregated tau and alpha-synuclein in neurodegeneration. Brain. 2017;140(2):266-78.
3. Golde TE, Borchelt DR, Giasson BI, Lewis J. Thinking laterally about neurodegenerative proteinopathies. J Clin Invest. 2013;123(5):1847-55.
4. Thomas M, Alegre-Abarrategui J, Wade-Martins R. RNA dysfunction and aggrephagy at the centre of an amyotrophic lateral sclerosis/frontotemporal dementia disease continuum. Brain. 2013;136(Pt 5):1345-60.
5. Braak H, Braak E. Neuropathological stageing of Alzheimer-related changes. Acta Neuropathol. 1991;82(4):239-59.
6. Braak H, Del Tredici K, Rub U, de Vos RA, Jansen Steur EN, Braak E. Staging of brain pathology related to sporadic Parkinson's disease. Neurobiol Aging. 2003;24(2):197-211.
7. Braak H, de Vos RA, Bohl J, Del Tredici K. Gastric alpha-synuclein immunoreactive inclusions in Meissner's and Auerbach's plexuses in cases staged for Parkinson's disease-related brain pathology. Neurosci Lett. 2006;396(1):67-72.
8. Al-Chalabi A, Hardiman O. The epidemiology of ALS: a conspiracy of genes, environment and time. Nat Rev Neurol. 2013;9(11):617-28.
9. Thal DR, Rub U, Orantes M, Braak H. Phases of A beta-deposition in the human brain and its relevance for the development of AD. Neurology. 2002;58(12):1791-800.
10. Jellinger KA. The pathomechanisms underlying Parkinson's disease. Expert Rev Neurother. 2014;14(2):199-215.
11. Holmqvist S, Chutna O, Bousset L, Aldrin-Kirk P, Li W, Bjorklund T, et al. Direct evidence of Parkinson pathology spread from the gastrointestinal tract to the brain in rats. Acta Neuropathol. 2014;128(6):805-20.
12. Mulak A, Bonaz B. Brain-gut-microbiota axis in Parkinson's disease. World J Gastroenterol. 2015;21(37):10609-20.
13. Van Den Berge N, Ferreira N, Gram H, Mikkelsen TW, Alstrup AKO, Casadei N, et al. Evidence for bidirectional and trans-synaptic parasympathetic and sympathetic propagation of alpha-synuclein in rats. Acta Neuropathol. 2019.
14. Chandra R, Hiniker A, Kuo YM, Nussbaum RL, Liddle RA. alpha-Synuclein in gut endocrine cells and its implications for Parkinson's disease. JCI insight. 2017;2(12).
15. Verstreken P, editor. Parkinson's Disease: Molecular Mechanisms Underlying Pathology Academic Press; 2017.
16. Turrigiano GG. The dialectic of Hebb and homeostasis. Philos Trans R Soc Lond B Biol Sci. 2017;372(1715).
17. Turrigiano G. Homeostatic synaptic plasticity: local and global mechanisms for stabilizing neuronal function. Cold Spring Harb Perspect Biol. 2012;4(1):a005736.
18. Turrigiano GG, Nelson SB. Homeostatic plasticity in the developing nervous system. Nat Rev Neurosci. 2004;5(2):97-107.
19. Abbott LF, Nelson SB. Synaptic plasticity: taming the beast. Nat Neurosci. 2000;3 Suppl:1178-83.
20. Kordower JH, Olanow CW, Dodiya HB, Chu Y, Beach TG, Adler CH, et al. Disease duration and the integrity of the nigrostriatal system in Parkinson's disease. Brain. 2013;136(Pt 8):2419-31.

21. Tononi G, Edelman GM, Sporns O. Complexity and coherency: integrating information in the brain. Trends Cogn Sci. 1998;2(12):474-84.
22. Breakspear M, Stam CJ. Dynamics of a neural system with a multiscale architecture. Philos Trans R Soc Lond B Biol Sci. 2005;360(1457):1051-74.
23. Fornito A, Zalesky A, Breakspear M. The connectomics of brain disorders. Nat Rev Neurosci. 2015;16(3):159-72.
24. Bullmore E, Sporns O. Complex brain networks: graph theoretical analysis of structural and functional systems. Nat Rev Neurosci. 2009;10(3):186-98.
25. Spillantini MG, Schmidt ML, Lee VM, Trojanowski JQ, Jakes R, Goedert M. Alpha-synuclein in Lewy bodies. Nature. 1997;388(6645):839-40.
26. Verma M, Vats A, Taneja V. Toxic species in amyloid disorders: Oligomers or mature fibrils. Ann Indian Acad Neurol. 2015;18(2):138-45.
27. Jackson WS. Selective vulnerability to neurodegenerative disease: the curious case of Prion Protein. Dis Model Mech. 2014;7(1):21-9.
28. Walsh DM, Selkoe DJ. A critical appraisal of the pathogenic protein spread hypothesis of neurodegeneration. Nat Rev Neurosci. 2016;17(4):251-60.
29. Luk KC, Kehm V, Carroll J, Zhang B, O'Brien P, Trojanowski JQ, et al. Pathological alpha-synuclein transmission initiates Parkinson-like neurodegeneration in nontransgenic mice. Science. 2012;338(6109):949-53.
30. Luk KC, Kehm VM, Zhang B, O'Brien P, Trojanowski JQ, Lee VM. Intracerebral inoculation of pathological alpha-synuclein initiates a rapidly progressive neurodegenerative alpha-synucleinopathy in mice. J Exp Med. 2012;209(5):975-86.
31. Volpicelli-Daley LA, Luk KC, Lee VM. Addition of exogenous alpha-synuclein preformed fibrils to primary neuronal cultures to seed recruitment of endogenous alpha-synuclein to Lewy body and Lewy neurite-like aggregates. Nat Protoc. 2014;9(9):2135-46.
32. Abounit S, Bousset L, Loria F, Zhu S, de Chaumont F, Pieri L, et al. Tunneling nanotubes spread fibrillar alpha-synuclein by intercellular trafficking of lysosomes. EMBO J. 2016;35(19):2120-38.
33. Bieri G, Gitler AD, Brahic M. Internalization, axonal transport and release of fibrillar forms of alpha-synuclein. Neurobiol Dis. 2017.
34. Bak P, Tang C, Wiesenfeld K. Self-organized criticality. Physical review A, General physics. 1988;38(1):364-74.
35. Beggs JM, Plenz D. Neuronal avalanches in neocortical circuits. J Neurosci. 2003;23(35):11167-77.
36. Beggs JM, Plenz D. Neuronal avalanches are diverse and precise activity patterns that are stable for many hours in cortical slice cultures. J Neurosci. 2004;24(22):5216-29.
37. Tetzlaff C, Okujeni S, Egert U, Worgotter F, Butz M. Self-organized criticality in developing neuronal networks. PLoS Comput Biol. 2010;6(12):e1001013.
38. Moretti P, Munoz MA. Griffiths phases and the stretching of criticality in brain networks. Nature communications. 2013;4:2521.
39. Hesse J, Gross T. Self-organized criticality as a fundamental property of neural systems. Front Syst Neurosci. 2014;8:166.
40. Massobrio P, Pasquale V, Martinoia S. Self-organized criticality in cortical assemblies occurs in concurrent scale-free and small-world networks. Sci Rep. 2015;5:10578.
41. Valverde S, Ohse S, Turalska M, West BJ, Garcia-Ojalvo J. Structural determinants of criticality in biological networks. Front Physiol. 2015;6:127.

42. Yada Y, Mita T, Sanada A, Yano R, Kanzaki R, Bakkum DJ, et al. Development of neural population activity toward self-organized criticality. Neuroscience. 2017;343:55-65.
43. Muñoz MA. Colloquium: Criticality and dynamical scaling in living systems. Reviews of Modern Physics. 2018;90(3).
44. Rubinov M, Sporns O, Thivierge JP, Breakspear M. Neurobiologically realistic determinants of self-organized criticality in networks of spiking neurons. PLoS Comput Biol. 2011;7(6):e1002038.
45. Friedman EJ, Landsberg AS. Hierarchical networks, power laws, and neuronal avalanches. Chaos (Woodbury, NY). 2013;23(1):013135.
46. Rybarsch M, Bornholdt S. Avalanches in self-organized critical neural networks: a minimal model for the neural SOC universality class. PLoS One. 2014;9(4):e93090.
47. Shew WL, Plenz D. The functional benefits of criticality in the cortex. Neuroscientist. 2013;19(1):88-100.
48. Pasquale V, Massobrio P, Bologna LL, Chiappalone M, Martinoia S. Self-organization and neuronal avalanches in networks of dissociated cortical neurons. Neuroscience. 2008;153(4):1354-69.
49. Kirkeby A, Nelander J, Parmar M. Generating regionalized neuronal cells from pluripotency, a step-by-step protocol. Front Cell Neurosci. 2012;6:64.
50. Kirkeby A, Nolbrant S, Tiklova T, Heuer A, Kee N, Cardoso T, et al. Predictive Markers Guide Differentiation to Improve Graft Outcome in Clinical Translation of hESC-Based Therapy for Parkinson's Disease. Cell stem cell. 2016;20:1-14.
51. Doi D, Samata B, Katsukawa M, Kikuchi T, Morizane A, Ono Y, et al. Isolation of human induced pluripotent stem cell-derived dopaminergic progenitors by cell sorting for successful transplantation. Stem cell reports. 2014;2(3):337-50.
52. Heiney K, valderhaug VD, Sandvig I, Sandvig A, Tufte G, Hammer HL, et al. Evaluation of the criticality of in vitro neuronal networks: Towards an assessment of computational capacity. arXiv. 2019.
53. Clauset A, Shalizi CR, Newman MEJ. POwer-law distributions in empirical data. Society for Industrial and Applied Mathematics. 2009;51(4):661-703.
54. Kuan W-L, Bennett N, He X, Skepper JN, Martynyuk N, Wijeyekoon R, et al. α-Synuclein pre-formed fibrils impair tight junction protein expression without affecting cerebral endothelial cell function. Exp Neurol. 2016;285, Part A:72-81.
55. Shahmoradian SH, Lewis AJ, Genoud C, Hench J, Moors TE, Navarro PP, et al. Lewy pathology in Parkinson's disease consists of crowded organelles and lipid membranes. Nat Neurosci. 2019;22(7):1099-109.
56. Haldeman C, Beggs JM. Critical branching captures activity in living neural networks and maximizes the number of metastable States. Phys Rev Lett. 2005;94(5):058101.
57. Pu J, Gong H, Li X, Luo Q. Developing neuronal networks: Self-organized criticality predicts the future. Sci Rep. 2013;3:1081.
58. Lapasset L, Milhavet O, Prieur A, Besnard E, Babled A, Ait-Hamou N, et al. Rejuvenating senescent and centenarian human cells by reprogramming through the pluripotent state. Genes Dev. 2011;25(21):2248-53.
59. Patterson M, Chan DN, Ha I, Case D, Cui Y, Van Handel B, et al. Defining the nature of human pluripotent stem cell progeny. Cell Res. 2012;22(1):178-93.
60. Marom S, Shahaf G. Development, learning and memory in large random networks of cortical neurons: lessons beyond anatomy. Q Rev Biophys. 2002;35(1):63-87.

61. Cotterill E, Charlesworth P, Thomas CW, Paulsen O, Eglen SJ. A comparison of computational methods for detecting bursts in neuronal spike trains and their application to human stem cell-derived neuronal networks. J Neurophysiol. 2016;116(2):306-21.
62. Kirwan P, Turner-Bridger B, Peter M, Momoh A, Arambepola D, Robinson HP, et al. Development and function of human cerebral cortex neural networks from pluripotent stem cells in vitro. Development. 2015;142(18):3178-87.
63. Barker AJ, Ullian EM. New roles for astrocytes in developing synaptic circuits. Commun Integr Biol. 2008;1(2):207-11.
64. Braak H, Rub U, Gai WP, Del Tredici K. Idiopathic Parkinson's disease: possible routes by which vulnerable neuronal types may be subject to neuroinvasion by an unknown pathogen. Journal of neural transmission (Vienna, Austria : 1996). 2003;110(5):517-36.
65. Luk KC, Song C, O'Brien P, Stieber A, Branch JR, Brunden KR, et al. Exogenous alpha-synuclein fibrils seed the formation of Lewy body-like intracellular inclusions in cultured cells. Proc Natl Acad Sci U S A. 2009;106(47):20051-6.
66. Sacino AN, Brooks M, McKinney AB, Thomas MA, Shaw G, Golde TE, et al. Brain injection of alpha-synuclein induces multiple proteinopathies, gliosis, and a neuronal injury marker. J Neurosci. 2014;34(37):12368-78.
67. Sacino AN, Brooks M, Thomas MA, McKinney AB, McGarvey NH, Rutherford NJ, et al. Amyloidogenic alpha-synuclein seeds do not invariably induce rapid, widespread pathology in mice. Acta Neuropathol. 2014;127(5):645-65.
68. Nouraei N, Mason DM, Miner KM, Carcella MA, Bhatia TN, Dumm BK, et al. Critical appraisal of pathology transmission in the alpha-synuclein fibril model of Lewy body disorders. Exp Neurol. 2018;299(Pt A):172-96.
69. Delic V, Chandra S, Abdelmotilib H, Maltbie T, Wang S, Kem D, et al. Sensitivity and specificity of phospho-Ser129 alpha-synuclein monoclonal antibodies. J Comp Neurol. 2018;526(12):1978-90.
70. Polinski NK, Volpicelli-Daley LA, Sortwell CE, Luk KC, Cremades N, Gottler LM, et al. Best Practices for Generating and Using Alpha-Synuclein Pre-Formed Fibrils to Model Parkinson's Disease in Rodents. J Parkinsons Dis. 2018;8(2):303-22.
71. Volpicelli-Daley LA, Luk KC, Patel TP, Tanik SA, Riddle DM, Stieber A, et al. Exogenous alpha-synuclein fibrils induce Lewy body pathology leading to synaptic dysfunction and neuron death. Neuron. 2011;72(1):57-71.
72. Friedman LG, Lachenmayer ML, Wang J, He L, Poulose SM, Komatsu M, et al. Disrupted autophagy leads to dopaminergic axon and dendrite degeneration and promotes presynaptic accumulation of alpha-synuclein and LRRK2 in the brain. J Neurosci. 2012;32(22):7585-93.
73. Winslow AR, Chen CW, Corrochano S, Acevedo-Arozena A, Gordon DE, Peden AA, et al. alpha-Synuclein impairs macroautophagy: implications for Parkinson's disease. J Cell Biol. 2010;190(6):1023-37.
74. Ragagnin A, Guillemain A, Grant NJ, Bailly YJR. Neuronal Autophagy and Prion Proteins. 2013. In: Autophagy - A Double-Edged Sword [Internet].
75. Chavarria C, Rodriguez-Bottero S, Quijano C, Cassina P, Souza JM. Impact of monomeric, oligomeric and fibrillar alpha-synuclein on astrocyte reactivity and toxicity to neurons. Biochem J. 2018;475(19):3153-69.
76. Paumier KL, Luk KC, Manfredsson FP, Kanaan NM, Lipton JW, Collier TJ, et al. Intrastriatal injection of pre-formed mouse alpha-synuclein fibrils into rats triggers alpha-synuclein pathology and bilateral nigrostriatal degeneration. Neurobiol Dis. 2015;82:185-99.

Supplementary materials and results

Materials and methods

iPSCs to neural networks reprogramming protocol:

Day 0 - 4	EB formation			
NIM - media		Stock (mg/mL)	orking conc.	Total 100 mL
	DMEM/ F12 Media	1X	1X	48ml
	Neurobasal	1X	1X	48ml
	l-Glutamine	200mM	2mM	1000ul
	NEAA (Non Essential Amino acids)	100X	1X	1000ul
	2-mercaptoethanol	25mM	12.5uM	50ul
	Pen-Strep	1X	1X	1000ul
	N2 supplement	100X	1X	1000ul
DAY 0 - 1				
	ROCK inhibitor Y-27632	10mM	20uM	200ul
	*SB43152	10mM (1000X)	5uM	50ul
	*LDN1931892	2mM (10 000X)	100nM	5ul
DAY 1- 4				
	ROCK inhibitor Y-27632	10mM (50X)	20uM	200ul
	*SB43152	10mM (1000X)	5uM	50ul
	*LDN1931892	2mM (10 000X)	100nM	5ul
	* Shh (25II)	10ug/ml (1000X)	100ng/ml	100ul
	*CHIR99021 (light sensitive)	10mM	0.7-0.8uM	7.5ul

DAY 4-11	Coat: Lam-111			
NPM - media		Stock (mg/mL)	orking conc.	Total 100 mL
	DMEM/F12 Media	1X	1X	48ml
	Neurobasal Media	1X	1X	48ml
	l-Glutamine	200mM	2mM	1000ul
	NEAA (Non Essential Amino Acids)	100X	1X	1000ul
	Pen-Strep	1X	1X	1000ul
	N2 supplement	100X	0.5X	500ul
Day 4-9				
	ROCK inhibitor Y-27632	10mM (50X)	20uM	200ul
	*SB43152	10mM (1000X)	5uM	50ul
	*LDN1931892	2mM (10 000X)	100nM	5ul
	* Shh (25II)	10ug/ml (1000X)	100ng/ml	100ul
	*CHIR99021 (light sensitive)	10mM	0.7-0.8uM	7.5ul
Day 9 - 11				
	***FGF8b**	10ug/ml (1000X)	50ng/ml	50ul
	B27 Supplement minus AO	50X	1X	2ml

DAY 11-16	Dissociate using Accutase, replate on Lam-111			
NDM - media		Stock (mg/mL)	orking conc.	Total 100 mL
	Neurobasal	1X	1X	97ml
	l-Glutamine	200mM	2mM	1000ul
	NEAA	100X	1X	1000ul
	Pen-Strep	1X	1X	1000ul
Supplements				
	ROCK inhibitor Y-27632	10mM (50X)	20uM	200ul
	BDNF	10ug/ml (1000X)	20ng/ml	200ul
	AA	0.4mg/ml (1000X)	0.4ug/ml	100ul
	*FGF8b	10ug/ml (1000X)	50ng/ml	50ul
	B27 Supplement minus AO	50X	1X	2ml

Day 16------> Optional Maturation			PLO/lam	
NDM - media		Stock (mg/mL)	orking conc.	Total 100 mL
	Neurobasal	1X	1X	97ml
	l-Glutamine	200mM	2mM	1000ul
	Pen-Strep	1X	1X	1000ul
	NEAA	100X	1X	1000ul
	DAPT	100mM	10uM	10ul
Supplements	B27	50X	1X	2ml
	Ascorbic acid (A)	0.4mg/ml (1000X)	0.4ug/ml	100ul
	ROCK inhibitor (RI)	10mM (50X)	20uM	200ul
	BDNF	10ug/ml (1000X)	20ng/ml	200ul

* Patterning factors

TEM preparation of neural network samples:

Gelatine embedding: All samples were washed for 2x10 min in 0.1M phosphate buffer, mixed 1:1 with gelatine (6% porcine, dissolved in 0,1M phosphate buffer) and incubated for 15-20min in 37-40°C. The samples were then centrifuged, cooled off, and post fixed with glutataldehyde. Surplus gelatine was cut away and the samples were cut and shaped into 1x1mm (or smaller) pieces.

Dehydration: The samples were washed 2x10min in 0.1M cacodylate buffer, and post-fixed in the dark for 1 hour in 2% OsO_4 + 1.5% potassium ferrocyanide in 0,1M cacodylate buffer. A series of washing and dehydration steps followed: 2x5min 0,1M cacodylate buffer, 2x5 min phosphate buffer, 1x10 min in 50% alcohol, 1x10 min in 70% alcohol, 1x10 min in 90% alcohol, 4x10 min in absolute alcohol, and 2x15min in ABS acetone.

Infiltration and embedding: 10ml epoxy was mixed with 0,15ml DMP-30. The samples were then placed in acetone and epoxy in the following dilutions: (2:1) for 2 hours, (1:1) for 2 hours, and (1:2) overnight. The samples were then placed in epoxy for 8 hours on a rotator, where the solution was replaced every 2 hours for better infiltration. The samples where then placed in plastic moulds, labelled, and polymerized at 60°C for 3 days.**)**

Supplementary Result

Immunocytochemistr

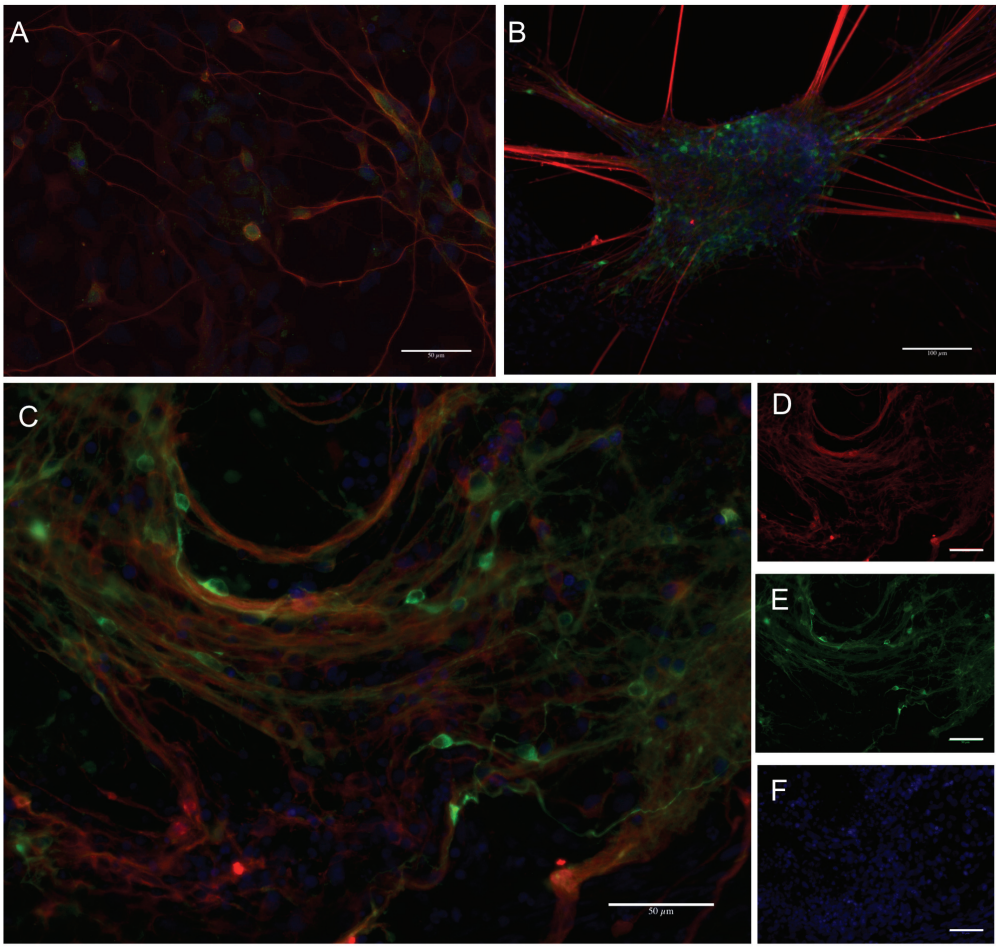

Figure. S1 Antigenic profile of engineered neural networks after 30 days of maturation. (**A**) Immunostaining with the neuron-specific cytoskeletal antibody beta-3 tubulin (red), the catecholamine neurotransmitter precursor antibody tyrosine hydroxylase (TH) (green), and counterstaining with hoechst (blue) (40X). (**B**) Immunostaining with the mature axonal antibody neurofilament heavy (red), TH (green) and counterstaining with hoechst (20X). (**C**). Image showing immunostaining with an antibody for endogenous alpha-synuclein (red) and TH (green), together with hoechst counterstain (blue) (40X). Images **D**, **E** and **F** are the single channel versions of **C**, showing endogenous alpha-synuclein, TH and Hoechst, respectively.

Verification of alpha-synuclein PFF seeds

UV-visible absorbance spectra and AFM of the PFFs showed a clear difference in both absorbance and structure of PFFs before and after water bath ultrasonication, indicating that the ultrasonication is effective in breaking the PFFs into smaller seeds.

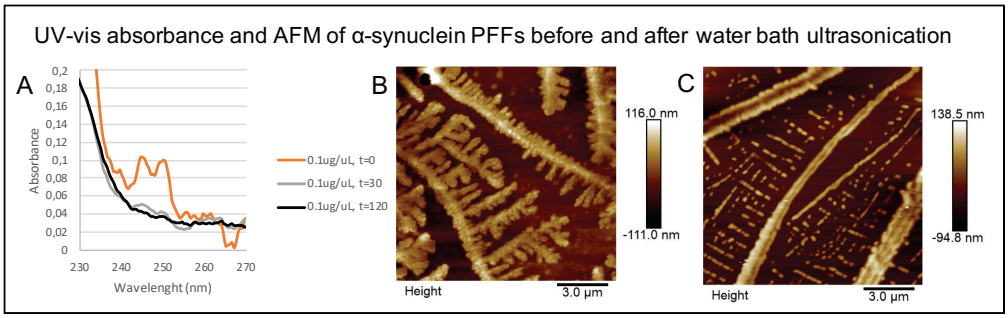

Figure S2.: **UV-visible absorbance spectra and atomic force microscopy (AFM) of pre-formed fibrils (PFFs). A**) UV-vis absorbance of α-synuclein PFFs show that before ultrasonication, the PFFs display a doublet absorption peak between λ_{240} - λ_{250}. Absorption between λ_{240} - λ_{250} stems from $\pi \rightarrow \pi^*$ transitions of the pyrimidine and purine rings in nucleobases. After ultrasonication, the absorption at 240nm – 250 nm is reduced, which suggest less stacking of aromatic rings. AFM images **B**) before (t=0) and **C**) after (t=120 min) sonication show that treatment with ultrasonication disintegrates the branched structure of the PFFs.

Verification of the presence of intracellular alpha-synuclein aggregates after PFF addition in engineered neural networks

The antibody for alpha-synuclein phosphorylated at S129 (ab51253) was used to visualize intracellular aggregates by immunofluorescence in PFA-fixed and protein-extracted samples (TritonX-100) 2 weeks or more after addition of PFF seeds to the neuronal media. Although consistent positive intracellular labelling by the S129 antibody was observed in the PFF treated neural networks, both perinuclearly and at distal neuronal sites, background staining and unspecific labelling was also consistently observed in the control conditions (both in the DPBS and in the monomer control). Positive control labelling with the S129 antibody was observed at a range of different dilutions (1:100-1:750), with 3 different secondaries (488nm, 568nm, 647nm), for two different antibody batches, and after 10, 15, and 20 minutes' protein extraction by TritonX-100. Representative images of these results are shown in **S3**. The immunocytochemistry was thus inconclusive.

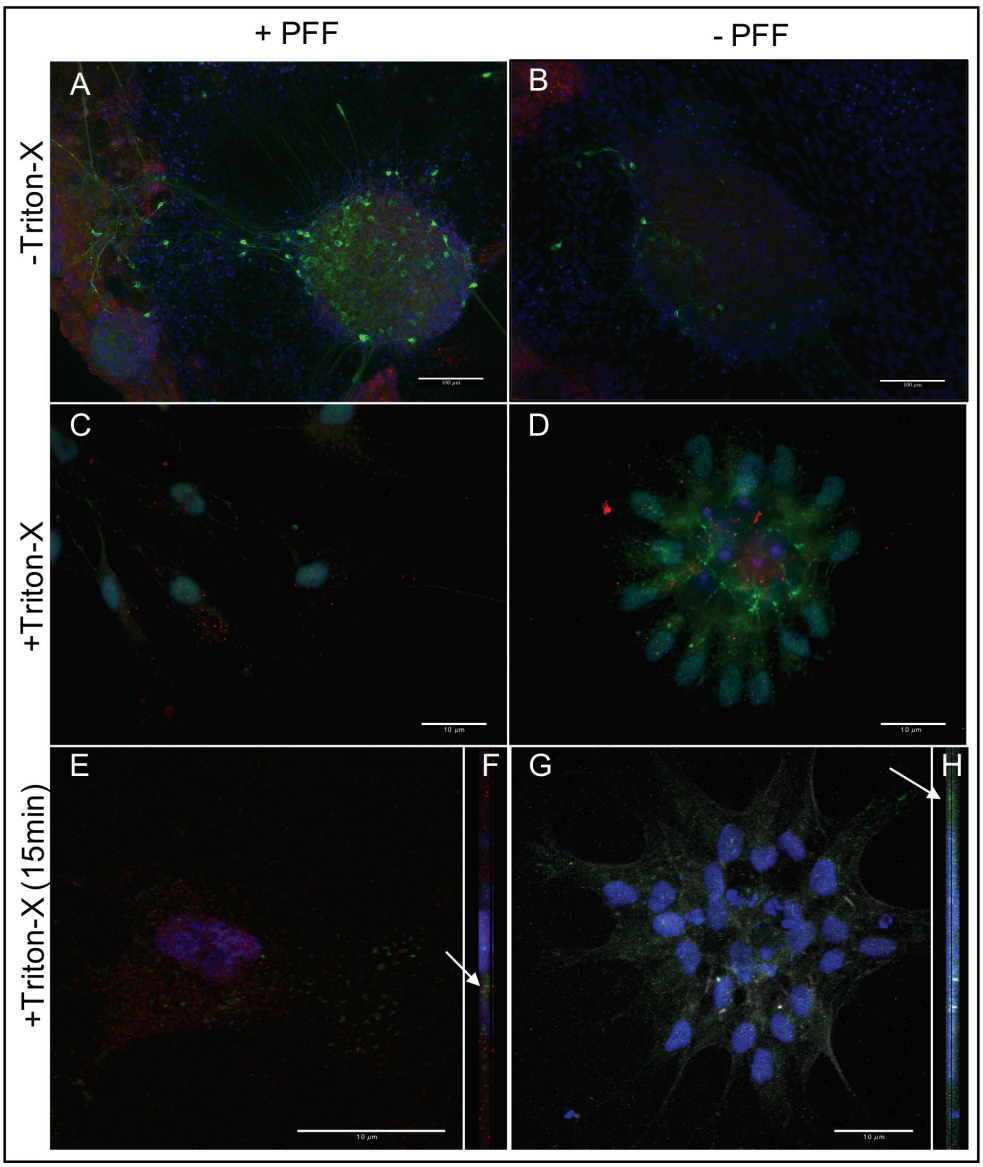

Figure S3. Immunostaining of intracellular alpha-synuclein aggregates. Immunofluorescent images displaying the detection of anti-alpha-synuclein phosphorylated at S129 antibody after different lengths of protein extraction in PFF cultures (**A,C,E** and **F**) and in control cultures (**B,D,G** and **H**). **A,B**) Immunocytochemistry of the mature engineered neural networks fixated without TritonX-100 extraction, displaying immunofluorescence with antibodies for tyrosine hydroxylase (green), for alpha synuclein phosphorylated at S129 (red) and with the nuclear counterstain hoechst (blue) (100um scale bar). **C,D**) Immunocytochemistry of cultures which were TritonX-100 extracted for 10 min prior to fixation, displaying immunofluorescent labelling with a phalloidin probe (green), the S129 antibody (red) and the nuclear counterstain hoechst (blue) (10um scale bar). **E and F)** Confocal image of a PFF treated culture which was TritonX-100 extracted for 15 min prior to fixation,

displaying immunofluorescent labelling with a phalloidin probe (red), the S129 antibody (green) and the nuclear counterstain hoechst (blue) (10um scale bar) **F)** Side-view of **E)** created by confocal stacking (white arrow indicates intracellular localization of the S129 antibody). **G and H)** Confocal image of a control culture which was TritonX-100 extracted for 15 min prior to fixation, with immunofluorescent labelling with a phalloidin probe (grey), the S129 antibody (green) and the nuclear counterstain hoechst (blue) (10um scale bar) **H**) Side-view of **G**) created by confocal stacking (white arrow indicates intracellular localization of the S129 antibody).

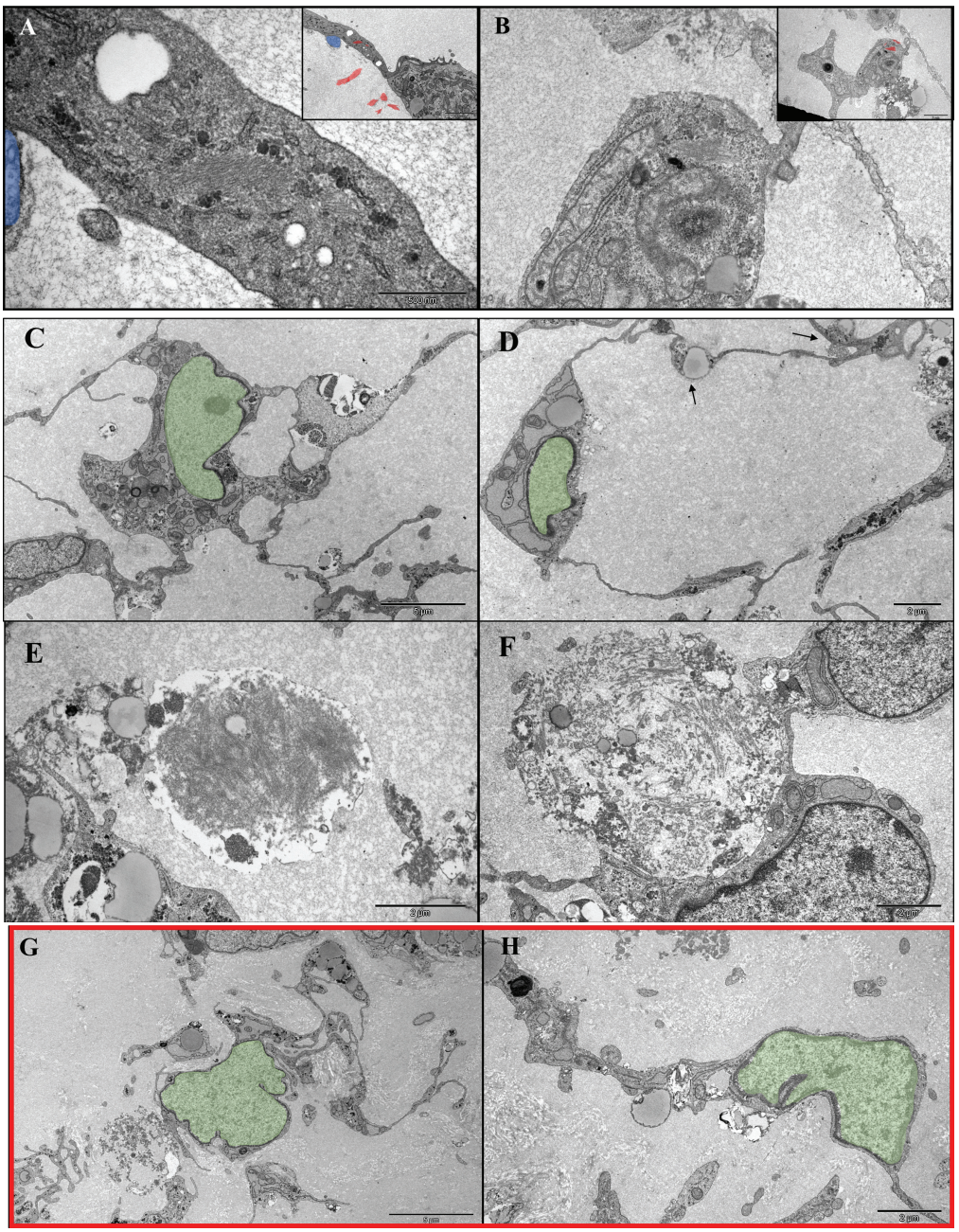

Figure S4 Ultrastructural observations of fibrillization, inclusion bodies and neuritic atrophy A) shows fibrillization within a neurite from the PFF condition. Upper right corner shows an overview image of the area, with red highlighting fibril structures, and blue indicating an axo-dendritic synapse. **B**) shows another cell from the PFF condition containing cytosolic fibrils. Upper right corner shows an overview image of the area, with red highlighting fibril structures **C)** Ultrastructural sample showing an abundance of membrane-enveloped "inclusion bodies", both in the cytosol and within neurites of a neuron from the PFF condition (green = nucleus). **D**) shows a neuron from the PFF condition with signs of membrane degradation and

atrophic neurites (arrow = swelling). **E**) and **F**) shows dead cells observed in the PFF condition with clear signs of fibril condensation. **G** and **H**) shows comparable neurons from the monomer control samples (green = nucleus).

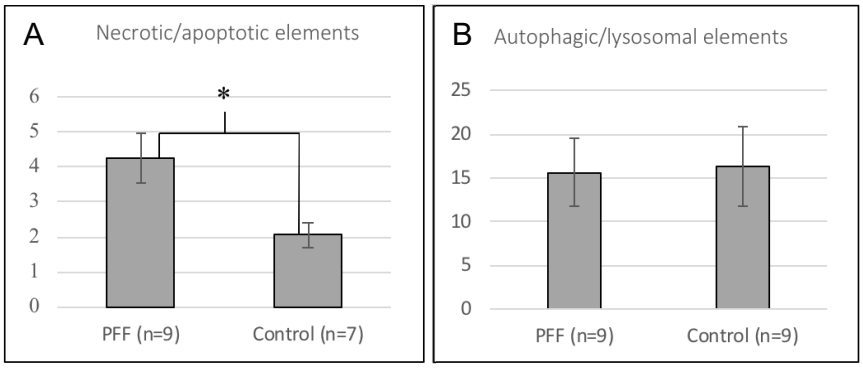

Figure S5 Necrotic/apoptitic elements and autophagosomal/lysosomal activation. Results from the ultrastructural image analysis, where the amount of necrosis-apoptosis (**A**) and autophagic/lysosomal elements (**B**) was compared between samples taken from the PFF treated condition and samples taken from the monomer control condition. The bar graphs display the results of the independent samples T-tests (group means with standard error of means). **A**) Mean number of apoptotic/necrotic elements surrounding single neurons in the PFF samples and the monomer control samples. n is the number of ultrastructural images analyzed for each condition, where the number of necrotic/apoptotic elements counted was divided by the number of morphologically intact neurons in the image (a total of 42 neurons from the PFF samples, and 39 from the monomer control samples). * significant at $p<.05$ **B**) No significant difference was found between the PFF samples and the monomer control samples in observed intracellular autophagic/lysosomal events. n denotes the number of single neurons analyzed.

Fig.S6 shows representative overview images of samples used for ultrastructural analysis of extracellular necrotic/apoptotic elements. The regions of interest were selected based on the presence of a homogenous distribution of neurons.

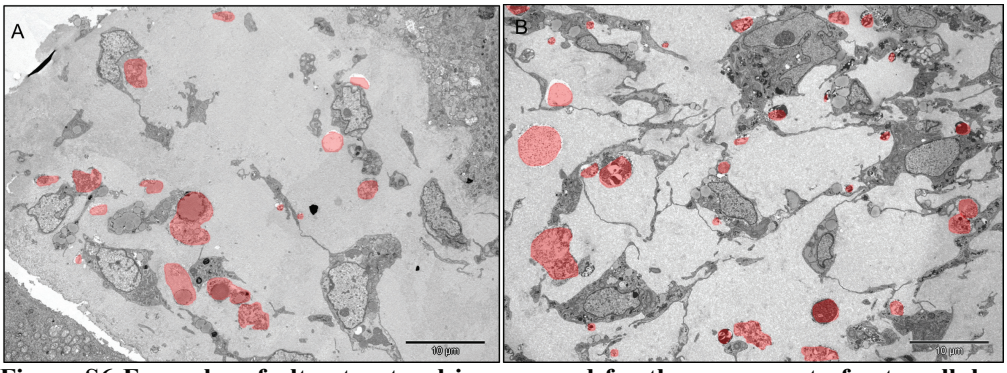

Figure S6 Examples of ultrastructural images used for the assessment of extracellular necrotic/apoptotic elements: A representative overview image from a monomer control sample (**A**) and a PFF treated sample **(B)**, illustrating the observed differences in the extracellular environment surrounding the neurons. Red = highlighted residues of apoptotic/necrotic elements.

Fig.S7 shows representative images used for the ultrastructural assessment of intracellular autophagic/lysosomal activation. The images analyzed were selected based on the presence of a number of neuron-specific ultrastructural features (axon/dendrites, synapses, nucleolus, shape and color of nucleus, as well as cytoplasmic electron density and heterochromatin condensation relative to other cell types identified in the preparation) (Peters and Folger; Rhodin 1974). Notice also the extracellular (filamentous) necrotic/apoptotic elements immediately adjacent to the neuron from the PFF condition displayed in **Fig.S5**.

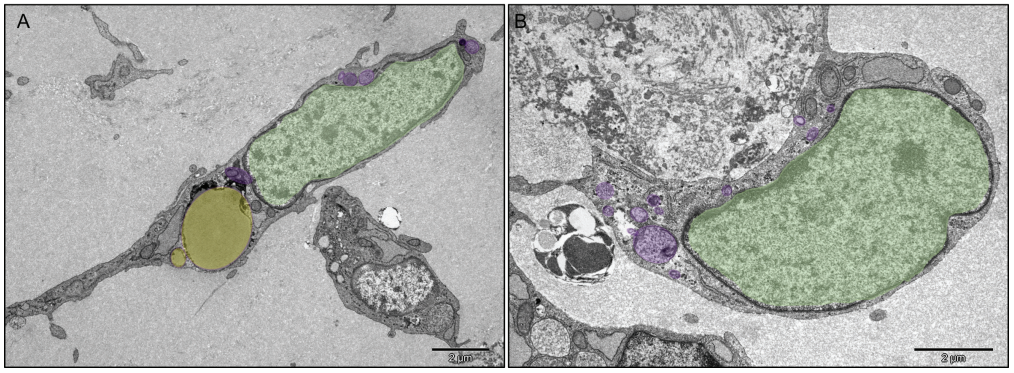

Figure S7 Examples of ultrastructural images used for the assessment of autophagosomal/lysosomal activation: Representative overview image of a single neuron from the monomer control samples (**A**) and from the PFF samples (**B**) illustrating the observed intracellular autophagic and lysosomal activity. Nucleus (green), purple autophagic/lysosomal activity (purple), lipid body (yellow).

PAPER 2

Research Report

Structural and functional alterations related to the LRRK2 G2019S mutation revealed in structured human neural networks

Vibeke Devold Valderhaug[1], Rosanne van de Wijdeven[2], Ola Huse Ramstad[1], Kristine Heiney[3], Stefano Nichele[3], Axel Sandvig[1,4,5], and Ioanna Sandvig[1]*

[1]Department of Neuromedicine and Movement Science, Faculty of Medicine, Norwegian University of Science and Technology (NTNU), Trondheim, Norway
[2]Department of Clinical and Molecular Medicine, Faculty of Medicine and Health Sciences, NTNU, Trondheim, Norway
[3]Department of Computer Science, Faculty of Technology, Art and Design; Oslo Metropolitan University (OsloMet), Oslo, Norway
[4] Department of Neurology and Clinical Neurophysiology, St Olav´s Hospital, Trondheim, Norway
[5] Department of Pharmacology and Clinical Neuroscience, Division of Neuro, Head and Neck, Umeå University Hospital, Umeå, Sweden

***Corresponding author**
Ioanna Sandvig PhD
Department of Neuromedicine and Movement Science, NTNU
3rd Floor, Nevro East
Edvard Grieg´s gate 8
7030 Trondheim, Norway
Email: ioanna.sandvig@ntnu.no
Tel: +47 72575620

Running title
Structure and function in engineered human LRRK2 networks

Total number of pages: 40
Total number of words: (i) whole manuscript: 7922; (ii) abstract: 244

Keywords
morphogenetic neuroengineering, microfluidic chips, microelectrode arrays, electrophysiology, *in vitro* disease modelling

Manuscript under revision by The European Journal of Neuroscience (EJN) (submitted 18.07.2019)

Abstract
Mutations in the LRRK2 gene have been widely linked to Parkinson´s disease. The G2019S variant has been shown to contribute uniquely to both familial and sporadic forms of the disease. LRRK2-related mutations have been extensively studied, yet the wide variety of cellular and network events directly or indirectly related to these mutations remain poorly understood. In this study, we structured multi-nodal human neural networks carrying the G2019S mutation using custom-designed microfluidic chips coupled to microelectrode-arrays. By applying live imaging approaches, immunocytochemistry and computational modelling, we have revealed alterations in both the structure and function of the resulting neural networks when compared to controls. We provide first evidence of increased neuritic density associated with the G2019S LRRK2 mutation, while previous studies have found either a strong decrease, or no change, compared to controls. Additionally, we corroborate previous findings regarding increased baseline network activity compared to control neural networks. Furthermore, we can reveal additional network alterations attributable to the specific mutation by selectively inducing transient overexcitation to confined parts of the structured multi-nodal networks. These alterations, which we were able to capture both at the micro- and mesoscale manifested as differences in relative network activity and correlation, as well as in mitochondria activation, neuritic remodelling, and synaptic alterations. Our study thus provides important new insights into early signs of neural network pathology significantly expanding upon the current knowledge relating to the G2019S Parkinson's disease mutation.

1. Introduction

Mutations in the leucine-rich repeat kinase 2 (LRRK2) (PARK8 locus) gene are linked to both late-onset familial and sporadic forms of Parkinson's disease (PD) (Healy et al., 2008). Although rare, LRRK2 gene mutations have been termed a potential "Rosetta stone" of parkinsonian disorders as all of the major pathologies related to parkinsonism have been observed, in addition to there being end-stage variability, within families carrying the same pathogenic variant (Joanne Trinh et al., 2006). Moreover, the Lewy body and Lewy neurite pathology commonly observed in brain autopsies from PD patients, are rarely observed in relation to LRRK2 mutations (Moore, 2008). The LRRK2 gene is expressed both in the brain and in other tissues throughout the body and is translated into the LRRK2 protein, which has enzymatic kinase activity involved in a range of cellular processes (Joanne Trinh et al., 2006). Pathogenic variants are postulated to augment this kinase activity, resulting in a toxic gain-of-function through an increase in both autophosphorylation and phosphorylation of LRRK2 substrates (Joanne Trinh et al., 2006, Sheehan and Yue, 2018, Jaleel et al., 2007, Zhao et al., 2012, Smith et al., 2006, Greggio et al., 2006, Steger et al., 2016).

Studies using both *in vitro* and *in vivo* models of PD suggest that synaptic alterations and axonal dysfunction represent the earliest detectable signs of the disease (MacLeod et al., 2006, Cheng et al., 2010, Dagda et al., 2014) and that initiation of pathology at the axon terminals might signify the start of the retrograde degeneration of the neurons (Tagliaferro and Burke, 2016, Sheehan and Yue, 2018). This also fits with the latest estimates compiling observations from several independent studies, concluding with 50-70% loss of striatal terminals at symptom onset of PD, while "only" 30% of dopaminergic neurons in the substantia nigra are lost at the same timepoint (as opposed to the often reported 60-80% dopaminergic neuron loss) (Cheng et al., 2010). Moreover, there is now abundant evidence that the molecular mechanisms of axonal degeneration are distinct from those of programmed cell death, implying that the two mechanisms should be considered separately, both in disease modelling and therapeutics (Cheng et al., 2010, Tagliaferro and Burke, 2016). Dendritic spine loss and shortening and simplification of the dendritic arbor are also regularly observed in post mortem tissues from patients with Alzheimer's disease and amyotrophic lateral sclerosis (Brizzee, 1987, Stephens et al., 2005, Baloyannis, 2006, Sasaki and Iwata, 2007, Cherra et al., 2013, Dagda et al., 2014, Genc et al., 2017). Such changes are often accompanied by a loss or impairment of dendritic mitochondria, a feature which is central in PD pathogenesis (Bose and Beal, 2016, Verma et al., 2017, Singh et al., 2019). Furthermore, these alterations have been linked to increased excitatory stimulation and calcium handling (Caudle and Zhang, 2009, Verma et al., 2018).

The advancement and availability of tools for morphogenetic neuroengineering now enable modelling of selected pathological aspects of neurodegenerative disease in human neural networks in vitro. In this study, we utilize healthy human cortical neural networks and equivalent networks carrying the Parkinson's related LRRK2 G2019S mutation to study early expression of pathology, both at the micro- and mesoscale. Among the LRRK2 mutations, the particular G2019S mutation represents the most commonly identified cause of late-onset PD, and has been shown to contribute uniquely to both familial and sporadic forms of the disease (Kachergus et al., 2005, Bouhouche et al., 2017, Joanne Trinh et al., 2006, Moore, 2008). Moreover, it has been shown to result in differential regulation of a variety of cellular pathways highly relatable to several aspects of PD pathology, among which are axonal guidance, cytoskeletal transport, cell growth, differentiation and communication (Habig et al., 2013, Habig et al., 2008).

In this study we investigate whether in vitro neural networks carrying the LRRK2 G2019S mutation display a different structural and functional profile compared to healthy controls during development and in response to induced perturbation consistent with excitotoxicity. To address these aims, we structured human neural networks with and without the LRRK2 G2019S mutation using tailor-made multi-nodal microfluidic chips (van de Wijdeven et al., 2018, van de Wijdeven et al., 2019). These microfluidic chips incorporate axon tunnels and synaptic compartments interconnecting three cell chambers, thus allowing selective manipulation of the neural network. Furthermore, each microfluidic chip incorporates a microelectrode-array (MEA), which enables electrophysiological recording of neural network activity within different interconnected nodes. We have subsequently monitored early network structure, function and dysfunction related to the G2019S LRRK2 mutation using this platform. Importantly, based on the two-hit hypothesis of PD, according to which a combination of genetic susceptibility and environmental factors may contribute to the onset and progression of the disease, we have selectively induced a transient, topologically confined neural overexcitation event, monitored network responses and revealed associated alterations at the micro- and mesoscale.

2. Materials and Methods

Structuring cortical neural networks using microfluidics chips with directional inter-nodal connectivity

Control human induced pluripotent stem cell (iPSC)-derived H9N neural stem cells (NSCs) (ax0019) and iPSC derived H9N NSCs homozygously carrying the LRRK2 G2019S (GGC>AGC) mutation (ax0310) (Axol Bioscience, Cambridge, United Kingdom) were cultured and expanded on 0.01 % poly-L-ornithine (PLO) (Sigma) and L-15 laminin (L15 medium containing 1:60 natural mouse laminin and 1:41 sodium bicarbonate) coated culture vessels in neural expansion medium (ax0030) supplemented with human FGF2 and EGF (ax0047 and ax0047X), and kept in a standard humidified air incubator (5% CO^2, 20%O^2, 37°C) (full cell culture protocol, as well as further information on each cell line available in the supplementary data). Each microfluidic chip was coated with the same combination of PLO and L-15 laminin and seeded with $1.1x10^5$ NSCs (37000 cells per cell chamber), from which point synchronous differentiation and maturation of the NSCs into cortical neurons was carried out until day 15, using an NSC reagent bundle and media (ax0101) in accordance with the manufacturer´s protocol.

Excitatory stimulation of structured neural networks using Kainic Acid

Fifteen days post seeding, the cortical networks in the microfluidics chips were stimulated with Kainic acid (KA) and subsequently investigated with live staining assays. KA (10µM) was applied to the top cell chamber for 30 minutes, after which all cell chambers were washed 3x with Dulbecco's phosphate buffered saline (PBS) and resupplied with media. A flow barrier created by a 10µl media level difference between the stimulated chamber and the non-stimulated chambers ensured the confinement of the KA to the top cell chamber only. The same procedure was carried out for each cell line using only PBS as a control condition. A total reactive oxygen species (ROS) assay kit 520nm (Thermo Fisher Scientific) fluorescently labeling ROS production was applied to verify a cellular response and the confinement of the stimulation by fluorescence microscopy (EVOS FL auto 2, Invitrogen, California, United States), where the microscope was set to image simultaneously in each of the microfluidics chips chambers every 10 minutes for 1 hour immediately following KA stimulation.

Axonal mitochondrial distribution in structured neural network

To investigate the mitochondria distribution in the control and LRRK2 neural networks, 0.1% Tetramethylrhodiamine (TMRM, T668, Invitrogen) was applied for 30 minutes at 37°C to all microfluidic chip chambers, rinsed in PBS, and imaged using a Zeiss 510 META Live confocal scanning laser microscope in a heated chamber (37°C). As a baseline measure, 3 image series were taken every 10 minutes, where an image was taken every second for 1 consecutive minute. Thirty minutes after a confined KA stimulation of the cortical neurons in the top chamber (as described in the previous section), the imaging procedure was repeated.

Cell viability assay

On day 16 (i.e. 24 hours post KA stimulation), a LIVE/DEAD viability/cytotoxicity kit (MP03224, Invitrogen) was applied to the neural networks in the microfluidics chips to determine whether the KA stimulation was sublethal. 0.8ul Ethidium homodimer-1 (2mM in DMSO/H_2O 1:4) and 0.4µl Calcein AM (4mM in anhydrous DMSO) was diluted in 2ml PBS and applied to all chambers in the microfluidic chips for 15 minutes in 37°C. The fluorescently labelled neural networks were then washed with PBS and imaged (EVOS FL auto 2).

Immunocytochemistry of the structured neural networks

24 hours post KA stimulation (or PBS as a control condition), structured neural networks from both the control and LRRK2 group were fixed and used for immunocytochemistry assays to assess the neurite and spine morphology. For fixation, 2% paraformaldehyde (PFA) was applied for 15 minutes followed by 4% PFA for 10-minutes and 3x15 minute washes at room temperature (RT). Blocking solution consisting of PBS with 5% normal goat serum (NGS) and 0.3% Triton-X was applied for 2 hours at room temperature and was followed by overnight incubation in primary anti-body solution (PBS with 1% NGS, 0.1% Triton-X) in 4°C. The following antibodies were used: Rabbit anti-Piccolo antibody (1:400) (ab20664), mouse-anti PSD95 (1:200) (ab13552), rabbit anti-CaMKII (1:250) (ab134041), rabbit anti-GRIK5 (1:200) (PA-5-41401), rabbit anti-Glutamate receptor 1 (AMPA) (1:500) (ab109450), mouse anti-MAP2 (1:400) (131500, Thermo Fisher Scientific), mouse anti-beta III tubulin (1:400) (ab119100), rabbit anti-total alpha synuclein (ab131508), mouse anti-mitochondria (ab3298), and chicken anti-neurofilament heavy (1:1000) (ab4680). The structured neural networks were then washed 3x15 minutes in PBS, and incubated for 3 hours in secondary antibody solution (PBS with 1% NGS, 0.1% Triton-X) in the dark, at RT. A combination of Alexa Fluor™ 488, 568, 647 secondary antibodies (Thermo Fisher, MA, USA) were used at a dilution of 1:1000. CytoPainter Phalloidin 647 (1:500) (ab176759) was added for the final 20 minutes of incubation, and Hoechst (1:10000) was added for the final 5 minutes before another 3x15 min wash in PBS was conducted. To avoid dilution of the solutions used for these immunocytochemistry procedures by the media already present in the axon tunnels of the microfluidic chips, some of the appropriate solution was used to flush through the tunnels prior to the actual incubation with each relevant solution. Images used for separate quantification of the fluorescently immunolabeled neural networks were taken using either a Zeiss Axiovert 1A fluorescent microscope (Carl Zeiss, Germany) with a 100x/1.3 oil objective or a Zeiss (510 META Live) confocal laser scanning microscope with a 63X/1.4 oil objective. ImageJ, MatLab and PowerPoint were used to post-process the images.

Image analysis

Analysis of ROS expression was done using the Fiji plugin Particle analyzer. The two-channel fluorescent images from the viability assay were merged, adjusted for brightness/contrast for maximal separation and clarity of both signals, and the cells manually counted using the Cell counter Fiji-plugin. The area close to the active zone in the microfluidic chip was selected for analysis as this area showed better separation of the signals due to a consistent lower cell density

across all conditions. The number and size of the TMRM-labelled mitochondria within the axonal tunnels were extracted using a simple image analysis pipeline implemented in MATLAB. First, nonuniform background illumination was removed by applying a top hat filter. The image was then binarized by Otsu thresholding, and the 8-connected components were extracted from the resulting binary image. Artefacts at the edges of the images, which tended to be large and elongated, were removed by eliminating components if their size exceeded 5 μm^2 or eccentricity exceeded 0.995. The number of mitochondria was then extracted as the number of remaining 8-connected components in the image. The size of each detected mitochondrion was computed from the number of pixels comprising each as-detected component. Additional analysis of fixed samples from this experiment were analyzed in Fiji using ROI manager. Two channel 100X images of fluorescent mitochondria and total alpha synuclein in the neural networks were binarized by Otsu thresholding, and the area covered by the fluorescence in each channel was selected and measured using the ROI manager. A ratio of the area covered by mitochondria/total alpha synuclein was calculated and used for statistical analysis in Prism8 (GraphPad, California, United States).

The fluorescence images of Piccolo-immunolabelled neurites were analyzed using a semi-automated process implemented in MATLAB and Fiji to count the number of neuritic boutons present in the images. Most boutons were counted in an automated fashion in MATLAB. Top hat filtering was applied to suppress nonuniform background illumination before the contrast of the resulting images was enhanced using adaptive histogram equalization. The contrast-enhanced images were binarized using Otsu thresholding, and salt noise in the binarized images was removed by median filtering. Neurite fragments were then joined by morphological closing, and any remaining small fragments were removed by applying hole filling to the inversion of the resulting image. Thinning was then applied to obtain a skeleton of the neurites in the image. From this thinned image, endpoint detection was used to obtain a preliminary bouton count. Because the automated analysis missed some boutons, the endpoint labelled images were visually inspected and the missed boutons were manually counted using the Cell counter in Fiji and added to the final results. The area covered by the neurites was calculated by means of the Particle analyzer after binarization with Otsu thresholding. Together, the boutons counted divided by the area covered with neurites created a ratio used for statistical analysis. For the measure of co-occurring Piccolo and PSD95 immunolabelling, an automatic threshold was applied for each channel (Otsu for Piccolo and Triangle for PSD95) in Fiji, the thresholded areas selected as ROIs, and areas containing both ROIs were selected for particle analysis. A cut-off at 15μm was set as an upper limit, and the number and average size measurement from each image were used for statistics.

Electrophysiological investigation of the structured neural networks

Using an identical microfluidic chip design interfaced with a custom-made microelectrode array (MEA), the electrophysiological activity of the structured neural networks and their response to KA stimulation were recorded through the MEA2100 in vitro Headstage, interface system and suit software (Multi Channel Systems; Reutlingen, Germany). Similar to the procedure described earlier, the MEA-interfaced microfluidic chips were coated with a combination of PLO and L15-laminin and seeded with $5x10^4$ NSCs per chamber (i.e. a total of 1.5 $x10^5$ per microfluidics chip), from which point synchronous differentiation and maturation of the NSCs into cortical neurons was carried out according to the manufacturer's protocol until day 15. The electrophysiological activity of each MEA-interfaced structured neural network was recorded for a duration of 7 minutes immediately before KA stimulation, during stimulation, and at 24 hours post stimulation (10kHz sampling rate, 300Hz high-pass filter, with a ± 5 standard deviations upper- and lower spike detection threshold). For each of the two experimental groups

(control neural networks vs LRRK2 neural networks) 6 MEA-interfaced neural networks were recorded and analyzed (3 controls, 3 KA stimulated). All raw data recordings are published in Mendeley Data Repository (doi: 10.17632/dnjv26msvk.4, doi: 10.17632/92568tpp39.4).

Statistical analyses

Analyses were performed and visualized using Prism8 (GraphPad, California, United States). Quantifications from each assay were assessed for normality and homoscedasticity before being assigned a two-tailed parametric or non-parametric statistical test for comparing groups.

Post-processing and analysis of electrophysiological data

Electrophysiological data analysis was performed with NeuroExplorer 4 (Nex Technologies, Colorado, United States) and MATLAB (MathWorks 2018, Massachusetts, United States). Following filtering and spike detection, the spikes were binned (1 sec) and the electrodes ordered according to chamber or channel of origin. Mean firing rates (MFRs) were estimated across conditions and recording time points as both total MFR and relative percentage deviation from baseline. Correlation was mapped using Pearson's correlation coefficient r for concurrent spiking across 1-second spike binnings. Schemaballs (MATLAB central File Exchange, Komarov, Oleg, retrieved 2017.01.15) and heatmaps were used to display inter-electrode spike correlation ordered by chamber. Total network correlation was computed as mean r across electrodes per recording.

To illustrate the electrophysiological behavior of the LRRK2 neural networks in response to KA stimulation, a single electrode (electrode 63) was randomly selected for more detailed analysis. As before, spikes were detected by applying a simple thresholding approach to the electrophysiological data after bandpass filtering (passband: 300 Hz to 3 kHz). The spikes were then sorted using principal component analysis (PCA) to distinguish spikes from a single neuron that showed a period of enhanced firing rate accompanied by attenuation in spike amplitude, followed by an abrupt silencing. The firing rate was computed by convolving an alpha function kernel ($\alpha = 1\ s^{-1}$, size = 10 s) with a spike train consisting of Dirac delta impulses at each spike time. The attenuation rates of the negative and trailing positive phases of the spikes were computed by fitting a line to the amplitude data during the period of high firing rate.

3. Results

Neural networks derived from both the control and LRRK2-mutated NSCs were successfully structured using the microfluidic chips (**Fig.1,** see also **Fig.6** is **STAR Method** for detailed microfluidic chip layout). Following 15 days of differentiation and maturation, immunocytochemistry confirmed the presence of neurons (MAP2), with neuron specific microtubules (beta-III tubulin) and mature axons (neurofilament heavy) containing both pre- and post-synaptic elements (Piccolo and PSD95, respectively), as well as expressing calmodulin-dependent protein kinase II (CamKII), a marker related to synaptic connectivity and long-term potentiation. Importantly, both kainic acid receptors (GRIK5) and AMPA receptors (GluR1) were also present (**Fig.1D, E and I**).

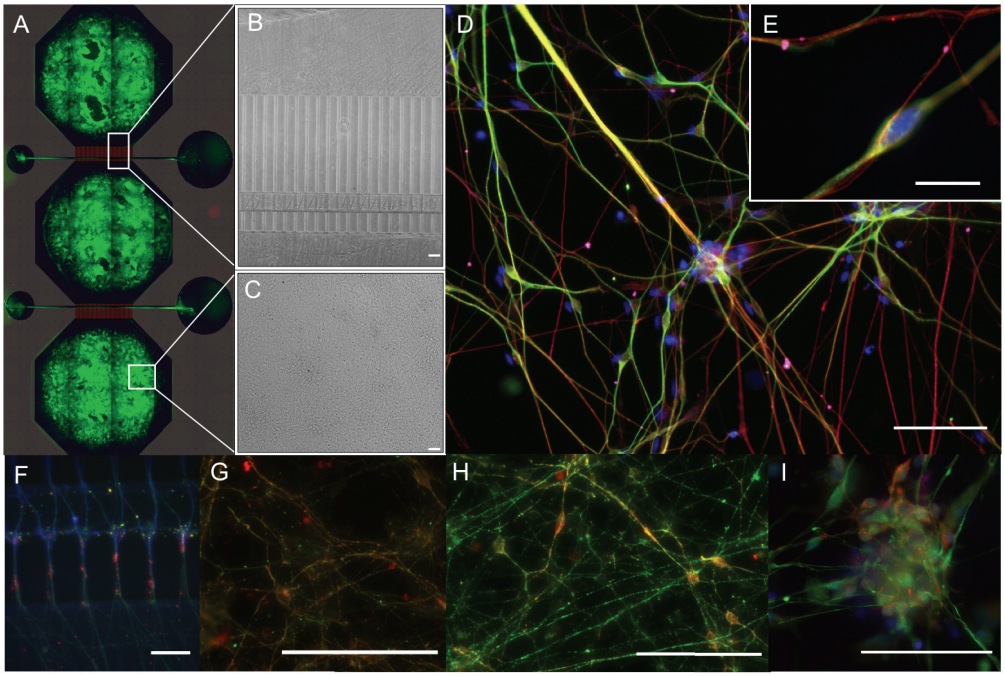

Fig.1 Structured neural networks. Following 15 days of NSC differentiation and maturation, immunocytochemistry confirmed the presence of mature neural networks in the microfluidic chips. **A**) Tiled image of a fluorescently labelled cortical neural network structured within a microfluidic chip, overlaid by a schematic of the design. **B**) Brightfield image of the developing neural network in a microfluidic chip, showing the area containing the axon tunnels, synaptic compartment and active zones, while **C**) Brightfield image from the cell chamber area. **D**) **F**luorescently labelled LRRK2 neural network with markers for neurons (MAP2, green), neuron specific microtubules (beta-III tubulin, red), and kainic acid receptors (GRIK5, magenta) together with the counterstain Hoechst (blue), with E) showing equivalent markers in a control neural network (10um scale bar). The remaining images show the neural networks fluorescently labelled with markers for **F**) neurons (MAP2, red) expressing (CaMKII, green)**, G**) with presynaptic vesicles (Piccolo, green), postsynaptic densities (PSD95, red) and F-actin (Phalloidin, blue) expressed in the axon tunnels and synaptic area, **H**) neuronal specific microtubules (beta-III tubulin, red) together with CaMKII (green), and **I**) neurofilament heavy (green) together with AMPA receptors (red) and Hoechst counterstain. 50µm scale bars.

Sublethal induction of overexcitation in structured neural networks by confined KA stimulation

Following a 30-minute KA stimulation targeting the neurons in the top cell chamber of a structured neural network, live microscopy of fluorescently labelled ROS production confirmed that the stimulation was successfully confined to the top cell chamber (**Fig.2A-E**). Furthermore, 24 hours post KA stimulation, the structured neural networks were fluorescently labelled with a live/dead viability assay kit, imaged and manually counted to determine whether the KA induced overexcitation was sublethal (**Fig.2F-H**). Two areas from each cell chamber were counted in two separate structured neural networks (a total of >2000 cells/network) for each condition (PBS condition vs KA) in each group (control vs LRRK2 neural networks), where the percentage of live cells found in each image was used for statistical analysis. To investigate whether there was a difference in cell viability between the KA-receiving and non-KA receiving chambers of the same neural networks, and between the different conditions in each group, a repeated measures two-way ANOVA was used. No statistically significant differences were

found between chambers, indicating that the viability of the cells was not altered by the KA stimulation (p=0.3063). A statistically significant difference was found between the groups however ($F_{3,12}$=25.3,7 p<0.0001). A post hoc Tukey's multiple comparisons test found no significant difference between the KA stimulated and PBS condition within the same group (n_1=n_2=12 for both control and LRRK2 neural networks, with p=0.9996 and p=0.1921, respectively), confirming that the level of KA stimulation was sublethal. Interestingly, a significant difference was found for the PBS condition between the different neural populations (p=0.0004, DF=18.17), where a consistently higher percentage of viable cells was found in the LRRK2 neural networks compared to the control neural networks (**Fig.2H)**.

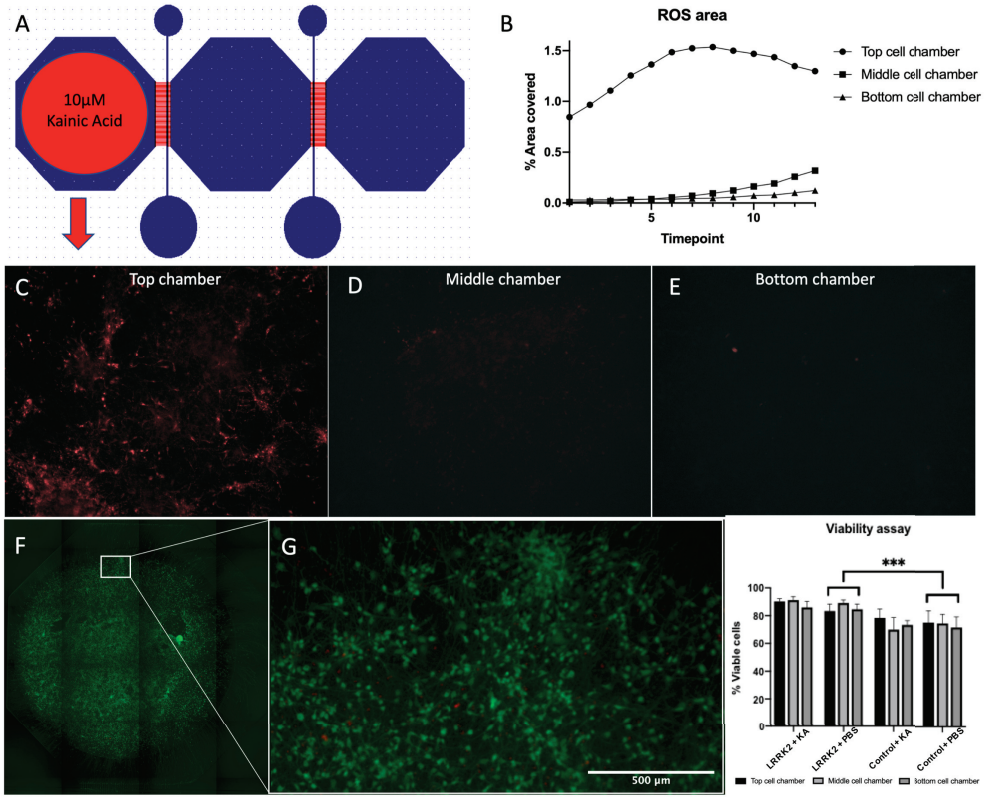

Fig.2 Confined sublethal kainic acid (KA) stimulation of neural networks in microfluidics chips. **A**) Microfluidic chip design, with a red circle indicating the top cell chamber used for confined KA stimulation (10µM). **B**) Line-graph where the reactive oxygen species (ROS) production of a structured neural network following a targeted KA stimulation has been analysed, with a clear difference between the ROS production in the top cell chamber compared to the two other chambers. Images (10X) were taken from each of the cell chambers every 5 minutes over the course of one hour following a KA stimulation. **C, D** and **E**) Representative images of fluorescently labelled ROS from each of the cell chambers, 45 minutes after the targeted KA stimulation. **F)** Tiled image of the middle cell chamber of a structured neural network fluorescently labelled with Calcein-Am (green) and Ethidium homodimer-1 (red) 24 hours post KA. **G**) Close-up of the area selectively chosen for analysis. **H**) Bar-graph showing the percentage of viable cells counted in each chamber, for each condition with standard deviation bars. A statistically significant difference was found between the control and the LRRK2 groups in the PBS condition (p=0.0004, N1=N2=12, DF=18.17) by post hoc Tukey's multiple comparisons test, where N= the number of images counted. No significant difference was found between the KA and control condition within the same group, nor between the different chambers, demonstrating that the KA stimulation was sublethal as intended.

Mitochondrial distribution in the axonal tunnels and synaptic compartments

Active mitochondria were successfully labelled with TMRM and could be visualized live in the structured neural networks using a Zeiss 510 META live confocal scanning microscope with a heated incubator. Single z-stacks containing all of the TMRM labelled mitochondria enclosed within a representative segment of the synaptic compartment were obtained at baseline for both the LRRK2 (n=6) and control (n=6) neural networks. Volumetric figures were produced for visualization of these data, and can be seen in **Fig.3A,B**. Height measures calculated from the z-stacks showed a statistically significant difference between the control and LRRK2 neural networks (two-tailed, independent samples t-test, t_{10}=7.96, p<0.0001), with the LRRK2 neural networks containing mitochondria spanning on average over 3 times the height of the control neural networks ($mean_{KA}$=35.38μm vs $mean_{healthy}$=10.83μm) (**Fig.3A-E**). As the axonal tunnels restrict the movement of the mitochondria in the z-plane to a much greater extent than the synaptic compartment, they were chosen as the area for further imaging. The active mitochondria contained within a 145μm long segment of four axon tunnels (63X objective) were analyzed for the 6 control neural networks and the 5 LRRK2 neural networks, both at baseline and after KA or PBS addition. A statistically significant difference was found in the number of TMRM labelled mitochondria contained within the axon tunnels (Mann-Whitney U=659.5, N_1=48, N_2=40, p= 0.0114) between the control and LRRK2 neural networks at baseline, showing that the LRRK2 networks were characterized by the presence of a greater number of active mitochondria (median=164.5 vs 136) (**Fig.3F**). To investigate whether the number of active mitochondria was influenced by the KA stimulation, Wilcoxon matched-pairs signed ranks test was applied for the baseline and after KA stimulation timepoints in each group. A significant difference was found (pairs=24, p=0.0432) for the control neural networks, with a reduced number of active mitochondria measured after the KA stimulation. Although not statistically significant (pairs=24, p=0.1578), the same trend was observed for the KA stimulated condition in the LRRK2 neural networks, with fewer active mitochondria measured at the second timepoint than at baseline (**Fig.3I**). To control for potential degradation of the TMRM labelling over the time-course of the imaging, or a reduction of active mitochondria due to temperature changes moving from the incubator to the heated imaging-stage, or due to PBS-washing following the KA stimulation, networks (receiving only PBS) from each group were also imaged at the same timepoints. No significant difference was found between the two timepoints in the PBS condition for the control neural networks (pairs= 24, p=0.214) (**Fig.3H**). For the LRRK2 neural networks, a significant difference was found for the PBS condition, however, this time there were more active mitochondria at the latter timepoint (pairs=16, p=0.029). The mitochondrial sizes were also assessed for each condition; however, no significant differences were found between the baseline measures of mitochondrial size between the control and LRRK2 neural networks, nor between the baseline and KA stimulated condition in either group (data not shown).

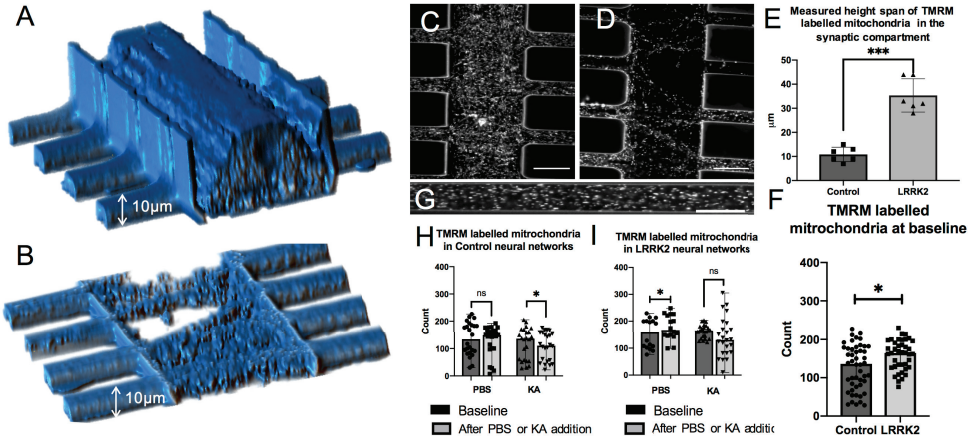

Fig.3 Mitochondrial distribution in the synaptic compartment and axon tunnels of the structured neural networks. The structured neural networks were labelled with TMRM, and the active mitochondria contained within 4 axonal tunnels were imaged live at two time points (baseline and after KA or PBS) for 3 neural networks from both groups, i.e. the control and LRRK2 neural networks. Additionally, image z-stacks were taken from the synaptic compartment at baseline for both groups to capture the height span of the active mitochondria. **A** and **B**) Volumetric view of the area containing fluorescently labelled mitochondria in the synaptic compartment from an **A**) LRRK2 neural network (height = 44µm) and a **B**) control neural network (height = 9µm). One of the z-slices from each of the stacks making up the volumetric figure in **A** and **B** are shown in **C** and **D**, respectively. Some autofluorescence in the PDMS walls of the microfluidic chips outline the structure of the synaptic compartment and axon tunnels (30µm scale bars). **E**) shows a bar-graph with scatter plots of the mean height in the synaptic compartment measured to contain fluorescently labelled mitochondria in each group, with standard deviation bars. An independent samples t-test showed that the LRRK2 neural networks contained active mitochondria within 3 times the height span of the control neural networks ($p<0.0001$, $N=6$) where N equals the number of networks investigated in each group. **G**) shows fluorescently labelled mitochondria contained within a single axonal tunnel in a control neural network, at baseline (20µm scale bar). **F**) Bar-graph with the median number of mitochondria counted within single axonal tunnels at baseline for both control and LRRK2 neural networks, with range bars and scatter plots. The LRRK2 neural networks displayed significantly more TMRM labelled mitochondria contained within the axonal tunnels compared to the control neural networks at baseline ($p=0.0114$, $U=659.5$, $N_1=48$, $N_2=40$) by Mann-Whitney U test. **H** and **I**) Bar-graphs with the median number of mitochondria measured at each timepoint, with range bars and scatter plots, for both the PBS and KA stimulated condition, within both groups. **H**) The control neural networks were found by Wilcoxon matched-pairs signed rank test to have significantly fewer active mitochondria after KA stimulation compared to the baseline ($p=0.0432$, pairs=24), while the LRRK2 neural networks **I**) showed the same trend without it being statistically significant. A statistically significant difference was found between the two timepoints in the PBS condition of the LRRK2 neural networks however ($p=0.029$, pairs=16), with more active mitochondria being measured after PBS addition.

Furthermore, to get an indication of whether the significant difference in number of TMRM labelled mitochondria observed at baseline between the control and LRRK2 neural networks (**Fig.3F**) was due to a greater mitochondrial content within each neurite in the LRRK2 neural networks compared to the control neural networks, a supplementary investigation of fluorescently labelled mitochondria was conducted in fixed samples from both groups. No statistically significant difference was found between the groups ($p=0.4293$, $N_{LRRK2}=8$, $N_{control}=10$) by independent samples t-test in this measure, indicating that the baseline difference

in TMRM labelled mitochondria might be due to a larger number of neurites containing TMRM labelled mitochondria being visible, rather than a greater number of mitochondria being contained within each neurite, in the LRRK2 networks (**Supplementary Fig.S1**).

Neurite morphology and internodal synaptic contacts

High-magnification microscopy images of the control neural networks fluorescently labelled with the anti-Piccolo antibody were used for morphological investigations of the neurites in the synaptic compartment, as well as for quantification of synaptic contacts through co-occurrence with the fluorescently labelled anti-PSD95 antibody, 24hours post KA stimulation (or PBS) (**Fig.4A-D**). Based on semi-automated image processing (see method section), a ratio of neuritic boutons/neurite was used to assess the morphology of the neurites, where a statistically significant difference was found between the PBS condition and the KA stimulated condition in the control neural networks (Mann-Whitney $U=73$, $n_1=22$, $n_2=18$, $p=0.0004$), with substantially fewer boutons observed after KA stimulation ($median_{PBS}=10.24$ vs $median_{KA}= 6.32$). Furthermore, image analysis quantifying the number and size of co-occurring Piccolo and PSD95 labelling revealed a significant difference in size (μm) between the PBS and KA stimulated condition in the control neural networks (Mann-Whitney $U=153.5$, $n_1=26$, $n_2=24$, $p=0.0017$), with larger synaptic contact areas in the KA stimulated condition ($median_{PBS}=0.1915$ vs $median_{KA}= 1.651$), but no significant difference in number of contacts ($median_{PBS}=314.5$ vs $median_{KA}=493.5$, $p=0.2504$) (**Fig.4C, D**). Due to the high density of neurites contained within the synaptic compartment of the LRRK2 neural networks, z-stacks were taken to capture morphology of the neurites and the co-occurring Piccolo and PSD95 labelling (**Fig.S2** and **S3**). The bottommost image slice from each stack was used for quantification of synaptic contacts through co-occurring Piccolo and PSD95 labelling (**Fig.4E,F**), while investigating the morphology of single neurites proved not feasible due to the overall compactness and density of the neurites in this group (**Fig.4G**, **Fig.S2**). No statistically significant differences were found in size ($median_{PBS}= 0.1190$μm vs $median_{KA}= 0.1060$μm) or number ($median_{PBS}=832$ vs $median_{KA}=677$) between the PBS and KA stimulated condition in the LRRK2 neural networks in co-occuring Piccolo and PSD95 (Mann-Whitney U test).

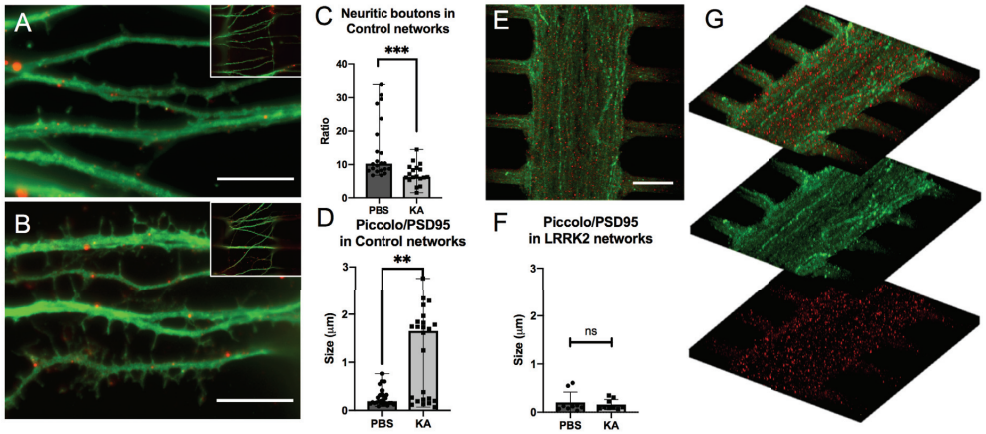

Fig.4 Neurite morphology and internodal synaptic contacts in the structured neural networks. Images were taken from the synaptic compartment area and show cortical neural networks fluorescently immunolabelled with Piccolo (green) and PSD95 (red). **A** and **B** Representative images from the two conditions (KA and PBS) in the control neural networks, where **A**) shows immunolabelling in the synaptic compartment of a KA stimulated neural network and **B**) from the synaptic compartment of a PBS neural network. Both images are enlarged (with representative full-view images in the top right corner) (10µm scale bars). **E**) Similarly, representative image from the KA stimulated condition in an LRRK2 neural network (20µm scale bar), illustrating the lower level of morphological detail available due to the density of neurites contained within the synaptic compartment. **C**) Bar-graph with the median ratio of neuritic boutons contained within the synaptic compartment for each condition in the control neural networks, with range bars. A statistically significant reduction of neuritic boutons was found in the KA stimulated condition (Mann-Whitney $U=73$, $n_1=22$, $n_2=18$, $p=0.0004$) compared to the PBS condition, where n equals the number of images analysed. **D** and **F**) Bar-graphs with the median size of the synaptic contacts (Piccolo/PSD95 co-occurrence) with range bars, measured within the synaptic compartment for both the control and LRRK2 neural networks, respectively. For the control neural networks, a statistically significant difference was found in the synaptic size measurements between the conditions (Mann-Whitney $U=153.5$, $n_1=26$, $n_2=24$, $p=0.0017$), with much larger areas of co-occurrence between Piccolo and PSD95 found at the neurites of the KA stimulated condition compared to the PBS condition. For the LRRK2 neural networks, no significant difference was found between the conditions in synaptic contact size. Furthermore, to illustrate the difference in neuritic density **G**) shows 10µm thick z-stack volume projections of the LRRK2 neural network in **E**, with Piccolo and PSD95 merged (top), followed by Piccolo (green) and PSD95 (red) alone.

Electrophysiological activity of the structured neural networks

Electrophysiological measurements of the structured neural networks at baseline revealed a consistent trend in network activity and functional connectivity across all networks, both for control and LRRK2 neural networks, reflecting reproducible structure-function traits imposed on the networks through the physical structuring of the microfluidic chip. Higher mean firing rates (MFR) were consistently found at the top and bottom cell chambers relative to the middle cell chamber, and within-chamber (intra-nodal) correlations (Pearson's correlation) were found to be consistently higher than between-chamber correlations, for both the LRRK2 and control neural networks **(Fig.S4).** Interestingly, the average MFR of the LRRK2 neural networks was far greater than that of the control neural networks at baseline (4.5 spikes/sec vs 2 spikes/sec) (**Fig.S4, Fig.5A**), while at the same time, the total network correlation was lower for the LRRK2 neural networks ($r=0.085$) than that of the control neural networks ($r=0.12$). Furthermore, average MFR and total network correlation measures from the PBS condition for both the LRRK2 and control neural networks (where some media was moved to create a flow barrier

during the stimulation timepoint) follow each other quite closely (**Fig.5B, D**), with a comparable 33-39% drop in average MFR and a 43-44% increase in total network correlation at the 24 hours post-stimulation timepoint, relative to the baseline measures. The neural networks receiving KA produced differential responses however.

The KA addition successfully produced a transient overexcitation. The activity measured at a randomly chosen electrode (number 63) in the top chamber of an LRRK2 neural network during KA stimulation has been used to illustrate this in **Fig.5C** and **Fig.S4**., in which a transient period of substantially increased firing rate (i.e. from 2Hz to 14Hz) followed by an abrupt activity drop can be seen. Overall however, the average MFR during the entirety of the stimulation timepoint was reduced relative to the baseline, for both the LRRK2 and control neural networks (**Fig.5A**). The relative MFR calculated from the baseline measures showed that the LRRK2 neural networks had a greater percentage drop in MFR during KA stimulation (38%) compared to the control neural networks (11%) (**Fig.5B**). At the same time, the LRRK2 neural networks exhibited a minor relative increase in total network correlation (3%) while the control neural networks displayed a relative reduction (64%) in total network correlation during the KA stimulation (**Fig.5D**). Although the overexcitation as demonstrated in **Fig.5C** was not observed in the PBS condition, the MFR and correlation measures from the networks in this condition also display large variations from the baseline during the stimulation timepoint, indicating that the simple procedure of creating a flow barrier alters the network activity.

24 hours later however, the neural networks in the PBS condition from both groups follow each other quite closely with comparable drops in MFRs and increases in total network correlations, as noted. The neural networks in the KA stimulated condition from both groups also display very similar, but reduced correlations at this timepoint, with the LRRK2 neural networks exhibiting a total network correlation of 85% and the control networks 83% relative to their baselines (**Fig.5D**). Interestingly, the KA stimulated networks differed widely in their relative MFR at this timepoint, where the LRRK2 neural networks exhibited a 57% drop, and the control neural networks exhibited a drastic 83% drop in MFR, relative to their baselines (**Fig.5B**). A representative KA stimulated LRRK2 neural network is used to visualize the overall network trend with correlation scheme balls from each of the timepoints in **Fig.5E-D**.

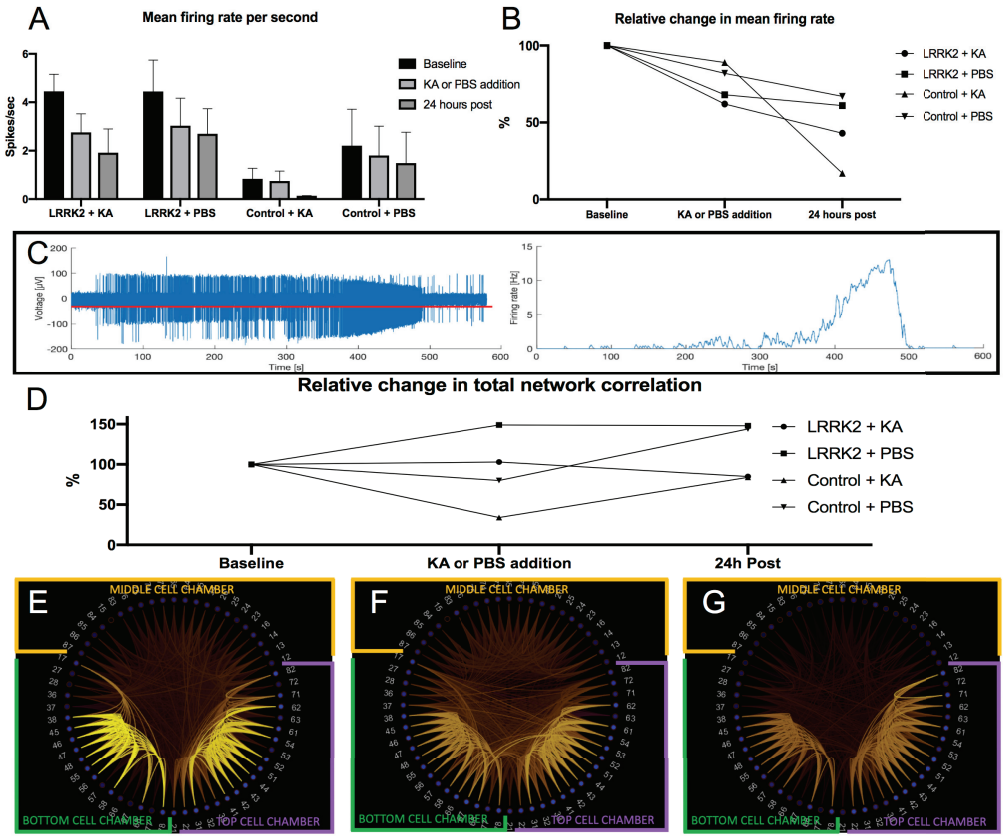

Fig.5 Electrophysiological measurements of the structured neural networks during baseline, KA stimulation, and 24 hours post stimulation. A) Bar graph of mean MFR with standard deviations measured for each group at the three different experimental timepoints (baseline, stimulation, 24hours post), with each group consisting of measurements from 3 different networks in each condition (PBS and KA) from both the control and LRRK2 group. The average MFR of the LRRK2 neural networks are consistently higher at all timepoints compared to the control neural networks, particularly at baseline. **B**) The same data as in **A**) but plotted as a line graph displaying the variation of the measures from the baseline condition. 24 hours post KA stimulation both the LRRK2 and control neural networks display a drop in MFR, however, the difference from the baseline is much larger for the control networks. **C**) Network overexcitation induced by the KA stimulation. The graph on the left shows the activity measured at a single electrode located in the top cell chamber of an LRRK2 neural network during the KA stimulation, with the red line indicating the threshold set for spike detection. The firing rate (Hz) profile of a single neuron recorded by the same electrode is plotted on the right (see Suppl.fig.4 for spike sorting details), where a drastic increase in firing can be observed from 350-500 seconds into the recording, followed by an abrupt activity drop. **D**) Line graph of the relative total network correlation change measured for each group at the three experimental timepoints in relation to the baseline values. At the 24 hours post KA or PBS addition timepoint, a similar increase in total network correlation change can be observed for the PBS condition of both the LRRK2 and control neural networks (+44-48%) relative to the baseline, while the KA stimulated networks display a similar decrease in total network correlation (-25-27%). **E-G**) Schemaball correlation maps of a representative LRRK2 neural network during the baseline, KA stimulation, and 24 hours post, respectively. Colour intensity of the lines interconnecting each channel indicates the correlation between their activity (from r 0-1), with 0 being black and 1 being bright yellow.

4. Discussion

Baseline network activity measurements

One of the most striking findings in this report is the major difference in neuritic density observed at baseline between the neural networks carrying the G2019S LRRK2 mutation and the control neural networks (**Fig.3** and **5, Fig.S2, S3**). Several other studies have reported the involvement of the LRRK2 gene in neurite process morphology (West et al., 2005, Smith et al., 2005, MacLeod et al., 2006, Smith et al., 2006, Plowey et al., 2008, Dachsel et al., 2010, Gillardon, 2009, Meixner et al., 2011, Cherra et al., 2013, Habig et al., 2013, Sepulveda et al., 2013), where the specific G2019S PD-associated LRRK2 mutation has been found by most to increase kinase activity, resulting in a progressive reduction in neuritic length and branching (West et al., 2005, Smith et al., 2006, MacLeod et al., 2006, Plowey et al., 2008, Nguyen et al., 2011, Chan et al., 2011, Winner et al., 2011, Sanchez-Danes et al., 2012, Cherra et al., 2013, Reinhardt et al., 2013, Qing et al., 2017, Dagda et al., 2014, Greggio et al., 2006), with one exception demonstrating non-impaired neuritic morphology (Dachsel et al., 2010). Furthermore, knockdown and knock-out models resulting in LRRK2 deficiencies present with a progressive increase in neuritic length in some studies (MacLeod et al., 2006, Dachsel et al., 2010, Winner et al., 2011, Habig et al., 2013, Sepulveda et al., 2013), while others find the opposite (Gillardon, 2009, Meixner et al., 2011).

Interestingly, we provide the first evidence of increased neuritic density in human neurons with the G2019S mutation. This was demonstrated with immunocytochemistry of the neurites in the synaptic compartment (**Fig.4** and **Fig.S2**) and was further corroborated through several approaches using brightfield microscopy, Calcein-AM labelled cells (**Fig.S3**) and fluorescently labelled mitochondria (**Fig.3,S1**), all of which indicated a striking increase in neuritic density in LRRK2 neurons relative to the control neural networks. One of the studies mentioned above found the growth substrate to significantly influence the motility and outgrowth of neurites in culture (Sepulveda et al., 2013), with “fast-growth” coating substrates like laminin masking the effect of the mutation, and “slow-growth” substrates like poly-L-lysine enhancing them, something which might explain some of the variation between studies reported in the literature. Furthermore, structuring the neural networks with microfluidic chips in itself might enhance or reduce such traits (Dowell-Mesfin et al., 2004, Micholt et al., 2013). Thus, in our study, the combination of PLO and laminin as a growth substrate, together with structuring the neural networks in the microfluidic chip are likely to have influenced the resulting neuritic profile and may also partially explain some of the difference in relation to other studies. These factors do not explain the difference between our two groups, however, as the neural networks from both the LRRK2 and control group were treated in the exact same way, using identical protocols for coating, surface substrates, microfluidic chip structuring, cell differentiation and maturation, thus excluding differential culturing and handling as a potential source of variation between these populations. Furthermore, as the neural networks in the control and LRRK2 are derived from the same iPSC source, differences stemming from cell-line variability can also be excluded. Other possible influencing factors could be related to the source material, where most other studies use neural networks derived from rodents, and in some cases more region-specific cells related to the neurodegenerative pattern of PD, such as midbrain dopaminergic neurons, all of which might lead to variation in the results (West et al., 2005, Smith et al., 2006, MacLeod et al., 2006, Plowey et al., 2008, Nguyen et al., 2011, Chan et al., 2011, Winner et al., 2011, Sanchez-Danes et al., 2012, Cherra et al., 2013, Reinhardt et al., 2013, Qing et al., 2017, Dagda et al., 2014). Nevertheless, these apparent differences suggest that there are indeed subtleties in

the mechanism underlying neuritic outgrowth and profile relating to the G2019S mutation that remain to be established.

As expected from the striking difference observed in neuritic profile between the networks, a significant difference in the average number of active mitochondria contained within the axonal tunnels in favor of the LRRK2 neural networks was also found (**Fig.3F**). Further investigation of fluorescently labelled mitochondria in fixed samples from each group revealed no significant difference in mitochondrial content within the cells of control versus LRRK2 neural networks (**Fig.S1**), suggesting that the observed difference in active TMRM labelled mitochondria is due to the larger volume of neurites being visible, rather than a larger number of active mitochondria within each neurite. Moreover, no significant difference in mitochondrial size was found at baseline between the two groups.

A greater volume of neurites should in theory provide greater opportunity for synapses to form and facilitate more efficient signal transduction, thus enabling greater structural connectivity. However, the LRRK2 neural networks displayed a lower total network correlation (r=0.085) at baseline compared to the control neural networks (r=0.12) (a difference which was reproduced in a second trial). Another fascinating observation is the major difference in baseline average MFR, where the LRRK2 neural networks consistently displayed about twice the MFR of the healthy neural networks (**Fig.5, Fig.S4**). In line with our observations, other recent studies have found the LRRK2-G2019S mutation to cause an increase in neural activity (Sweet et al., 2015, Volta et al., 2017, Matikainen-Ankney et al., 2016). Interestingly, one study has implicated increased neural activity as a pathogenic change preceding dendritic alteration in cortical neurons carrying this mutation (Plowey et al., 2014). Furthermore, G2019S-related hyperactivity has been shown (in vivo) to appear at an early point during development, which is proposed to affect the structure and function of the resulting striatal and other developing neural circuits, likely contributing to the progression of PD (Benson et al., 2018). Together this suggests a strong timescale-dependence of both the neural activity- and neuritic profile resulting from this mutation, where a difference in experimental timeframe might underlie some of the variation observed between studies of these features.

Taken together, our baseline measures show that the LRRK2 neural networks have an increase in neurites and in neural activity (MFR), which in turn is less well correlated across electrodes, relative to what is observed in the control neural networks. The elevated MFR and simultaneous low correlation represent *in vitro* neural network traits that are generally more prominent at very early time points, potentially pointing towards an overall impairment in LRRK2 neural network development. This notion of impaired development may be supported by another observation, i.e. that of differential growth cone profile at very early stages of LRRK2 neurons in culture compared to controls (**Fig.S6**). This may in turn explain what is observed as aberrant (and resultingly inefficient) network wiring in the microfluidic chips, where in the LRRK2 networks, large numbers of neurites can be seen crossing perpendicular to the axonal tunnels in the synaptic compartment (**Fig.4EG**, **Fig.S2, S3**). Furthermore, within the synaptic compartment, LRRK2 neurites show random outgrowth (**Fig.S3J**), compared to the directional, fasciculated outgrowth observed in the control networks (**Fig.S3E).** Taken together, these observations strongly suggest impaired axonal growth and guidance in the LRRK2 neurons. Another study also lends merit to this theory by finding altered neural growth cone morphology and number after knocking down LRRK2 (Habig et al., 2013). Furthermore, the altered neuritic profile might affect neurotransmission efficacy, resulting in less efficient signal propagation within the network, which may partially explain the observed increase in neural activity (assessed as MFR).

Unveiling different network stress responses through transient overexcitation

The two hit-theory of PD postulates that a combination of both genetic susceptibility and environmental factors contribute to the onset and development of the disease. Based on this and the variability in disease progression in patients with LRRK2 associated PD, it is reasonable to assume that some phenotypic expression of the mutation may become apparent only following a significant or stressful challenge (Benson et al., 2018). Contrary to what one might expect, the neural networks carrying the G2019S LRRK2 mutation did not demonstrate a greater overall response to the transient overexcitation event compared to control neural networks. In fact, our one-off, sublethal, overexcitation event resulted in larger responses from the control neural networks in almost all measures, displaying a greater reduction in active mitochondria contained within the axonal tunnels immediately after the stimulation, as well as a more marked relative decrease in MFR, a more prominent alteration in neurite morphology, and greater synaptic remodeling 24 hours post stimulation, relative to the LRRK2 neural networks.

The highly significant difference found in neurite morphology in the control neural networks 24 hours post KA stimulation (**Fig.4A-C**) suggests neuritic remodeling in response to the transient excitatory stimulation event, with a retraction/reduction of boutons observed in the synaptic chambers in response to the KA overexcitation. At the same time, the number of synapses (co-occurrence of Piccolo and PSD95) in the control neural networks was unaltered, but the size of their overlapping area was significantly different, with much larger synaptic areas measured 24 hours after overexcitation (**Fig.4D**). This rapid, activity dependent alteration in spine morphology is likely an expression of a regular mechanism for converting short-term synaptic activity to long term lasting changes in connectivity and function. In line with our baseline measurements, the size range of the postsynaptic density is usually within 0.2-0.5μm, and can be localized to both spiny and non-spiny structures. Furthermore, this area contains both the kainate and AMPA receptors (Sheng, 2001), i.e. glutamatergic receptors targeted by our stimulation. During synaptic plasticity, the PSD increases in size in response to potentiation events, and the glutamate receptors contained within can be modulated by neural activity on a timescale from minutes to weeks (Sheng, 2001). In contrast to the observed neuritic alteration in the control neural networks, no significant alteration in synaptic number or size was found in the synaptic compartment of the LRRK2 mutated neural networks 24 hours after overexcitation, suggesting impaired synaptic plasticity. Some *in vivo* studies have implicated LRRK2 in the development, maturation and function of synapses, where the G2019S mutation has been shown to result in impaired long-term depression (Benson et al., 2018, Sweet et al., 2015). However, since our study investigates immediate and intermediate reactions (focused within the first 24 hours) to a single KA stimulation, no conclusions can be drawn about longer-term processes.

Furthermore, other studies have found increased vulnerability to oxidative stress, higher levels of mtDNA damage, and impaired mitochondrial movement as a result of the G2019S mutation, indicating compromised mitochondrial function (Cooper et al., 2012, Sanders et al., 2014, Hsieh et al., 2016, Schwab et al., 2017, Bose and Beal, 2019). Mitochondrial function alterations have in turn been shown to affect the plasticity of synapses and morphology of neurites as the availability of mitochondria is both essential and limiting for the support and maintenance of these structures (Li et al., 2004). In our study, both the control and the LRRK2 neural networks showed a reduction in the number of active mitochondria contained within the axon tunnels closest to the stimulated chamber immediately following the KA stimulation, however, only the change in the control networks was statistically significant. The energy status of the neuron greatly affects the motility and distribution of mitochondria (Saxton and

Hollenbeck, 2012), and a retraction of the mitochondria towards the soma during or following an overexcitation event is to be expected as this corresponds to the location of greatest metabolic demand at the time. Loss of membrane potential in some of the mitochondria could also explain our results, as the TMRM labelling fades when this potential is disrupted. However, loss of mitochondrial membrane potential is the second observable step in classic excitotoxicity, preceded by ROS production, and followed by an opening of the permeability transition pore and induction of programmed cell death. Although our KA stimulation elicited a ROS response (as demonstrated in **Fig.2**), it did not result in any observable difference in cell viability 24 hours later, demonstrating a sublethal overexcitation as intended, effectively excluding classic excitotoxicity as the initiated process. A retraction of mitochondria towards the seat of greatest metabolic demand thus seems the most likely scenario. The statistically non-significant reduction in mitochondria observed in the LRRK2 neural networks following the overexcitation thus suggests an alteration in mitochondrial transport and/or function as a result of the G2019S mutation. The LRRK2 protein has been found to localize, among other sites, to mitochondrial structures where it interacts with a number of key regulators of mitochondrial fission/fusion, as well as to mitochondrial autophagy and motility (Biskup et al., 2006, Wang et al., 2012, Rosenbusch and Kortholt, 2016). Several other studies have found prominent signs of mitochondrial dysfunction relating both to size and distribution as a result of the G2019S mutation (MacLeod et al., 2006, Mortiboys et al., 2010, Li et al., 2014, Esteves et al., 2014, Yue et al., 2015, Singh et al., 2019), which strongly implies a role for LRRK2 in mitochondrial homeostasis. The initiating process leading to these mitochondrial alterations, however, are still elusive. Some possible factors are reduced mitochondrial biogenesis, impaired cytoskeletal elements and consequently cytoskeletal trafficking, direct functional and structural damage to the mitochondria by LRRK2 localized to the organelle, or impairment in the autophagic-lysosomal machinery resulting in accumulating damaged mitochondria (Yue et al., 2015, Tagliaferro and Burke, 2016, Franco-Iborra et al., 2018, Verma et al., 2018, Verma et al., 2017, Singh et al., 2019).

Intriguingly, 24 hours after the overexcitation, both the LRRK2 and the control neural networks displayed very well aligned decreases in relative total network correlations. This decrease becomes even more apparent when compared to the neural networks in the PBS condition from both groups, which drastically increased their correlations relative to the baseline at this point. This increase in PBS condition network correlations suggests that the neural networks were still maturing at the point of intervention, and that their natural trajectory was one towards greater correlation. The observed decrease in total network correlations is perhaps to be expected following such a stimulation as the overexcitation indiscriminately excites related connections that are both functional and non-functional, as well as produces both long-term potentiation and long-term depression of synapses based on coincidental activity at each connection. However, it is worth reiterating that these results were obtained after the neural networks were subjected to a single overexcitation event, while prolonged and/or repeated overexcitations would likely produce different results. The latter approach was beyond the scope of our current study. Nonetheless, both the LRRK2 and control neural networks also displayed a great drop in average MFR 24 hours after the overexcitation, where the relative drop was far greater for the control neural networks. Although much less prominent, the neural networks in the PBS condition also exhibited a drop in average MFR at this point, demonstrating that a media change alone may have created a fluctuation of this measure within our chosen timeframe. Still, the difference in relative MFR in the KA stimulated condition demonstrates yet another impaired response in the LRRK2 neural networks comparted to the control neural networks.

In summary, in this study we provide the first evidence of increased neuritic density in structured, human neural networks carrying the G2019S LRRK2 mutation compared to control neural networks. At the same time, other network traits reported in the literature to result from this mutation are corroborated by our study, with the LRRK2 mutated neural networks displaying an increase in baseline neural activity (MFR) compared to the healthy control neural networks. Furthermore, eliciting a transient, confined, overexcitation through KA stimulation revealed different responses between the LRRK2 and control neural networks, both immediately after stimulation and 24 hours later. The control neural networks demonstrated a greater reduction in active mitochondria within the neurites immediately after the stimulation, as well a greater reduction in relative network activity (MFR), greater neuritic remodelling, and synaptic alterations, 24 hours later, compared to the LRRK2 neural networks.

It is thus clear that early signs of pathology relating to the G2019S LRRK2 mutation are captured within our chosen timeframe and reflected through both micro- and mesoscale investigations. Through a combination of neuroengineering, microfluidics, electrophysiology and fluorescence imaging strategies, we were able to selectively induce perturbations within interconnected network nodes and unveil these distinctions in a highly reproducible manner. Furthermore, as our neural networks were engineered from human cells with a homozygous Crispr-Cas9 inserted G2019S mutation, containing no artificially inserted gene or forced high or low levels of LRRK2, our *in vitro* setup builds on conditions genetically and physiologically more relevant to PD than networks engineered from model animal organisms. Moreover, as individuals homozygously carrying the G2019S mutation do not have more aggressive phenotypes compared to heterozygous carriers, there does not seem to be a dose-dependent increase in severity, and the results between studies of these two variants should be largely comparable (Ishihara et al., 2006, Lewis, 2019). Expanding the current platform to investigate these traits in even more detail and at greater length thus seems a logical next step. Several other mechanisms, which were out of the scope of this study, are of interest and might be involved in G2019S LRRK2 pathology, such as mitochondrial motility (Saxton and Hollenbeck, 2012, Singh et al., 2019), calcium overload and excitatory mitochondrial excitotoxicity (Verma et al., 2018, Verma et al., 2017), impaired synaptic endocytosis (Matta et al., 2012, Verstreken, 2017), alterations in the autophagosomal-lysosomal machinery (Sheehan and Yue, 2018, Verma et al., 2018, Pan et al., 2018, Singh et al., 2019), compromised AMPA receptor trafficking (Sweet et al., 2015), differential PKA regulation or altered Rab activity (Benson et al., 2018). Furthermore, as some of the investigated responses might also rely on cell-type specific mechanisms (Sweet et al., 2015, Pan et al., 2017, Benson et al., 2018), conducting a similar study with selectively vulnerable dopaminergic neurons or medium spiny neurons of the striatum might bring us even closer to understanding and unveiling pathological mechanisms of PD.

Acknowledgements
This work was supported by The Department of Neuromedicine and Movement Science, Faculty of Medicine and Health Sciences, NTNU; The Liaison Committee for Education, Research and Innovation in Central Norway (Samarbeidsorganet HMN, NTNU); The Joint Research Committee between St Olav's Hospital and the Faculty of Medicine and Health Sciences, NTNU; and the Research Council of Norway, Norwegian Micro- and Nano-Fabrication Facility, NorFab, project number 245963/F50, NTNU program for Enabling Technologies, (Nanotechnology). All imaging procedures requiring the use of the EVOS2 or the Zeiss 510 META live confocal scanning microscope were performed at the Cellular and Molecular Imaging Core Facility (CMIC), Norwegian University of Science and Technology

(NTNU). CMIC is funded by the Faculty of Medicine at NTNU and Central Norwegian Regional Health Authority.

Competing interests
The authors have no competing interests to declare

Author contributions
V.D.V. Designed the study, conducted the experiments, collected and analyzed the data, and wrote the paper; R.W. Designed the study, the microfluidic chips and MEAs, contributed in execution of the experiments and data collection, contributed to data analysis and writing of the paper; O.H.R. Designed the study, performed the electrophysiology analysis, contributed to the data collection and writing of the methods; K.H. contributed with data analysis and writing of the methods; S.N provided supervision and valuable discussion in relation to the electrophysiology data analysis and techniques; A.S. Conceived and supervised the study, contributed to the study design, and critically reviewed the paper; I.S. Conceived and supervised the study, contributed to the study design, edited, and critically reviewed the paper.

Data accessibility
All electrophysiology datasets have been deposited onto Mendeley and can be accessed through the following links:
doi: 10.17632/dnjv26msvk.4
doi: 10.17632/92568tpp39.4

Abbreviations

CamKII	calmodulin-dependent protein kinase II
iPSC	induced pluripotent stem cell
KA	kainic acid
LRRK2	leucine-rich repeat kinase 2
MEA	microelectrode array
MFR	mean firing rate
NGS	normal goat serum
NSC	neural stem cell
PBS	phosphate buffered saline
PCA	principal component analysis
PD	Parkinson´s disease
PDMS	polydimethylsiloxane
PFA	paraformaldehyde
PLO	poly-L-ornithine
PSD	post-synaptic density
ROS	reactive oxygen species
RT	room temperature
TMRM	tetramethylrhodiamine

STAR Method

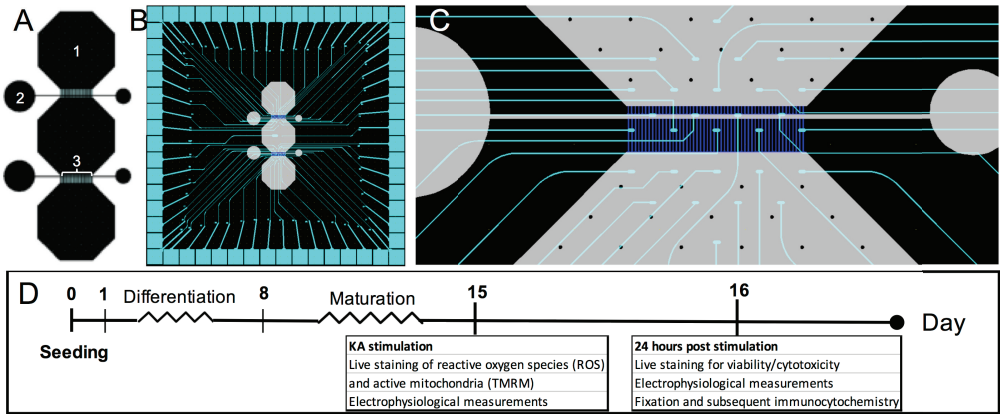

Fig.6 Experiment layout. A) Microfluidic chip design, with (1) indicating the top cell chamber/node, (2) the inlet/outlet connected via the synaptic compartment, and (3) the axonal/dendritic tunnels. Directionality of the inter-nodal connectivity is imposed on the network through different tunnel lengths, where mainly the axons from the top and bottom cell chambers connect to the dendrites and axons from the middle cell chamber in the two synaptic compartments. **B**) Outline of microfluidic chip interfaced with the custom made multielectrode array for electrophysiological investigation. **C**) Electrode layout in the area connecting the bottom and middle cell chamber through axonal/dendritic tunnels and the synaptic compartment. **D**) Timeline of the experiment, indicating the time points and assays used to assess the LRRK2 and control neural networks.

References

BALOYANNIS, S. J. 2006. Mitochondrial alterations in Alzheimer's disease. *J Alzheimers Dis,* 9**,** 119-26.

BENSON, D. L., MATIKAINEN-ANKNEY, B. A., HUSSEIN, A. & HUNTLEY, G. W. 2018. Functional and behavioral consequences of Parkinson's disease-associated LRRK2-G2019S mutation. *Biochem Soc Trans,* 46**,** 1697-1705.

BISKUP, S., MOORE, D. J., CELSI, F., HIGASHI, S., WEST, A. B., ANDRABI, S. A., KURKINEN, K., YU, S. W., SAVITT, J. M., WALDVOGEL, H. J., FAULL, R. L., EMSON, P. C., TORP, R., OTTERSEN, O. P., DAWSON, T. M. & DAWSON, V. L. 2006. Localization of LRRK2 to membranous and vesicular structures in mammalian brain. *Ann Neurol,* 60**,** 557-69.

BOSE, A. & BEAL, M. F. 2016. Mitochondrial dysfunction in Parkinson's disease. *J Neurochem,* 139 Suppl 1**,** 216-231.

BOSE, A. & BEAL, M. F. 2019. Mitochondrial dysfunction and oxidative stress in induced pluripotent stem cell models of Parkinson's disease. *Eur J Neurosci,* 49**,** 525-532.

BOUHOUCHE, A., TIBAR, H., BEN EL HAJ, R., EL BAYAD, K., RAZINE, R., TAZROUT, S., SKALLI, A., BOUSLAM, N., ELOUARDI, L., BENOMAR, A., YAHYAOUI, M. & REGRAGUI, W. 2017. LRRK2 G2019S Mutation: Prevalence and Clinical Features in Moroccans with Parkinson's Disease. *Parkinsons Dis,* 2017**,** 2412486.

BRIZZEE, K. R. 1987. Neurons numbers and dendritic extent in normal aging and Alzheimer's disease. *Neurobiol Aging,* 8**,** 579-80.

CAUDLE, W. M. & ZHANG, J. 2009. Glutamate, excitotoxicity, and programmed cell death in Parkinson disease. *Exp Neurol,* 220**,** 230-3.

CHAN, D., CITRO, A., CORDY, J. M., SHEN, G. C. & WOLOZIN, B. 2011. Rac1 protein rescues neurite retraction caused by G2019S leucine-rich repeat kinase 2 (LRRK2). *J Biol Chem,* 286**,** 16140-9.

CHENG, H. C., ULANE, C. M. & BURKE, R. E. 2010. Clinical progression in Parkinson disease and the neurobiology of axons. *Ann Neurol,* 67**,** 715-25.

CHERRA, S. J., 3RD, STEER, E., GUSDON, A. M., KISELYOV, K. & CHU, C. T. 2013. Mutant LRRK2 elicits calcium imbalance and depletion of dendritic mitochondria in neurons. *Am J Pathol,* 182**,** 474-84.

COOPER, O., SEO, H., ANDRABI, S., GUARDIA-LAGUARTA, C., GRAZIOTTO, J., SUNDBERG, M., MCLEAN, J. R., CARRILLO-REID, L., XIE, Z., OSBORN, T., HARGUS, G., DELEIDI, M., LAWSON, T., BOGETOFTE, H., PEREZ-TORRES, E., CLARK, L., MOSKOWITZ, C., MAZZULLI, J., CHEN, L., VOLPICELLI-DALEY, L., ROMERO, N., JIANG, H., UITTI, R. J., HUANG, Z., OPALA, G., SCARFFE, L. A., DAWSON, V. L., KLEIN, C., FENG, J., ROSS, O. A., TROJANOWSKI, J. Q., LEE, V. M., MARDER, K., SURMEIER, D. J., WSZOLEK, Z. K., PRZEDBORSKI, S., KRAINC, D., DAWSON, T. M. & ISACSON, O. 2012. Pharmacological rescue of mitochondrial deficits in iPSC-derived neural cells from patients with familial Parkinson's disease. *Sci Transl Med,* 4**,** 141ra90.

DACHSEL, J. C., BEHROUZ, B., YUE, M., BEEVERS, J. E., MELROSE, H. L. & FARRER, M. J. 2010. A comparative study of Lrrk2 function in primary neuronal cultures. *Parkinsonism Relat Disord,* 16**,** 650-5.

DAGDA, R. K., PIEN, I., WANG, R., ZHU, J., WANG, K. Z., CALLIO, J., BANERJEE, T. D., DAGDA, R. Y. & CHU, C. T. 2014. Beyond the mitochondrion: cytosolic PINK1 remodels dendrites through protein kinase A. *J Neurochem,* 128**,** 864-77.

DOWELL-MESFIN, N. M., ABDUL-KARIM, M. A., TURNER, A. M., SCHANZ, S., CRAIGHEAD, H. G., ROYSAM, B., TURNER, J. N. & SHAIN, W. 2004. Topographically modified surfaces affect orientation and growth of hippocampal neurons. *J Neural Eng,* 1**,** 78-90.

ESTEVES, A. R., SWERDLOW, R. H. & CARDOSO, S. M. 2014. LRRK2, a puzzling protein: insights into Parkinson's disease pathogenesis. *Exp Neurol,* 261**,** 206-16.

FRANCO-IBORRA, S., VILA, M. & PERIER, C. 2018. Mitochondrial Quality Control in Neurodegenerative Diseases: Focus on Parkinson's Disease and Huntington's Disease. *Front Neurosci,* 12**,** 342.

GENC, B., JARA, J. H., LAGRIMAS, A. K., PYTEL, P., ROOS, R. P., MESULAM, M. M., GEULA, C., BIGIO, E. H. & OZDINLER, P. H. 2017. Apical dendrite degeneration, a novel cellular pathology for Betz cells in ALS. *Sci Rep,* 7**,** 41765.

GILLARDON, F. 2009. Leucine-rich repeat kinase 2 phosphorylates brain tubulin-beta isoforms and modulates microtubule stability--a point of convergence in parkinsonian neurodegeneration? *J Neurochem,* 110**,** 1514-22.

GREGGIO, E., JAIN, S., KINGSBURY, A., BANDOPADHYAY, R., LEWIS, P., KAGANOVICH, A., VAN DER BRUG, M. P., BEILINA, A., BLACKINTON, J., THOMAS, K. J., AHMAD, R., MILLER, D. W., KESAVAPANY, S., SINGLETON, A., LEES, A., HARVEY, R. J., HARVEY, K. & COOKSON, M. R. 2006. Kinase activity is required for the toxic effects of mutant LRRK2/dardarin. *Neurobiol Dis,* 23**,** 329-41.

HABIG, K., GELLHAAR, S., HEIM, B., DJURIC, V., GIESERT, F., WURST, W., WALTER, C., HENTRICH, T., RIESS, O. & BONIN, M. 2013. LRRK2 guides the actin cytoskeleton at growth cones together with ARHGEF7 and Tropomyosin 4. *Biochim Biophys Acta,* 1832**,** 2352-67.

HABIG, K., WALTER, M., POTHS, S., RIESS, O. & BONIN, M. 2008. RNA interference of LRRK2-microarray expression analysis of a Parkinson's disease key player. *Neurogenetics,* 9**,** 83-94.

HEALY, D. G., FALCHI, M., O'SULLIVAN, S. S., BONIFATI, V., DURR, A., BRESSMAN, S., BRICE, A., AASLY, J., ZABETIAN, C. P., GOLDWURM, S., FERREIRA, J. J., TOLOSA, E., KAY, D. M., KLEIN, C., WILLIAMS, D. R., MARRAS, C., LANG, A. E., WSZOLEK, Z. K., BERCIANO, J., SCHAPIRA, A. H., LYNCH, T., BHATIA, K. P., GASSER, T., LEES, A. J. & WOOD, N. W. 2008. Phenotype, genotype, and worldwide genetic penetrance of LRRK2-associated Parkinson's disease: a case-control study. *Lancet Neurol,* 7**,** 583-90.

HSIEH, C. H., SHALTOUKI, A., GONZALEZ, A. E., BETTENCOURT DA CRUZ, A., BURBULLA, L. F., ST LAWRENCE, E., SCHULE, B., KRAINC, D., PALMER, T. D. & WANG, X. 2016. Functional Impairment in Miro Degradation and Mitophagy Is a Shared Feature in Familial and Sporadic Parkinson's Disease. *Cell Stem Cell,* 19**,** 709-724.

ISHIHARA, L., WARREN, L., GIBSON, R., AMOURI, R., LESAGE, S., DURR, A., TAZIR, M., WSZOLEK, Z. K., UITTI, R. J., NICHOLS, W. C., GRIFFITH, A., HATTORI, N., LEPPERT, D., WATTS, R., ZABETIAN, C. P., FOROUD, T. M., FARRER, M. J., BRICE, A., MIDDLETON, L. & HENTATI, F. 2006. Clinical features of Parkinson disease patients with homozygous leucine-rich repeat kinase 2 G2019S mutations. *Arch Neurol,* 63**,** 1250-4.

JALEEL, M., NICHOLS, R. J., DEAK, M., CAMPBELL, D. G., GILLARDON, F., KNEBEL, A. & ALESSI, D. R. 2007. LRRK2 phosphorylates moesin at threonine-558: characterization of how Parkinson's disease mutants affect kinase activity. *Biochem J,* 405**,** 307-17.

JOANNE TRINH, MATTHEW FARRER, OWEN A ROSS & GUELLA, I. 2006. LRRK2-Related Parkinsons Disease. *In:* ADAM MP, ARDINGER HH & RA, P. (eds.). Seattle (WA): University of Washington, Seattle: GeneReviews® [Internet].

KACHERGUS, J., MATA, I. F., HULIHAN, M., TAYLOR, J. P., LINCOLN, S., AASLY, J., GIBSON, J. M., ROSS, O. A., LYNCH, T., WILEY, J., PAYAMI, H., NUTT, J., MARAGANORE, D. M., CZYZEWSKI, K., STYCZYNSKA, M., WSZOLEK, Z. K., FARRER, M. J. & TOFT, M. 2005. Identification of a novel LRRK2 mutation linked to autosomal dominant parkinsonism: evidence of a common founder across European populations. *Am J Hum Genet,* 76**,** 672-80.

LEWIS, P. A. 2019. Leucine rich repeat kinase 2: a paradigm for pleiotropy. *J Physiol,* 597**,** 3511-3521.

LI, J. Q., TAN, L. & YU, J. T. 2014. The role of the LRRK2 gene in Parkinsonism. *Mol Neurodegener,* 9**,** 47.

LI, Z., OKAMOTO, K., HAYASHI, Y. & SHENG, M. 2004. The importance of dendritic mitochondria in the morphogenesis and plasticity of spines and synapses. *Cell,* 119**,** 873-87.

MACLEOD, D., DOWMAN, J., HAMMOND, R., LEETE, T., INOUE, K. & ABELIOVICH, A. 2006. The familial Parkinsonism gene LRRK2 regulates neurite process morphology. *Neuron,* 52**,** 587-93.

MATIKAINEN-ANKNEY, B. A., KEZUNOVIC, N., MESIAS, R. E., TIAN, Y., WILLIAMS, F. M., HUNTLEY, G. W. & BENSON, D. L. 2016. Altered Development of Synapse Structure and Function in Striatum Caused by Parkinson's Disease-Linked LRRK2-G2019S Mutation. *J Neurosci,* 36**,** 7128-41.

MATTA, S., VAN KOLEN, K., DA CUNHA, R., VAN DEN BOGAART, G., MANDEMAKERS, W., MISKIEWICZ, K., DE BOCK, P. J., MORAIS, V. A., VILAIN, S., HADDAD, D., DELBROEK, L., SWERTS, J., CHAVEZ-GUTIERREZ, L., ESPOSITO, G., DANEELS, G., KARRAN, E., HOLT,

M., GEVAERT, K., MOECHARS, D. W., DE STROOPER, B. & VERSTREKEN, P. 2012. LRRK2 controls an EndoA phosphorylation cycle in synaptic endocytosis. *Neuron,* 75**,** 1008-21.

MEIXNER, A., BOLDT, K., VAN TROYS, M., ASKENAZI, M., GLOECKNER, C. J., BAUER, M., MARTO, J. A., AMPE, C., KINKL, N. & UEFFING, M. 2011. A QUICK screen for Lrrk2 interaction partners--leucine-rich repeat kinase 2 is involved in actin cytoskeleton dynamics. *Mol Cell Proteomics,* 10**,** M110.001172.

MICHOLT, L., GARTNER, A., PRODANOV, D., BRAEKEN, D., DOTTI, C. G. & BARTIC, C. 2013. Substrate topography determines neuronal polarization and growth in vitro. *PLoS One,* 8**,** e66170.

MOORE, D. J. 2008. The biology and pathobiology of LRRK2: implications for Parkinson's disease. *Parkinsonism Relat Disord,* 14 Suppl 2**,** S92-8.

MORTIBOYS, H., JOHANSEN, K. K., AASLY, J. O. & BANDMANN, O. 2010. Mitochondrial impairment in patients with Parkinson disease with the G2019S mutation in LRRK2. *Neurology,* 75**,** 2017-20.

NGUYEN, H. N., BYERS, B., CORD, B., SHCHEGLOVITOV, A., BYRNE, J., GUJAR, P., KEE, K., SCHULE, B., DOLMETSCH, R. E., LANGSTON, W., PALMER, T. D. & PERA, R. R. 2011. LRRK2 mutant iPSC-derived DA neurons demonstrate increased susceptibility to oxidative stress. *Cell Stem Cell,* 8**,** 267-80.

PAN, P. Y., LI, X., WANG, J., POWELL, J., WANG, Q., ZHANG, Y., CHEN, Z., WICINSKI, B., HOF, P., RYAN, T. A. & YUE, Z. 2017. Parkinson's Disease-Associated LRRK2 Hyperactive Kinase Mutant Disrupts Synaptic Vesicle Trafficking in Ventral Midbrain Neurons. *J Neurosci,* 37**,** 11366-11376.

PAN, P. Y., ZHU, Y., SHEN, Y. & YUE, Z. 2018. Crosstalk between presynaptic trafficking and autophagy in Parkinson's disease. *Neurobiol Dis*.

PLOWEY, E. D., CHERRA, S. J., 3RD, LIU, Y. J. & CHU, C. T. 2008. Role of autophagy in G2019S-LRRK2-associated neurite shortening in differentiated SH-SY5Y cells. *J Neurochem,* 105**,** 1048-56.

PLOWEY, E. D., JOHNSON, J. W., STEER, E., ZHU, W., EISENBERG, D. A., VALENTINO, N. M., LIU, Y. J. & CHU, C. T. 2014. Mutant LRRK2 enhances glutamatergic synapse activity and evokes excitotoxic dendrite degeneration. *Biochim Biophys Acta,* 1842**,** 1596-603.

QING, X., WALTER, J., JARAZO, J., ARIAS-FUENZALIDA, J., HILLJE, A. L. & SCHWAMBORN, J. C. 2017. CRISPR/Cas9 and piggyBac-mediated footprint-free LRRK2-G2019S knock-in reveals neuronal complexity phenotypes and alpha-Synuclein modulation in dopaminergic neurons. *Stem Cell Res,* 24**,** 44-50.

REINHARDT, P., SCHMID, B., BURBULLA, L. F., SCHONDORF, D. C., WAGNER, L., GLATZA, M., HOING, S., HARGUS, G., HECK, S. A., DHINGRA, A., WU, G., MULLER, S., BROCKMANN, K., KLUBA, T., MAISEL, M., KRUGER, R., BERG, D., TSYTSYURA, Y., THIEL, C. S., PSATHAKI, O. E., KLINGAUF, J., KUHLMANN, T., KLEWIN, M., MULLER, H., GASSER, T., SCHOLER, H. R. & STERNECKERT, J. 2013. Genetic correction of a LRRK2 mutation in human iPSCs links parkinsonian neurodegeneration to ERK-dependent changes in gene expression. *Cell Stem Cell,* 12**,** 354-67.

ROSENBUSCH, K. E. & KORTHOLT, A. 2016. Activation Mechanism of LRRK2 and Its Cellular Functions in Parkinson's Disease. *Parkinsons Dis,* 2016**,** 7351985.

SANCHEZ-DANES, A., RICHAUD-PATIN, Y., CARBALLO-CARBAJAL, I., JIMENEZ-DELGADO, S., CAIG, C., MORA, S., DI GUGLIELMO, C., EZQUERRA, M., PATEL, B., GIRALT, A., CANALS,

J. M., MEMO, M., ALBERCH, J., LOPEZ-BARNEO, J., VILA, M., CUERVO, A. M., TOLOSA, E., CONSIGLIO, A. & RAYA, A. 2012. Disease-specific phenotypes in dopamine neurons from human iPS-based models of genetic and sporadic Parkinson's disease. *EMBO Mol Med,* 4**,** 380-95.

SANDERS, L. H., LAGANIERE, J., COOPER, O., MAK, S. K., VU, B. J., HUANG, Y. A., PASCHON, D. E., VANGIPURAM, M., SUNDARARAJAN, R., URNOV, F. D., LANGSTON, J. W., GREGORY, P. D., ZHANG, H. S., GREENAMYRE, J. T., ISACSON, O. & SCHULE, B. 2014. LRRK2 mutations cause mitochondrial DNA damage in iPSC-derived neural cells from Parkinson's disease patients: reversal by gene correction. *Neurobiol Dis,* 62**,** 381-6.

SASAKI, S. & IWATA, M. 2007. Mitochondrial alterations in the spinal cord of patients with sporadic amyotrophic lateral sclerosis. *J Neuropathol Exp Neurol,* 66**,** 10-6.

SAXTON, W. M. & HOLLENBECK, P. J. 2012. The axonal transport of mitochondria. *J Cell Sci,* 125**,** 2095-104.

SCHWAB, A. J., SISON, S. L., MEADE, M. R., BRONIOWSKA, K. A., CORBETT, J. A. & EBERT, A. D. 2017. Decreased Sirtuin Deacetylase Activity in LRRK2 G2019S iPSC-Derived Dopaminergic Neurons. *Stem Cell Reports,* 9**,** 1839-1852.

SEPULVEDA, B., MESIAS, R., LI, X., YUE, Z. & BENSON, D. L. 2013. Short- and long-term effects of LRRK2 on axon and dendrite growth. *PLoS One,* 8**,** e61986.

SHEEHAN, P. & YUE, Z. 2018. Deregulation of autophagy and vesicle trafficking in Parkinson's disease. *Neurosci Lett*.

SHENG, M. H.-T. 2001. The postsynaptic specialization *In:* COWAN, W. M., SÜDHOF, T. C. & STEVENS, C. F. (eds.) *Synapses.* The John Hopkins University Press.

SINGH, A., ZHI, L. & ZHANG, H. 2019. LRRK2 and mitochondria: Recent advances and current views. *Brain Res,* 1702**,** 96-104.

SMITH, W. W., PEI, Z., JIANG, H., DAWSON, V. L., DAWSON, T. M. & ROSS, C. A. 2006. Kinase activity of mutant LRRK2 mediates neuronal toxicity. *Nat Neurosci,* 9**,** 1231-3.

SMITH, W. W., PEI, Z., JIANG, H., MOORE, D. J., LIANG, Y., WEST, A. B., DAWSON, V. L., DAWSON, T. M. & ROSS, C. A. 2005. Leucine-rich repeat kinase 2 (LRRK2) interacts with parkin, and mutant LRRK2 induces neuronal degeneration. *Proc Natl Acad Sci U S A,* 102**,** 18676-81.

STEGER, M., TONELLI, F., ITO, G., DAVIES, P., TROST, M., VETTER, M., WACHTER, S., LORENTZEN, E., DUDDY, G., WILSON, S., BAPTISTA, M. A., FISKE, B. K., FELL, M. J., MORROW, J. A., REITH, A. D., ALESSI, D. R. & MANN, M. 2016. Phosphoproteomics reveals that Parkinson's disease kinase LRRK2 regulates a subset of Rab GTPases. *Elife,* 5.

STEPHENS, B., MUELLER, A. J., SHERING, A. F., HOOD, S. H., TAGGART, P., ARBUTHNOTT, G. W., BELL, J. E., KILFORD, L., KINGSBURY, A. E., DANIEL, S. E. & INGHAM, C. A. 2005. Evidence of a breakdown of corticostriatal connections in Parkinson's disease. *Neuroscience,* 132**,** 741-54.

SWEET, E. S., SAUNIER-REBORI, B., YUE, Z. & BLITZER, R. D. 2015. The Parkinson's Disease-Associated Mutation LRRK2-G2019S Impairs Synaptic Plasticity in Mouse Hippocampus. *J Neurosci,* 35**,** 11190-5.

TAGLIAFERRO, P. & BURKE, R. E. 2016. Retrograde Axonal Degeneration in Parkinson Disease. *J Parkinsons Dis,* 6**,** 1-15.

VAN DE WIJDEVEN, R., RAMSTAD, O. H., BAUER, U. S., HALAAS, O., SANDVIG, A. & SANDVIG, I. 2018. Structuring a multi-nodal neural network in vitro within a novel design microfluidic chip. *Biomed Microdevices,* 20**,** 9.

VAN DE WIJDEVEN, R., RAMSTAD, O. H., VALDERHAUG, V. D., KOLLENSPERGER, P., SANDVIG, A., SANDVIG, I. & HALAAS, O. 2019. A novel lab-on-chip platform enabling axotomy and neuromodulation in a multi-nodal network. *Biosens Bioelectron,* 140**,** 111329.

VERMA, M., CALLIO, J., OTERO, P. A., SEKLER, I., WILLS, Z. P. & CHU, C. T. 2017. Mitochondrial Calcium Dysregulation Contributes to Dendrite Degeneration Mediated by PD/LBD-Associated LRRK2 Mutants. *J Neurosci,* 37**,** 11151-11165.

VERMA, M., WILLS, Z. & CHU, C. T. 2018. Excitatory Dendritic Mitochondrial Calcium Toxicity: Implications for Parkinson's and Other Neurodegenerative Diseases. *Front Neurosci,* 12**,** 523.

VERSTREKEN, P. (ed.) 2017. *Parkinson's Disease: Molecular Mechanisms Underlying Pathology* Academic Press.

VOLTA, M., BECCANO-KELLY, D. A., PASCHALL, S. A., CATALDI, S., MACISAAC, S. E., KUHLMANN, N., KADGIEN, C. A., TATARNIKOV, I., FOX, J., KHINDA, J., MITCHELL, E., BERGERON, S., MELROSE, H., FARRER, M. J. & MILNERWOOD, A. J. 2017. Initial elevations in glutamate and dopamine neurotransmission decline with age, as does exploratory behavior, in LRRK2 G2019S knock-in mice. *Elife,* 6.

WANG, X., YAN, M. H., FUJIOKA, H., LIU, J., WILSON-DELFOSSE, A., CHEN, S. G., PERRY, G., CASADESUS, G. & ZHU, X. 2012. LRRK2 regulates mitochondrial dynamics and function through direct interaction with DLP1. *Hum Mol Genet,* 21**,** 1931-44.

WEST, A. B., MOORE, D. J., BISKUP, S., BUGAYENKO, A., SMITH, W. W., ROSS, C. A., DAWSON, V. L. & DAWSON, T. M. 2005. Parkinson's disease-associated mutations in leucine-rich repeat kinase 2 augment kinase activity. *Proc Natl Acad Sci U S A,* 102**,** 16842-7.

WINNER, B., MELROSE, H. L., ZHAO, C., HINKLE, K. M., YUE, M., KENT, C., BRAITHWAITE, A. T., OGHOLIKHAN, S., AIGNER, R., WINKLER, J., FARRER, M. J. & GAGE, F. H. 2011. Adult neurogenesis and neurite outgrowth are impaired in LRRK2 G2019S mice. *Neurobiol Dis,* 41**,** 706-16.

YUE, M., HINKLE, K. M., DAVIES, P., TRUSHINA, E., FIESEL, F. C., CHRISTENSON, T. A., SCHROEDER, A. S., ZHANG, L., BOWLES, E., BEHROUZ, B., LINCOLN, S. J., BEEVERS, J. E., MILNERWOOD, A. J., KURTI, A., MCLEAN, P. J., FRYER, J. D., SPRINGER, W., DICKSON, D. W., FARRER, M. J. & MELROSE, H. L. 2015. Progressive dopaminergic alterations and mitochondrial abnormalities in LRRK2 G2019S knock-in mice. *Neurobiol Dis,* 78**,** 172-95.

ZHAO, J., HERMANSON, S. B., CARLSON, C. B., RIDDLE, S. M., VOGEL, K. W., BI, K. & NICHOLS, R. J. 2012. Pharmacological inhibition of LRRK2 cellular phosphorylation sites provides insight into LRRK2 biology. *Biochem Soc Trans,* 40**,** 1158-62.

Supplementary figures

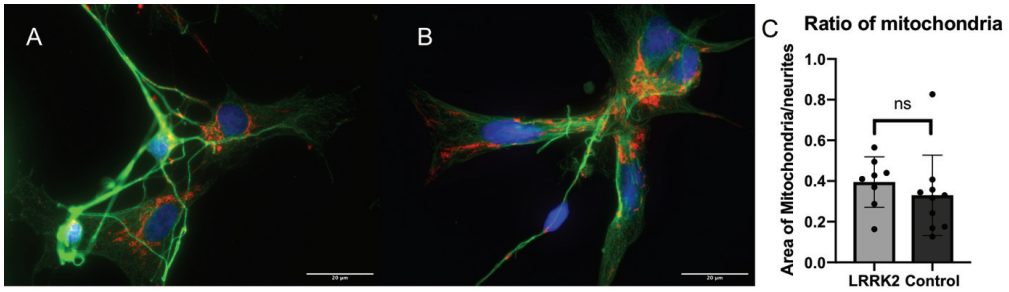

Fig.S1. Supplementary investigation of mitochondria A) shows a LRRK2 neural network labelled with fluorescent mitochondria (red (ab3298)), total-alpha synuclein (green) and hoechst conterstain (blue). **B**) shows an equivalent image of a fluorescently labelled control neural network (100X objective). **C**) shows a bar graph of the ratio calculation of mitochondria contained within samples from both the LRRK2 and Control neural networks at baseline, with example images used for the calculation displayed in panel **A**) and **B**). No statistically significant difference was found between the groups in mitochondrial content (ratio = area of fluorescently labelled mitochondria/ area of fluorescently labelled alpha-synuclein) ($p=0.4293$) by an unpaired t-test. Each dot represents a different sample (100X image) investigated, where $N_{LRRK2}=8$, and $N_{Control}=10$.

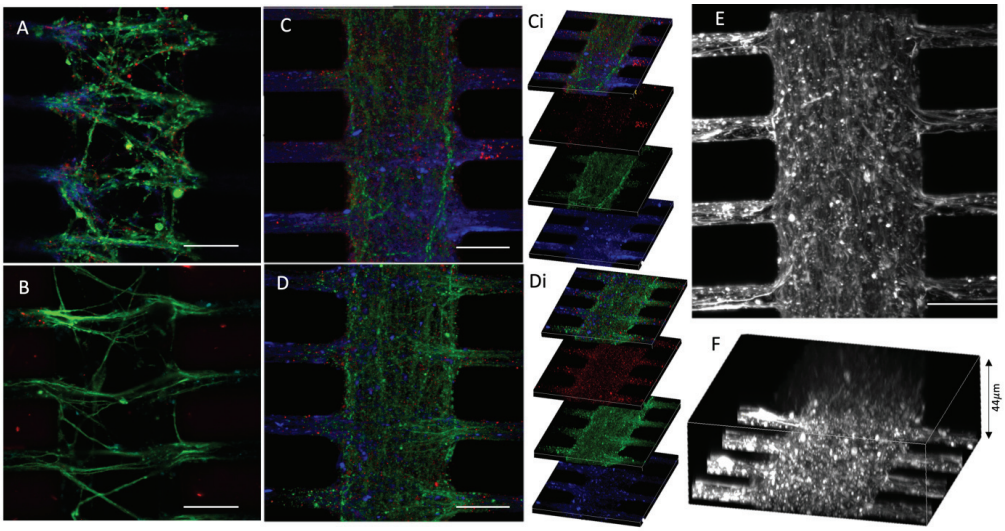

Fig.S2 Difference in neuritic density. **A** and **B**) Example images from the control neural networks fluorescently labelled with the presynaptic marker Piccolo (green), the post synaptic marker PSD95 (red) and the f-actin filament marker Phalloidin (blue) (30µm scale bar). **C** and **D**) Equivalent example images from the LRRK2 neural networks. **Ci** and **Di**) show the 10µm thick z-stacks compiled into **C** and **D**, respectively. **E** and **F** show an LRRK2 neural network labelled with phalloidin, where a z-stack has been taken to capture the entire volume of neurites contained within this section of the synaptic compartment, where **F** shows the volumetric sideview illustrating a neuritic bundle thickness of 44µm.

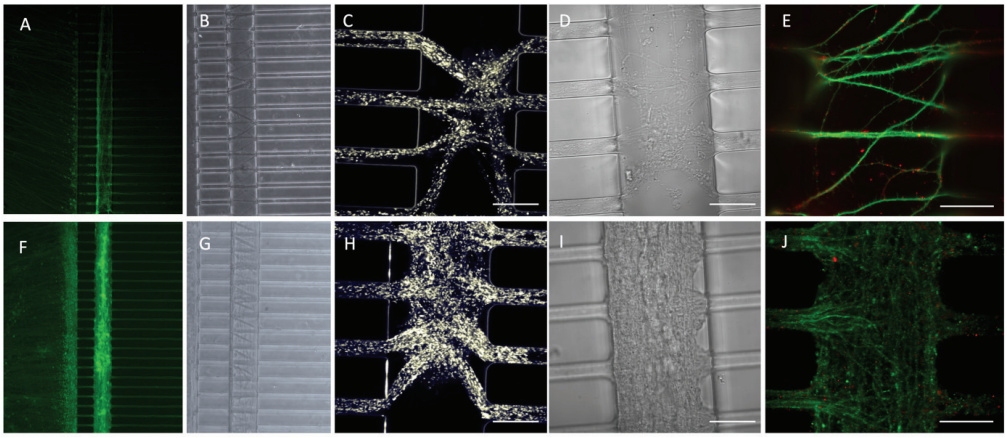

Fig.S3 Difference in neural network morphology visible at all levels. A-E) Example images from different control neural networks during each assay, while **F-J**) Equivalent images from the LRRK2 neural networks. There is a striking difference in the neurite outgrowth profile within the synaptic compartments, with clear fasciculation observed in **E)** control networks as opposed to **J)** aberrant growth in LRKK2 ones. All images have a 30µm scale bar, apart from E and J, which have a 20mµ scale bar.

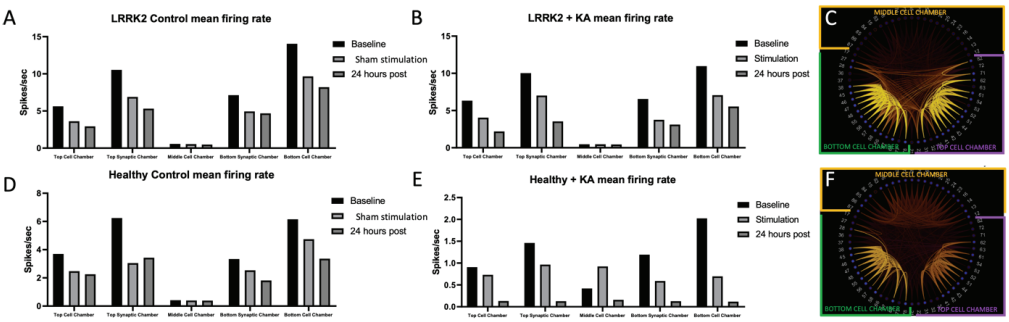

Fig.S4 Reproducibility of network activity traits and functional connectivity through structuring using a multi-nodal microfluidic chip. Mean firing rate (MFR) bar graphs organized by the different microfluidic chip areas, of both the (**A**) LRRK2 and (**D**) healthy neural network control groups clearly demonstrate that the activity of the structured neural networks is reproducibly influenced by the microfluidic chip physical structuring. Furthermore, the same trend is visible at the baseline timepoint of both the (**B**) LRRK2 and (**E**) healthy neural networks receiving KA. Although the MFR of the LRRK2 neural networks is far greater than the MFR of the healthy neural networks (relative x-axis), they follow the same trend, with much greater network activity measured at the top and bottom cell chambers than in the middle cell chamber. This is also visible from the correlation scheme balls presented in **C** and **F** of a baseline measurement from the LRRK2 and healthy neural networks, respectively, where greater correlations are found between the activity measured within each chamber than between, and stronger correlation found in the top and bottom cell chamber than in the middle.

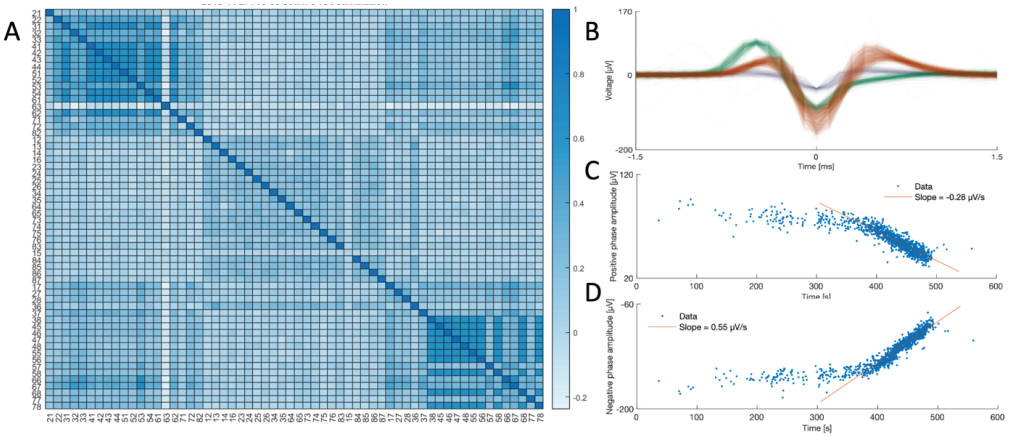

Fig.S5 Electrophysiological activity in LRRK2 neural network during KA stimulation. A) shows the correlation map of the activity measured during KA stimulation of the LRRK2 neural network shown in **Fig.6E-G**. **B**) shows the three distinct spike clusters measured at a randomly chosen electrode (number 63) of this network during the stimulation period. **C** and **D**) respectively show the trailing positive and negative phase amplitudes of the spikes from the neuron represented in red in **B** over time. The firing rate of this neuron can be seen to increase drastically 300-500 s into the recording session (see also **Fig.6C**), firing at the maximal rate allowed by the refractory period. This period coincides with both the negative and positive amplitudes of its signal becoming progressively reduced, followed by an abrupt silencing. This electrode is located in the top, stimulated cell chamber. Interestingly, from the MFR map in **A** it is clear that it is the only electrode that is negatively correlated (mean r = -0.2) with the activity of some other electrodes located in the same chamber, as well as some electrodes in the bottom cell chamber, indicating that the neuron whose spikes are plotted in red in **B** exerts an inhibitory effect.

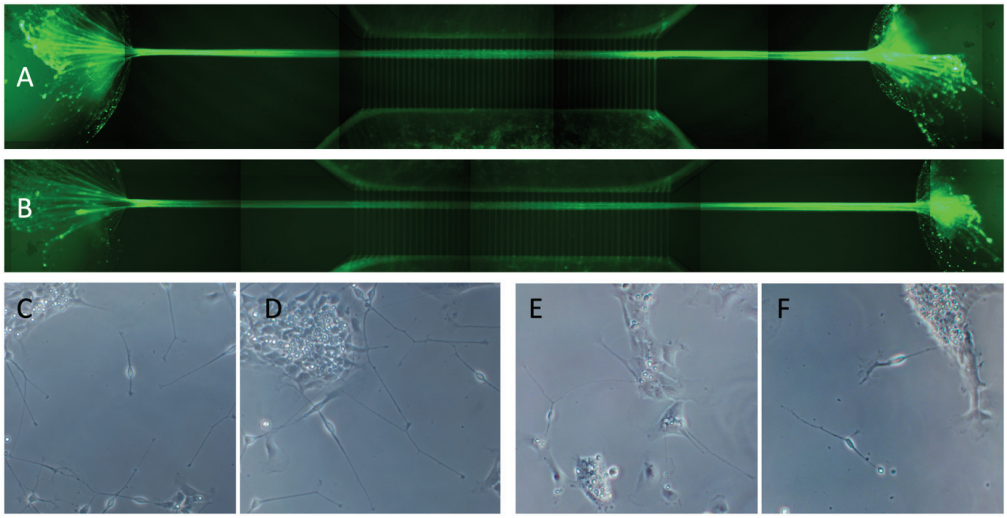

Fig.S6. **Aberrant neurite outgrowth and growth cone differences in LRRK2 neural networks versus controls. A,B**) show LRRK2 neural networks labelled with the fluorescent Calcein-AM, where massive bundles of neurites can be seen exiting at both ends of the synaptic compartments (the inlet and outlet), where there are no cells to connect up with. These bundles

are perpendicular to the axon tunnels interconnecting the cell chambers. **C,D**) shows brightfield images of LRRK2 NSCs, and **E,F**) of control neural networks after 1 day of differentiation, demonstrating differences in neurite outgrowth and growth cone profile, i.e. qualitatively more growth cones and branching neurites present in the LRRK2 neurons compared to controls.

Supplementary information on cell lines and culturing (Materials and Methods)

iPSC-derived H9N neural stem cells (ax0019) (control) and iPSC-derived H9N neural stem cells homozygous inserted with the LRRK2 G2019S (ax0310) purchased form Axol Bioscience were used for the experiments. Both lines are derived from the same donor dermal fibroblasts (female, 64 yr). General gene expression profiles from Axol's iPSC-derived NSCs is published in Gene expression omnibus (GEO) of the National Center for Biotechnology information (NCBI) (https://www.ncbi.nlm.nih.gov/geo/query/acc.cgi?acc=GSE61358).

Furthermore, gene editing and genotyped example data, as well as the CRISPR plasmid donor scheme for the LRRK2 line (ax0310) is shown below with the permission of Axol Bioscience. Certificates of analysis (COAs) for each cell line is provided in supplementary materials 3. For further information on these cell lines, contact Axol Bioscience.

Project	# Clones	# KI/KI	# KI/+	# KI/-	other
LARRK2	31	2	6	4	16

➢ 1 (KI/KI) and 2 (KI/+) clones fully genotyped; example data below:

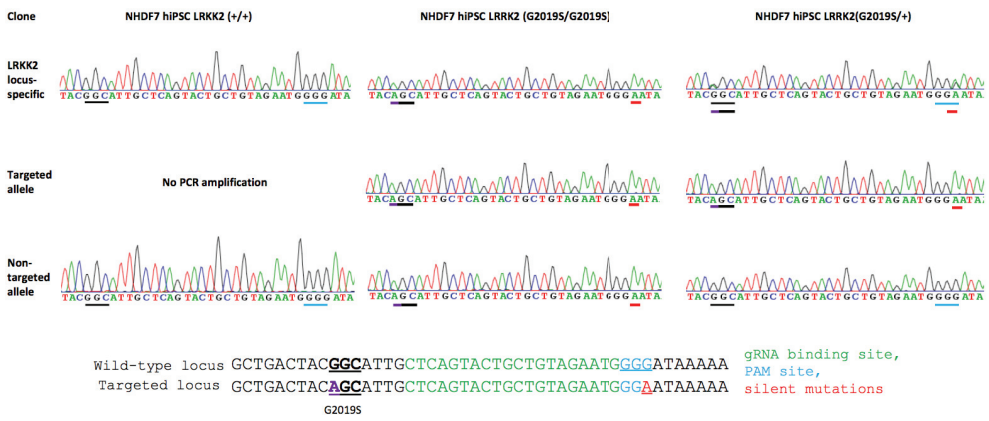

LRRK2 G2019S

➢ **CRISPR + plasmid donor**

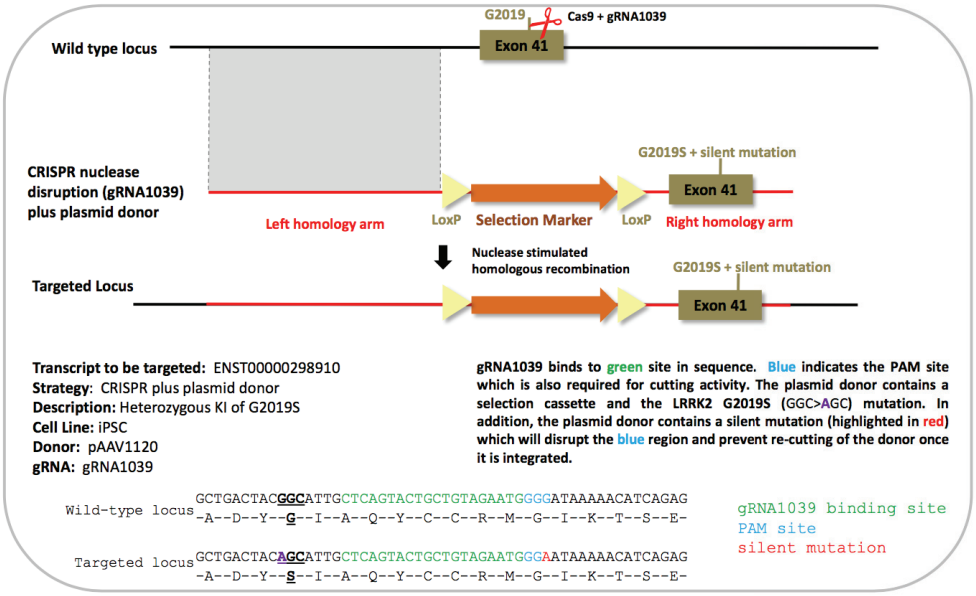

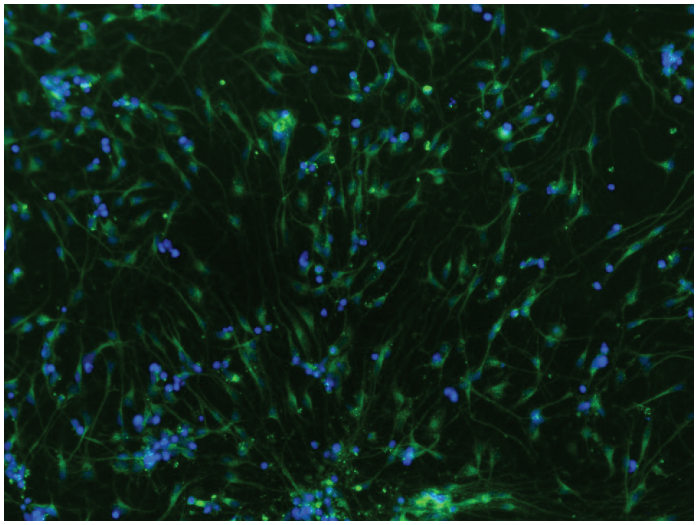

Expression of LRRK2 protein (green) in neurons derived from axolGEM Neural Stem Cells LRRK2 G2019S HOM. DAPI (blue) stains cell nuclei. The neural stem cells were differentiated to neurons over a two week period prior to fixation and staining for marker expression. (Provided with permission from Axol Bioscience webpage)

Protocol for culture of H9N NSCs (ax0019 and ax0310), adapted from Axol Bioscience's protocol (Human iPSC-derived Neural Stem Cell master protocol (version 5.0)
System A

List of media and supplements
Neural Expansion -XF Medium (ax0030-500)
Neural Maintenance - XF Medium (ax0032-500)
Neual Differentiation – XF Medium (ax0034-125)
Sure Growth recombinant human FGF2 (ax0047)
Sure Growth X recombinant human EGF (ax0047X)
0.01% Poly-L-Ornithine solution (PLO) (Sigma, P4967)
Natural Mouse Laminin (Thermo Fisher Scientific, 23017015)
L15 Lebovitz medium (Sigma, L5521)
KnockOut serum replacement (KOSR, Thermo Fisher Scientific, 10828010)

L15/laminin coating solution
3ml L15 Medium
48ul Natural mouse laminin (1mg/ml)
75ul Sodium Bicarbonate

Day before seeding:
Coat one well of a 6-well plate with PLO for 2 hours in incubator, wash with sterile MQ water, and leave overnight with L15-laminin in fridge.
Thaw an aliquot of Expansion medium (from -80 freezer) overnight in fridge
(Protect from light, can be kept for 1 week if supplemented (EGF, FGF2), 2 weeks if not)

Day of seed:
Prepare Neural Expansion medium with supplements (for spinning and seeding).

10ml Neural Expansion medium
2ul FGF2 (20ng/ml) (stock is 100ug/ml)
2ul EGF (20ng/ml)
10ul Rock Inhibitor (only when thawing/ splitting)
100ul Pen-Strep

Aspirate coating and add Neural Expansion medium to the well (ca 1,5ml) and return to incubator until seeding.
Thaw vial of cells in water bath (no shaking)
Pre-coat pipette with KOSR, (dropwise add cells to tube containing 10ml warm expansion medium. Spin for 200g x 5 min. Aspirate supernatant, precoat pipette with KOSR, resuspend cells in 0,5-1ml expansion medium and seed in 6-well.

Expansion:
Every 2 days, replace all the medium with Neural Expansion medium (supplemented with FGF and EGF). When the culture is 70-80% confluent, they are ready to undergo passage. This usually takes a long time (> one week). Do not expand more than 3 passages.

Splitting:
1/2 split. Coat 2 6-well wells.
Thaw a vial of Axols “Unlock” (aliquoted and stored in -80 in a box at the bottom).
Prepare Expansion medium (+ Rock inhibitor).

Aspirate media and rinse surface with DPBS--. Add Unlock (1ml /10cm^2), place in incubator for 5 min. Use 4x (unlock volume) of Neural expansion medium to stop reaction. Spin for 200g x 5min. Aspirate and resuspend in supplemented Neural Expansion medium, seed 50% in each of the 6-wells.

Synchronous Differentiation

When you have expanded long enough and are ready to start differentiating:
Full media change to Neural Expansion medium without supplements. Thaw aliquot of Neural Differentiation medium overnight in fridge.
24 hours later, conduct a full media change to Neural Differentiation medium (no supplements)
Every three days change 50% of the medium with fresh Neural Differentiation medium. A pure neuronal population takes anywhere between 3-10 days to achieve (dependent on the confluency, <60% = 3 days ++, >60% confluency takes up to 10 days, fully confluent may never become pure).

Maintenance

When fully differentiated, thaw an aliqot of Neural Maintenance medium overnight in fridge. Replace half of the medium with Neural Maintenance medium. 24 hours later, replace half the medium with Neural Maintenance.
After this, replace 50% of the medium with Neural Maintenance medium every 3 days. Might have to add extra laminin if the cells start detaching.

PAPER 3

ROYAL SOCIETY OPEN SCIENCE

royalsocietypublishing.org/journal/rsos

Research

Cite this article: Valderhaug VD, Glomm WR, Sandru EM, Yasuda M, Sandvig A, Sandvig I. 2019 Formation of neural networks with structural and functional features consistent with small-world network topology on surface-grafted polymer particles. *R. Soc. open sci.* **6**: 191086. http://dx.doi.org/10.1098/rsos.191086

Received: 24 June 2019
Accepted: 10 September 2019

Subject Category:
Cellular and molecular biology

Subject Areas:
biomaterials/neuroscience/structural biology

Keywords:
neural networks, three-dimensional structuring, polymer particles, small-world, electrophysiology, connectivity

Author for correspondence:
Ioanna Sandvig
e-mail: ioanna.sandvig@ntnu.no

Electronic supplementary material is available online at https://doi.org/10.6084/m9.figshare.c.4690445.

THE ROYAL SOCIETY PUBLISHING

Formation of neural networks with structural and functional features consistent with small-world network topology on surface-grafted polymer particles

Vibeke Devold Valderhaug[1], Wilhelm Robert Glomm[2], Eugenia Mariana Sandru[2], Masahiro Yasuda[3], Axel Sandvig[1,4,5] and Ioanna Sandvig[1]

[1]Department of Neuromedicine and Movement Science, Faculty of Medicine, Norwegian University of Science and Technology (NTNU), 7030 Trondheim, Norway
[2]SINTEF AS, Department of Biotechnology and Nanomedicine, Trondheim, Norway
[3]Department of Chemical Engineering, Osaka Prefecture University, 1-1 Gakuen-cho, Naka-ku, Sakai, Osaka 599-8531, Japan
[4]Department of Neurology and Clinical Neuroophysiology, St Olav's Hospital, Trondheim, Norway
[5]Department of Pharmacology and Clinical Neuroscience, Division of Neuro, Head and Neck, Umeå University Hospital, Umeå, Sweden

VDV, 0000-0001-5523-0725

In vitro electrophysiological investigation of neural activity at a network level holds tremendous potential for elucidating underlying features of brain function (and dysfunction). In standard neural network modelling systems, however, the fundamental three-dimensional (3D) character of the brain is a largely disregarded feature. This widely applied neuroscientific strategy affects several aspects of the structure–function relationships of the resulting networks, altering network connectivity and topology, ultimately reducing the translatability of the results obtained. As these model systems increase in popularity, it becomes imperative that they capture, as accurately as possible, fundamental features of neural networks in the brain, such as small-worldness. In this report, we combine *in vitro* neural cell culture with a biologically compatible scaffolding substrate, surface-grafted polymer particles (PPs), to develop neural networks with 3D topology. Furthermore, we investigate their electrophysiological network activity through the use of 3D multielectrode arrays. The resulting neural network activity shows emergent behaviour

consistent with maturing neural networks capable of performing computations, i.e. activity patterns suggestive of both information segregation (desynchronized single spikes and local bursts) and information integration (network spikes). Importantly, we demonstrate that the resulting PP-structured neural networks show both structural and functional features consistent with small-world network topology.

1. Introduction

Combining *in vitro* neural network models with tools for electrophysiological investigation is an established (modelling) approach for exploring the emerging activity and function of neural networks. Recent advances in morphogenetic neuroengineering have led to a surge of scientific interest aimed at using these already established tools in novel ways. The well-established, standard neural network modelling approach has been to create monolayer neural networks from dissociated neural tissue or from neural stem cells, and to measure the emerging network activity using microelectrode arrays (MEAs). Some fundamental traits of brain networks, such as self-organization and spontaneous network formation and activity, are recapitulated by these models, making them attractive reductionist paradigms for neuroscientific research. Some evidence, however, points towards a prominent activity feature emerging in these *in vitro* neural networks that is largely incompatible with the activity of the brain, namely highly synchronized activity [1–3]. This discrepancy limits the relatability and thus the potential information that can be gained from this otherwise valuable approach. Knowledge gained in the field of connectomics, however, suggests that this limitation can be overcome. A highly interdependent nature of structure and function in the neural networks of the brain has been uncovered [4–6], which implies that a more realistic topology may need to be recapitulated in our standard modelling systems if they are to produce networks with activity and function traits more relatable to those seen in the brain.

The pattern of physical interconnections and the activity of a neural network are critically interdependent, where the strength and directness of the physical interconnections between neuronal ensembles have been shown to determine and constrain their functional interactions [4,5]. Several attempts at structuring *in vitro* neural networks have therefore been reported [7], as standard monolayer culture mainly allows connections to form in one plane (X,Y), disregarding the third (Z) dimension which greatly influences the structure of biological neural networks. A few of these studies have also compared the electrophysiological network activity of monolayer neural networks and neural networks structured in three dimensions (3D) using standard two-dimensional (2D) MEAs, where the results indicate an effect on global network synchrony and random spiking due to the structuring [1,8]. Further supporting this strategy is the small-world topology of the brain, a characteristic feature which facilitates the simultaneous capacity of information integration and segregation, the two emerging network phenomena recognized as the basis of behaviour [2,5,9,10]. Computational functions which are spatially and temporally segregated into functional modules in the brain are dynamically engaged and disengaged through transient phase or frequency locking, i.e. oscillations/ synchronization, and thus integrated into transitory coordinated global functions [2]. Furthermore, the small-world topology, characterized through its simultaneous high clustering and characteristic short path lengths [5,11], has been shown to facilitate the spread of disease to a greater extent than other network architectures [12–15]. This might relate to the development of neurodegenerative disorders such as Alzheimer's and Parkinson's disease, or dementia with Lewy body pathology, which have all been hypothesized to progress through the propagation of pathological protein aggregates through interconnected brain areas [16,17]. Thus, basic features of the human brain connectome, such as small-worldness and internodal connectedness, influence both network function and dysfunction, highlighting the fundamental importance of capturing these features in our modelling systems.

In this report, we show that we can capture some of the complexity of neural networks in the brain through interfacing *in vitro* neural cell cultures with surface-grafted, non-conducting, polymer particles (PPs) to create neural networks with 3D topology. Previously, these PPs have been successfully employed as microenvironments for creating 3D bone marrow culture systems, which have been used for both haematopoietic stem cell studies [18–20] and chemosensitivity studies [21]. In the present study, we report the structuring of neural networks using PPs combined with 3D MEAs for electrophysiological network measurements and show how the resulting structural and functional network traits relate to a small-world network topology.

2. Material and methods

2.1. Fabrication of polymer particles with surface-grafted chains

Poly(vinyl pyrrolidone) K90 (PVP) of average molecular weight approximately 360 000 g mol^{-1}, pentaerythritol triacrylate (PETA), methacrylic acid (MA) glycidyl methacrylate (GMA) and toluene were purchased from Sigma Aldrich. Methyl methacrylate (MMA) was purchased from Fluka. 2,2′-Azobis(isobutyronitrile) (AIBN) was obtained from Akzo Nobel. 2,2′-azobis[*N*-(2-propenyl)-2-methylpropionamide] (APMPA) was obtained from Wako Pure Chemical Co. (Osaka, Japan). All reagents were used without further purification.

2.1.1. Synthesis of PPs

PPs with surface-grafted epoxy-containing polymer chains were synthesized via suspension polymerization using a protocol adapted from Yasuda *et al.* [20]. Briefly, 56 ml of an aqueous 2% PVP solution was added to a 100 ml temperature-controlled glass reactor with an impeller, and stirred (500 r.p.m.) at 25°C. In a separate vessel, 0.2 g of AIBN, 0.3 g of APMPA, 3.8 g of MMA and 3.8 g of PETA were mixed and the resulting monomer mixture was added dropwise to the reactor under stirring (500 r.p.m.). Polymerization was done in the reactor first at 70°C for 3 h and then at 80°C for 2 h under stirring (350 r.p.m.). Following synthesis, the particles were washed three times in DI water and dried using azeotropic distillation prior to further functionalization. Particle size distribution was analysed via optical microscopy and laser diffraction, and ranged from 100 to 1000 µm, with a volume average around 300 µm. The stability of the resulting surface-grafted PPs in cell culture medium (RPMI 1640 with 10% FBS, 1% L-Glut and 1% PenStrep (1 : 1 penicillin/streptomycin)) was subsequently investigated, revealing a 54% reduction in volume average diameter after 24 days.

2.1.2. Functionalization of PPs

Surface grafting of epoxy-containing copolymer chains was done using a protocol adapted from Yasuda *et al.* [20]. In a typical procedure, 5 g of PPs, 12.5 g of GMA and 3.1 g of MA were added to a three-neck flask together with 125 g of toluene. The grafting reaction was carried out for 8 h at 105°C under stirring (100 r.p.m.), and the reaction mixture was subsequently gradually cooled down to room temperature. After filtration, the particles were washed three times with ethanol and three times with water and stored in ethanol at 4°C until use in cell cultures.

2.2. Establishment of 3D neural networks on PPs

Rat fetal neural stem cells (NSCs) (Gibco) were seeded onto CellStart® (Gibco) coated vessels and maintained in Complete Stem Pro® NSC SFM media (Gibco) supplemented with 1% penicillin–streptomycin. For seeding together with the PPs, the media were further supplemented with 1% BSA, 0.1% ROCK inhibitor, and 0.5 µg ml^{-1} fibronectin.

The PPs were transferred with a spatula to 1.5 ml Eppendorf tubes (about 200 µl of dry PPs in each tube), where they were washed three times in PBS, and three times in PBS containing 10% FBS. The supernatant was then removed, and an equivalent amount of cell suspension (200 µl containing 2×10^5 NSCs) was added to each tube and mixed gently. The mixture was then transferred to the relevant culture vessel and incubated in 37°C for 1 h before more media were added to the NSC cultures with PPs. Differentiation towards neural lineage was initiated 2 days post-seeding through the use of a differentiation medium consisting of Neurobasal supplemented with 2% B27, 1% GlutaMAX and 1% penicillin–streptomycin.

2.2.1. Microelectrode array preparation

Sixty-electrode 3D MEAs (60-3DMEA200/12/50iR-Ti; Multichannel Systems) with ring covers were used as culture vessels for cell seeding and for recording spontaneous electrophysiological activity of the developing neural networks on the PPs. Recordings were obtained through the MEA2100 *in vitro* system and suite software (Multi Channel Systems; Reutlingen, Germany). In addition, seeding rings (MEA ALA-inserts; Multi Channel Systems; Reutlingen, Germany) were used to reduce movement and keep the PPs in place over the electrodes throughout the experimental period.

Before seeding, the 3D MEAs were washed with 65% ethanol, incubated in sterile water and UV-treated. To make the culture surface hydrophilic, the MEAs were subsequently treated with fetal bovine serum (FBS) for 60 min.

Prior to seeding on 3D MEAs, the NSCs were labelled with a carbocyanine lipophilic tracer, DilC18 (5) DiD (L7781, Invitrogen) (excitation 644 nm). A 5 µl cell-labelling solution was mixed into 1 ml cell suspension containing 1×10^6 rat NSCs by gentle pipetting. The resulting solution was then incubated for 20 min at 37°C, washed and centrifuged three times at 200*g* for 3 min. The cells were then mixed with the PPs as described above and transferred into the seeding ring on the 3D MEAs using a spatula. An additional 100 µl of cell suspension was added once the mixture was in place within the seeding ring. The resulting NSC cultures with PPs on 3D MEAs were then incubated at 37°C for 1 h for the cells to adhere, before another 350 µl of media were added. The NSC were differentiated and the derived 3D neural networks on the PPs were maintained on the 3D MEAs for three to four weeks post-seeding, throughout which fluorescence microscopy and electrophysiological recordings were obtained.

2.2.2. Immunocytochemistry of neural networks on PPs

For fixation, 2% paraformaldehyde (PFA) was added to the 3D neural networks on the PPs for 10 min, followed by 4% PFA for 10 min and two 15 min washes in PBS. This was followed by a 1 h incubation in blocking solution consisting of PBS with 5% normal goat serum and 0.3% Triton-X, and an overnight incubation in primary antibody solution (PBS containing 1% normal goat serum, 0.1% Triton-X) at 4°C. The following primary antibodies from Abcam were used: rabbit anti-CaMK2 (1 : 400), rabbit anti-Synaptophysin (1 : 250), rabbit anti-GFAP antibody (1 : 1000), mouse anti-CNPase antibody (1 : 500), mouse anti-PSD95 (1 : 300), mouse anti-β 3 tubulin (1 : 1000) and chicken anti-MAP2 antibody (1 : 1000), chicken anti-neurofilament heavy (1 : 500) and chicken anti-GFAP antibody (1 : 1000). The neural networks on the PPs were then washed twice for 15 min in PBS and incubated in secondary antibody solution (PBS containing 1% normal goat serum, 0.1% Triton-X) in the dark, at room temperature, with the following secondary Alexa Fluor™ 568, 488 and 647 antibodies (Thermo Fisher, MA, USA) at a dilution of 1 : 1000. Hoechst (1 : 10 000) was added for the final 5 min before another two 15 min wash in PBS was conducted. Images were taken using a Zeiss Axiovert 1A fluorescent microscope (Carl Zeiss, Germany) and Zen 2.3 Lite, Blue Ed. Software. ImageJ and PowerPoint were used to post-process the images.

2.2.3. Investigation of structural topology by scanning electron microscopy of neural networks on PPs

Samples of the 3D neural networks on the PPs were washed twice in PBS before being fixed in a solution of 2.5% glutaraldehyde with 2% PFA in 0.1 M Hepes buffer for 3 h at room temperature, followed by overnight fixation in 4°C. The samples were then washed twice for 5 min in Hepes buffer, subsequently dehydrated in 5 min steps using increasing ethanol concentrations (20–50–70–90–100–100% ethanol), and dried in 10 min steps using hecamethyldisiloxane (HMDS) (50% and 2× 100%) before being air-dried in a desiccator. The samples were subsequently mounted on aluminium pins with double-sided carbon tape and sputter coated (Polaron) with Gold/Palladium (30 nm thickness). The samples were then examined using a scanning electron microscope (SEM) (Teneo SEM, Thermo Fisher Scientific) at 10–15 kV with an ETD detector.

2.2.4. MEA recordings and data analysis

Recordings were obtained through the MEA2100 *in vitro* head stage, interface system and suite software (Multi Channel Systems; Reutlingen, Germany), and are available within the Mendeley data repository (http://dx.doi.org/10.17632/r9gd7g8zcy.4 [22]). Samples of the electrophysiological activity of the 3D neural networks on the PPs were recorded for durations of approximately 90 consecutive seconds throughout the experimental period, with a sampling rate of 10 kHz, where a waveform amplitude exceeding a threshold of ±5 s.d. from the mean was registered as a spike. An in-house developed MEA data analysis Toolbox (available for download at https://github.com/helgeanl/MEA_toolbox) was used to visualize the waveforms of each spike, and activity raster plots were produced based on the timestamp of each spike. After the final electrophysiological recording, the media were replaced with PBS, and the 3D neural networks were left to dry on the 3D MEAs at room temperature, followed by an overnight UV-treatment to terminate the cells. Recordings were subsequently obtained from these 3D MEAs as a control to test whether the PPs themselves produced any electrophysiological artefacts. In addition, impedance measurements were made to test whether any damage had been done to the electrodes.

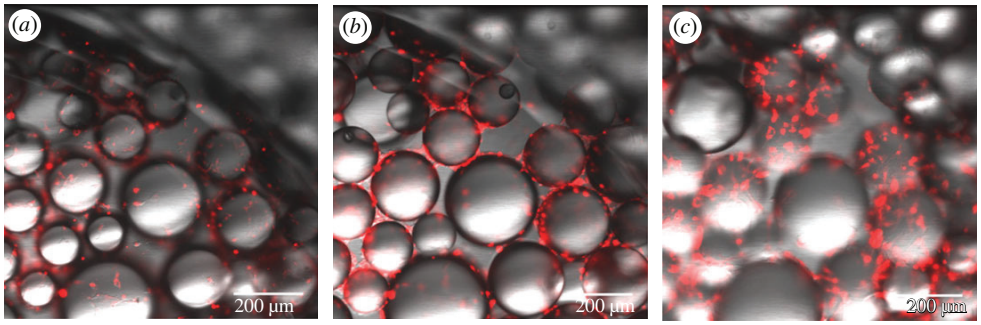

Figure 1. Confocal images demonstrating the emergence of 3D neural networks on the surface-grafted PPs 4 days after seeding, with different *z*-planes showing the fluorescently labelled cells (red) attached at different levels/heights of the same PPs (brightfield) (10X). (*a*) The bottommost focus level with fluorescently labelled cells attached to the well plate as well as the bottom of the PPs. (*b*) The fluorescently labelled cells about 100 µm further up in the *z*-plane, and (*c*) 200 µm further above that.

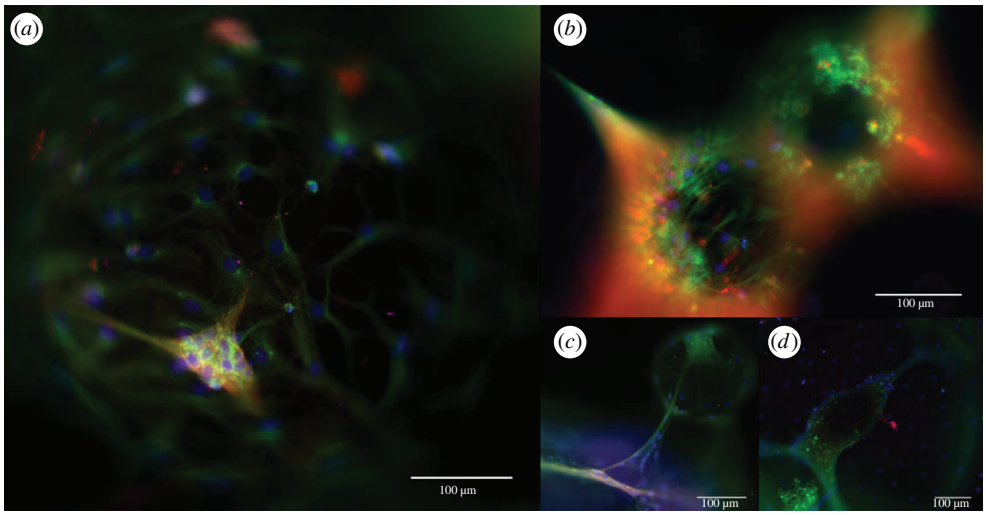

Figure 2. ICC of neural networks on surface-grafted PPs. Following one month of differentiation and maintenance of the neural networks on the PPs, ICC confirmed the presence of mature cells attached to the surface of the PPs. The images show neural networks expressing fluorescently labelled markers for (*a*) calcium/calmodulin protein-dependent kinase-II (CAMK2) (green), post-synaptic densities-95 (PSD95) (red) and nuclear marker Hoechst (blue), (*b*) for synaptophysin (red), GFAP (astrocytic marker) (green) and Hoechst (blue), (*c*) for PSD95 (red), CAMK2 (green), neurofilament heavy (grey) and Hoechst (blue) and (*d*) for synaptophysin (red), GFAP (green) and Hoechst (blue). Scale bar, 100 µm.

3. Results

3.1. Neural network culture

Rat NSCs were successfully seeded and maintained among the PPs. The resulting neural networks could be imaged with fluorescence microscopy, showing cells labelled with a lipophilic tracer growing underneath, around and on top of the PPs as early as 4 days post-seeding (figure 1). Although we contend with some loss of cells with each media change, we were able to maintain the neural cell cultures on the PPs for over one month. After this point, the cultures were fixed and immunolabelled with neural lineage markers. The immunocytochemistry (ICC) confirmed the presence of neurons ($MAP2^+$), as well as astrocytes ($GFAP^+$) and oligodendrocytes ($CNPase^+$) attached to the surface of the PPs after one month in culture (electronic supplementary material, figure S1). Furthermore, the neural networks were positively immunolabelled with markers for mature axons (neurofilament heavy polypeptide) as well as synaptic vesicles (synaptophysin), post-synaptic elements (PSD95), calcium/calmodulin protein-dependent kinase-II (CAMK2), which is involved in neurotransmitter secretion, synaptic connectivity and long-term potentiation, and GFAP (figure 2).

Based on standard morphological characteristics as well as careful comparison with the demonstrated ICC results, topographical SEM investigation confirmed that the PPs did indeed support the

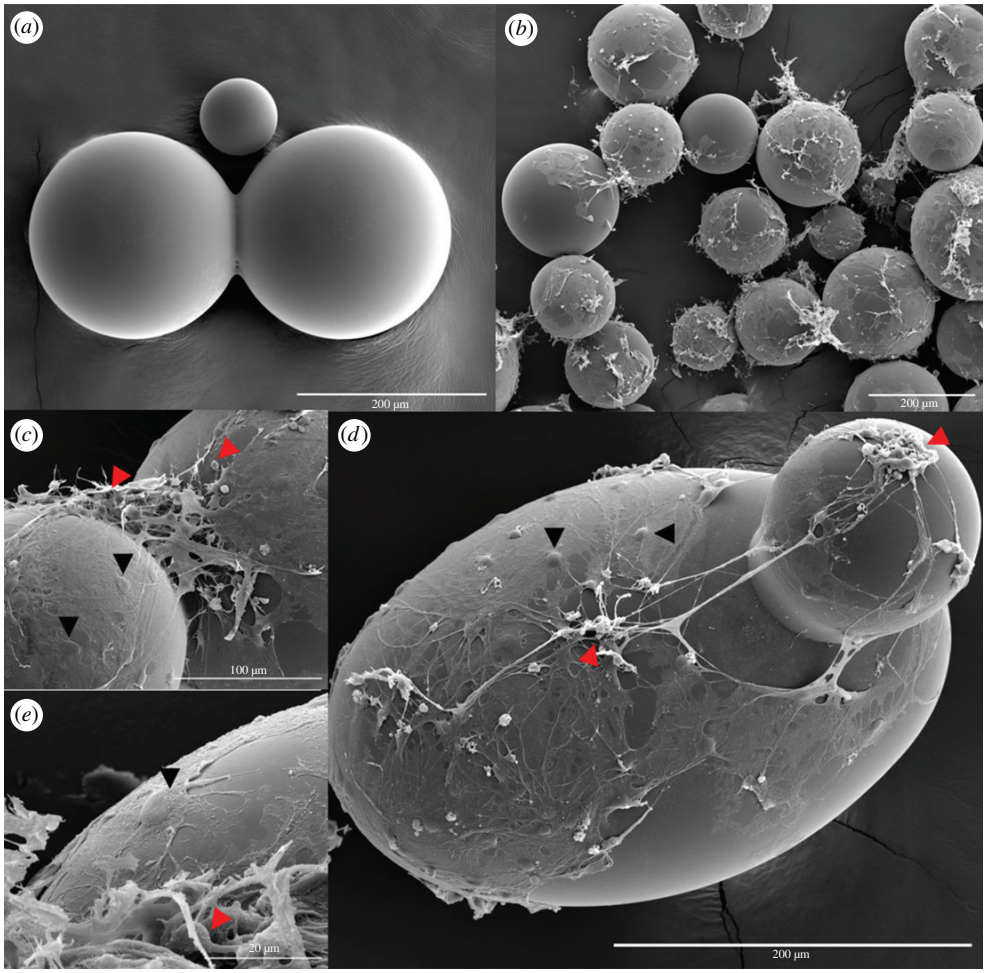

Figure 3. Prominent 3D neural network formation on surface-grafted PPs. Topography investigation by SEM confirmed the presence of extended neural networks with 3D topology on the surface of, and connecting between, the PPs three weeks post-seeding. (*a*) SEM image displaying the PPs alone (200 µm scale bar) and (*b*) after establishment of 3D neural networks (200 µm scale bar). (*c*) Higher magnification image of the intricate 3D neural network connections spanning the gap between two PPs (100 µm scale bar). Neuronal cell bodies (red arrowhead) with axonal projections can be distinguished within the network, as well as glial cell bodies (black arrowhead) with thin membranous extensions covering the particle surface. (*d*) Image revealing clusters of neurons (red arrowhead) connected through suspended axonal bundles on different PPs. Glial cell bodies (black arrowheads) can be distinguished regularly tiling most of the particle surface (200 µm scale bar). (*e*) Detailed image displaying another neuronal cell body (red arrowhead) with thin neurites and a thicker axonal projection, as well as another glial cell (black arrowhead) covering the surface with a thin membranous sheath (20 µm scale bar).

establishment of prominent 3D neural networks (figure 3). These networks covered the surface of the PPs as well as interlaced among them. Furthermore, glial cell bodies were observed regularly tiling the surface and wrapping most of the PPs with thin membranous extensions, while neuronal clusters connected through axonal projections could be observed on top. Importantly, several suspended axon bundles interconnecting neuronal clusters on different PPs could be observed, providing structural 'short-cut' connections between neuronal clusters located at different levels in the network (figure 3*d*).

3.2. Electrophysiological measurements of the developing 3D neural networks on the PPs using 3D MEAs

Three-dimensional neural networks on the PPs were successfully developed and maintained on 3D MEAs for a period of three to four weeks. A lipophilic tracer used to label the rat NSCs prior to seeding and differentiation on the 3D MEAs made it possible to visualize some of the cells among the PPs during

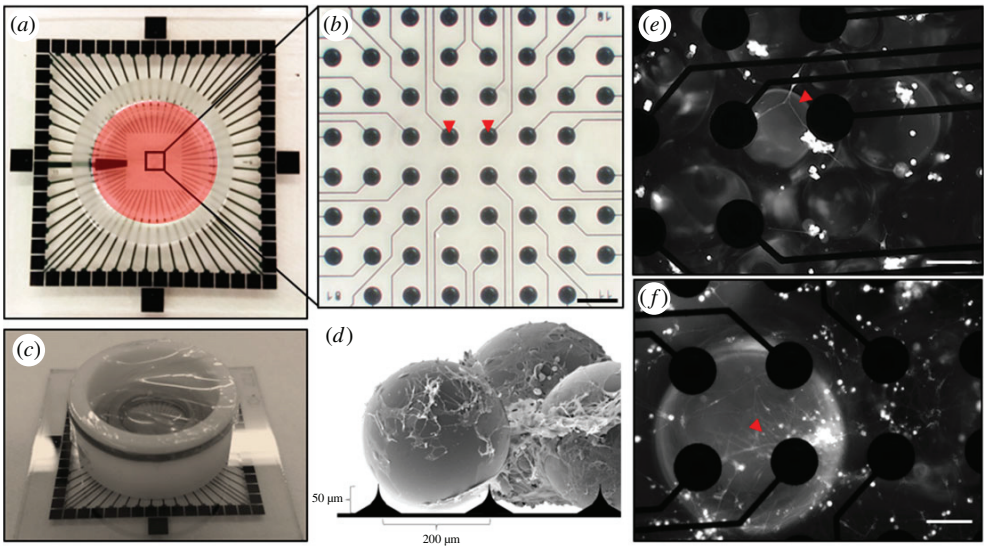

Figure 4. Three-dimensional MEA set-up for electrophysiological recording of the developing 3D neural networks on surface-grafted PPs. (*a*) Image of a 3D MEA. The cell culture chamber is highlighted in red. The recording area containing the electrodes are boxed in and displayed magnified in (*b*), where the red arrowheads indicate two of the 60 recording electrodes (200 µm scale bar). (*c*) Sideview of the same 3D MEA, with a ring cover protecting the 3D neural networks on the PPs from contamination during recordings. (*d*) Cartoon illustrating the PP structured neural networks together with the 3D electrodes on the MEAs. (*e*) Image displaying developing neural networks labelled with a fluorescent lipophilic tracer on the PPs 2 days after seeding on the 3D MEAs. The red arrowhead indicates neurites connecting cell clusters (100 µm scale bar). (*f*) Image displaying the fluorescently labelled developing neural networks 3 days after seeding on the 3D MEAs. The red arrowhead indicates weakly labelled neurites extending from a cell cluster centred around a single 3D recording electrode (100 µm scale bar).

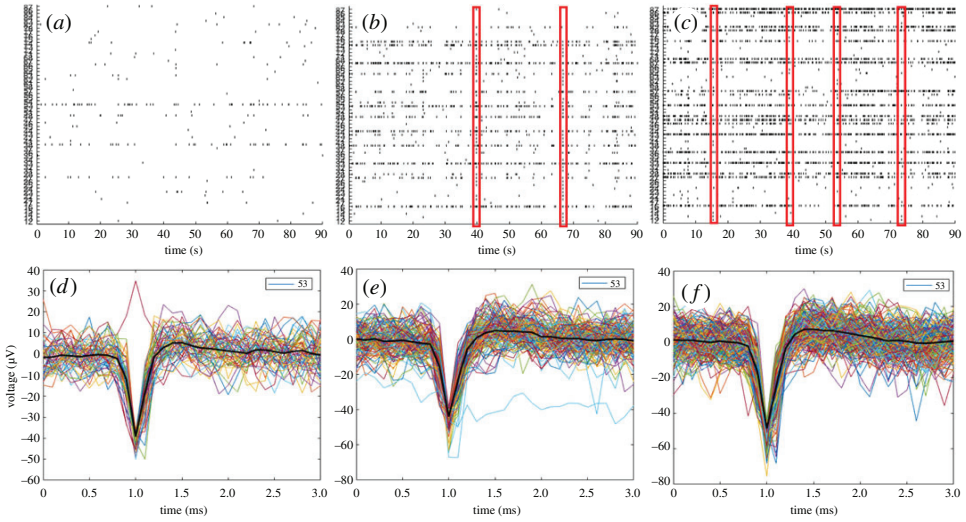

Figure 5. Three-dimensional developing neural network activity on surface-grafted PPs as measured from 3D MEAs. (*a–c*) Activity maps (raster plots) from a 3D neural network on an MEA ($n = 4$) at one, two and three weeks post-seeding, respectively. Each spike recorded during a 90 s sampling period is indicated for each of the 60 electrodes (numbered on the *y*-axis). Network spikes, events in which a spike or several spikes are detected at most of the active electrodes in the network at the same time, are highlighted in red. (*d–f*) The spike shape of each recorded spike at electrode 53 for each of the three timepoints (*x*-axis = ms, *y*-axis = µV).

the initial culture period (figure 4). Electrophysiological recordings performed throughout a period of three to four weeks demonstrated the emergence of electrically active, developing 3D neural networks on the PPs as shown by the activity raster plots of a representative neural network in figure 5*a–c*. The recordings performed during the first week showed sporadic, largely unsynchronized spontaneous action potentials scattered among the electrodes. Sample recordings performed during the second week of development demonstrated the presence of maturing networks, as patterns of more regular spiking and bursting

behaviour emerged. Indeed, even some network spikes (synchronization), i.e. single or multiple spikes detectable by most of the active electrodes in the culture within the same time period, were observed. During the third, final week of recordings, transient, regular, local bursting behaviour as well network spikes interspaced with longer periods of unsynchronized, scattered action potentials typified the electrical activity of the 3D neural networks on the PPs ($n = 4$). Furthermore, the shape of each recorded spike at one of the most active electrodes (electrode 53) is displayed for each of the three timepoints (figure 5*d–f*). By contrast, as a control measure, no electrical activity exceeding the threshold for noise was observed with the PPs alone, and no indication of damage to the electrodes could be read from impedance measurements or visual inspection.

4. Discussion

Several studies employing various scaffolds for 3D neural tissue culture have attempted to capture the basic structural dimensionality of neural networks in the brain [7]. However, very few of these studies provide electrophysiological measurements of the resulting network activity, and those that do use standard planar (2D) MEAs for this purpose [1,8]. Since the 3D MEA electrodes used in this study can measure electrical activity up to 50 µm away from a cell body along the entire surface area of the electrode, they cover a much greater area than the electrodes on conventional 2D MEAs, and are as such better suited to obtaining electrophysiological activity originating from several levels of the neural network, rather than mainly from the bottommost layers.

Two novel findings have been described in this report: firstly, we show that the presented PPs can function as long-term scaffolds for 3D neural network structuring, as they allow the attachment, survival, differentiation and maturation of neural networks for over one month (figures 2, 3 and 5; electronic supplementary material, S1). Differentiation and maturation were demonstrated with ICC through the presence of neurons with mature axons containing synaptic vesicles, post-synaptic densities and proteins involved in long-term potentiation. Furthermore, suspended neuronal connections interlacing between the PPs (figure 3*c*,*d*), connecting remote neuronal clusters on distant and otherwise independent surface areas at different levels demonstrated the 3D of the structured neural networks. These structural 'short-cuts' provide a much quicker path between the clusters than what would be possible if the connections were confined to the surface, as in standard monolayer neural networks, and provide physical connectivity features consistent with small-world network topology. Secondly, we demonstrate through electrophysiological measurements that these PP-structured 3D neural networks are functional, i.e. that they spontaneously develop emergent behaviour consistent with maturing neural networks capable of performing computations through activity patterns suggestive of information segregation (desynchronized spikes and local bursts) and information integration (network spikes) (figure 5). Furthermore, some emergent activity features consistent with a developing small-world topology were revealed in the final week of electrophysiological recordings, where the 3D neural networks displayed higher local activity clustering interspaced with a few synchronized network events.

Previously, similar PPs have been used as scaffolds for growing a range of non-neural cell types, such as fibroblasts, osteoblasts and chondrocytes, as well as for growing co-cultures of MS-5 stromal cells and HeLa cells, haematopoietic stem cell and leukaemic cells [18–21]. However, these cell types are much more robust and less sensitive to mechanical stress or fluctuations in environmental parameters such as temperature and pH compared to cells of a neural lineage. It is therefore an important finding that the PPs support the development and survival of *in vitro* neural networks as well.

In the present study, the gain of dimensionality obtained through structuring the neural networks added complexity to the network connectomes, particularly in relation to the possible 'shortest path length' of the structural connections between distant neural clusters/nodes. This can be readily observed by studying the physical interconnections preserved in the SEM preparation displayed in figure 3*d*, where a suspended axonal bundle spans the gap between two PPs and interconnects the neuronal clusters found on each of them. This suspension provides the shortest possible path between the remote neuronal clusters, reducing the topographical distance and processing length between the connected neuronal clusters/nodes, which is a direct result of the structuring. A similar gain of 'directness' in the connectivity between neuronal ensembles located on otherwise independent surface areas can be observed in figure 3*c*. This directly observable structural connectivity trait of local neural clusters interconnected with other distant neural clusters through a few axon bundles is highly consistent with a small-world network topology [11,14,15]. Furthermore, these features can determine the possible functional interactions of the neuronal clusters/nodes and the overall efficiency of the 3D

neural networks [23], as the shortest path between interconnected nodes in a network has implications for the signal propagation speed, computational power and synchronizability [11].

The electrophysiological activity of an *in vitro* neural network should reflect basic emergent phenomena of the brain, namely the simultaneous capacity of information integration and segregation [2,5,9,10]. As can be seen from the raster plots in figure 5 showing electrophysiological development, the 3D neural networks which emerge among the PPs during the second and third week post-seeding display simple forms of both unsynchronized, local bursting behaviour, consistent with segregation, as well as single network spikes/bursts transiently engaging most of the active nodes in the network, suggestive of integration. However, these electrophysiological neural network traits are also present in *in vitro* monolayer neural networks and represent basic emergent behaviour of neural networks in general [24,25]. Nonetheless, in contrast with the highly synchronized network activity often observed in *in vitro* monolayer neural networks, largely desynchronized and local/clustered network activity was observed during the final weeks of development recorded of the PP-structured neural networks in this study. Together with the observed structural connectivity showing distant neuronal clusters connected through 'short-cut' suspended connections, these features of higher activity clustering interspaced with a few synchronized network events suggest that structuring the neural networks with the PPs facilitates the establishment of small-world topology, both at a structural and functional level.

This initial study has pointed towards key topological features consistent with small-world topology of the PP-structured neural networks, which are more in line with the *in vivo* reality than classical monolayer neural networks. Nevertheless, further investigations and optimizations are needed before a conclusion can be made about the utility of this platform. These particular PPs allow for tuning of the cell–surface interaction via the length and chemical composition of the surface-grafted chains, as well as the available volume for cell growth and connectivity, via the particle size and polydispersity, which could be further optimized for neuronal cultures. Furthermore, the biological relevance of the PPs could be increased by harnessing their capacity for graded compound release through incorporation of programmable degradability. Combined with other *in vitro* platforms, such as microfluidic chips, this could be used to model, for instance, the effect of neuroprotective compounds/new drugs on network degradation in relation to neurodegenerative diseases in a more biologically relevant manner than what is possible at the moment.

5. Conclusion

In vitro models for inferring neural activity at a population/network level hold tremendous potential for elucidating underlying features of neural network function in healthy and perturbed condition. It is therefore imperative that the basic characteristics of these widely applied *in vitro* neural network models capture fundamental structural and functional features of neural networks in the brain as accurately as possible. As we have shown, the application of neural interfaces such as the PPs presented in this report has the potential of recapitulating an important aspect of self-organization and connectivity, namely the 3D character of biological neural networks. Importantly, we have shown that the PP structuring increases the possible connectedness between remote, local neuronal clusters through suspended axon bundles, i.e. 'structural short-cuts', this paradigm has the capacity of more realistically capturing features of the small-world architecture of the brain, an attribute which can be pivotal for elucidating structure–function mechanisms translatable to the actual functional (or dysfunctional) human brain from *in vitro* neural network models. Furthermore, although we show features consistent with both structural and functional small-world topology in the PP-structured neural networks in this initial study, further investigations and optimizations of the PPs are needed before a definitive conclusion can be made about the utility of this platform in neural network modelling.

6. Limitations

The electrophysiological data were not post-processed, as the in-house built toolbox for MEA analysis does not allow for filtering of the recorded signal. Ideally, a bandpass filter of 300–3000 Hz should be applied to reduce the influence of local field potentials on the recorded signal. In this study, the spike timestamps used to produce the activity maps (raster plots) were based on a standard thresholding system available through the Multichannel Systems recording software, which manually sets the threshold for each channel at the start of each recording (±5 s.d.). Although relatively common, this approach is not optimal as it does not account for potential signal-drift during the recording period. However, manual inspection of the spikes measured at each channel *post hoc* confirmed that the

recorded spikes tend to correspond to expected values of extracellularly measured action potentials (figure 5) as identified through the signal slope (spike shape) and voltage fluctuation.

Data accessibility. The electrophysiological raw-data files are available within Mendeley as Devold Valderhaug, Vibeke; Sandvig, Axel; Sandvig, Ioanna (2019), 'oeRecordings from 3D NSC-derived neural networks', http://dx.doi.org/10.17632/r9gd7g8zcy.4 [22] under a CC-BY licence. The MEA Analysis Toolbox is available for download at https://github.com/helgeanl/MEA_toolbox.

Authors' contributions. V.D.V. carried out the cell-based experiments and data collection, performed the analysis and wrote the paper; W.R.G. contributed to the conception and design of the study, performed analysis on the size distribution of the polymer particles and wrote parts of the Material and methods section; E.M.S. contributed with functionalization and size distribution analysis of the polymer particles, and contributed to the writing of the Material and methods section; M.Y. contributed to design and functionalization of the polymer particles; A.S. conceived and designed the study, and helped draft and critically revise the manuscript; I.S. conceived and designed the study, carried out the cell-based experiments, and helped draft and critically revise the manuscript. All authors gave final approval for publication and agree to be held accountable for the work performed therein.

Competing interests. We declare we have no competing interests.

Funding. This work was supported by the Department of Neuromedicine and Movement Science, Faculty of Medicine and Health Sciences, NTNU; The Liaison Committee for Education, Research and Innovation in Central Norway; the Joint Research Committee between St Olav's Hospital and the Faculty of Medicine and Health Sciences, NTNU; and internal strategic funding at SINTEF AS.

Acknowledgements. The scanning electron microscopy (SEM) preparation and imaging were provided by the Cellular and Molecular Imaging Core Facility (CMIC), Norwegian University of Science and Technology (NTNU). CMIC is funded by the Faculty of Medicine at NTNU and Central Norwegian Regional Health Authority. Activity maps (raster plots) were produced using an in-house Matlab toolbox created by Helge-André Langåker and Martinius Knudsen at the Department of Engineering Cybernetics at NTNU.

References

1. Frega M, Tedesco M, Massobrio P, Pesce M, Martinoia S. 2014 Network dynamics of 3D engineered neuronal cultures: a new experimental model for in-vitro electrophysiology. *Sci. Rep.* **4**, 5489. (doi:10.1038/srep05489)
2. Tognoli E, Kelso JA. 2014 The metastable brain. *Neuron* **81**, 35–48. (doi:10.1016/j.neuron.2013.12.022)
3. Dranias MR, Ju H, Rajaram E, VanDongen AM. 2013 Short-term memory in networks of dissociated cortical neurons. *J. Neurosci.* **33**, 1940–1953. (doi:10.1523/JNEUROSCI.2718-12.2013)
4. Sporns O. 2010 Connectome. *Scholarpedia* **5**, 5584. (doi:10.4249/scholarpedia.5584)
5. Sporns O, Chialvo DR, Kaiser M, Hilgetag CC. 2004 Organization, development and function of complex brain networks. *Trends Cogn. Sci.* **8**, 418–425. (doi:10.1016/j.tics.2004.07.008)
6. Sporns O, Tononi G. 2002 Classes of network connectivity and dynamics. *Complexity* **7**, 28–38. (doi:10.1002/cplx.10015)
7. Murphy AR, Laslett A, O'Brien CM, Cameron NR. 2017 Scaffolds for 3D *in vitro* culture of neural lineage cells. *Acta Biomater.* **54**, 1–20. (doi:10.1016/j.actbio.2017.02.046)
8. Tedesco M, Frega M, Martinoia S, Pesce M, Massobrio P. 2015 Interfacing 3D engineered neuronal cultures to micro-electrode arrays: an innovative *in vitro* experimental model. *J. Vis. Exp.* **105**, e53080. (doi:10.3791/53080)
9. Zeki S, Shipp S. 1988 The functional logic of cortical connections. *Nature* **335**, 311–317. (doi:10.1038/335311a0)
10. Tononi G, Edelman GM, Sporns O. 1998 Complexity and coherency: integrating information in the brain. *Trends Cogn. Sci.* **2**, 474–484. (doi:10.1016/S1364-6613(98)01259-5)
11. Watts DJ, Strogatz SH. 1998 Collective dynamics of 'small-world' networks. *Nature* **393**, 440–442. (doi:10.1038/30918)
12. Moore C, Newman ME. 2000 Epidemics and percolation in small-world networks. *Phys. Rev. E Stat. Phys. Plasmas Fluids Relat. Interdiscip. Topics* **61**(5 Pt B), 5678–5682. (doi:10.1103/PhysRevE.61.5678)
13. Fornito A, Zalesky A, Breakspear M. 2015 The connectomics of brain disorders. *Nat. Rev. Neurosci.* **16**, 159–172. (doi:10.1038/nrn3901)
14. Bassett DS, Bullmore E. 2006 Small-world brain networks. *Neuroscientist* **12**, 512–523. (doi:10.1177/1073858406293182)
15. Bassett DS, Bullmore ET. 2017 Small-world brain networks revisited. *Neuroscientist* **23**, 499–516. (doi:10.1177/1073858416667720)
16. Verma M, Vats A, Taneja V. 2015 Toxic species in amyloid disorders: oligomers or mature fibrils. *Ann. Indian Acad. Neurol.* **18**, 138–145. (doi:10.4103/0972-2327.150606)
17. Goedert M, Masuda-Suzukake M, Falcon B. 2017 Like prions: the propagation of aggregated tau and alpha-synuclein in neurodegeneration. *Brain* **140**, 266–278. (doi:10.1093/brain/aww230)
18. Harada T, Hirabayashi Y, Hatta Y, Tsuboi I, Glomm WR, Yasuda M, Aizawa S. 2015 Kinetics of hematopoietic stem cells and supportive activities of stromal cells in a three-dimensional bone marrow culture system. *Growth Factors* **33**, 347–355. (doi:10.3109/08977194.2015.1088534)
19. Hirabayashi Y, Hatta Y, Takeuchi J, Tsuboi I, Harada T, Ono K, Glomm WR, Yasuda M, Aizawa S. 2011 Novel three-dimensional long-term bone marrow culture system using polymer particles with grafted epoxy-polymer-chains supports the proliferation and differentiation of hematopoietic stem cells. *Exp. Biol. Med. (Maywood)* **236**, 1342–1350. (doi:10.1258/ebm.2011.011075)
20. Yasuda M, Kunieda H, Ono K, Ogino H, Iwasaki T, Hiramoto M, Glomm WR, Hirabayashi Y, Aizawa S. 2011 Adhesive cell cultivation on polymer particle having grafted epoxy polymer chain. *Tissue Cell* **43**, 115–124. (doi:10.1016/j.tice.2010.12.007)
21. Fukino N, Harada T, Tsuboi I, Fukui S, Yasuda M, Aizawa S. 2016 *In vitro* chemosensitivity study of human leukemic cells in a three-dimensional bone marrow culture system. *System* **10**, 13–16.
22. Valderhaug V, Sandvig A, Sandvig I, 2019. Data from: Recordings from 3D NSC-derived neural networks. *Mendeley Data. v4*. (doi:10.17632/r9gd7g8zcy.4)
23. Latora V, Marchiori M. 2001 Efficient behavior of small-world networks. *Phys. Rev. Lett.* **87**, 198701. (doi:10.1103/PhysRevLett.87.198701)
24. Marom S, Shahaf G. 2002 Development, learning and memory in large random networks of cortical neurons: lessons beyond anatomy. *Q. Rev. Biophys.* **35**, 63–87. (doi:10.1017/S0033583501003742)
25. Bettencourt LM, Stephens GJ, Ham MI, Gross GW. 2007 Functional structure of cortical neuronal networks grown *in vitro*. *Phys. Rev. E Stat. Nonlin. Soft Matter Phys.* **75**(2 Pt 1), 021915. (doi:10.1103/PhysRevE.75.021915)

Supplementary information

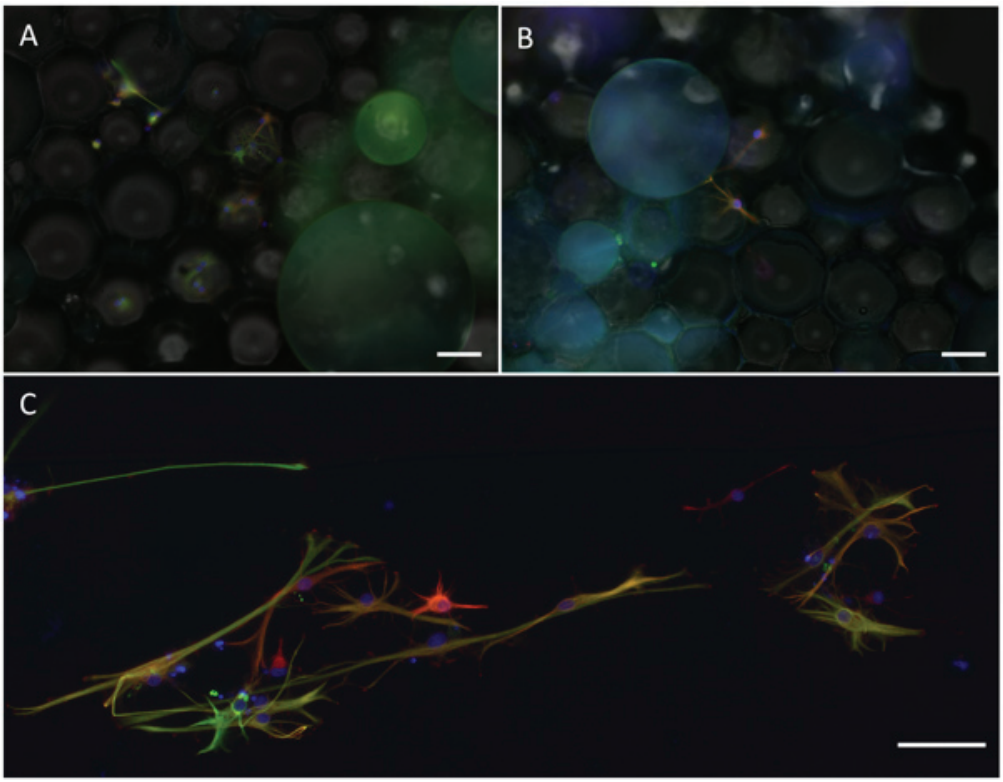

Supplementary Figure 1. Immunocytochemistry demonstrating the presence of neural lineage markers in the neural networks developed on the surface-grafted polymer particles (PPs). Following 1 month of differentiation and maintenance of the rat NSCs on the PPs, immunocytochemistry confirmed the presence of differentiated cells attached to the surface of the particles. **A,B**) Fluorescently labelled single cells attached to the surface of the PPs. The anti-CNPase antibody (red) shows oligodendrocytes, while anti-GFAP antibody (green) shows astrocytes and other glial cells. Anti-MAP2 staining is also consistent with the presence of cells of a neuronal fate in **B** (magenta). The single-color channels are merged and overlaid by a brightfield image of the same area. **C**) Fluorescently labelled cells from the same sample attached to the well-plate surface. 100µm scalebars.